Alma Mater Studiorum – Università di Bologna

DOTTORATO DI RICERCA IN

NANOSCIENZE PER LA MEDICINA E PER L'AMBIENTE

Ciclo 35

Settore Concorsuale: 03/A2 – MODELLI E METODOLOGIE PER LE SCIENZE CHIMICHE

Settore Scientifico Disciplinare: CHIM/02 – CHIMICA FISICA

MULTI-FUNCTIONAL ELECTROCATALYSTS FOR CO_2 REDUCTION REACTION: TOWARDS THE MODULATION OF SELECTIVITY

Presentata da: Miriam Moro

Coordinatore Dottorato

Dario Braga

Supervisore

Giovanni Valenti

Co-supervisore

Francesco Paolucci

Esame finale anno 2023

Summary

Abstract

The continuous increase in the concentration of CO_2 in the atmosphere by human activities is the main cause of global warming and climate change. In this context, there are also scarce energy sources, which have to cope with an ever-increasing demand. From this point of view, the electrocatalytic reduction of CO_2 is a captivating strategy for the conversion of CO_2 into fuels, for the realization of a carbon neutral circular economy. In recent years, research has focused on the development of new materials and technologies capable of capturing and converting CO_2 into useful products. Among the various CO_2 reduction products, formic acid, and syngas (mixture of hydrogen and carbon monoxide) are particularly interesting. Formic acid has a high hydrogen volumetric density, low toxicity, and liquid state, making it a valuable hydrogen storage vector. While syngas, H_2/CO mixture, finds various applications, from the production of energy to the synthesis of chemical reagents. The main problem of CO_2 reduction reaction (CO_2RR) is given by the poor selectivity of this reaction which can lead to the formation of numerous reaction products, to the detriment of efficiencies. For this reason, the design of new electrocatalysts that reduce CO_2 in a selective and efficient fashion is a key step for future exploitation of this technology. Here we present a new class of electrocatalysts, designed with a modular approach, namely, deriving from the combination of different building blocks in a single nanostructure. With this approach it is possible to obtain materials with an innovative design and new functions, useful for creating a high selectivity for CO_2RR.

By combining the unique physic-chemical properties of carbon nanostructures (CNS) with nanocrystalline metal oxides (MO), we are able to modulate the selectivity of CO_2RR, with the production of formic acid and syngas at low overpotentials (e.g., in the Chapter I, MWCNT@CeO_2 reach the 65 % of FE_{HCOOH} at -0.02 V overpotential). The CNS have not only the task of stabilizing the MO nanoparticles, but the creation of an optimal interface between two nanostructures is able to improve the catalytic activity of the active phase of the material (e.g., Chapter II, the rGO@Bi@Bi_2O_3 achieves the 38 % FE_{HCOOH} compared to 0 % of Bi_2O_3 without rGO). While the presence of oxygen atoms in the active phase creates defects that accelerate the reaction kinetics and stabilize certain reaction intermediates, selecting the reaction pathway. In this thesis, it will be demonstrated how the interconnections between the various components are fundamental for the efficient reduction of CO_2 to formic acid and syngas, opening up new possibilities in the design of optimized electrocatalytic materials.

Finally, a part will be dedicated to the study of the experimental parameters that influence the CO_2RR, beyond the electrocatalyst used, trying to improve the experimental set up in order to achieve commercial catalytic performances.

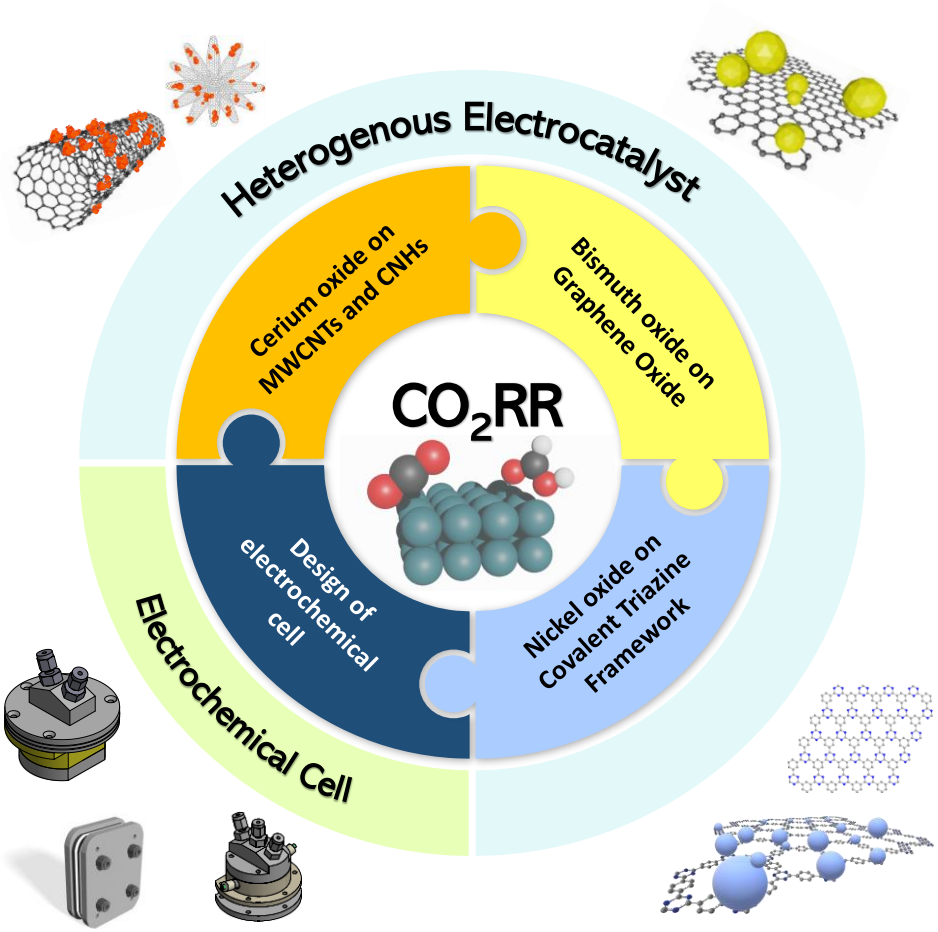
Heterogenous Electrocatalyst
Cerium oxide on MWCNTs and CNHs
Bismuth oxide on Graphene Oxide
CO_2RR
Design of electrochemical cell
Nickel oxide on Covalent Triazine Framework
Electrochemical Cell

Introduction

I.1 Overview of CO_2

The average CO_2 concentration in atmosphere increased from about 277 parts per million (ppm) in 1750 to 414 ppm in 2020 (up 49%) (Figure I.1). Initially, the increase in atmospheric CO_2 from pre-industrial values was due to deforestation and other land-use change activities. While the emission of CO_2 from fossil fuels began with the Industrial Era, becoming the main source of anthropogenic emission, whose value is constantly increasing.[1] For millions of years, the CO_2 produced has been assimilated by plants to form energy-rich compounds (carbohydrates) with photosynthesis, in this way nature has been able to maintain a carbon neutral cycle and a sustainable environment. The advent of the industrial revolution and modern civilization, the intense use of fossil fuels has meant that human activity influenced the natural carbon cycle, releasing more CO_2 into the atmosphere than can be consumed.[2]

The CO_2 is one of the greenhouse gases (GHG) that contribute most to global warming. In fact, the GHG absorb the Infrared Radiation (IR) emitted by the Earth, preventing it from leaving the atmosphere, and causing an increase the surface temperature of the Earth. The increase in the concentration of CO_2 in the

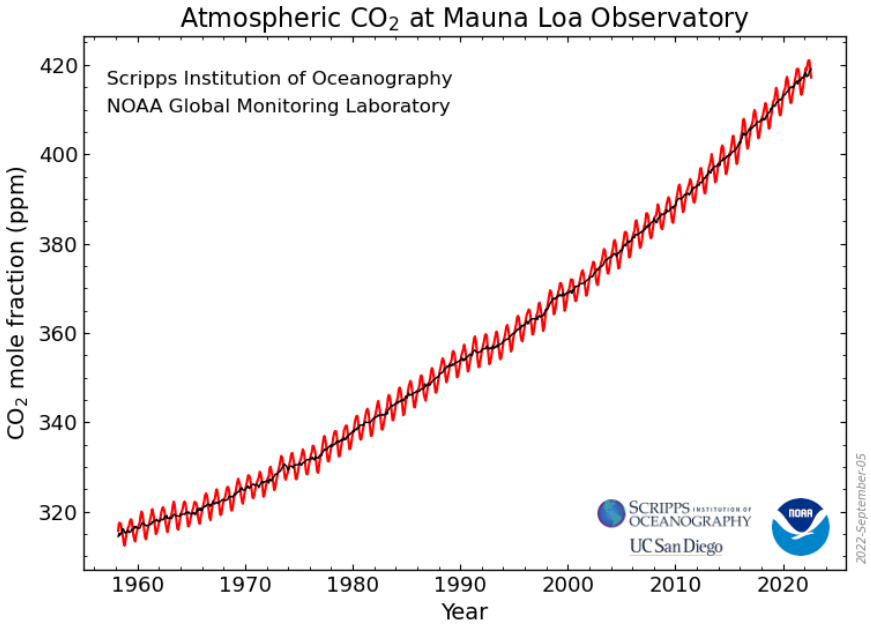

Figure I.1 The graphs show monthly mean carbon dioxide measured at Mauna Loa Observatory, Hawaii. The red lines represent the monthly mean values, centered on the middle of each month. The black lines represent the same, after correction for the average seasonal cycle. The last year of data are still preliminary. Data are reported as a dry air mole fraction defined as the number of molecules of carbon dioxide divided by the number of all molecules in air, including CO_2 itself, after water vapor has been removed. The mole fraction is expressed as parts per million (ppm).

atmosphere and consequently of global warming is causing irreversible climatic changes. To the negative impact on humanity and ecosystems, the global warming is the most important environmental problem the world faces.[3] To cope with global warming and its inexorable consequences, it was necessary to establish the *Intergovernmental Panel Climate Change* (IPCC) with the aim of studying and reporting on climate change. The latest report revealed the need to contain the increase in the global mean surface temperature (GMST) to 1.5 ° C compared to pre-industrial values by 2100[4]. In fact, an increase of 2 °C would lead to catastrophic and irreversible climate changes: extreme atmospheric phenomena, desertification, floods, floods, acidification of the seas and the loss of habitat and animal species.[5]

Despite the numerous policies implemented to mitigate and reduce the emission of anthropogenic CO_2, these emissions do not tend to decrease, indeed they continue to increase inexorably. Although the goal of investing more in renewable energy, independence from fossil fuels is unthinkable. In fact, it has been estimated that in 2100, 65% of the global energy demand will still be met by fossil fuels.[6]

For this reason, research is already working to reduce excess CO_2 in the atmosphere by adopting other methods, such as carbon capture and storage (CCS). The direct capture of CO_2 from the exhaust fumes of industrial plants and power plants is an excellent way to prevent its emission into the atmosphere. However, these methods suffer from significant limitations due to saturation, capacity and permanence limits during the capture and storage processes. In addition, the high implementation costs, inefficient framework, and power penalties are other obstacles when using CCS technology.[7] Another method of limiting CO_2 in the atmosphere is its recycling, or rather, converting CO_2 into a useful product, such as a carbon source in the synthesis of chemicals or fuels.[8]

I.2 CO_2 conversion

There are numerous CO_2 conversion methods: thermochemical, chemical, photochemical, biochemical, and electrochemical. The CO_2 is a particularly stable molecule, consequently, the pure splitting is mainly ineffective (the Gibbs free energy of formation for C –O bond is −394 kJ/mol), indeed, to take place it requires the use of a high thermal energy and highly reactive catalyst.[7] Direct splitting of CO_2 in CO and O_2 with the use of membranes and high temperatures is absolutely not feasible on an industrial scale, due to the high costs, low efficiencies and high energies. Moreover, this gas mixture at high temperatures becomes explosive.

The photocatalytic approach for the CO_2 reduction is eco-friendly approach, because to be realized it require a very low temperature and a small amount of input energy, which derives by abundant solar light. This makes the process advantageously economical.[7,9] The photochemical conversion of CO_2 takes place in five main steps: light absorption, charge separation, CO_2 adsorption, surface redox reaction and product

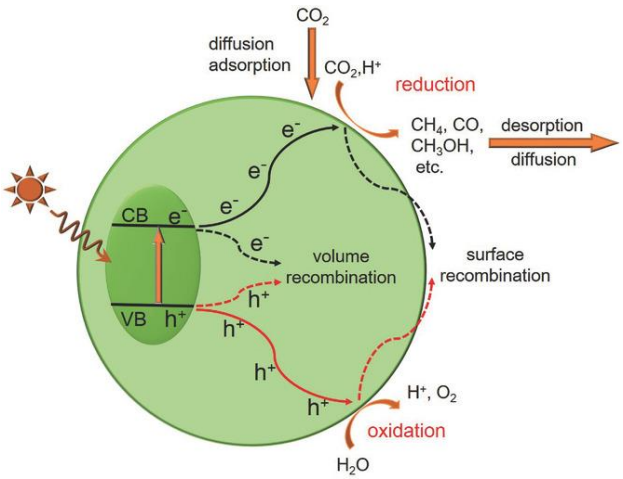

Figure I.2 Diagram describing the five fundamental steps of the photocatalytic reduction of CO_2. Reprinted from Adv.Sci.2017, 4, 1700194.[10]

desorption. With the absorption of photons by the semiconductor there is the excitation of the electrons that pass from the valence band (VB) to the conduction band (CB), generating the holes in the VB. To reduce CO_2 and oxidize water, the electrons or photogenerated holes must be energetically favourable, so the photocatalysts must have an adequate band structure. CB must have a more negative energy value than the redox potential of CO_2 reduction, while VB must be more positive than the redox potential of water oxidation. The photocatalysts must have a band gap greater than the difference potential between the two redox reactions, but small enough to absorb a large part of the solar spectrum.[10] The second step involves the spatial separation of the electrons and the photogenerated holes. The problem is that this process is in direct competition with the charge recombination process, which is usually favoured. Subsequently, with the adsorption of CO2 on the surface of the material, there is the initiation of the redox reaction with the transfer of electrons and photogenerated holes. The latter is a purely electrochemical step. However, as can be seen from the description of the reaction mechanism, this process is very complicated, so that the photocatalytic activity and efficiency are very low.[8]

The biological approach aims to mimic the mechanisms already present in nature for the conversion of CO_2 into biomass or biofuel. The fixing and conversion capabilities of the biological can be enhanced via metabolic engineering.[11] But this approach has numerous limitations: enzymes need high optimal temperatures to work which are not compatible with organisms; different enzymes can have different optimal temperatures; some synthetic enzymes are lethal to cells; high concentrations of CO_2 (>5%) can reduce the growth and regeneration of microorganisms.[11,12] Therefore, there is still a lot of work to be done to make this process efficient and feasible on an industrial scale.

The electrochemical conversion is one of the most attractive methods thank to its advantages:

- the process can be performed at room temperature and ambient pressure;
- it requires low energy;

- electronic power can be obtained from renewable sources such as solar, wind, hydroelectric, geothermal, tidal, and thermoelectric processes;
- the process is highly controllable, in fact by controlling the potential and the temperature the reaction products can be controlled;
- this conversion process is modular, compact, on-demand and can easily be scaled up for different applications.[13]

All these advantages combined with the possibility of reusing the electrolyte without emitting new CO_2 into the atmosphere makes the electrochemical reduction process the best option for CO_2 conversion (Figure I.3).

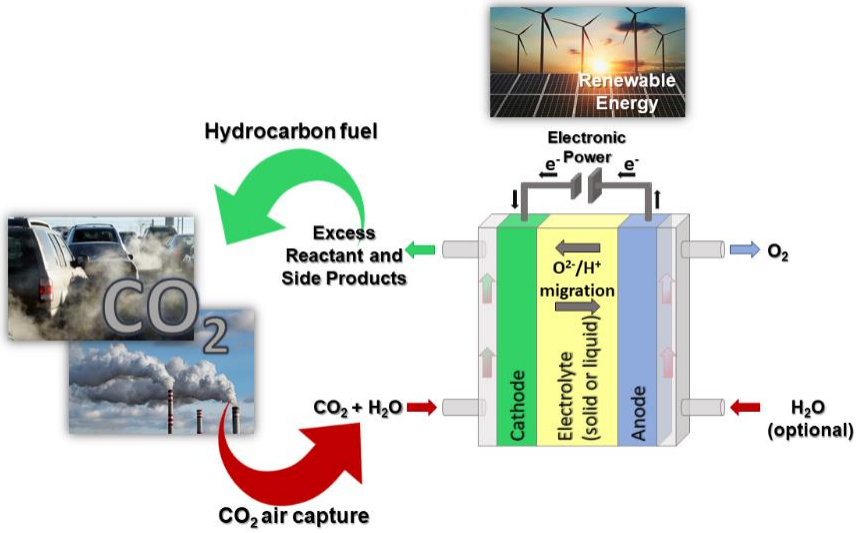

Figure I.3 Graphic representation of the production of high-value products by the electrochemical reduction of CO_2 making use of renewable energy sources.

I.3 CO_2 Electrochemical Reaction

As with other approaches, electrochemical conversion also presents challenges. As previously mentioned, the CO_2 molecule is thermodynamically stable, where the carbon atom is bonded to two oxygen atoms via a strong double bond (the Gibbs free energy of formation for C –O bond is −394 kJ/mol). This means that the system requires a very high energy input for the breaking of the double bonds. In fact, the potential to be supplied to the system for the direct reduction with the formation of the $CO_2^{\bullet-}$ radical anion is -1.90 V vs SHE.[14,15] For this reason, in order that the reaction to take place it is necessary to use a catalyst that reduces the overpotential. The use of a catalyst modifies its reaction mechanisms, in fact, the electrochemical reduction occurs in several steps with the multiple exchange of protons and electrons and the formation of products “P” and water:

$$kCO_2 + n(H^+ + e^-) \rightleftarrows P + mH_2O \qquad \text{(I.1)}$$

where k,n and m are the coefficients that change in base on reaction product. Table I.1 shows the main reaction products with their respective potential standards.[16]

Table I.1Main Products of the Electrochemical Reduction of CO_2

Product name and formula	***k***	***n***	***m***	**E^0 (V vs RHE)**
Carbon monoxide, CO	1	2	1	-0.10
Formic acid, HCOOH	1	2	0	-0.20 *(for pH < 4)*; -0.20-0.059[pH-4] *(for pH > 4)*
Formaldehyde, HCHO	1	4	1	-0.07
Methanol, CH_3OH	1	6	1	0.02
Methane, CH_4	1	8	2	0.17
Ethanol, CH_3CH_2OH	2	12	3	0.09
Ethylene, C_2H_4	2	12	4	0.08

The use of the catalyst makes it possible to circumvent the problem of the high energy required to activate the reduction of CO_2, but it introduces another problem: selectivity. Indeed, the CO_2 reduction reaction (CO_2RR) can lead to the formation of numerous products, which have very similar thermodynamic potentials (Figure I.4).[17] In the same window of potential, another reaction competing with the CO_2RR takes place, namely the hydrogen evolution reaction (HER). The reduction of the water, contained in the electrolyte, further reduces the efficiency of the catalyst. Therefore, it is essential to make a catalyst with a reasoned

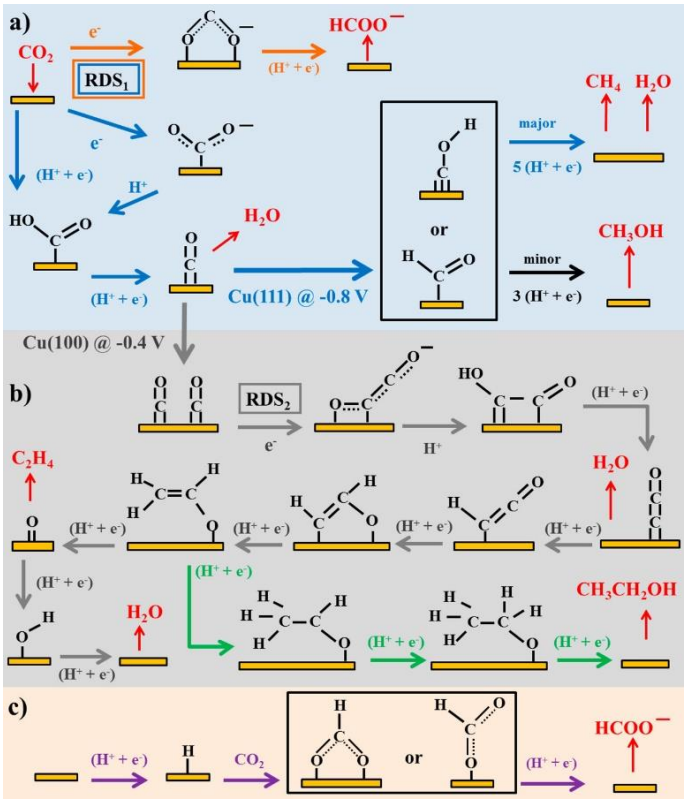

Figure I.4 Possible reaction routes for the electrocatalytic reduction of CO_2 on transition metals and molecular catalysts. Reprinted with permission from J. Phys. Chem. Lett. 2015, 6, 20, 4073–4082. Copyright© 2015, American Chemical Society.[16]

design so that there is a high selectivity for CO_2 reduction and the contribution to hydrogen evolution is minimized.

The selectivity of CO_2RR depends on numerous factors: electrolyte, pH, potential, catalyst material and its crystallinity. All these factors can influence the reaction intermediates and, thus the final products. The role of the electrolyte is fundamental. In fact, the type of solvent and the pH affect the concentration of the reactants, CO_2, H^+ and *H (adsorbed hydrogen on catalyst surface). Moreover, the presence of determined cations and anions in the electrolyte can stabilize some reaction intermediates and inhibit others.[18] The reaction can only take place at acidic and neutral pH. This happens because, when CO_2 is dissolved in aqueous electrolytes it changes its pH, acting on the equilibrium of the carbonate in water according to these reactions (I.2), (I.3), (I.4):[19]

$$CO_2(aq) + H_2O(l) \rightleftarrows H_2CO_3(aq) \quad \text{(I.2)}$$

$$H_2CO_3(aq) \rightleftarrows H^+(aq) + HCO_3^-(aq) \quad \text{(I.3)}$$

$$HCO_3^-(aq) \rightleftarrows H^+(aq) + CO_3^{2-}(aq) \quad \text{(I.4)}$$

Depending on the CO_2 concentration in the solution, the pH and the concentration of the species can be modified (Figure I.5).

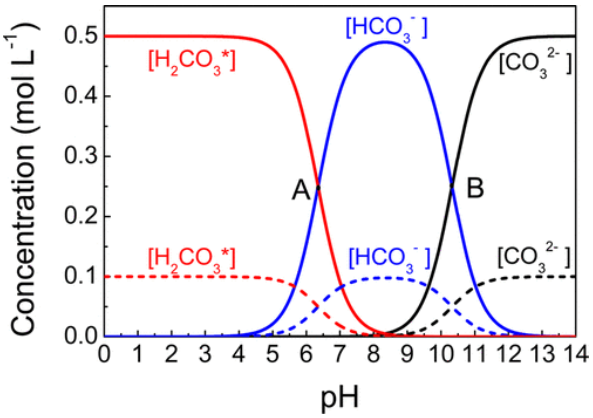

Figure I.5 Distribution of carbonaceous species in water solution with pH at different total dissolved carbon concentrations (TC= sum of dissolved CO_2 and H_2CO_3). The solid line is for TC concentration of 0.5 M, while the dashed line for 0.1 M at temperature 25 °C. Reprinted with permission from J. Phys. Chem. C 2015, 119, 1, 55–61. Copyright© 2015, American Chemical Society.[17]

For this reason, it is a good solution to use a buffer solution to keep the pH constant. In this way, the only pH fluctuations will occur in the proximity of the electrode (local pH) based on the consumption of protons or the generation of OH^- ion during the reaction. In aqueous electrolytes, in addition to the HER problem, the low solubility of CO_2 is also added, which limits the process. One way to solve both problems is to use aprotic solvents, where the absence of water increases the efficiency of CO_2 reduction, and totally modifies its selectivity.[16] First of all, the solubility of CO_2 in DMSO and acetonitrile (AN) is about four times higher than

that in water, while in CH_3OH and DMF it is about five and twenty times higher.[20] In the absence of protons, CO_2RR can no longer occur by means of the proton-coupled electron transfer reaction mechanism, as a result, the mechanism and also the population of the reaction products changes. In aprotic solvents only two reaction products are identified: oxalate anion and CO.[21] For metals such as Pt, Pd, Au and Zn, the main reaction products are the carbonate ion and CO, which are generated through a reductive disproportion:

$$CO_2^{\bullet -} + CO_2 + e^- \rightarrow CO + CO_3^{2-} \quad \text{(I.5)}$$

While for metals such as Pb, In, Sn, and Hg, the oxalate anion is produced by dimerization:[22]

$$(CO_2)_{ads} + e^- \rightarrow (CO_2^{\bullet -})_{ads} \quad \text{(I.6)}$$

$$(CO_2^{\bullet -})_{ads} + (CO_2)_{ads} \rightarrow (O_2C - CO_2^{\bullet -})_{ads} \quad \text{(I.7)}$$

$$(O_2C - CO_2^{\bullet -})_{ads} + e^- \rightarrow {}^-O_2C - CO_2^- \quad \text{(I.8)}$$

But the use of non-aqueous solvents inhibits the commercial application of this conversion method, both for the conditions of use and for the limited reaction products.

I.4 Electrocatalyst for CO_2RR

A catalyst for CO_2RR must have high selectivity, stability, and sufficient electronic conductivity. The key parameters to evaluate the performance of a catalyst are: i) overpotential, is the potential difference between a thermodynamic reaction potential and the potential at which the redox event occurs experimentally; ii) the faradaic efficiency (FE), which describes the efficiency with which charge (electrons) is transferred in a catalyst facilitating an electrochemical reaction, in this case the percentage of electrons exchanged to form a determinate product in relation to total charge supplied, moreover, it also provides an indication of the selectivity of the material.; iii) the current density, as a parameter of reaction rate; iv) stability [23] The catalyst for CO_2RR can be divided in two categories: homogeneous and heterogenous catalyst (Figure I.6).[24]

I.4.1 Homogeneous electrocatalyst for CO_2RR

Homogeneous catalysts are molecular catalysts, typically consisting of organometallic complexes, which are able to electrochemically reduce CO_2 when dissolved in organic electrolytes. The catalyst acts as a redox mediator between the electrode and the reagent molecule, so it must have a well-defined standard potential, i.e., between the standard potential of the global electrochemical reaction and the potential where the direct electrochemical reaction takes place.[25] In molecular catalysis, the electrode does not play an active role in the electrochemical reaction, but acts as an electron donor (or acceptor), while the true active species is

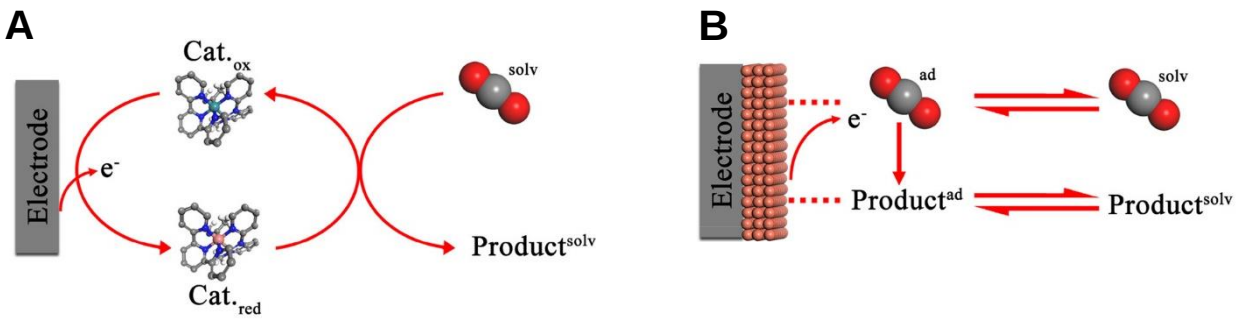

Figure I.6 Schemes for CO_2 reduction by different electrocatalysts: (A) homogeneous and (c) heterogeneous way. Adapted with permission from Acc. Chem. Res. 2020, 53, 1, 255–264. Copyright© 2020, American Chemical Society.[24]

electrogenerated in situ: when the electrode is polarized, the organometallic complex is reduces, forming an active species which in turn reacts with the reactant molecule. Given the type of process involved, only a small part of the catalyst in solution will be directly involved in the reaction, namely, the species confined near the electrode surface.[26]

An example of a homogeneous electrocatalyst for CO_2RR is the ruthenium-based complex, $[Ru(bpy)_2(CO)_2]^{2+}$, which has been shown to reduce CO_2 to CO in acetonitrile and methanol.[27] While, complex analogues of rhodium and iridium, in which the same type of binder has been used, are capable of producing formate, although competing with the evolution of hydrogen.[28] Numerous experimental and theoretical studies have been conducted to understand the electrochemical CO_2 reduction mechanism on metal complexes, however the details on the mechanistic pathways still remain uncertain.[16] Although the homogeneous catalysts show excellent performances in terms of efficiency and selectivity, their application is inhibited by their high toxicity, low long-term stability and by the difficulty of separating the reaction products from the catalyst.

I.4.2 Heterogenous electrocatalyst for CO_2RR

In contrast, the heterogeneous electrocatalysts allow to separate the reaction products from the catalysts without problems, and there aren't risk about the toxicity. The main heterogeneous catalysts are made up of transition metals, as their electronic structure (i.e., density of state) allow determinate the reaction pathway in based on adsorption energy of intermediates. Indeed, the specific interaction of the metal site with H^+, CO_2 or CO_2RR intermediates determines the selectivity of the overall process.[26] It is possible to subdivide the transition metals on the basis of this interaction, and therefore of the final products. Metals such as Sn, In, Pb, and Bi lead to the formation of formate ($HCOO^-$) because *OCHO is the reaction intermediate energetically favoured (Figure I.4 light blue route[29]). While metals, where the *COOH is energetically favoured, and *CO is weak bind, lead to the formation of CO (Figure I.7 yellow route). In this case, the metals are Au, Ag, Zn, Ni and Pd.[30] If the bond of the *CO is slightly stronger, it can undergo other reactions (chemical / electrochemical) with the formation of other products, such as hydrocarbons and

alcohols. This is the case of Cu. While, if the bond of the *CO is excessively strong, there is catalyst poisoning, with total blocking of the catalytic sites, as in the case of Pt.[26]

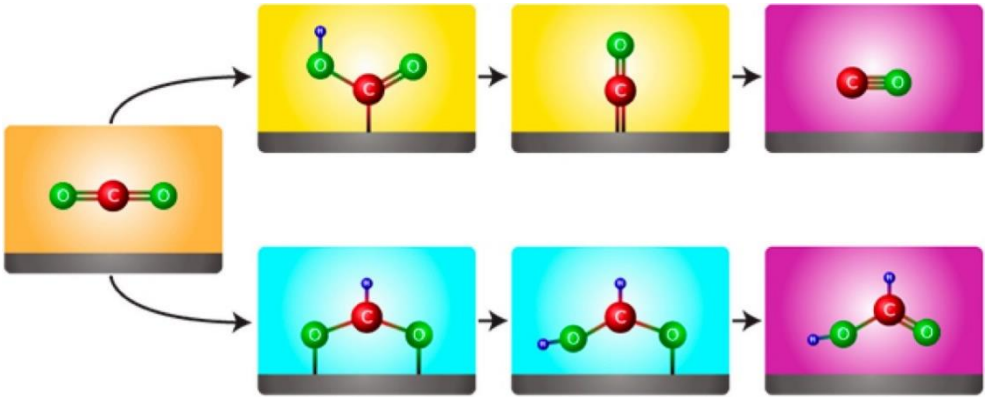

*Figure I.7 Representation of two reaction mechanisms for CO and $HCOO^-$ production from CO_2. In the first electrochemical step, the CO_2 can bind to the electrode surface through the carbon or the oxygens, resulting in an adsorption intermediate, *COOH, or a bidentate *OCHO intermediate, respectively. The second electrochemical step results in the production of CO or $HCOO^-$. Reprinted with permission from ACS Catal. 2017, 7, 7, 4822–4827. Copyright© 2017, American Chemical Society.[29]*

I.5 Strategies for Catalyst Development

Therefore, knowing the properties of the materials allows to modulate the catalytic activity for CO_2RR. For this reason, in recent years research has focused on the study and development of new catalysts with superior catalytic properties, both in terms of efficiency and selectivity. There are two main strategies to improve the catalytic activity of electrocatalyst: increasing the number of active site and increasing the intrinsic activity of the material (Figure I.8)[31]. These two properties can be modulated through surface engineering, nanostructuring and introduction of heterogenous atoms.

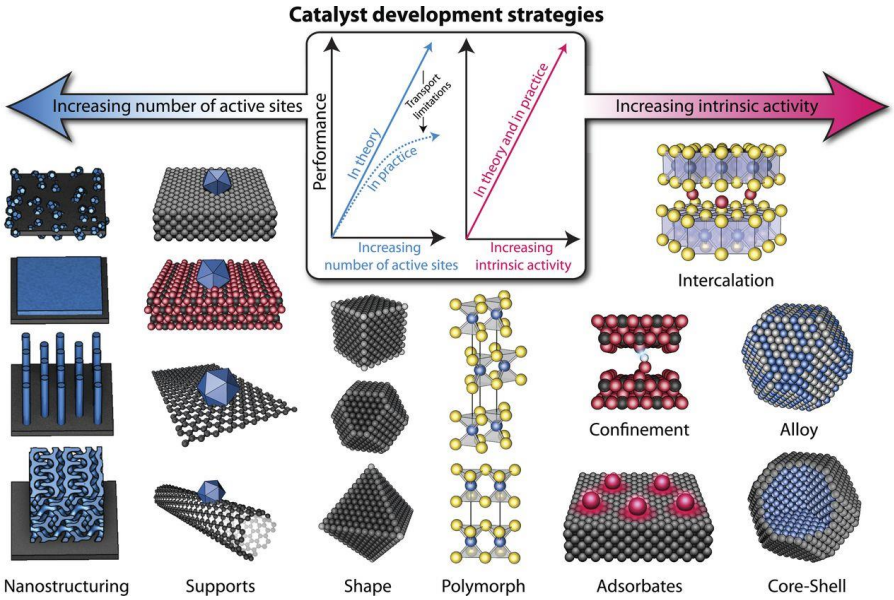

*Figure I.8 Schematic representation of various catalyst development strategies: increasing the number of active sites and increasing the intrinsic activity. Figure from She, Z. W. et al., Combining theory and experiment in electrocatalysis: Insights into materials design, Science, **355**, (2017).* [31]

I.5.1 Surface Engineering and Nanostructuring

A strategy for modifying catalytic activity is surface engineering. In fact, a number of studies, both experimental and theoretical, have shown that the surface morphology of the electrocatalyst has a strong impact on the performance of CO_2RR. The best known example derives from the work of *Hori*, who studied the effect of the morphologies of Cu for the selectivity and efficiency of CO_2RR, highlighting how the Cu (100) lead to the formation preferentially of ethylene, while on Cu (111), the methane is the main reaction product.[32] In this study it was highlighted how certain crystalline planes of the same element can show completely different activities and selectivity. Of course, these properties not only concern Cu, but also other transition metals have been shown to influence the reaction pathway according to the crystallographic planes exposed. In fact, crystalline planes with undercoordinated metal atoms (e.g., high Miller index surfaces) have been shown to have stronger interactions with reaction intermediates than highly coordinated atoms, resulting in greater selectivity at lower potentials. An example is given by the work of *Back et al.*, who showed that Au (211) binds the *COOH intermediate with a stronger interaction, compared to the surface Au (111), which is close-packed surface.[33]

There are different strategies to create catalytic sites with a low coordination number, through the regulation of the shape and size of the catalysts (nanostructuring), and through epitaxial growth of crystals. The latter method involves the epitaxial growth of the catalyst on a single crystal, which is used as a substrate. The use of a monocrystalline substrate allows to control the orientation of the growth of the material through the interfacial energy.[34] Physical vapor deposition (PVD) techniques are usually used to create epitaxial growths of this type.

In the case of nanostructuring, there is a reduction in the size of materials at the nanoscale. This approach allows to obtain nanostructured electrocatalysts with unique electronic structures and physical properties, completely different from the corresponding bulk materials.[30] First of all, with nanostructuring a greater density of the active sites available is obtained, since, for the same mass, the exposed surface of the material increases. Furthermore, with nanostructuring it is possible to create crystallographic faces with undercoordinated atoms, which can favour CO_2RR, accelerating it and stabilizing some reaction intermediates. *Cuenya et al.* investigated the effect of Cu nanoparticle size for CO_2RR, observing how size affected the coordination number of atoms, resulting in selectivity for CO_2RR rather than HER.[35] In fact, the bond strength with the reaction intermediates is conditioned by the state of coordination of the surface atoms, not to mention that in a sufficiently large surface the availability of neighbouring intermediates increases, which can undergo further reactions (hydrocarbons production). Besides controlling the size and shape of the nanostructures, from which certain properties derive, nanostructuring allows to influence the local electric field.

In fact, when an electric field is applied in nanostructures with high curvature, they generate an amplification, which leads to an increase in the local concentration of cations in the electrolyte. This effect results in a higher concentration of CO_2 near the surface of the catalyst.[36]

Unfortunately, one of the main problems of nanostructured materials is their stability under electrolysis conditions, with the formation of large aggregates, or the growth of larger nanoparticles. In both cases there is a loss of performance. Usually, this phenomenon is caused by aggregation or coalescence processes.[37] One way to increase the stability of the nanostructure is to combine it with supports, generating nanocomposite materials.[38]

I.5.2 Introduction of Heterogeneous Atoms

The intrinsic activity of the catalyst can be modulated by introducing heterogeneous atoms, which (i) modify the electronic structure of the transition metals by means of the ligand effect, (ii) offer additional bonding geometries for reaction intermediates, or (iii) create lattice deformations.[30] These effects can be achieved by introducing several heteroatoms. In the case of the introduction of a second metal species, a massive alloy is formed. While in the case of doping, a small concentration of heteroatoms is introduced, which locally alter the oxidation state of the metal species. The example is provided by *Zhou et al.*, who made a material of Cu doped with boron, highlighting how the Cu close to the doped sites had a more positive valence state than pure Cu.[39] This higher oxidation state led to an increase in the strength of interaction with the intermediate *CO, inducing easy dimerization. In fact, on this material an FE for C_{2+} products are obtained at about 79% at -1.1 V vs RHE.

Among the materials modified with the introduction of heteroatoms, we find the oxide-derivatives, which show interesting properties. They are metal oxides, which under the conditions of CO_2 electrolysis undergo a partial or total electrochemical reduction, as they are thermodynamically favourable to reduce at negative potentials. The chemical state of metals depends on various conditions, such as pH, potential, temperature, and concentrations. An indication of the state of the metal can be obtained, using the Pourbaix diagrams, a graphical representation of the thermodynamic equilibrium potentials between a metal and its various oxidized species for various pH.[40]

There are several benefits deriving from this treatment: metastable electronic structures, roughened surfaces, rising local pH, and increased grain boundaries.[30] There is an increase in local pH due to the release of OH^- ions during the reduction of the metal oxide, and it has been shown that increasing pH inhibits HER.[41] Moreover, once the metal oxide is reduced, it forms a porous surface and rich in defects, which is affected electronically, thus modifying the interaction with the reaction intermediates.[42] Without forget that, in the

partially reduced metal oxides, the presence of oxygen modifies the electro-donation effect of the metallic site. All these properties make metal oxide-based catalysts particularly promising for CO_2RR.

I.6 Design of electrochemical cell for CO_2RR

One of the key aspects in CO_2 reduction is the design of the electrochemical cell. Beyond the catalyst and electrolyte used, the cell design can considerably affect the efficiency and selectivity of the reaction.

The H-cells are the most used cells in laboratory tests, due to their low cost, easy maintenance, and assembly. Basically, they consist of two chambers, one cathodic and one anodic, separated by an ionic membrane, where the cathode is completely immersed in the electrolyte. Here one of the great problems and limitations of the CO_2RR: low CO_2 solubility in aqueous electrolytes. The solubility of CO_2 in aqueous electrolytes and under ambient condition is only 0.034 M, this limits the CO_2 reduction, leading to current densities below $j <$ 100 mA cm^{-2}.[20] Furthermore, this configuration further limits the process due to the limited electrode area and the large gap between the electrodes. To resolve these problems, the flow reactor was proposed. In the flow cell, a gaseous stream of CO_2 is injected directly onto the cathode, solving mass transport problems, and increasing the current density. In addition to these aspects, a reactor allows greater control of the temperature, and of the residence time of the reaction mixture in the reactor.[43]There are different reactor configurations, but the universal architecture is formed by two flow channels (Figure I.9 A), one for the catholyte and the other for the anolyte, divided by ion-exchange membrane. In this cell, the electrocatalysts is immobilized on the gas diffusion layer (GDL), a thin electrode with a porous structure, equipped high electrical and thermal conductivity and chemical/corrosion resistance. The electrocatalyst immobilized on the GDL constitutes the gas diffusion electrode (GDE) (Figure I.9 B).

The GDL usually consists of carbon fibers or compressed carbon particles. The GDL has a double function: to allow the optimal transport of material on the surface of the catalyst and to ensure an excellent electrical contact between the electrocatalyst and the collector. The porous structure allows the permeation of gaseous CO_2 into the electrode, with the formation of a three-phase contact (gas-liquid-solid) CO_2-electrolyte-electrocatalyst. The porous structure, in addition to solving the problem of mass transport, increases the surface area of the electrode and the exposure of the active sites of the catalyst.[44] To obtain a perfect triphasic contact, an excellent combination of hydrophobicity / hydrophilicity of the GDL is necessary: the solution must remain in contact with the catalytic site enough for the reaction to take place, but not too much to favor the parasite reaction.[43] Research has found a way to solve this problem and increase the stability of GDLs by introducing hydrophobic scaffold of polytetrafluoroethylene (PTFE) into GDLs.[45] The use of electrodes with interesting properties such as GDLs, and innovative cell designs, allow to improve the CO_2RR with the increase of the current at commercial values ($j >$ 200 mA cm^{-2}). If the flow cell allows to improve some critical aspects of CO_2RR, it modifies others, all still to be studied. In fact, a different residence

time of the reactants and products on the catalyst surface can modify their selectivity. In addition to the stabilization of the local pH on the electrode surface due to the electrolyte flow.[43,46]

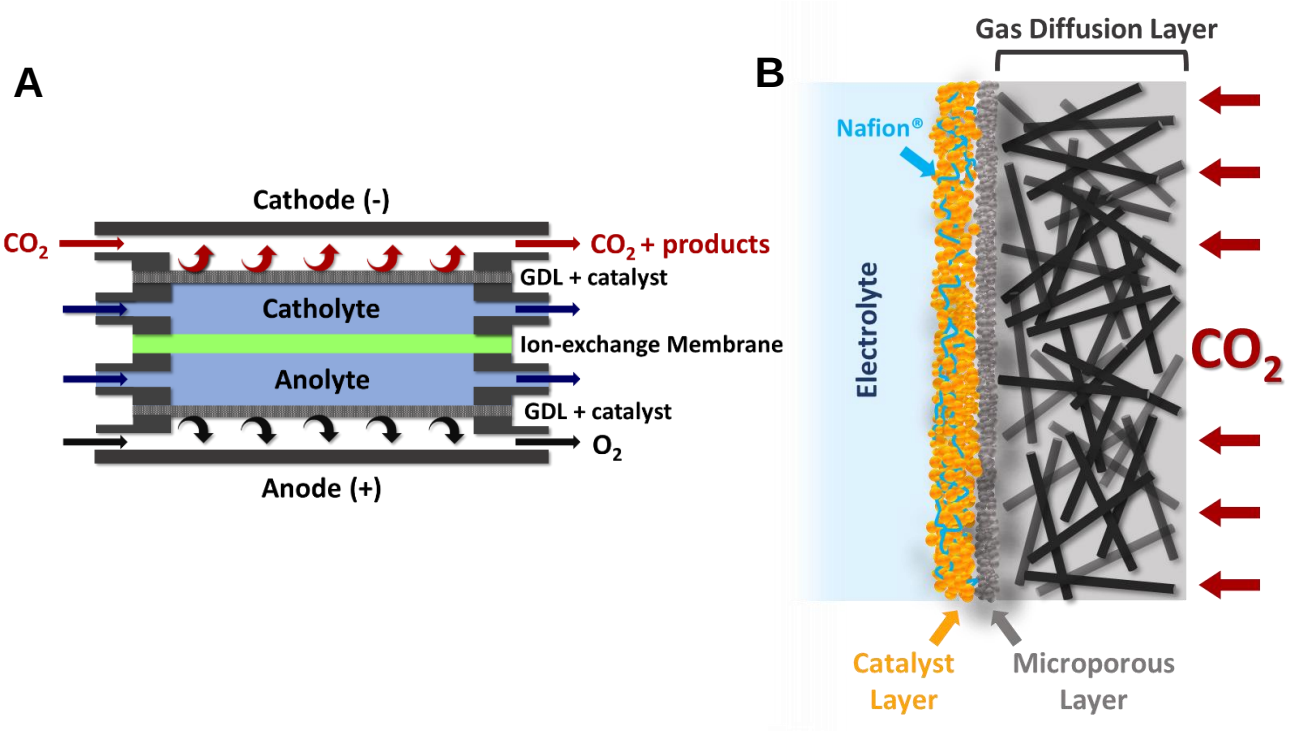

Figure I.9 Graphical representation of A) a flow cell and B) GDE.

Reference

1. Friedlingstein, P. *et al.* Global Carbon Budget 2021. *Earth Syst. Sci. Data* **14**, 1917–2005 (2022).

2. Peter, S. C. Reduction of CO_2 to Chemicals and Fuels: A Solution to Global Warming and Energy Crisis. *ACS Energy Lett.* **3**, 1557–1561 (2018).

3. Solomon, S., Plattner, G. K., Knutti, R. & Friedlingstein, P. Irreversible climate change due to carbon dioxide emissions. *Proc. Natl. Acad. Sci. U. S. A.* **106**, 1704–1709 (2009).

4. Arnell, N. W., Lowe, J. A., Lloyd-Hughes, B. & Osborn, T. J. The impacts avoided with a 1.5 °C climate target: a global and regional assessment. *Clim. Change* **147**, 61–76 (2018).

5. Intergovernmental Panel on Climate Change. *Global warming of 1.5°C*. *Special Report on Global Warming of 1.5°C* (2019).

6. Mac Dowell, N., Fennell, P. S., Shah, N. & Maitland, G. C. The role of CO_2 capture and utilization in mitigating climate change. *Nat. Clim. Chang.* **7**, 243–249 (2017).

7. Mustafa, A., Lougou, B. G., Shuai, Y., Wang, Z. & Tan, H. Current technology development for CO_2 utilization into solar fuels and chemicals: A review. *J. Energy Chem.* **49**, 96–123 (2020).

8. Singh, N. B. Conversion of CO_2 into useful products. *Ind. Waste* 319–344 (2021). doi:10.1515/9783110674941-009

9. Shehzad, N., Tahir, M., Johari, K., Murugesan, T. & Hussain, M. A critical review on TiO_2 based photocatalytic CO_2 reduction system: Strategies to improve efficiency. *J. CO2 Util.* **26**, 98–122 (2018).

10. Wu, J., Huang, Y., Ye, W. & Li, Y. CO_2 Reduction: From the Electrochemical to Photochemical Approach. *Adv. Sci.* **4**, 1–29 (2017).

11. Nisar, A. *et al.* Bio-conversion of CO_2 into biofuels and other value-added chemicals via metabolic engineering. *Microbiol. Res.* **251**, 126813 (2021).

12. Marpani, F., Pinelo, M. & Meyer, A. S. Enzymatic conversion of CO_2 to CH_3OH via reverse dehydrogenase cascade biocatalysis: Quantitative comparison of efficiencies of immobilized enzyme systems. *Biochem. Eng. J.* **127**, 217–228 (2017).

13. Agarwal, A. S., Zhai, Y., Hill, D. & Sridhar, N. The electrochemical reduction of carbon dioxide to formate/formic acid: Engineering and economic feasibility. *ChemSusChem* **4**, 1301–1310 (2011).

14. Lei, W. Carbon Dioxide as a Raw Material: The Synthesis of Formic Acid and Its Derivatives from CO_2.

Angew. Chem., Int. Ed **34**, 2207–2221 (1995).

15. Benson, E. E., Kubiak, C. P., Sathrum, A. J. & Smieja, J. M. Electrocatalytic and homogeneous approaches to conversion of CO_2 to liquid fuels. *Chem. Soc. Rev.* **38**, 89–99 (2009).

16. Kortlever, R., Shen, J., Schouten, K. J. P., Calle-vallejo, F. & Koper, M. T. M. M. Catalysts and Reaction Pathways for the Electrochemical Reduction of Carbon Dioxide. *J. Phys. Chem. Lett.* **6**, 4073–4082 (2015).

17. Saha, P., Amanullah, S. & Dey, A. Selectivity in Electrochemical CO2Reduction. *Acc. Chem. Res.* **55**, 134–144 (2022).

18. Hori, Y. Electrochemical CO_2 Reduction on Metal Electrodes. in *Modern Aspects of Electrochemistry, vol 42.* (eds. Vayenas, C. G., White, R. E. & Gamboa-Aldeco, M. E.) **42**, (Springer, New York, NY, 2008).

19. Zhong, H., Fujii, K., Nakano, Y. & Jin, F. Effect of CO_2 bubbling into aqueous solutions used for electrochemical reduction of CO_2 for energy conversion and storage. *J. Phys. Chem. C* **119**, 55–61 (2015).

20. Sun, Z., Ma, T., Tao, H., Fan, Q. & Han, B. Fundamentals and Challenges of Electrochemical CO_2 Reduction Using Two-Dimensional Materials. *Chem* **3**, 560–587 (2017).

21. Kuntyi, O. *et al.* CO_2 Electroreduction in Organic Aprotic Solvents: A Mini Review. *J. Chem.* **2022**, 1306688 (2022).

22. Jitaru, M., Lowy, D. A., Toma, M., Toma, B. C. & Oniciu, L. Electrochemical reduction of carbon dioxide on flat metallic cathodes. *J. Appl. Electrochem.* **27**, 875–889 (1997).

23. Wang, Y., Han, P., Lv, X., Zhang, L. & Zheng, G. Defect and Interface Engineering for Aqueous Electrocatalytic CO_2 Reduction. *Joule* **2**, 2551–2582 (2018).

24. Zhang, S., Fan, Q., Xia, R. & Meyer, T. J. CO_2 Reduction : From Homogeneous to Heterogeneous Electrocatalysis. *Acc. Chem. Res.* **53**, 255–264 (2020).

25. Savéant, J. M. Molecular Catalysis of Electrochemical Reactions. mechanistic Aspects. *Chem. Rev.* **108**, 2348–2378 (2008).

26. Franco, F., Rettenmaier, C., Jeon, H. S. & Roldan Cuenya, B. Transition metal-based catalysts for the electrochemical CO_2 reduction: From atoms and molecules to nanostructured materials. *Chem. Soc. Rev.* **49**, 6884–6946 (2020).

27. Ishida, H., Tanaka, H., Tanaka, K. & Tanaka, T. Selective formation of HCOO- in the electrochemical CO 2 reduction catalysed by [Ru(bpy)2(CO)2] 2+ (bpy = 2,2'-bipyridine). *J. Chem. Soc. Chem. Commun.*

131–132 (1987). doi:10.1039/C39870000131

28. Mark Bolinger, C., Nicole Story, B., Sullivan, P. & Meyer, T. J. Electrocatalytic Reduction of Carbon Dioxide by 2,2'-Bipyridine Complexes of Rhodium and Iridium. *Inorg. Chem.* **27**, 4582–4587 (1988).

29. Feaster, J. T. *et al.* Understanding Selectivity for the Electrochemical Reduction of Carbon Dioxide to Formic Acid and Carbon Monoxide on Metal Electrodes. *ACS Catal.* **7**, 4822–4827 (2017).

30. Li, M. *et al.* Toward Excellence of Transition Metal-Based Catalysts for CO_2 Electrochemical Reduction: An Overview of Strategies and Rationales. *Small Methods* **4**, 2000033 (2020).

31. She, Z. W. *et al.* Combining theory and experiment in electrocatalysis: Insights into materials design. *Science (80-.).* **355**, (2017).

32. Hori, Y., Wakebe, H., Tsukamoto, T. & Koga, O. Adsorption of CO accompanied with simultaneous charge transfer on copper single crystal electrodes related with electrochemical reduction of CO_2 to hydrocarbons. *Surf. Sci.* **335**, 258–263 (1995).

33. Back, S., Yeom, M. S. & Jung, Y. Active Sites of Au and Ag Nanoparticle Catalysts for CO_2 Electroreduction to CO. *ACS Catal.* **5**, 5089–5096 (2015).

34. Hahn, C. *et al.* Engineering Cu surfaces for the electrocatalytic conversion of CO_2: Controlling selectivity toward oxygenates and hydrocarbons. *Proc. Natl. Acad. Sci. U. S. A.* **114**, 5918–5923 (2017).

35. Reske, R., Mistry, H., Behafarid, F., Roldan Cuenya, B. & Strasser, P. Particle size effects in the catalytic electroreduction of CO_2 on Cu nanoparticles. *J. Am. Chem. Soc.* **136**, 6978–6986 (2014).

36. Liu, M. *et al.* Enhanced electrocatalytic CO_2 reduction via field-induced reagent concentration. *Nature* **537**, 382–386 (2016).

37. Meier, J. C. *et al.* Design criteria for stable Pt/C fuel cell catalysts. *Beilstein J. Nanotechnol.* **5**, 44–67 (2014).

38. Melchionna, M., Fornasiero, P., Prato, M. & Bonchio, M. Electrocatalytic CO_2 reduction: Role of the cross-talk at nano-carbon interfaces. *Energy Environ. Sci.* **14**, 5816–5833 (2021).

39. Zhou, Y. *et al.* Dopant-induced electron localization drives CO_2 reduction to C_2 hydrocarbons. *Nat. Chem.* **10**, 974–980 (2018).

40. Huang, L. F., Hutchison, M. J., Santucci, R. J., Scully, J. R. & Rondinelli, J. M. Improved Electrochemical Phase Diagrams from Theory and Experiment: The Ni-Water System and Its Complex Compounds. *J. Phys. Chem. C* **121**, 9782–9789 (2017).

41. Ma, M., Trześniewski, B. J., Xie, J. & Smith, W. A. Selective and Efficient Reduction of Carbon Dioxide to Carbon Monoxide on Oxide-Derived Nanostructured Silver Electrocatalysts. *Angew. Chemie - Int. Ed.* **55**, 9748–9752 (2016).

42. Pander, J. E. *et al.* Understanding the Heterogeneous Electrocatalytic Reduction of Carbon Dioxide on Oxide-Derived Catalysts. *ChemElectroChem* **5**, 219–237 (2018).

43. Endrődi, B. *et al.* Continuous-flow electroreduction of carbon dioxide. *Prog. Energy Combust. Sci.* **62**, 133–154 (2017).

44. Chen, Y., Su, D., Chen, Y., Zhu, Z. & Li, W. Three-phase interface-assisted advanced electrochemistry-related applications. *Cell Reports Phys. Sci.* **2**, 100602 (2021).

45. Dinh, C. T. *et al.* CO2 electroreduction to ethylene via hydroxide-mediated copper catalysis at an abrupt interface. *Science (80-.).* **360**, 783–787 (2018).

46. Fan, L. *et al.* Strategies in catalysts and electrolyzer design for electrochemical CO_2 reduction toward C_{2+} products. *Sci. Adv.* **6**, 1–18 (2020).

Chapter I

Carbon Nanostructures decorated with Cerium Oxide in multi-functional electrocatalysts for CO_2 reduction

Synthesis and characterization were performed in collaboration with
Prof. Paolo Fornasiero, Prof. Michele Melchionna, Prof. Tiziano Montini and
Prof. Maurizio Prato of the University of Trieste
Prof. Marcella Bonchio research group at the University of Padova
Dr. Lucia Nasi and Dr. Giovanni Bertoni of IMEM-CNR

1.1 Introduction

As already mentioned at the beginning, the CO_2 reduction reaction represents an excellent strategy for the consumption of CO_2 emissions with the production of products useful for the economy. The CO_2 reduction reaction leads to the formation of numerous products. Among different reaction products, the formic acid is particularly attractive. First of all, the CO_2 conversion into formic acid is considered feasible, thanks to the vast market and wide application range.[1] The formate is relatively environmentally friendly, it can be used as chemical intermediate for industrial application.[2] Formic acid is an excellent storage vector of hydrogen, due to its low toxicity, its physical state (liquid) and high volumetric hydrogen density of FA (4.4 wt %). All these features make it ideal for application in direct formic acid fuel cells (DFAFCs), thus solving the problem of storage and transport of hydrogen.[3] Currently, more than 90% of production of formic acid takes place through the carbonylation of methanol to methyl formate ($CH_3OH + CO \rightarrow HCOOCH_3$) and its subsequent hydrolysis ($HCOOCH_3 + H_2O \rightarrow HCOOH + CH_3OH$). Unfortunately, this process, in addition to being expensive, is ecologically unsustainable due to the high CO2 emissions. In fact, to take place, this production process requires high operating temperatures (80 °C), the use of CO deriving from fossil fuels, and the presence of an excess of water, which must be removed by distillation once the process is complete.[4] On the other hand, the electrochemical conversion of CO_2 would lead to the production of green formic acid, consuming CO2. In this regard, there are several technical-economic studies that evaluate the feasibility of the industrial application of CO_2RR for the production of formic acid, the price of which varies according to the parameters considered and the current market. The current market price of formic acid derived from fossil fuels is 0.74 \$/kg,[5] while the estimated average price for electrocatalytic production is 0.96 \$/kg, with a standard deviation of 81%.[6] Unfortunately, the high error makes it difficult to accurately estimate the economic advantage/disadvantage of this technology. *De Luna et al.* highlight the economic and ecological advantage of the production of formic acid by electrochemical way, associating a production cost of 108 \$/ton and a CO_2 emission equal to -0.22 tCO_2/tFA, against the production deriving from fossil fuels equal to 570 \$/ton and a carbon emission of 2 tCO_2/tFA.[7] *Nitopi et al.* consider the production of formic acid to be one of the best applications of the electrochemical conversion of CO_2, with economic benefits in the near-term.[8] They highlighted this data through a graph (figure 1.1), where the market price of the relative reaction product was set as a function of the minimum energy required to make the reaction take place, considering both the costs of capturing the CO_2 and the costs of electricity required from renewable sources (dotted line). All CO_2-derived products above the dotted line are considered cost-effective, including formic acid.

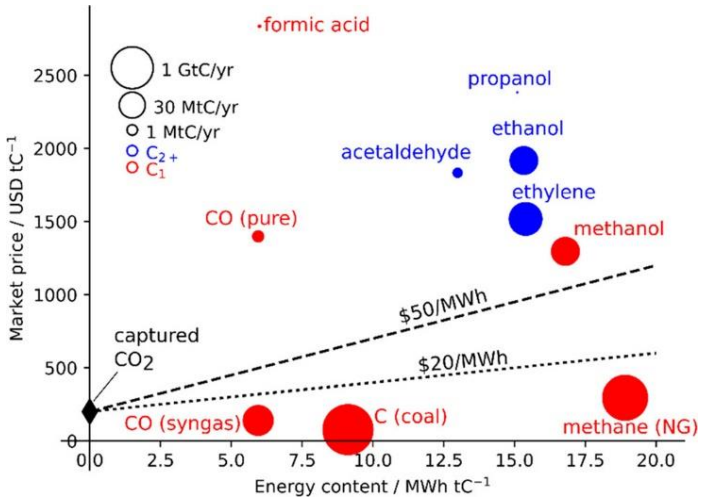

Figure 1.1 Market price of CO_2 recycling products as a function of energy content. The dotted lines indicate the minimum cost of production given a captured CO_2 price ($200/tC) and the electricity price between $50/MWh and $20/MWh (solar energy). The size of the indicator indicates the global market size (on a logarithmic scale) of the product. All economic quantities are normalized to the mass of carbon. Reprinted from Chem. Rev. 2019, 119, 7610−7672.[8]

Nonetheless, the achievement of an optimal synthesis of formic acid through the reduction of CO_2 still remains a great challenge, due to the numerous reaction products and the poor selectivity of the catalysts. Several strategies have been put in place to improve the selectivity of the catalysts. Starting from the choice of materials, whose electronic structure determines the affinity with the different reaction intermediates and therefore the pathway, to the structure and morphology, with the introduction of defects and creation of interfaces. Most of the materials studied for the CO_2 reduction reaction are based on transition metals, both in the metallic state and in the oxidized state. The latter bring numerous advantages, as under CO_2RR conditions they are naturally led to reduce and form a structure rich in defects, which play a fundamental role in determining the activity and selectivity of the catalyst.[9] Another advantageous feature is that of having multiple oxidation states, an ability that is not unique to transition metals, but is shared by Rare Earths (RE). An example of this is provided by the cerium oxide, which has two stable oxidation state Ce^{3+} and Ce^{4+}, in which f electron states are partially occupied or empty, respectively.

1.1.1 Cerium Oxide

Cerium is the most abundant element among the rare earths and is actually used in numerous applications such as magnetics, alloy, phosphors, and catalysts. Although it is a rare earth, it does not fall within the critical raw materials, and for this reason the procurement of this material and its price do not run particular risks (Figure 1.2).[10] The major use of cerium oxide is as catalyst or as a non-inert support in catalysts. In this context the most common applications are three way catalysts (TWCs),[11] CO oxidation,[12] in the solar reactor for thermal splitting of H_2O and CO_2.[13] The importance of ceria in catalytic application stems from its oxygen storage capacity. It has an incredible ability to change the redox state reversibly and quickly, to easily create oxygen vacancies and to diffuse them in particular towards the surface.

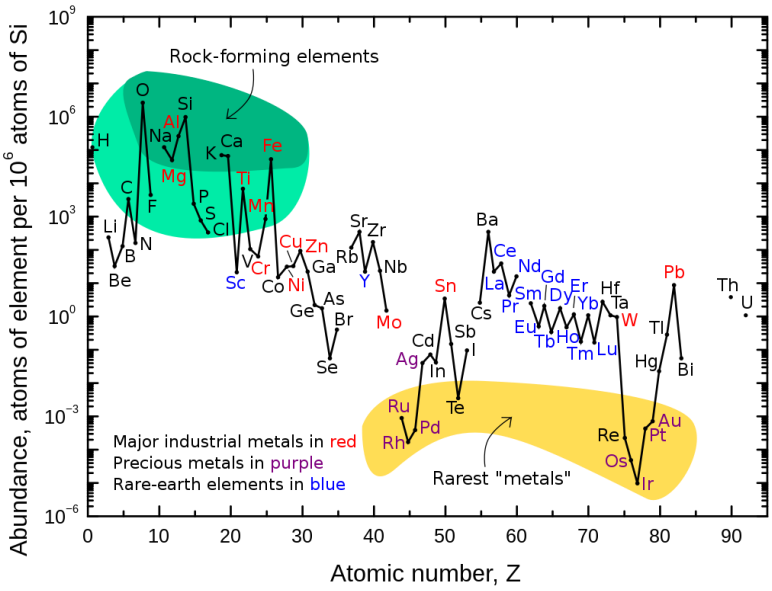

Figure 1.2 Abundance (atom fraction) of the chemical elements in Earth's upper continental crust as a function of atomic number. (Source: United States Geological Survey)

The cerium oxide can form different crystalline phases based on temperature and oxygen pressure. If we consider its oxidation states (III) and (IV), we can have two oxides with extreme compositions Ce_2O_3 and CeO_2 respectively. The CeO_2 crystallizes in the fluorite structure (CaF_2), with a face centered cubic structure (*fcc*), where the unit cell within the space group $Fm\bar{3}m$. In this structure eight oxygen anions are coordinated around each Ce cation at the corners of a cube, while the cations occupy the tetrahedral interstitial sites where each anion coordinated by four cations (Figure 1.3). Non-stoichiometric CeO_{2-x} derives from the release of oxygen atoms and with the reduction of a Ce site from Ce^{4+} to Ce^{3+}, with the co-occurring formation of an oxygen vacancy. The reaction can be expressed with Kröger-Vink notation:

$$2Ce_{Ce} + O_o \rightarrow V_{\ddot{O}} + 2Ce'_{Ce} + \frac{1}{2}O_2 \qquad (1.1)$$

The ability of ceria to change its oxidation state and engulf or release oxygen atoms is called oxygen storage capacity (OSC). The oxygen vacancies are mobile active sites which can act as centres for redox reactions, which make the cerium oxide particularly attractive for different application in the field of energy conversion, catalysis[14], biomedical application[15] etc.

The oxygen vacancies formation is not energetically favoured in equal measure in the three thermodynamically most stable surface planes (100) (110) and (111) (Figure 1.3).[16] In fact, several theoretical and experimental studies have shown that formation energy for oxygen vacancies follow the following order (110) < (100) < (111), where the (111) plane is the least favoured.[17] To increase the number of vacancies in the structure, and therefore the charge mobility in the material and the number of redox centres, various strategies can be implemented such as doping and reduction to size in the nanoscale.

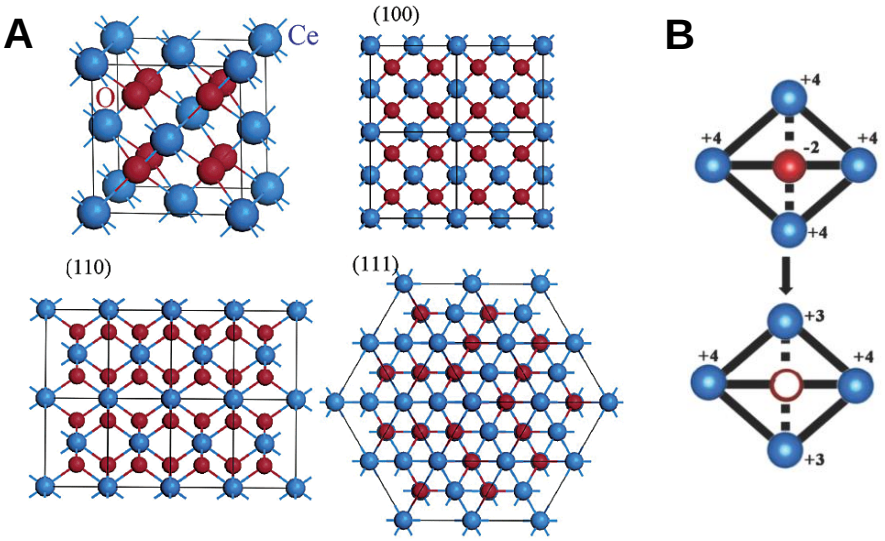

Figure 1.4 A) Unit cell of CeO_2 and the planes (100), (110), and (111). Reprinted with permission from J. Phys. Chem. B 2003, 107, 49, 13563–13566. Copyright© 2003 American Chemical Society.[18] *B) Schematic representation of charge redistribution following the formation of an oxygen vacancy in CeO_2. Ce atoms (blue), O atom (red), neutral O vacancy (empty). Reproduced with permission Part. Part. Syst. Charact., 2019, 36, 1800287.*[16]

The oxygen vacancies and OSC can be tuned by substitution of some Ce^{4+} with other cation with smaller size. By creating a partially unstable structure, the system will naturally be led to generate Ce^{3+} sites and oxygen vacancies to compensate for crystalline deformation.[19] *Li and al.* studied the effect of Hf^{4+} and Sn^{4+} doping in the structure and OSC of CeO_2. They found that, in the case of doping with electroneutrality, the smaller the doping atom, the greater the number of vacancies produced. Where they discovered that it was possible to reach high OSCs by manipulating the crystalline structural parameter of r_{cation}/r_{anion} in CeO_2, passing from a value of 0.184 mmol O_2 g^{-1} for undoped CeO_2, to OSC values of 0.403 and 0.258 mmol O_2 g^{-1} with a doping of 5 mol.% Hf^{4+} and 3 mol.% Sn^{4+}, respectively.[19]

Since the energy of formation of the oxygen vacancies depends on the crystallographic planes it is possible to control the shape, and therefore the exposed planes of the material through nanostructuring. *Tsunekawa et al.* discovered that there a correlation between nanoparticles size and the valence of Ce atoms: the monodisperse nanoparticles with sizes in the range between 2 and 8 nm show a notable increase in their lattice constant compared to bulk CeO_2, where this lattice relaxation is induced by the size of the nanoparticles. The smaller the nanoparticles, the greater the increase in the lattice constant, with a co-occurring reduction in the valence of the Ce. In fact, the reduction in charge from +4 to +3 of cerium ions results in a decrease in electrostatic forces which end induce an increase in the lattice constant.[20,21] The correlation between the nanoparticles size and the number of vacancies was identified by *Zhou and Huebner*, who showed that in the nanoparticles with dimensions smaller than 10 nm, the vacancies concentration increases significantly.[22] In fact, it has been found that in 2-4 nm nanoparticles it is easier to remove oxygen atoms than in extended CeO_2.[23] This behaviour explains why in CeO_2 nanoparticles increases the oxygen transfer with the metal particles[24] it supports and the oxidizing power.

Another way to check the exposed crystallographic planes of CeO_2, and therefore its properties, is through the shape of the material. The shape and morphology are aspects that are determined by a balance of thermodynamic and kinetic processes. Usually, a crystal will have a certain shape in which the crystallographic faces with the lowest surface energy will be exposed. For this reason, the nanoparticles usually have a typical octahedral or truncated octahedral geometries with (111) and (100) as major facets.[17] But it is possible to control the final shape of the crystals by growing the material in certain directions and blocking others. One method is to use organic/inorganic additives as capping agents to selectively block crystal growth in a specific direction and thus favour the development of certain surfaces.[25] Another method is to use templates to form hollow-shaped materials such as nanosphere and nanotubes.[26]

1.1.2 CeO_2 in catalysis application

The properties of ceria and the possibility of modifying them at will through the synthesis parameters, make it particularly interesting for various applications, especially in catalysis. Ceria has already been extensively studied as a co-catalyst for the CO oxidation reaction to CO_2, where is usually used as a support for noble metal nanoparticles such as Pt, Au and Pd. Theoretical and experimental studies have shown that oxidation occurs through two coexisting mechanisms: a purely electronic effect, with the transfer of electrons from the metal to the oxide, and an oxygen reverse spillover effect, with the transfer of oxygen activated from the CeO_2 to metal. The latter is an effect that occurs only when the CeO_2 is reduced to nanodimensions.[24] *Corma et al.* have demonstrated how the addition of CeO_2 nanoparticles that support Au nanoparticles can increase the catalytic activity for CO oxidation by two orders of magnitude.[27]

From the thermodynamic point of view, the theory of multiple proton-electron transfer provides that for all reactions in which only 2 electrons are transferred, there are catalysts capable of catalysing the corresponding redox reactions in both directions, namely, both in reduction and oxidation.[28] So, starting from this assumption, cerium oxide might be able to reduce CO_2.

Several studies have shown that ceria interfaced with another metal can reduce CO_2 with improved selectivity: starting from Au NPs on CeO_2 with the CO production,[29,30] to bismuth niobate (Bi_3NbO_7) interfaced with CeO_2 for the HCOOH production.[31]

1.1.3 Outlook

In all CO_2 works, CeO_2 always has a co-catalyst effect, where it improves the catalytic activity of the metal, exploiting its oxygen vacancies to adsorb CO_2 more easily or stabilize certain reaction intermediates, but it is never used as the main body of the catalyst. In the literature it has been observed how oxygen vacancies can be exploited for the adsorption and activation of CO_2 by metallic sites with different valences.[32] Based on

these premises, it was decided to create a catalyst with an innovative design using a modular approach, where the combination of different building-block with unique physical-chemistry propriety in a single nanostructure can give life to a completely new material with different functionality i.e. high selectivity for CO_2RR. In this case the active part of the catalyst is provided by the CeO_2 nanoparticles that decorate the multiwalled carbon nanotubes (MWCNTs). The MWCNTs not only act as a support for the nanoparticles, but actively increase the catalytic activity of the MO nanoparticles. The high surface area of MWCNTs guarantees a greater surface area of the catalyst, and therefore a greater number of active sites. MWCNTs were chosen in place of single-walled carbon nanotubes (SWCNTs), in order to ensure high electrical conductivity throughout the material, as it is more likely to obtain carbon nanotubes with metallic conductivity. In fact, it is not always possible to control the morphology of CNTs during synthesis, most of the time a mix of carbon nanotubes with metallic and semiconductor[33] behaviour is obtained. The high conductivity of the MWCNTs is another reason they were chosen: their conductivity counteracts the isolating effect of the CeO_2 nanoparticles and promotes the generation of Ce^{3+} sites with the consequent formation of oxygen vacancies. In this chapter we will see the synergistic effect of the two components in the resulting MWCNT@CeO_2 electrocatalyst with a high selectivity for formic acid at low overpotential. We will also see what the effect will be in the performance of CO_2RR following the replacement of the carbon scaffold, in order to create an adequate MO and CNS interface.

Finally, a short part will be devoted to the effect of the cation in CO_2RR on CeO_2 nanoparticles electrodeposited on Au. In this case, a polycrystalline Au electrode was chosen as a support for CeO_2, for two reasons: (i) the role of the cation for CO_2RR has already been studied on gold electrodes, so it is easier to understand the effect of cerium oxide in an Au@CeO_2 composite system, (ii) the study of the cation was carried out with a particular setup, where also the electrode was made to measure, whose only availability was a gold electrode.

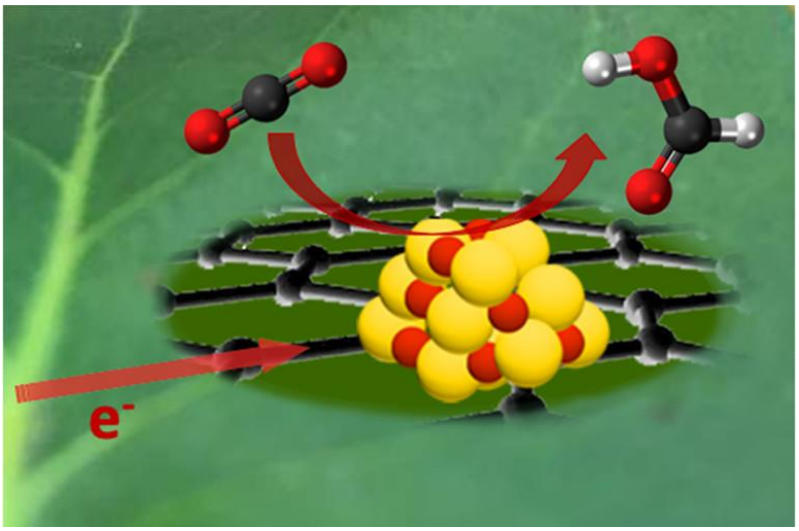

Figure 1.5 Graphic illustration of the CO_2 reduction to formic acid on CeO_2 nanoparticle supported by MWCNTs.

1.2 MWCNT@CeO_2 electrocatalyst for CO_2RR

1.2.1 Synthesis and characterization of MWCNT@CeO_2 electrocatalyst

MWCNT@CeO_2 was synthesized by adapting a previously reported procedure,[34] in which the oxidized MWCNTs are reacted in the presence of Ce^{4+} tetrakis(decyloxide), $Ce(ODe)_4$, as inorganic precursor. The oxidation of MWCNTs with HNO_3/H_2SO_4 is a fundamental step, as the oxidation creates oxygenated functional groups (COOH, C–OH and carbonyls) on the surface of the MWCNTs, these groups are essential to ensure the anchoring of $Ce(ODe)_4$. Subsequently, with a controlled hydrolysis of the $Ce(ODe)_4$ precursor there is the formation of islands of amorphous CeO_2 on the surface of the MWCNTs. Finally, the calcination at 250 °C allows the crystallization of CeO_2 nanoparticles. The nominal weight percentage of MWCNT was chosen on the basis of studies previously carried out on CNT@CeO_2 structures, in order to obtain MWCNTs not completely covered by a CeO_2 shell. In fact, an external shell that completely envelops the nanotube would completely isolate it, preventing direct electrical contact between the MWCNTs and the support electrode, drastically reducing the system performance.[35] Carbon nanostructures (including MWCNTs) have been reported to contain high levels of transition metal impurities such as Fe, Ni, Co, Mn, and Cu derived from catalysts (or precursors) used in the synthesis of nanomaterials with the risk that such metals may have a catalytic role in the reactions under study.[36,37] To get around the problem, before synthesis, MWCNTs were washed several times with diluted HCl and HNO_3 to remove such impurities. To confirm the absence of trace metals, inductively coupled Plasma optical emission spectrometry (ICP-OES) was performed on the washed MWCNTs. The analysis found that none of the typical metals were present above the detection limit of the instrument (10 ppb), with the exception of Ni, whose levels were, however, extremely low (<0.1 ppm) and probably due to impurities traces in the carbon-shell. The relatively mild calcination temperature does not introduce significant quantities of defects into the surface of the MWCNTs, so as to exclude their direct contribution in the catalysis. The thermogravimetric analysis (TGA) of the MWCNT@CeO_2 material indicates that the final material consists of 35% by weight of CNTs and the remaining 65% of CeO_2 NPs (Figure A.6).

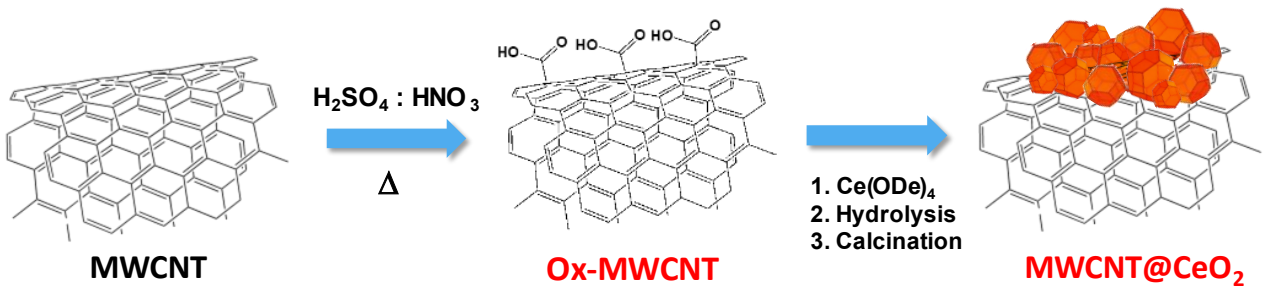

Figure 1. 6 Schema of synthesis of MWCNT@CeO2: in the first step there is the oxidation the MWCNT scaffolds, followed by decoration with CeO2-NPs, which are grown directly on the MWCNT surface by controlled hydrolysis of Ce^{4+}tetrakis(decyloxide), indicated as $Ce(ODe)_4$, and calcination at 250 °C.

The weight ratio between CeO_2 NP and CNTs is optimal for a good compromise between conductivity and stability of the material. Finally, it is noted that from the TGA analysis, the intimate contact between the CeO_2 NPs and the MWCNTs leads to a significant decrease in the combustion start temperature, where it begins at ~350 °C for the nanocomposite material, while for the individual nanotubes it occurs 600 ° C.

The sample was analysed by high-resolution and scanning transmission electron microscopy (HRTEM, STEM), in combination with high-angle annular darkfield imaging (STEM-HAADF), energy dispersive X-ray spectroscopy (EDX), mapping of the elements and reconstruction of the STEM tomography, which provide direct evidence of the morphology of the material. Microscope images analysis confirm the one-dimensional morphology (1D) of MWCNTs, with the diameter between 20 and 30 nm (Figure 1.6 A-C) and the presence of CeO_2 nanoparticles on the surface of MWCNTs, with an average size of 2.8 ± 0.5 nm (Figure 1.6D). Finally, it was possible to obtain information on the crystal lattice of CeO2, which has a face-centered cubic structure (*fcc*), which is obtained only after the calcination process.

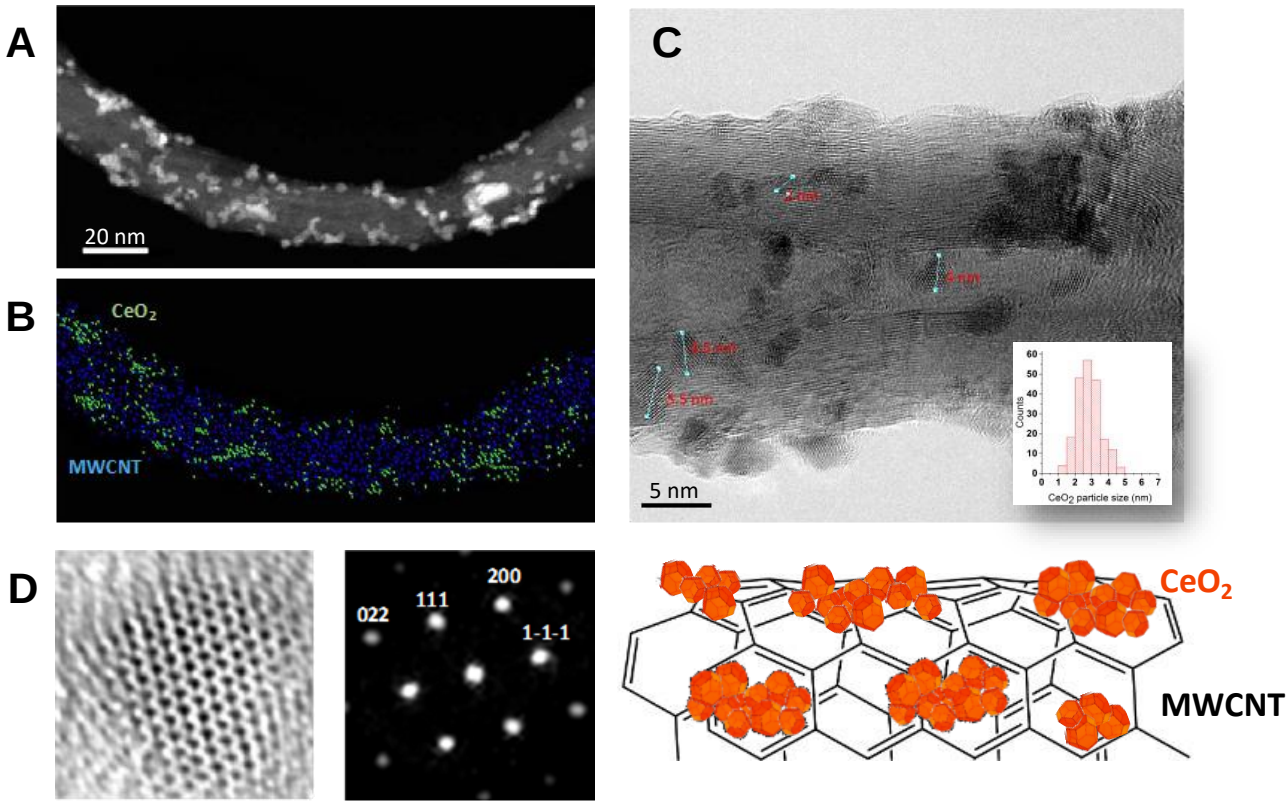

Figure 1.7 ***Electron microscopy study of the nanocomposites with graphical sketch of the nanostructure.*** *A) STEM-HAADF of MWCNT@CeO2 and B) its corresponding EDX map, which highlights the distribution of the elements of C (blue) and Ce (green). (C) HRTEM image of MWCNT@CeO_2 with graph of the dimensional distribution of CeO_2 nanoparticles. (D) An enlarged image of a CeO_2 nanoparticle seen along the axis of the zone (01$\bar{1}$) and its corresponding fast Fourier transform FFT, which can be indexed as the face-centered cubic structure (fcc) of the crystalline CeO_2 nanoparticles.*

Raman analysis was performed for the samples at different synthesis stages: after the functionalization of the nanotubes (Ox-MWCNTs), following the hydrolysis (ox-MWCTs@CeO_2) and after the calcination from which the final material is obtained (MWCNT@CeO_2) (Figure 1.7). The spectra show the typical pattern of graphitic materials, with the D and G bands, respectively, at ~1330 and ~1580 cm^{-1}, where the D band is generally associated with the presence of defects, which interrupt the graphitic network, which on the contrary the latter gives rise to the G band. Therefore, from their relationship it is possible to measure the extent of the defects on the surface of the CNTs.[38] In this case the intensity ratio of the two bands is D/G ~ 1.27, while that for pristine MWCNTs is 1.19. This low value, compared to those of pristine MWCNTs, is consistent with what was said previously. That is, the synthesis and the mild calcination temperature introduce only a slight modification of the properties of the carbon scaffold, indicating the absence of major defects. Finally, the appearance of the peak at 455 cm^{-1}, characteristic of the crystalline phase of CeO_2, confirms the formation of a crystalline phase of CeO_2 after calcination.[39]

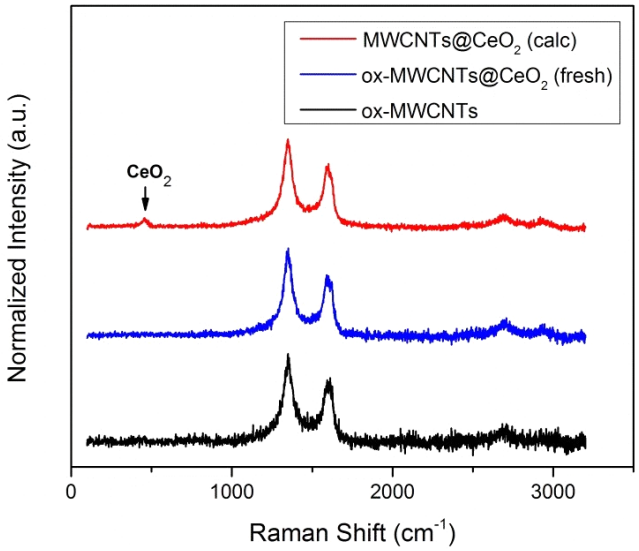

Figure 1.8 ***Raman spectra of the nanohybrids.*** *Raman spectra of ox-MWCNTs (black), ox-MWCNTs@CeO2 fresh (blue) and MWCNTs@CeO_2 calcined (red).*

The addition of MWCNTs, and the creation of an interface between the carbonaceous species and the metal oxide, facilitates the reduction of Ce^{4+} sites to Ce^{3+}, with the consequent increase in the population of oxygen vacancies in CeO_2.[10] It must be taken into consideration that the process of formation of oxygen vacancies in the cerium oxide is very complex, as different situations can coexist, from single vacancy to multiple vacancies.[40] A great deal of information can be obtained through X-ray spectroscopy. With the analysis of X-ray photoelectron spectroscopy (XPS) the initial fraction of Ce^{3+} was identified in the different materials: bulk CeO_2, CeO_2 nanoparticles and the MWCNT@CeO_2 nanocomposite (Figure 1.7). As already mentioned in the introductory paragraph, the nanostructuring of CeO_2 increases the number of reduced Ce^{3+} sites and consequently also the number of oxygen vacancies. This phenomenon has also been observed in these materials, where the relative content of Ce^{3+} increases with the downsizing of cerium oxide at the nanoscale,

and significantly improves with the integration of the carbon component of MWCNTs. In fact, the concentration of [Ce^{3+}]% is equal to 11 for the bulk CeO_2, 25 for the NPs and 33 for the nanocomposite material (Figure 1.8).[41] These data suggest that the creation of an interface between MWCNT and cerium oxide favours the transport/injection and delocalization of electrons into the CeO_2 layer, resulting in the accumulation of Ce^{3+} sites and oxygen vacancies. The increase in reduced and cerium oxide sites and oxygen vacancies are crucial both for the adsorption and activation of CO_2, and for the formation of reactive hydrides.[42,43]

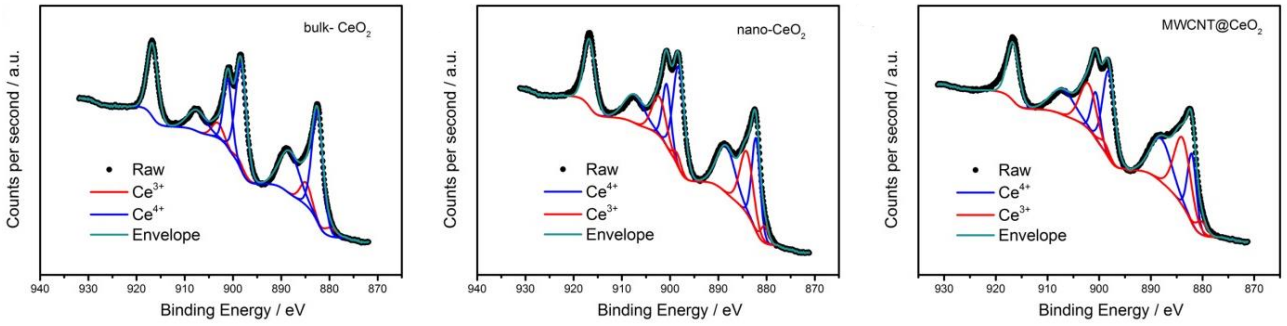

Figure 1.9 ***XPS analysis.*** *Deconvolution and fit of XPS spectrum of Ce3d core level of bulk CeO_2, CeO_2 NPs, and MWCNT@CeO_2.*

1.2.2 Electrochemical characterization and CO_2RR performance of MWCNT@CeO_2

The nanocomposite material was characterized by cyclic voltammetry (CV) in 0.1 M phosphate buffer (PB), as the redox peaks of cerium oxide are not always clearly visible in the other electrolytes, while in PB there is the formation of reversible redox species. In fact, after the reduction of Ce^{4+} to Ce^{3+} (Eq 1.2), surface CePO4 is formed, which can be monitored by cyclic voltammetry with a reversible peak at $E_{1/2}$= -1.1 V vs RHE (Figure 1.8), the reaction in progress follows equation (1.3):[44]

$$2CeO_{2\,(surface)} + 2e^- + 2H^+ \rightarrow Ce_2O_{3\,(surface)} + H_2O \qquad (1.2)$$

$$Ce_3(PO_4)_{4\,(surface)} + 3e^- + 3H^+ \rightarrow 3CePO_{4\,(surface)} + H_3PO_4 \qquad (1.3)$$

The formation of $CePO_4$ leads to surface passivation, which is harmful for CO_2RR. For this reason, phosphate-based electrolytes must be avoided when studying catalysis reactions on cerium oxide. Nonetheless, the cyclic voltammetries in PB are an excellent tool for estimating the amount of electrically active CeO_2, integrating the redox peaks centred at +1.1 V vs RHE. The estimation of the electroactive area of the CeO_2 is

a fundamental step not only to have an idea of how much material actually participates in the reaction, but also to determine the turnover frequency (TOF). The integration of the redox peaks reveals that about 20% of the total amount of CeO_2 deposited on the electrode is electrochemically reduced/oxidized. It can also be noted that the same redox process at $E_{1/2}$= +1.1 V vs RHE is almost completely suppressed on nano-crystalline CeO_2 films (Figure 1.9), providing further evidence of the essential role of MWCNTs in providing electrons on the CeO_2 surface, thus promoting the electrocatalytic activity of the material, which would otherwise be inhibited in the thicker and more insulating metal oxide films.

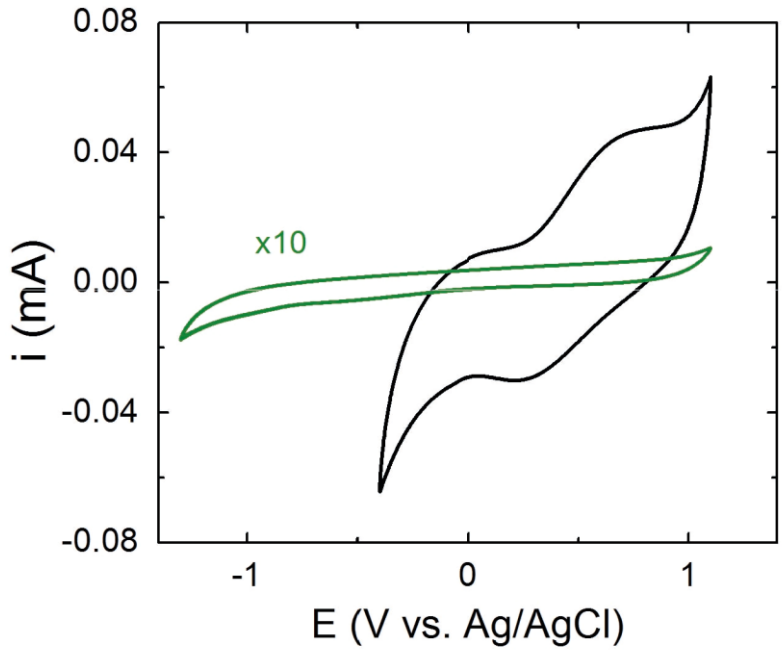

Figure 1.10 CVs of MWCNT@CeO_2 (black) and CeO_2 NPs(green) in 0.1 M PB (pH =6.8) with scan rate 50 mV s^{-1}.

The catalytic activity for CO_2RR of the nanocomposite material was first evaluated by linear scanning voltammetry (LSV) in HNO3 0.1 M and compared with the relative LSVs of CeO_2 nanoparticles and glassy carbon (GC) (Figure 1.10). The voltammetry of glassy carbon has been reported because to carry out the electrochemical characterization of the various materials it was necessary to deposit them on an electrode, in this case constituted precisely by glassy carbon. The glassy carbon electrode was chosen as it is usually an inert material in the potential window of our interest. But to eliminate any possible doubt, its catalytic activity under CO_2RR conditions was also evaluated.

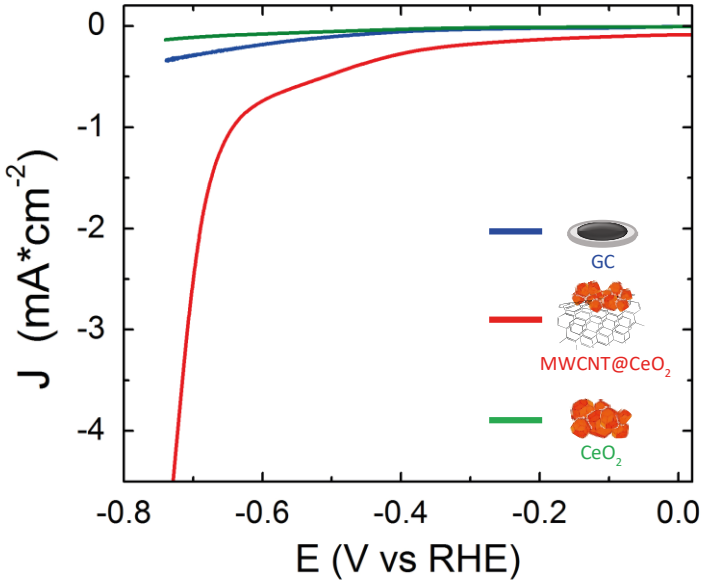

Figure 1.11 ***LSVs in CO_2 condition.*** *LSVs of the nanocomposites electrocatalyst MWCNT@CeO_2 (red), the bare GC electrode (blue), and CeO_2 NPs (green) in a CO_2-saturated HNO_3 0.1M with scan rate of 2 mV s^{-1}.*

The figure 1.10 shows the trend of LSVs. Two trends can be noted for the nanocomposite material MWCNT@CeO_2: a constant increase in the current starting from the potential -0.2 V up to -0.65 V vs RHE, after this potential there is a sudden increase in the current. The latter phenomenon is attributed to HER, which occurs at an unusually high overpotential on MWCNT@CeO_2. In this last potential window, the Tafel analysis reveals a slope of 140 mV dec^{-1}, typical of the HER in which the Volmer mechanism is the rate-determining step, i.e., the adsorption of the reactive proton on the surface of the material.[45] Under acidic conditions, the parasitic reaction of HER commonly occurs on electrocatalysts such as Cu, Pt or Pd at low potentials such as E ≥ -0.1 V vs RHE. In this case, the advantage of the shift to higher overpotentials for HER observed on MWCNT@CeO_2, allows a wide window of selectivity for CO_2RR. It can also be noted that the current of CeO_2 nanoparticles without nanotubes is practically zero, confirming that the catalytic activity of the nanocomposite material derives from the binomial and interaction between MWCNTs and CeO_2. Similarly, we can exclude any contribution to CO_2RR by glassy carbon in the potential window used to evaluate the CO_2 conversion.

Figure 1.11 shows the comparison between LSVs in Ar- and CO_2-saturated 0.1 M HNO_3 solution, for the MWCNT@CeO_2 catalyst (respectively blue and red), and also for ox-MWCNT in CO_2 (black). From the LSV profiles for the nanocomposite material, it can be seen how the current increases in the presence of CO_2 at low overpotential, while for the CeO_2-free carbon nanotubes there is no electrode response.

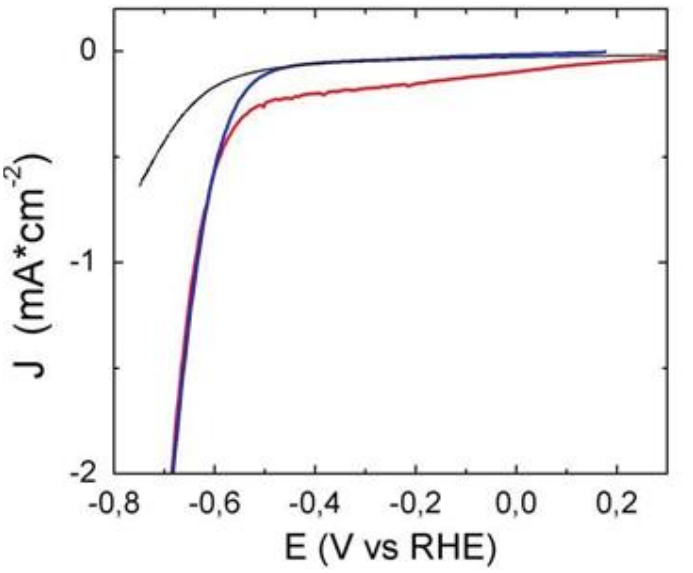

Figure 1.12 LSVs at 2 mV s^{-1} for the nanocomposite MWCNT@CeO_2 in Ar- (blue) and CO_2-saturated (red), and ox-MWCNT in CO_2-saturated (black) HNO3 0.1 M. Potentials are reported vs. RHE and are corrected for the uncompensated resistance.

The CO_2RR catalytic activity was evaluated as a function of applied potential, performing chronoamperometry (CA) experiments in CO_2-saturated HNO_3 0.1 M for 1 hour (ranging from -0.22 to -0.52 V vs RHE). The gas phase was quantified during the electrolysis using an online gas chromatograph (GC), while the liquid phase was analyzed in a second moment with ionic chromatography (IC) and ^{1}H-NMR. From these analyses, it was possible to determinate the product selectivity, reported as the Faraday efficiency (FE). The CA and FE are reported in figure 1.12. The analysis of the products revealed the presence of only hydrogen and formic acid. Further ^{1}H-NMR analysis carried out on the electrolyte post-electrolysis confirmed the absence of other reaction products in addition to formic acid. The absence of other reaction products confirms the high selectivity of this electrocatalyst, given by the binomial MWCNTs and CeO_2. In fact, cerium oxide is known to be a good co-catalyst capable of reducing CO_2 to CO.[29,30]

The interesting thing about this material is the ability to form formic acid at a potential very close to the standard potential of formic acid (-0.2 V vs RHE).[28] In fact, a value of about 60% of FE is obtained with an overpotential of η = -0.02 V. From this point of view, there is only one other material capable of producing formic acid close to the equilibrium potential, and that is the Pd, a noble metal.[46] *Kanan and al.* explain this phenomenon via an electrohydrogenation mechanism, in which the CO_2 is converted to HCO_2^- by electrochemically generated PdH, hence with the formation of a surface hydride. At higher potentials, the performance for CO_2RR collapses in favour of the parasitic reaction of hydrogen evolution, which becomes the dominant process. Interestingly, an inversion cross-point for the FE of hydrogen and formic acid at a potential between -0.3 V and 0.4 V vs RHE. This is indicative of a change in the electrocatalytic mechanism from the low to high overpotential regime. The data collected for CO_2RR are in agreement with the behaviours observed in the LSVs previously reported. Density functional theory (DFT) calculations

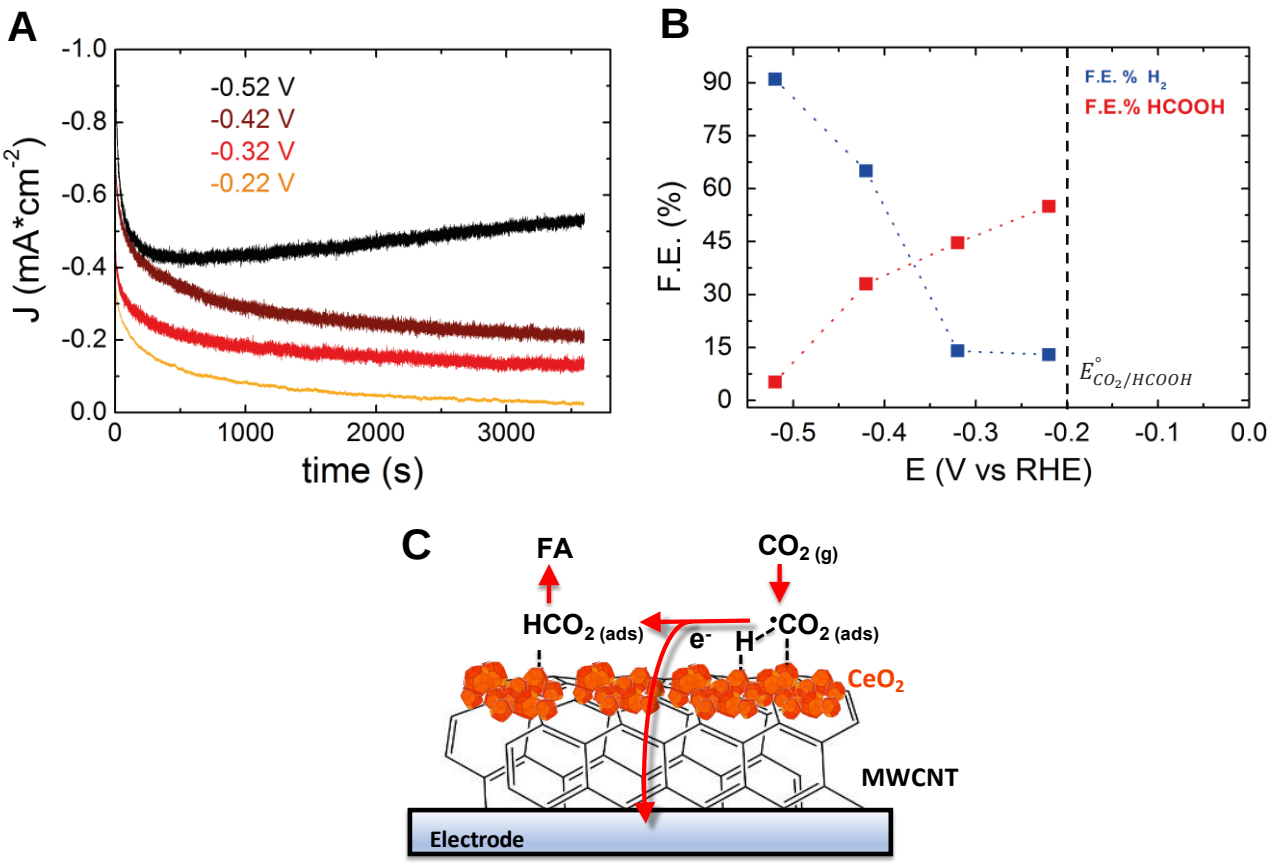

Figure 1.13 ***CO_2RR performance.*** *A) Chronoamperometry in the range from -0.22V to -0.52 V vs RHE (from orange to black, respectively) and B) the corresponding Faraday Efficiencies (FEs) of H_2 (blue) and HCOOH (red) for MWCNT@CeO_2 in CO_2-saturated HNO_3 0.1 M. C) Graphical representation of the CO_2 reduction mechanism on MWCNT@CeO_2.*

demonstrated the formation of a favourable bond of CO_2 on partially reduced CeO_2, namely, with the presence of Ce^{3+} sites and oxygen vacancies.[47,48] Furthermore, the electrochemical reduction of $Ce^{4+/3+}$ appears to be effectively mediated by the presence of MWCNTs, at E ≤ ~0.3 V vs RHE.[44] Therefore, we can state that under CO_2RR conditions, the generation of non-stoichiometric cerium oxide sites ($Ce^{4+/3+}O_{2-x}$) supported by MWCNTs is responsible for the activation and conversion of CO_2 into formic acid. Although the XPS results confirm the formation of a greater population of oxygen vacancies within the nanohybrid material, it is not possible to determine their exact location, neither with in situ techniques. This is even more true for CeO_2, where oxygen vacancies have great mobility in the material, especially with the application of potential.

Further control experiments were performed in the absence of CO_2. From these experiments it emerged that at low potentials there is no H_2 generation (-0.22 V < E_{RHE} <-0.52 V) (Figure 1.13). For this reason, the formation of H_2 which occurs at low overpotentials and in the presence of CO_2, can be attributed, not to HER, but to the dehydrogenation of formic acid which occurs in electrocatalytic conditions and represents about 10% of FE. Based on this information, the FE value for formic acid could be corrected to about 65% at low overpotentials, while HER takes over with FE down to approx. 90% at E <-0.6 V compared to RHE. This double

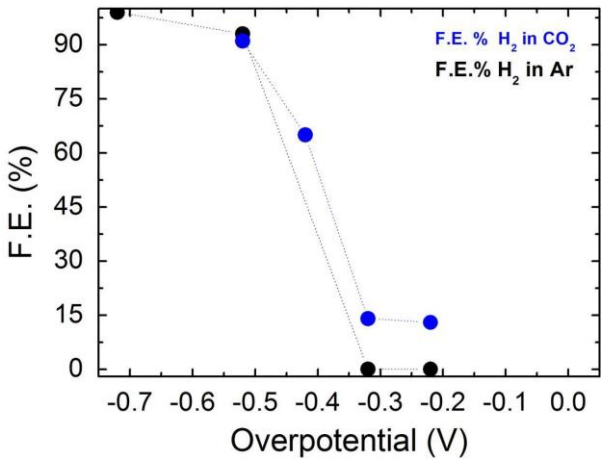

Figure 1.14 Faradaic Efficiency of MWCNT@CeO2 for H_2 in CO_2-(blue) and Ar-(black) saturated HNO_3 0.1 M as a function of the potentials.

catalytic regime is further confirmed by the Tafel slopes performed on the CAs, from whose analysis two slopes are identified (Figure 1.14): at low overpotentials there is a slope of 260 mV dec^{-1}, while at higher overpotentials there is a slope of 140 mV dec^{-1}. As previously mentioned, this latter slope is attributed to the HER where the Volmer mechanism is the rate determining step. While the high slope in the low potential region is attributed to CO_2RR, as multiple and sequential steps of chemical and electron transfer occur, including the reduction of $Ce^{4+/3+}$, absorption of CO_2/H^+ and protonation equilibria, the formation of Ce^{3+}-based hydride and the transfer to reaction intermediates, which limit the reaction kinetics, increasing the Tafel slope.[49]

The values of the Tafel slope and the selectivity for formic acid at low overpotential indicate an electrohydrogenation mechanism by MWCNT@CeO_2.[46] The TOF for formic acid production and H_2 evolution was derived from CAs and is found to be approximately 200 moles of formic acid per mol of CeO_2 for hours at -0.22 V vs RHE.

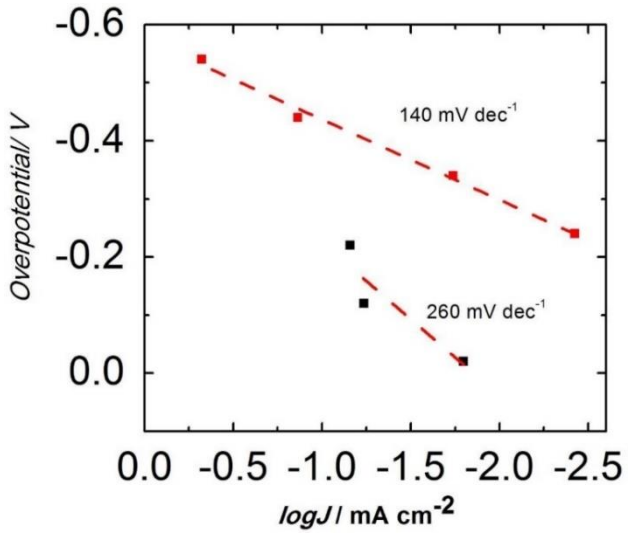

Figure 1.15 ***Tafel slope.*** *The Tafel plot for MWCNT@CeO2 extracted from the CA. Red dots refers to current data obtained for HER by correcting the current density for the HER FE and the corresponded overpotential is related to the $E°_{HER}$ ($\eta = E_{app} - E°_{[H2/H+]}$, where $E°_{[H2/H+]}$ = 0 V RHE). Black dots refer to current data obtained for CO_2RR by correcting the current density for the CO_2RR FE and the corresponded overpotential is related to the $E°_{[CO2/HCOOH]}$ ($\eta = E_{app} - E°_{[CO2/HCOOH]}$, where $E°_{[CO2/HCOOH]}$ = -0.2V RHE.*

As previously mentioned, the catalytic activity derives from the interaction between CeO_2 and the MWCNTs, as the individual components are not significantly reactive for CO_2RR, which is observed in the LSVs. To dispel any doubts about it, the catalytic activity of ox-MWCNT without CeO_2 was evaluated (Figure 1.15). The analysis shows that the maximum FE_{HCOOH} for ox-MWCNTs is 1.6% against 45% of the nanocomposite material, thus confirming what was said previously: the catalytic activity derives from the interaction of the metal oxide with the carbonaceous nanostructure, in the realization of a highly selective multi-functional electrocatalyst for CO_2RR.

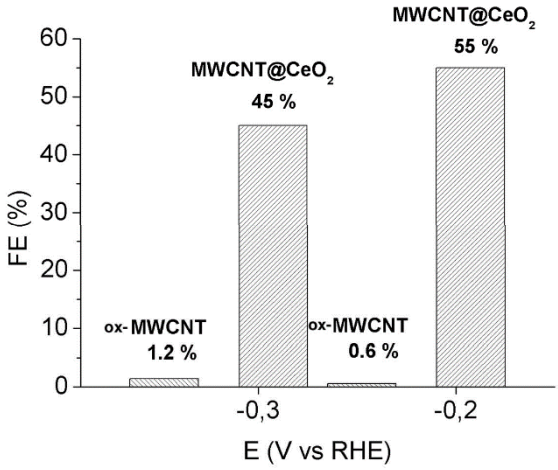

Figure 1.16 FE of MWCNT@CeO_2 and ox-MWCNT for formic acid production in CO_2-saturated HNO_3 0.1 M at the two different potentials of -0.3 V and -0.2 V vs RHE.

Finally, the stability of the nanocomposite material was evaluated. Although CeO_2 is known for its tendency to dissolve slowly in strongly acidic environments,[50] no presence of cerium oxide was detected in the post-electrolysis analyses. Therefore, MWCNTs not only play a fundamental role in catalysis, but also increase the mechanical stability of material, inhibiting the CeO_2 dissolution. This is further confirmed by prolonged electrolysis over time (> 16 h), where the amount of formic acid produced increases linearly over time, and with a slight decrease in the relative FE (Figure 1.16).

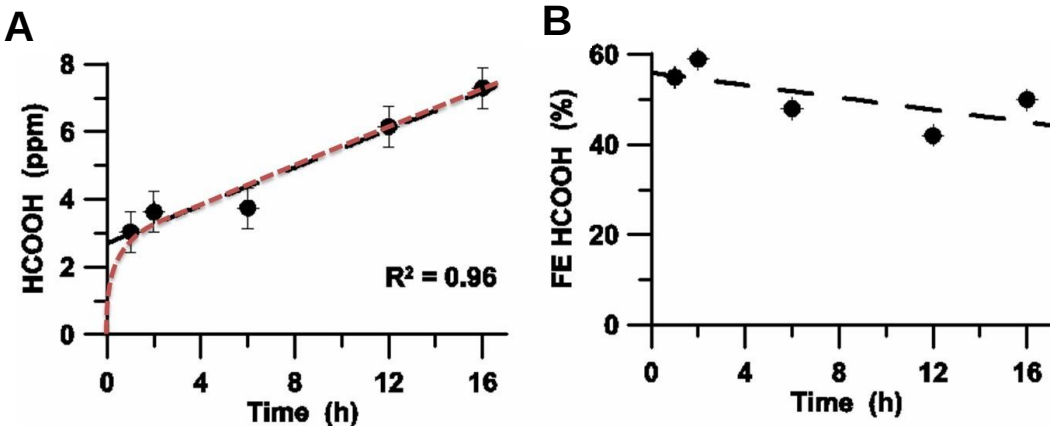

Figure 1.17 A) Formic acid production and B) FE as a function of the time realized at overpotential (η) = -0.02 V and the times chosen are t= 1, 2, 6, 12, 16 h.

The performances of the nanocomposite material are innovative because they derive from a material consisting of a metal oxide and a carbon scaffold, which are able to produce formic acid with an FE of 65% close to the thermodynamic potential and above all without the use of a noble metal. Given the positive effect of MWCNTs in increasing the electrocatalytic performance of CeO_2, it was decided to further modulate the efficiency and selectivity of the material by acting on the support. In this case, replacing the MWCNTs with a scaffold with a larger surface area and a different conductivity such as carbon nanohorns (CNHs), which we will see in detail in the next paragraph.

1.3 CNHs@CeO_2 electrocatalyst for CO_2RR

1.3.1 Synthesis and characterization CNHs@CeO_2 electrocatalyst

Carbon nanohorns were chosen instead of MWCNTs, because they have a higher surface area, and this would guarantee a greater number of active sites. Furthermore, their particular conical geometry makes the nano-tips work as electron collectors, improving the conductivity inside the material.[51] Carbon nanohorns are flower structures formed by the aggregation of individual single-wall carbon nanohorns (SWCNHs). The latter aspect further increases the surface area and consequently improves the adsorption behaviour of the gases on the surface.[52] Based on these characteristics, an improvement in the catalytic activity of CeO_2 is expected, caused by a different and improved interaction with CNHs.

The synthesis method of this electrocatalyst is exactly the same as adopted for MWCNTs (Figure 1.17). The only variation is in the quantity of cerium precursor introduced, with two different percentages: 20% and 30% (which will subsequently be indicated with 20CNHs@CeO_2 and 30CNHs@CeO_2). In fact, the effect of the different loading of CeO_2 on the carbonaceous scaffold will be analysed.

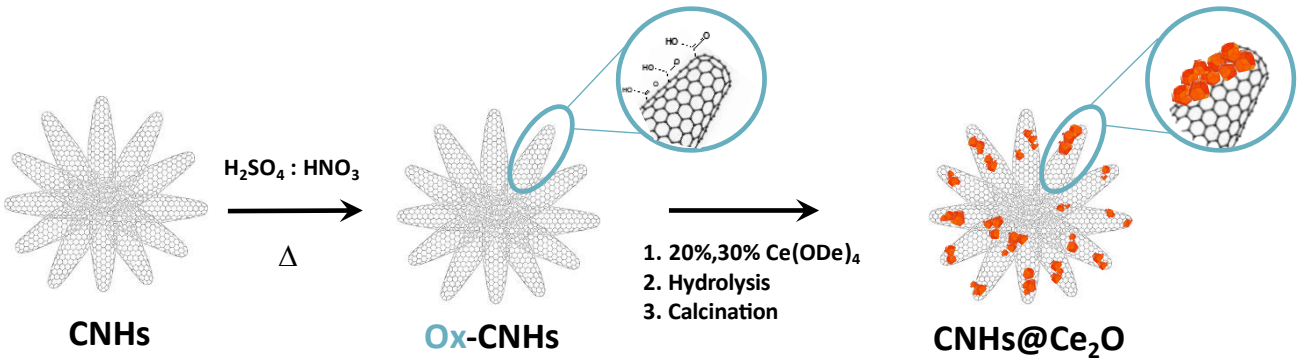

Figure 1.18 ***Scheme of synthesis CNHs@CeO_2****: in the first step there is the oxidation the CNHs scaffolds, followed by decoration with CeO_2-NPs, which are grown directly on the CNHs surface by controlled hydrolysis of Ce^{4+}tetrakis(decyloxide) present with two different percentages in weight (20% and 30%), indicated as $Ce(ODe)_4$, and calcination at 250 °C.*

Figure 1.18 shows the HRTEM images of the nanocomposite material. From these it can be seen the actual formation of a MO-CNS interface, confirming the effective synthesis method. Unlike MWCNTs, where the nanoparticles only partially covered the nanotubes, with a weight presence of 65%, here the nanoparticles form a complete shell around the nanoflower made up of carbon nanohorns. In fact, in this hybrid material, the nanoparticles are unable to penetrate inside the nanoflower and settle along the nanohorns but are limited to the terminal tip of the carbonaceous structure, despite the amount of precursor introduced is lower than in the previous sample (20% and 30%). The FFT analysis confirms the crystallization of CeO_2. Below we will see how this different interface will affect CO_2RR performance.

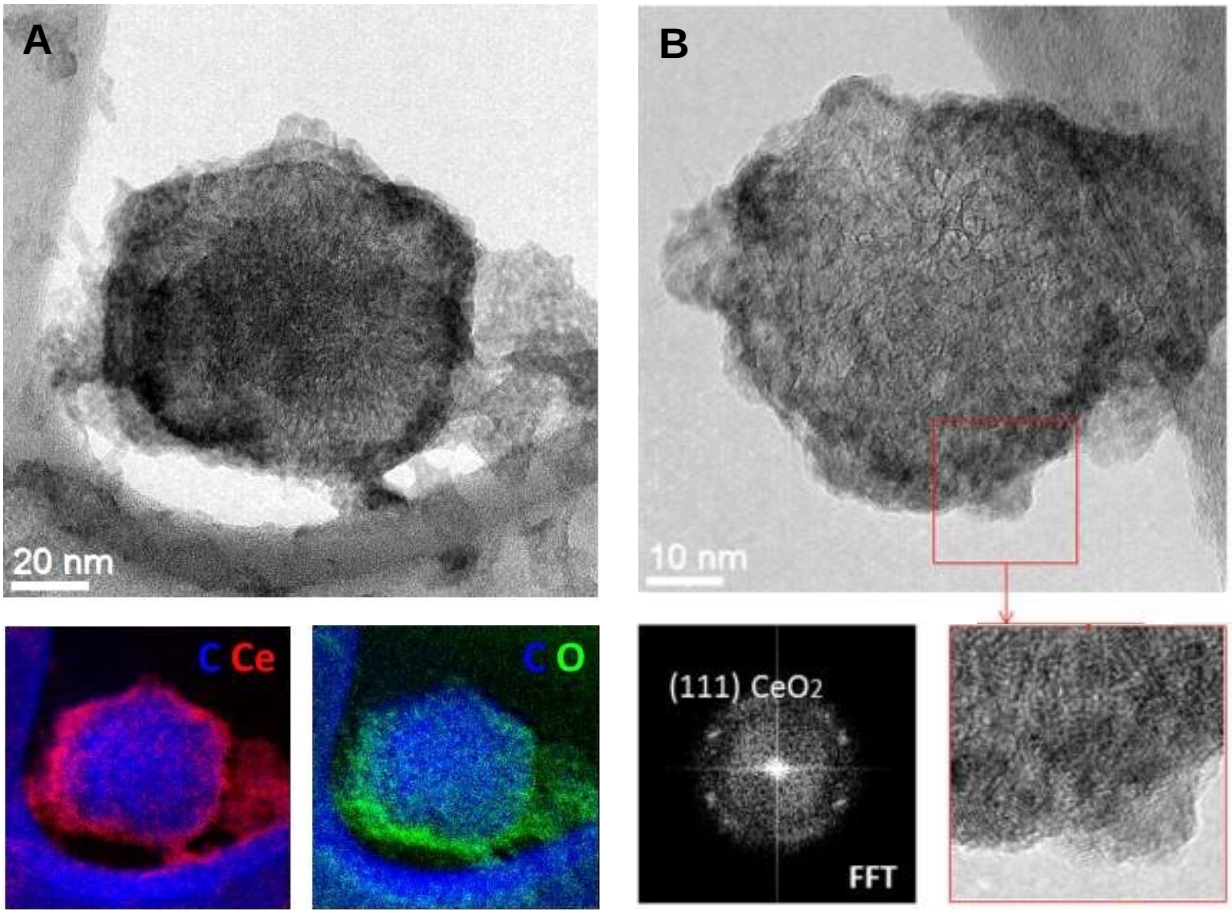

Figure 1.19 ***TEM Images****. A) HRTEM (top) and corresponding energy-filtered transmission electron microscopy, EFTEM, (bottom) of a typical CNH@CeO_2 nanohybrid particle. The EFTEM confirms the achieved interface between the carbon and the metal oxide. B) HRTEM and corresponding Fast Fourier Transform (FFT) in a selected area of the nanocomposite, confirming the layering of crystalline CeO_2 on the carbon scaffold.*

1.3.2 Electrochemical characterizations and CO_2RR performance of CNHs@CeO_2 electrocatalyst

Initially the system was evaluated by cyclic voltammetry in Ar-saturated HNO_3 0.1 M (Figure 1.19).

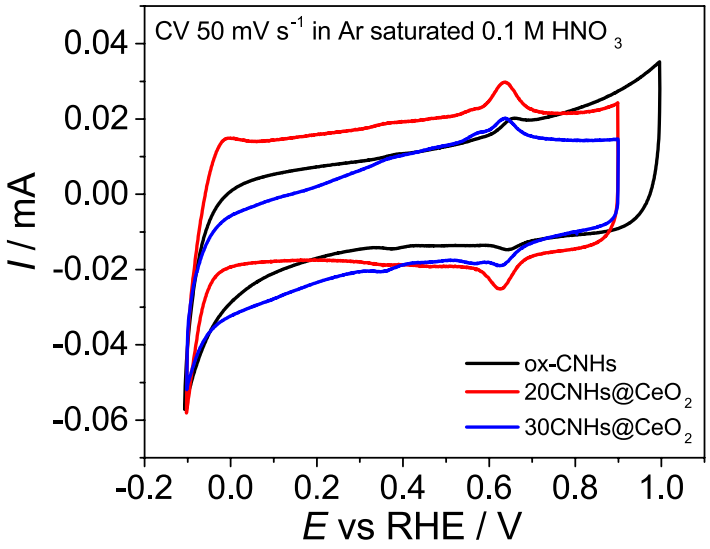

Figure 1.20 ***Cyclic voltammetry investigation.*** *Cyclic voltammetries at 50 mV s^{-1} in Ar-saturated HNO_3 0.1 M of ox-CNHs (black), 20CNHs@CeO_2 (red) and 30CNHs@CeO_2 (blue). The potentials were corrected post measurement for the ohmic drop, considering the resistance of system.*

In HNO_3 the redox processes of CeO_2 are not visible, as in the case of PB, but two reversible redox peaks can be observed in these CVs. Since these peaks are present in all three samples (ox-CNHs, 20CNHs@CeO_2 and 30CNHs@CeO_2), the electrochemical process is not attributable to CeO_2, but to CNHs, and given the shape of the peaks and their high reversibility, the redox process can be ascribed to metal traces present in CNHs, despite washing and acid purification. Two things can be seen from these CVs. The first is the increase of the capacitive current in the case of the 20CNHs@CeO_2 sample, probably due to a greater surface area in the material, given by a good quantitative ratio of MO and CNS. The second thing that can be noted is the increase in resistivity in the 30CNHs@CeO_2 sample, probably due to an excess of cerium oxide, which overall reduces the conductivity of the material and increases the insulating effect around the CNHs.

The chronoamperometry of the two electrocatalysts (MWCNT@CeO_2 and 20CNHs@CeO_2) were compared to a potential where CO_2RR was predominant in the MWCNTs system (-0.32 V vs RHE). This first comparison (Figure 1.20) highlights a positive aspect of the replacement of the carbonaceous scaffold, namely, the total charge increases of the 5-fold with the use of CNHs, thus confirming our initial hypothesis of a more efficient electrocatalyst. The current has given us a first indication on the behaviour of this new catalyst, but to understand its effective efficiency and selectivity we need to investigate the reaction products of CO_2 reduction.

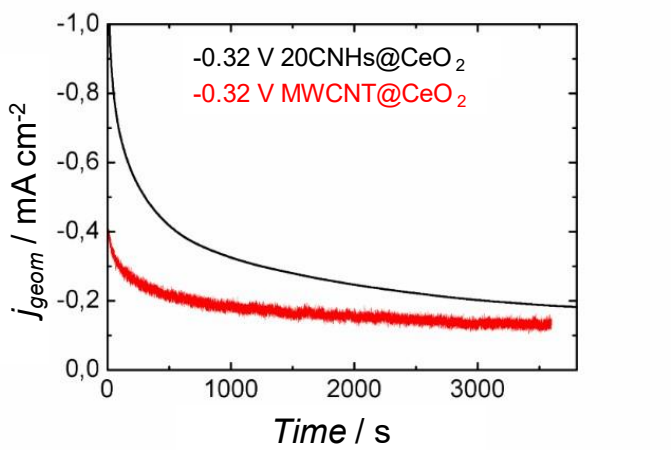

Figure 1.21 Chronoamperometries of two electrocatalysts MWCNT@CeO_2 (red) and 20CNH@CeO_2 in CO_2-saturated HNO_3 0.1 M at -0.32 V vs RHE.

The performances for CO_2RR were evaluated in CO_2-saturated $KHCO_3$ 0.5 M. It was decided to change the electrolyte to make the system comparable with other catalysts. This change of electrolyte could lead to a modification of the reaction mechanism, and to the formation of cerium carbonate on the surface of the catalyst. The use of bicarbonate instead of nitric acid, allows a better stabilization of the catalyst, which in acidic environments would tend to dissolve,[50] even if this possibility did not occur for MWCNT@CeO_2, and make the application of this catalyst commercial.

The figure 1.21 shows the FE for 20CNHs@CeO_2 and 30CNHs@CeO_2 in the range from -0.5 V to -0.9 V vs RHE. In this case, the studied range is shifted to higher potentials than MWCNT@CeO_2, because the pH changes, passing from 1 to 7.5, and consequently also changes the standard potential of the HCOOH, which at this pH is at -0.4 V vs RHE.[28] The analysis of the products revealed the presence of H_2, CO and HCOOH. The amount of CO produced is so low that it can be neglected, in fact the FE never exceed 0.5%, except for the 30CNHs@CeO_2 sample, where it reaches a maximum of 3% at -0.9 V vs RHE. In sample 20CNHs@CeO_2 there

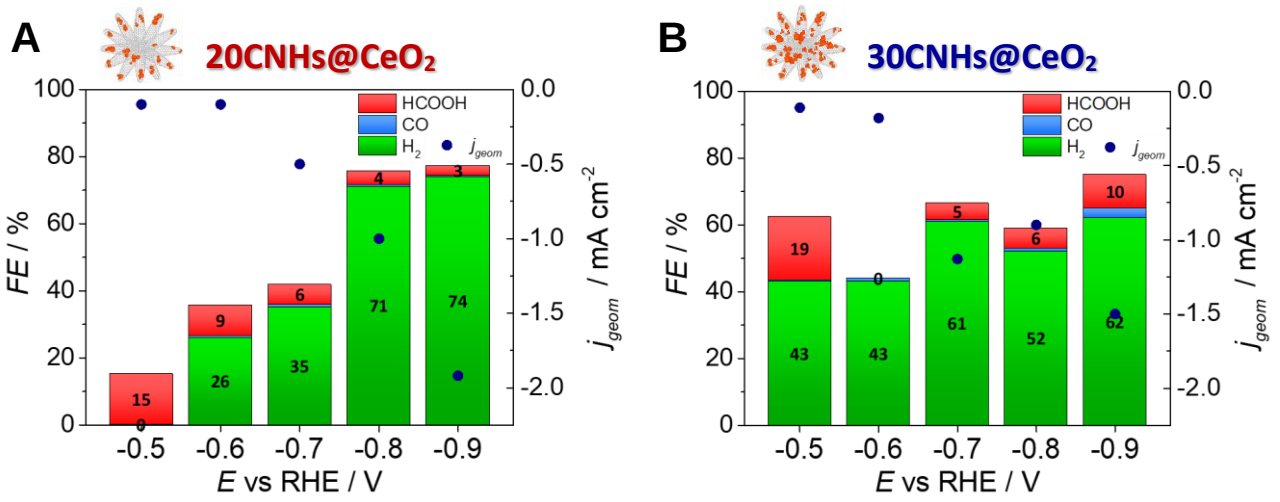

*Figure 1.22 **CO_2RR performance.** Faradaic Efficiency (FE) of detectable CO_2RR products in CO_2-saturated $KHCO_3$ 0.5 M (pH 7.5): H_2 (green), CO (light blue) and HCOOH (red) for A) 20CNHs@CeO_2 and B) 30CNHs@CeO_2. The blue points indicate the mean current density of sample at that potential; the values are shown on right axis.*

is a delay in the production of hydrogen, which occurs with an overpotential greater than 100 mV compared to 30CNHs@CeO_2. At potential -0.5 V and -0.6 V the current of 20CNHs@CeO_2 is lower than the sample 30CNHs@CeO_2, with the increase of potential, the HER becomes predominant with a sudden increase in the current. On the contrary, in the 30CNHs@CeO_2 sample the production of hydrogen remains in a high manner in all potentials. The 30CNHs@CeO_2 produces the maximum of FE for HCOOH with the 19% at -0.5 V vs RHE, against the 15% of 20CNHs@CeO_2 at the same potential. From this point of view the values are very similar, a difference between the two samples arises for the HER. The predominant presence of the parasitic reaction of hydrogen evolution in the sample 30CNHs@CeO_2 can be explained by the greater quantity of CeO_2 that covers the CNHs, and therefore by a greater presence of the electrochemically active phase. Finally, for both materials, at higher cathode potentials HER becomes the predominant process. An explanation for this behaviour can be found in the DFT calculations, which showed that the bond strength of atomic H increases monotonously with the increase in lattice strain induced by vacancies.[53] In stoichiometric CeO_2, the bond strength of the CO_2 is greater than that of atomic H. While in the non-stoichiometric CeO_2, the bond strength of atomic H exceeds than of CO_2, although the value of the latter increases in a co-occurring manner, while the adsorption of the hydroxyl OH is always favored.[54] Consequently, we can say that the catalytic activity for CO_2RR on CeO_2 results from a compromise in the number of vacancies and reduced sites. In fact, in a material with excessive defects, CO_2RR is disadvantaged. This is especially true for CNHs electrocatalysts, where the nano-tips work as electron collectors and increase the reduced sites in the CeO_2.

For these reasons, the performances obtained for these two electrocatalysts are not comparable with those of the MWCNT@CeO_2, where the latter was capable of producing formic acid with an FE of 65% close to equilibrium potential. The poor performances of the catalysts supported by the CNHs also derive from the morphology of the material. Unlike MWCNTs, in CNHs, CeO_2 NPs do not deposit directly on the surface of the nanohorn, but envelop the inner nanoflower, forming an outer shell of metal oxide, the only interface of which is created on the nanotips of the CNHs. Probably the interface created between MO and CNS is not adequate to favour CO_2RR. In fact, in the MWCNT@CeO_2 sample, the catalytic activity derives from a sharing between the MWCNTs and the CeO_2, in which the MO only partially covers the CNS, allowing an adequate balance between the two nanostructures and a favourable intimate interaction. To confirm the fact that the catalytic activity derives from the interaction of the two components, the performance of pristine CeO_2 NPs for CO_2RR was analysed (Figure 1.22). The analysis did not detect any CO_2 reduction products, but only HER at higher potentials of -0.9 V vs RHE, demonstrating the complete inactivity of pristine CeO_2 NPs for CO_2RR and reiterating the fundamental concept of interaction between MO and CNS.

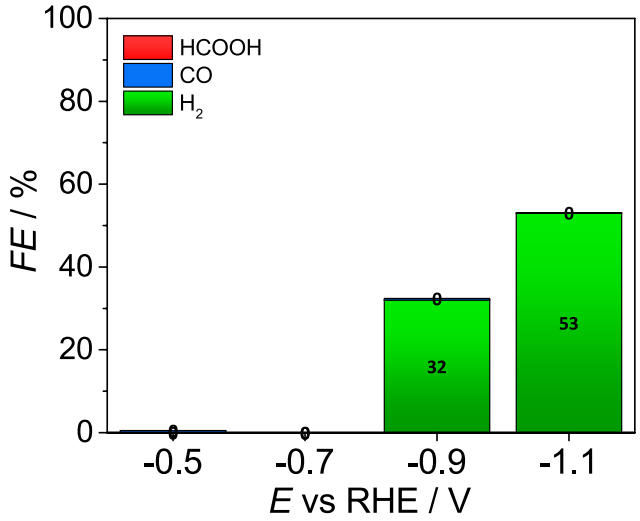

Figure 1.23 Faradaic Efficiency (FE) of detectable CO_2RR products in CO_2-saturated $KHCO_3$ 0.5 M (pH 7.5): H_2 (green), CO (light blue) and HCOOH (red) for CeO_2.

1.4 Role of cation for CO_2RR on CeO_2

Finally, in this last paragraph the effect of the cation in CO_2RR is analysed for ceria nanoparticles electrodeposited on a polycrystalline gold electrode. An interesting aspect of cerium oxide is its ability to modify the selectivity of the electrocatalyst according to the material with which it is combined. As already anticipated in the introduction of this paragraph, when cerium oxide is coupled with gold an electrocatalyst is obtained which is able to oxidize CO to CO_2 with high performance, and being this reaction reversible, it is also able to reduce CO_2 to CO with high selectivity. The origin of the cation effect in CO_2RR is somewhat controversial in recent literature. In this regard, there are three main theories on the role of the alkane metal cation: the modification of the local electric field, the buffering of the interfacial pH and the stabilization of reaction intermediates due to the effect of the local field.[55] It is not excluded that these effects may be present at the same time. Some suggest that hydrated cations act as proton donors and that they modify the local pH of the electrode by shifts the local potential at the outer Helmholtz plane (OHP) or by acting as a buffer near the electrode.[56] The experimental data coupled with theoretical calculations showed that the catalytic activity of CO_2RR increases with increasing metal alkaline cation size, follows this order: $Li^+ < Na^+ < K^+ < Cs^+$.[57]

Koper et al. have suggested that CO_2RR for CO formation on gold in the presence of a metal cation occurs through the following reaction path:[55]

$$CO_2 + e^- + * \rightarrow * CO_2^- \quad (1.4)$$

$$* CO_2^- + M^+ \rightarrow * CO_2^- - M^+ \quad (1.5)$$

$$* CO_2^- - M^+ + H_2O \rightarrow * COOH + M^+ + OH^- \quad (1.6)$$

$$* COOH + e^- \rightarrow * CO + OH^- \quad (1.7)$$

$$* CO \rightarrow CO(g) + * \quad (1.8)$$

In this section we will see what the effect of the cation will be on an Au electrode modified by cerium oxide. Of course, to have electrocatalytic properties, ceria must necessarily be nanocrystalline and enjoy a good interaction with its counterpart, as a mild interaction would lead to a drastic reduction in performance and destabilization of the ceria, with consequent dissolution. For this reason, the cerium oxide nanoparticles were directly electrodeposited on a polycrystalline gold electrode, using the procedure previously described by *Verlato et al.*[58] A solution of 0.1 M $NaNO_3$ and 0.4 mM of $Ce(NO_3)_3$ was used for the electrodeposition applying the potential of -0.5 V vs RHE, and unlike the procedure of the article, a charge of total deposit of 1 C, to ensure an adequate coating of the CeO_2 on the gold electrode (controlled by CV). A completely different setup was adopted for the study of the cation effect, using differential electrochemical mass spectrometry (DEMS) online, where a thin bilayer flow cell was coupled to the mass spectrometer for the quantitative detection of CO during the CO_2RR. In fact, this technique allows to keep track of the real-time evolution of the reaction products, minimizing possible contributions, such as mass transport and the formation of concentration gradients.[59,60] The measurements were conducted in CO_2-saturated 0.1 M $LiHCO_3$ + 0.4 M $LiClO_4$, 0.5 M $KHCO_3$ and 0.5 M $CsHCO_3$. In some cases, a mixture of perchlorate salts and carbonate salts was used, the reason being the low solubility of the salt of Li_2CO_3, in which the solution reached saturation and lower concentrations of 0.5 M. For this reason, it was added the corresponding perchlorate salt, to maintain the same concentration of the metal cation, without undergoing pH changes and minimizing the contribution of the anion, since the perchlorate anion is large. It was necessary to maintain a concentration of 0.5 M to minimize the contribution of the ohmic drop due to the particular set up used in the DEMS measurements.

The figure 1.23 A shows the CV of Au@CeO_2, where it is possible to see the redox peaks of the CeO_2 coordinated with the carbonate ion, proof of the electrodeposition. The potential window of this CV does not go to more positive potentials to observe the Au redox peaks, as these potentials destroy CeO_2. A CV was performed at more positive potentials only after DEMS measurements. In this case the presence of ceria is still observed, but to a much lesser extent than when it was just electrodeposited, it influences the CV of the Au, reducing the faradic current of the redox peaks and increasing the capacitive current and the resistivity of the system. as can be seen from the direct comparison with the polycrystalline Au electrode (Figure 1.23 B).

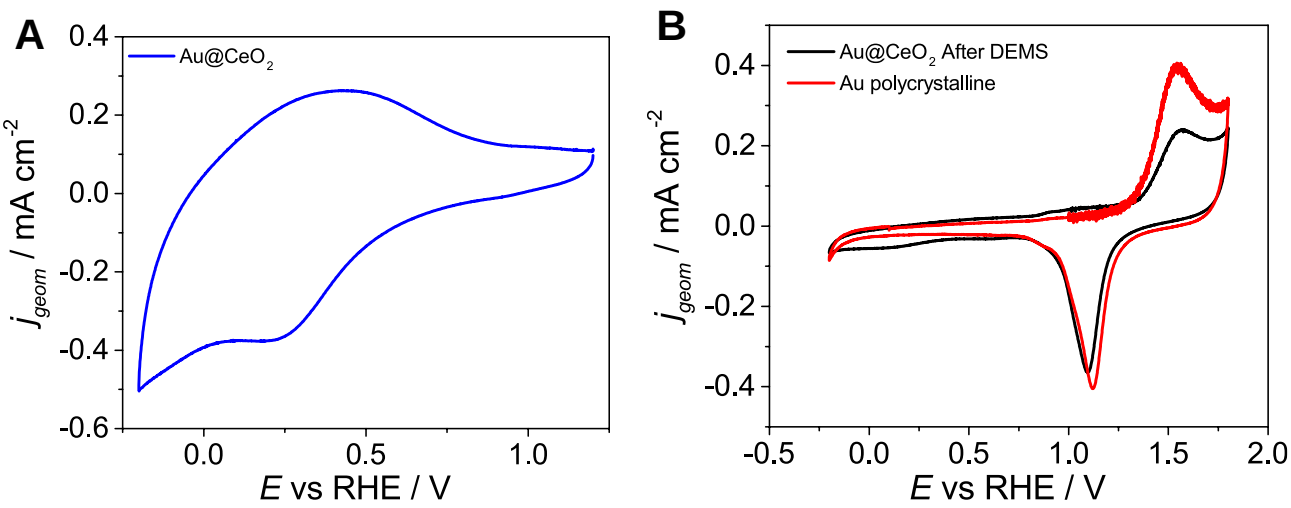

Figure 1.24 A) CV of Au@CeO_2 in Ar-saturated 0.05M Li_2CO_3 +0.4 M $LiCLO_4$. B) CVs of Au@CeO_2 after the DEMS measurements (black) and pristine Au polycrystalline electrode (red) in Ar-saturated 0.05M Li_2CO_3 +0.4 M $LiCLO_4$.

Figure 1.24 shows the LSVs performed in the DEMS measure, from which the respective FE were calculated. As you can see, the potential window adopted is not always the same for all 3 electrolytes, but in some cases it changes. The change is simply given by the high ohmic drop of the setup, which induced the potentiostat out of scale, going into overload, while in some cases, the formation of bubbles in the electrochemical system, caused the interruption of the contact between WE and CE (clearly visible for spikes in LSV of Cs^+). In fact, in a system saturated with hydrophobic CO_2, there is the formation of numerous bubbles in the microfluidic channels since the CO_2 tends to salt out in the thin channels of the cell body (consisting of Kel-F) during the course of the measurements. The collection of the last two measurements (-0.8 and -0.9 V vs RHE) for Li^+ was made possible by the application of the CAs. Among the reasons why it was not possible to report the trend of the Na^+ cation, is the poor solubility of the $NaHCO_3$ salt, which during electrochemical measurements tended to precipitate inside the microfluidic channels, totally blocking the flow of the electrolyte in the cell. While replacing the carbonated salt with the perchlorate ion, the potentiostat was unable to apply the potential as it was out of scale.

From the LSVs graph it is possible to notice an increasing trend of the faradic current as the size of the cation increases ($Li^+ < K^+ < Cs^+$), until -0.6 V vs RHE, where the current in K^+ exceeds that in Cs^+. Au@CeO_2 shows almost zero performance for CO_2RR in the Li^+ based electrolyte, where HER remains the dominant process. As we know from data in the literature, lithium ion has a hard hydration shell and for this reason it coordinates poorly with CO_2, resulting in a less effective stabilization effect.[55] As the size of the cation increases, an increase in the catalytic performance for the CO_2RR is noted, reaching the maximum in the presence of the K^+ ion (60% FE_{CO} at -0.6 V vs RHE). The reason why CO_2RR is favoured on K^+ and Cs^+ is that these metal cations have a softer hydration shell than Li^+ and are found in greater concentration at the electrode interface, coordinating with CO_2. Therefore, it is more likely that the metal cation will stabilize the CO_2 through a local interaction M^+–O(CO_2) .

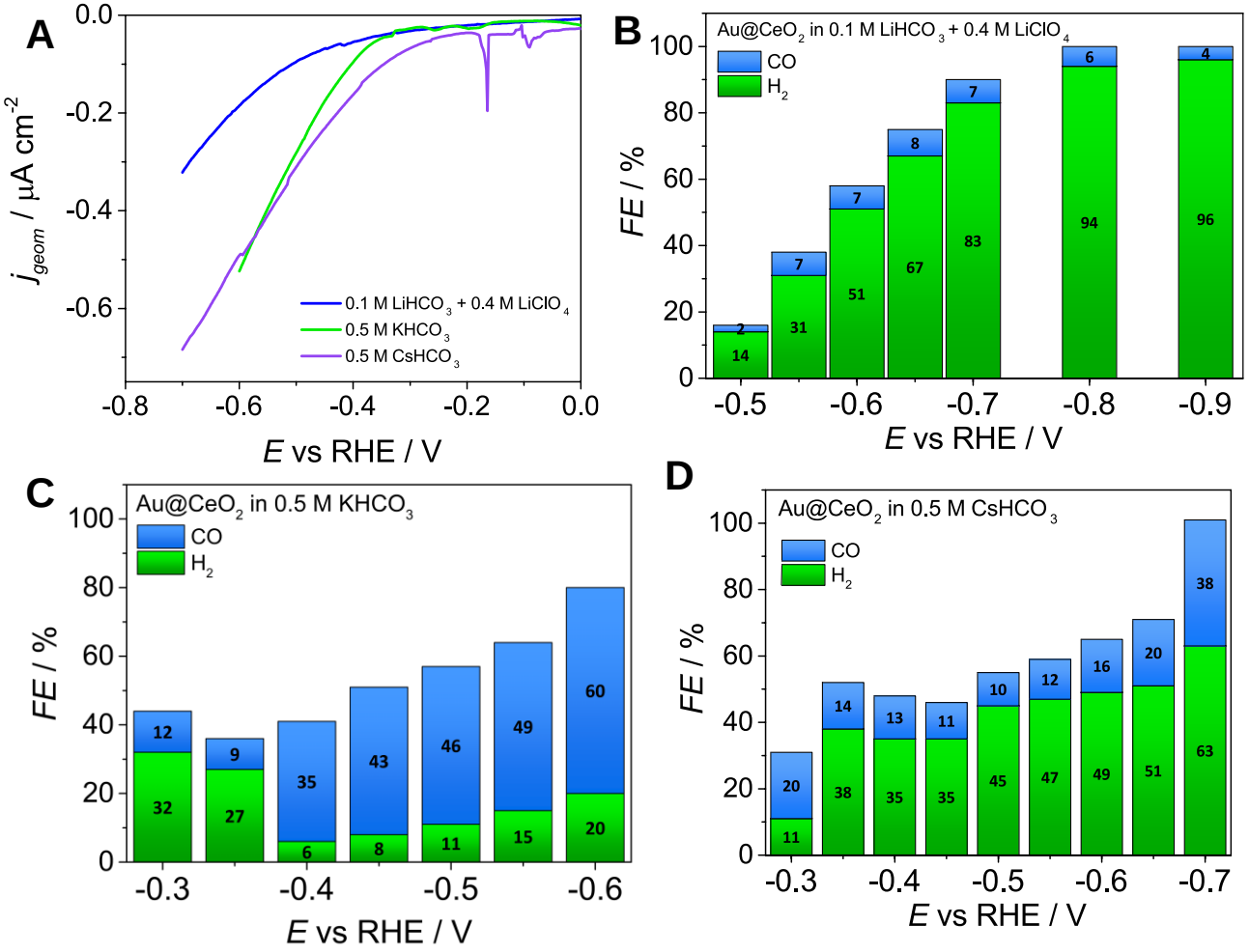

Figure 1.25 A) LSVs of Au@CeO_2 in CO_2-saturated 0.1 M $LiHCO_3$ + 0.4 M $LiClO_4$ (blue), 0.5 M $KHCO_3$ (green) and 0.5 M $CsHCO_3$ (purple). Faradaic Efficiency (FE) of H_2 (green) and CO (light blue) of Au@CeO_2 in CO_2-saturated B) 0.1 M $LiHCO_3$ + 0.4 M $LiClO_4$, C) 0.5 M $KHCO_3$ and D) 0.5 M $CsHCO_3$.

In this case, the system shows a contrasting particularity with the data found in the literature, as Au-based systems show the maximum of their electrocatalytic performance for the reduction of CO_2 in the presence of the Cs^+ ion. In fact, as mentioned earlier at the beginning of this paragraph, the catalytic activity of CO_2RR increases with increasing metal alkaline cation size, follows this order: $Li^+ < Na^+ < K^+ < Cs^+$.[57] In this case, the addition of CeO_2 seems to modify the reaction mechanism that leads to the formation of CO. It must also be considered that the measurements conducted were carried out by monitoring only the gas phase, as this set-up makes it impossible to quantify the liquid products. The possibility of obtaining other reaction products in the liquid phase, such as methanol, cannot be excluded.[54,61]

What is certain from these measures is that CeO_2 has a strong influence on the system and modifies the reaction mechanism, since in the presence of Cs^+ the HER increases again, reaching the maximum of the FE_{CO} with 38% at -0.7 V vs RHE.

These experimental data are interesting, but still require work and coupling with theoretical calculations to define the reaction mechanism in detail.

1.5 Conclusions

In this chapter, a multi-functional electrocatalyst was designed for CO_2RR. The approach used to create this catalyst is of the modular type, namely, through the combination of different building-blocks with unique chemical physical properties, it is possible to obtain a completely new material with certain functions. In this case, a high selectivity is obtained for the production of formic acid near its equilibrium potential, thanks to the combination of the CeO_2 nanoparticles with the MWCNTs. The result is a MWCNT@CeO_2 electrocatalyst capable of reducing CO_2 to formic acid with an FE of 65% close to equilibrium potential, by means of a CO_2 electrohydrogenation mechanism. These performances are considered unique, above all due to the lack of a noble metal inside the catalyst and the mere presence of a metal oxide. A direct comparison with other state-of-the-art electrocatalysts for CO_2RR places MWCNT@CeO_2 among the most promising systems reported so far in terms of low overpotential combined with high selectivity for CO_2RR (Figure 1.25). The catalytic activity of the nanocomposite material derives from an excellent compromise between the number of vacancies and reduced sites present on the metal oxide, conductivity and insulating effect given by the co-presence of MWCNTs and CeO_2, and finally from the creation of an excellent MO and CNS interface, which it allows the two systems to communicate adequately and preferentially reduce CO_2 with high selectivity. Based on these premises, an attempt was made to improve the performance of CeO_2 for CO_2RR, replacing the carbon scaffold with carbon nanohorns, in such a way as to obtain a greater surface area, and an improved conductivity that allows to increase the number of active sites in the material. Nevertheless, the experimental analysis has shown the ineffectiveness of the integration of CNHs into the system, where due to the large steric hindrance of the CNHs, the ceria nanoparticles tend to deposit around the nanoflower, forming an external shell that completely encompasses it. Consequently, the interface that is created between the MO and the CNS only involves the nanotips of the CNHs, thus resulting ineffective for CO_2RR. In conclusion, the creation of an adequate interface between MO and CNS allows to exploit to the maximum the potential of the different building-blocks and thus obtain a material with high selectivity and efficiency for CO_2RR, whose effect protracts in the overall stability of the electrocatalyst.

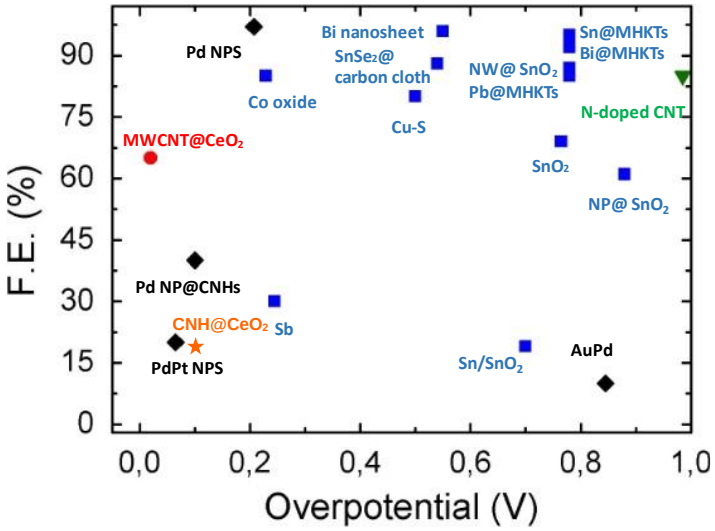

Figure 1.26 Graph of the state-of-the-art of electrocatalysts for CO_2RR, where FE refers to the production of the formate $HCOO^-$. The nanohybrid material MWCNT@CeO_2 is indicated in red, while the CNH@CeO_2 is indicated in orange. The values are reported as a function of the overpotential, as previously reported. The data were adapted for catalyst based on p-metals (blue squares), on d-metals (black diamonds) and for carbon-based catalyst (green triangle).

Reference

1. Lu, X., Leung, D. Y. C., Wang, H., Leung, M. K. H. & Xuan, J. Electrochemical Reduction of Carbon Dioxide to Formic Acid. *ChemElectroChem* **1**, 836–849 (2014).

2. Deng, P. *et al.* Bismuth Oxides with Enhanced Bismuth-Oxygen Structure for Efficient Electrochemical Reduction of Carbon Dioxide to Formate. *ACS Catal.* **10**, 743–750 (2020).

3. Moret, S., Dyson, P. J. & Laurenczy, G. Direct synthesis of formic acid from carbon dioxide by hydrogenation in acidic media. *Nat. Commun.* **5**, 1–7 (2014).

4. Thijs, B., Rongé, J. & Martens, J. A. Matching emerging formic acid synthesis processes with application requirements†. *Green Chem.* **24**, 2287–2295 (2022).

5. Jouny, M., Luc, W. & Jiao, F. General Techno-Economic Analysis of CO2 Electrolysis Systems. *Ind. Eng. Chem. Res.* **57**, 2165–2177 (2018).

6. Somoza-Tornos, A., Guerra, O. J., Crow, A. M., Smith, W. A. & Hodge, B. M. Process modeling, techno-economic assessment, and life cycle assessment of the electrochemical reduction of CO2: a review. *iScience* **24**, 102813 (2021).

7. De Luna, P. *et al.* What would it take for renewably powered electrosynthesis to displace petrochemical processes? *Science (80-.).* **364**, (2019).

8. Nitopi, S. *et al.* Progress and Perspectives of Electrochemical CO2 Reduction on Copper in Aqueous Electrolyte. *Chem. Rev.* **119**, 7610–7672 (2019).

9. Ganduglia-Pirovano, M. V., Hofmann, A. & Sauer, J. Oxygen vacancies in transition metal and rare earth oxides: Current state of understanding and remaining challenges. *Surf. Sci. Rep.* **62**, 219–270 (2007).

10. Montini, T., Melchionna, M., Monai, M. & Fornasiero, P. Fundamentals and Catalytic Applications of CeO2-Based Materials. *Chem. Rev.* **116**, 5987–6041 (2016).

11. Asif, B., Zeeshan, M., Iftekhar, S. & Sillanpää, M. Promoted three-way catalytic activity of the Co3O4/TiO2 catalyst by doping of CeO2 under real engine operating conditions. *Atmos. Pollut. Res.* **12**, 101088 (2021).

12. Pan, C., Zhang, D. & Shi, L. CTAB assisted hydrothermal synthesis, controlled conversion and CO oxidation properties of CeO2 nanoplates, nanotubes, and nanorods. *J. Solid State Chem.* **181**, 1298–1306 (2008).

13. Scheffe, J. R., Welte, M. & Steinfeld, A. Thermal reduction of ceria within an aerosol reactor for H2O

and CO2 splitting. *Ind. Eng. Chem. Res.* **53**, 2175–2182 (2014).

14. Rodriguez, J. A., Grinter, D. C., Liu, Z., Palomino, R. M. & Senanayake, S. D. Ceria-based model catalysts: Fundamental studies on the importance of the metal-ceria interface in CO oxidation, the water-gas shift, CO2 hydrogenation, and methane and alcohol reforming. *Chem. Soc. Rev.* **46**, 1824–1841 (2017).

15. Dong, H. *et al.* Lanthanide Nanoparticles: From Design toward Bioimaging and Therapy. *Chem. Rev.* **115**, 10725–10815 (2015).

16. Zhang, Y., Bals, S. & Van Tendeloo, G. Understanding CeO2-Based Nanostructures through Advanced Electron Microscopy in 2D and 3D. *Part. Part. Syst. Charact.* **36**, 1–32 (2019).

17. Trovarelli, A. & Llorca, J. Ceria Catalysts at Nanoscale: How Do Crystal Shapes Shape Catalysis? *ACS Catal.* **7**, 4716–4735 (2017).

18. Wang, Z. L. & Feng, X. Polyhedral Shapes of CeO2 Nanoparticles. *J. Phys. Chem. B* **107**, 13563–13566 (2003).

19. Min, P., Zhang, S., Xu, Y. & Li, R. Enhanced oxygen storage capacity of CeO 2 with doping-induced unstable crystal structure. *Appl. Surf. Sci.* **448**, 435–443 (2018).

20. Tsunekawa, S., Sahara, R., Kawazoe, Y. & Ishikawa, K. Lattice relaxation of monosize CeO2-x nanocrystalline particles. *Appl. Surf. Sci.* **152**, 53–56 (1999).

21. Tsunekawa, S., Wang, J. T. & Kawazoe, Y. Lattice constants and electron gap energies of nano- and subnano-sized cerium oxides from the experiments and first-principles calculations. *J. Alloys Compd.* **408**–**412**, 1145–1148 (2006).

22. Zhou, X. D. & Huebner, W. Size-induced lattice relaxation in CeO2 nanoparticles. *Appl. Phys. Lett.* **79**, 3512–3514 (2001).

23. Migani, A., Vayssilov, G. N., Bromley, S. T., Illas, F. & Neyman, K. M. Dramatic reduction of the oxygen vacancy formation energy in ceria particles: A possible key to their remarkable reactivity at the nanoscale. *J. Mater. Chem.* **20**, 10535–10546 (2010).

24. Vayssilov, G. N. *et al.* Support nanostructure boosts oxygen transfer to catalytically active platinum nanoparticles. *Nat. Mater.* **10**, 310–315 (2011).

25. Zhang, J. *et al.* Colloidal ceria nanocrystals: A tailor-made crystal morphology in supercritical water. *Adv. Mater.* **19**, 203–206 (2007).

26. Fuentes, R. O. *et al.* Formation and structural properties of Ce-Zr mixed oxide nanotubes. *Chem. Mater.* **20**, 7356–7363 (2008).

27. Carrettin, S., Concepción, P., Corma, A., López Nieto, J. M. & Puntes, V. F. Nanocrystalline CeO2 increases the activity of Au for CO oxidation by two orders of magnitude. *Angew. Chemie - Int. Ed.* **43**, 2538–2540 (2004).

28. Kortlever, R., Shen, J., Schouten, K. J. P., Calle-vallejo, F. & Koper, M. T. M. M. Catalysts and Reaction Pathways for the Electrochemical Reduction of Carbon Dioxide. *J. Phys. Chem. Lett.* **6**, 4073–4082 (2015).

29. Gao, D. *et al.* Enhancing CO2 Electroreduction with the Metal-Oxide Interface. *J. Am. Chem. Soc.* **139**, 5652–5655 (2017).

30. Fu, J. *et al.* Manipulating Au−CeO2 Interfacial Structure Toward Ultrahigh Mass Activity and Selectivity for CO2 Reduction. *ChemSusChem* **13**, 6621–6628 (2020).

31. Song, L., Liang, Z., Sun, M., Huang, B. & Du, Y. The interfacial effect induced by rare earth oxide in boosting the conversion of CO 2 to formate . *Energy Environ. Sci.* **15**, 3494–3502 (2022).

32. Gao, S. *et al.* Atomic layer confined vacancies for atomic-level insights into carbon dioxide electroreduction. *Nat. Commun.* **8**, (2017).

33. G., W. J. W., C., V. L., G., R. A., E., S. R. & C., D. Electronic structure of atomically resolved carbon nanotubes. *Nature* **391**, 59–61 (1998).

34. Cargnello, M. *et al.* Multiwalled Carbon Nanotubes Drive the Activity of Metal@oxide Core−Shell Catalysts in Modular Nanocomposites. *J. Am. Chem. Soc.* **134**, 11760–11766 (2012).

35. Beltram, A. *et al.* Improved activity and stability of Pd@CeO2 core-shell catalysts hybridized with multi-walled carbon nanotubes in the water gas shift reaction. *Catal. Today* **253**, 142–148 (2015).

36. Lum, Y. *et al.* Trace Levels of Copper in Carbon Materials Show Significant Electrochemical CO2 Reduction Activity. *ACS Catal.* **6**, 202–209 (2016).

37. Mazánek, V. *et al.* Ultrapure Graphene Is a Poor Electrocatalyst: Definitive Proof of the Key Role of Metallic Impurities in Graphene-Based Electrocatalysis. *ACS Nano* **13**, 1574–1582 (2019).

38. Dumitru, A., Mamlouk, M. & Scott, K. Effect of different chemical modification of carbon nanotubes for the oxygen reduction reaction in alkaline media. *Electrochim. Acta* **135**, 428–438 (2014).

39. Spanier, J. E., Robinson, R. D., Zhang, F., Chan, S. W. & Herman, I. P. Size-dependent properties of (formula presented) nanoparticles as studied by Raman scattering. *Phys. Rev. B - Condens. Matter Mater. Phys.* **64**, 1–8 (2001).

40. Esch, F. *et al.* Chemistry: Electron localization determines defect formation on ceria substrates.

Science (80-.). **309**, 752–755 (2005).

41. López, J. M. *et al.* The prevalence of surface oxygen vacancies over the mobility of bulk oxygen in nanostructured ceria for the total toluene oxidation. *Appl. Catal. B Environ.* **174**–**175**, 403–412 (2015).

42. Wu, Z. *et al.* Direct Neutron Spectroscopy Observation of Cerium Hydride Species on a Cerium Oxide Catalyst. *J. Am. Chem. Soc.* **139**, 9721–9727 (2017).

43. Yang, S. C. *et al.* Oxygen vacancy engineering of cerium oxides for carbon dioxide capture and reduction. *ChemSusChem* **6**, 1326–1329 (2013).

44. Cummings, C. Y. *et al.* Underpotential surface reduction of mesoporous CeO 2 nanoparticle films. *J. Solid State Electrochem.* **12**, 1541–1548 (2008).

45. Wang, J., Xu, F., Jin, H., Chen, Y. & Wang, Y. Non-Noble Metal-based Carbon Composites in Hydrogen Evolution Reaction: Fundamentals to Applications. *Adv. Mater.* **29**, 1605838 (2017).

46. Min, X. & Kanan, M. W. Pd-Catalyzed Electrohydrogenation of Carbon Dioxide to Formate: High Mass Activity at Low Overpotential and Identification of the Deactivation Pathway. *J. Am. Chem. Soc.* **137**, 4701–4708 (2015).

47. Cheng, Z., Sherman, B. J. & Lo, C. S. Carbon dioxide activation and dissociation on ceria (110): A density functional theory study. *J. Chem. Phys.* **138**, (2013).

48. Albrecht, P. M., Jiang, D. E. & Mullins, D. R. CO2 adsorption as a flat-lying, tridentate carbonate on CeO 2(100). *J. Phys. Chem. C* **118**, 9042–9050 (2014).

49. Kapałka, A., Fóti, G. & Comninellis, C. Determination of the Tafel slope for oxygen evolution on boron-doped diamond electrodes. *Electrochem. commun.* **10**, 607–610 (2008).

50. Virot, M. *et al.* Catalytic dissolution of ceria under mild conditions. *J. Mater. Chem.* **22**, 14734–14740 (2012).

51. Melchionna, M. *et al.* Pd@TiO2/carbon nanohorn electrocatalysts: Reversible CO2 hydrogenation to formic acid. *Energy Environ. Sci.* **11**, 1571–1580 (2018).

52. Bekyarova, E. *et al.* Single-wall nanostructured carbon for methane storage. *J. Phys. Chem. B* **107**, 4681–4684 (2003).

53. Ma, D. *et al.* Effect of lattice strain on the oxygen vacancy formation and hydrogen adsorption at CeO2(111) surface. *Phys. Lett. A* **378**, 2570–2575 (2014).

54. Kumari, N., Sinha, N., Haider, M. A. & Basu, S. CO2 Reduction to Methanol on CeO2 (110) Surface: a

Density Functional Theory Study. *Electrochim. Acta* **177**, 21–29 (2015).

55. Monteiro, M. C. O. *et al.* Absence of CO2 electroreduction on copper, gold and silver electrodes without metal cations in solution. *Nat. Catal.* **4**, 654–662 (2021).

56. Ringe, S. *et al.* Understanding cation effects in electrochemical CO2 reduction. *Energy Environ. Sci.* **12**, 3001–3014 (2019).

57. Monteiro, M. C. O., Dattila, F., López, N. & Koper, M. T. M. The Role of Cation Acidity on the Competition between Hydrogen Evolution and CO2Reduction on Gold Electrodes. *J. Am. Chem. Soc.* **144**, 1589–1602 (2022).

58. Verlato, E. *et al.* CO2 reduction to formic acid at low overpotential on BDD electrodes modified with nanostructured CeO2. *J. Mater. Chem. A* **7**, 17896–17905 (2019).

59. Goyal, A., Marcandalli, G., Mints, V. A. & Koper, M. T. M. Competition between CO2Reduction and Hydrogen Evolution on a Gold Electrode under Well-Defined Mass Transport Conditions. *J. Am. Chem. Soc.* **142**, 4154–4161 (2020).

60. Goyal, A., Bondue, C. J., Graf, M. & Koper, M. T. M. Effect of pore diameter and length on electrochemical CO2 reduction reaction at nanoporous gold catalysts†. *Chem. Sci.* **13**, 3288–3298 (2022).

61. Kumari, N., Haider, M. A., Agarwal, M., Sinha, N. & Basu, S. Role of Reduced CeO2(110) Surface for CO2 Reduction to CO and Methanol. *J. Phys. Chem. C* **120**, 16626–16635 (2016).

Chapter II

The electrocatalytic performance for CO_2 reduction through interface tuning in graphene oxide-bismuth oxide nanocomposites

Synthesis and characterization were performed in collaboration with

Prof. Paolo Fornasiero, Prof. Michele Melchionna and

Prof. Maurizio Prato of the University of Trieste

Dr. Lucia Nasi of IMEM-CNR

2.1 Introduction

As already described in the previous chapter, formic acid is one of the most interesting CO_2 reduction products. For this reason, research works in the development of materials capable of synthesizing formic acid starting from CO_2 with high performance.

There are many catalysts capable of producing formate/formic acid through the CO_2RR, they are mainly transition metals such as Pb[1], Cd[2], Hg[3], In[4] and Sn[5]. From this point of view, the great advantage of heavy metals is to have a higher overpotential for HER and CO production and a weak affinity with $CO_2^{\bullet-}$ intermediate, which tends to be easily protonated, thus favouring the formation of formic acid.[6] However, research has not paid particular attention to heavy metals, as their use entails high risks to both the environment and human health.[7] Currently, Sn-based catalysts are among the most promising, despite suffering from low selectivity due to the formation of H_2 and CO.[8,9]

Another element capable of producing formic acid with high selectivity is Bi. The Bi has a negligible environment impact, low toxicity, low price, and it is an earth-abundant element. These characteristics make it particularly attractive for a possible application in the production of formic acid.[6,10]

2.1.1 Bi-electrocatalysts in non-aqueous solution

A very interesting feature of Bi-based catalysts is the ability to modify its selectivity based on the environment in which it is found (electrolyte), and its nature. In non-aqueous environments (or aprotic), such as ionic liquids (IL) or acetonitrile, the Bi-based catalysts almost exclusively produce CO, due to the lack of proton donors that can protonate the reaction intermediates.[11] An example is given by the works of *Rosenthal and al.*, where they studied the effect given by low concentrations of ionic liquids contained within organic electrolytes on Bi-film: imidazolium-based ionic liquid, as 1-butyl-3-methylimidazolium ($[BMIM]^+$) dissolved in acetonitrile (MeCN) lead to the formation of CO[12], while protic ionic liquids (PIL), as conjugate acid of 1,8-diazabicyclo[5.4.0]undec-7-ene ($[DBU\text{-}H]^+$), promote the CO_2RR to formate with high selectivity.[13] The presence of determinate ionic liquids influences the transport of CO_2 on the electrode surface, the speed of process and the high selectivity towards CO or $HCOO^-$. These systems showed highly selective conversion of CO_2, in the case of imidazolium-based ionic liquids toward CO, with $FE_{CO} \sim 90\%$; while in the case of protic ionic liquids (PILs) the selectivity changes completely toward $HCOO^-$, with $FE_{FA} \sim 80\%$. These efficiencies are obtained despite the high viscosities of the neat IL electrolyte.

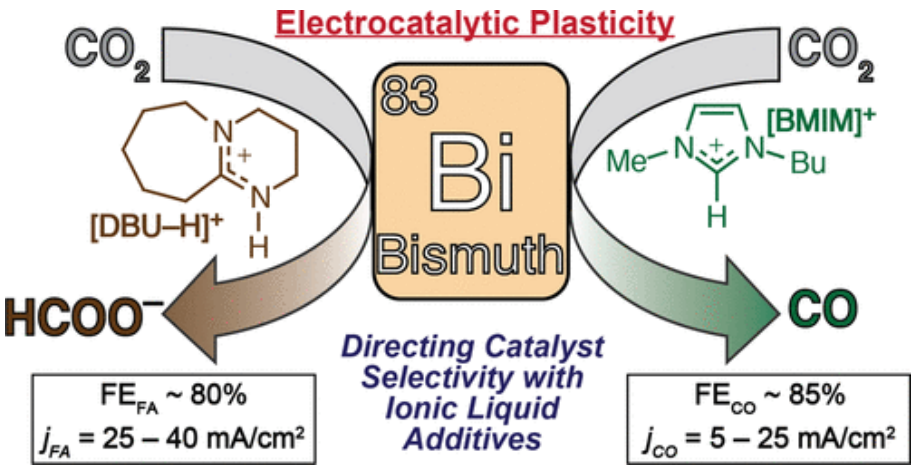

Figure 2.1 Electrochemical reduction of CO_2 selectively on Bi-based electrocatalysts under different ionic liquid conditions. Reprinted with permission from ACS Catal., 2018, 8, 4, 2857–2863. Copyright©2018 American Chemical Society[13]

2.1.2 Bi-electrocatalysts in aqueous solution

It was interesting to observe the versatility of Bi-catalysts and how they can modify their selectivity based on the reaction environment. Since the use of non-aqueous solvents inhibits the commercial application of this CO_2 conversion method, we will focus on Bi-based catalysts in aqueous solvents.

Different morphologies of Bi-based catalysts have been studied in the literature (single atom catalysts, nanoparticles[14], nanowires, nanotubes[15], nanosheets[6], nanoflakes[16], nanofilms, nanodendrites) with different types of synthesis methods (hydrothermal, chemical reduction, electrochemical reduction, electrodeposition).

Most of these materials exhibit almost exclusive selectivity for formic acid in aqueous electrolytes. The nanostructuring of metals allows to improve the performance of the material itself. In the first place, the structural engineering to nano-scale allows to significantly increase the surface area and therefore the number of active sites for the same mass of material used. Through nanostructuring it is possible to increase the catalytic activity creating a material with a rational design. An example is given by Bi nanoflakes, where the large numbers of exposed edges and corner sites lead to a high formate faradaic efficiency close to 100% -0.6 vs RHE.[16] Either the exposure of a specific crystallographic face can favour the reduction of CO_2. This is the case of work presented by *Zhang et al.*, where the Bi nanosheets have higher performance than Bi nanowires in the $HCOO^-$ production, because the former have greater number of exposed (012) crystallographic faced than the second, in which the prevalent face is (110).[17]

Among the simplest nanostructures to obtain and to control from the morphological point of view, we find nanoparticles. The synthesis of nanostructured Bi has major limitations given by bismuth precursors are easily hydrolysed to hydroxides or bismuth oxides in water, and the melting temperature of metal Bi is so low (271.3 °C) which leads to the agglomeration of Bi-based nanocrystals under over-heating.[10] Fortunately,

the oxidation of metallic bismuth during synthesis does not represent a total disadvantage, on the contrary it allows the creation of an oxide-derived catalyst. Bismuth oxide during CO_2 electrolysis is reduced to metallic Bi, releasing oxygen atoms, and forming a structure rich in defects. In some cases, the defects or structural disorders can influence the local electronic states and create under-coordinated sites with higher activity.[15] Without considering that the introduction of oxygen atoms into the bismuth structure influences the energy barriers for the formation of certain reaction intermediates.[18]

There are several strategies to get around the problem of aggregation during the synthesis: use of surfactant agent and/or carbon support. The use of surfactant agent avoids the aggregation of the material and allows to control the shape and size. While, the carbon supports have great advantageous, adding to support and stabilize the nanoparticles, they increase the electrical conductivity in the material and add new functionalities at the electrocatalyst. The carbon support can be carbon black, carbon powder, carbon nanotubes and graphene.

2.1.3 CO_2 mechanisms on bismuth-based electrocatalysts

The nano-size increase the catalytic power of Bi-based catalysts because increase the surface area, and thus the catalytic sites. The DFT calculations help to understand the reaction mechanisms of CO_2 reduction on Bi-based electrocatalysts, and to differentiate the catalytic contributions of the different sites. As said previously, the Bi-based catalysts tend to reduce the CO_2 to formate with high efficiency, selectivity in aqueous solutions. The theoretical calculations speculate that the CO_2RR happens through proton-coupled electron-transfer (PCET) mechanism, where *OCHO is the reaction intermediate, whose reaction pathway leads to the formation of formate (Figure 2.2). Moreover, the adsorbates with O–Bi bonds are more stable than those with C–Bi bonds.[19] Due to the slow kinetics of CO_2RR, the HER is a parasitic reaction which considerably accompanies the reduction process, especially at moderate potentials.[20] Therefore, in order to bypass the problem of HER and improve the efficiency of CO_2RR, the rational design of electrocatalyst through nanostructuring can resolve the problems and add new functionality at the material. The

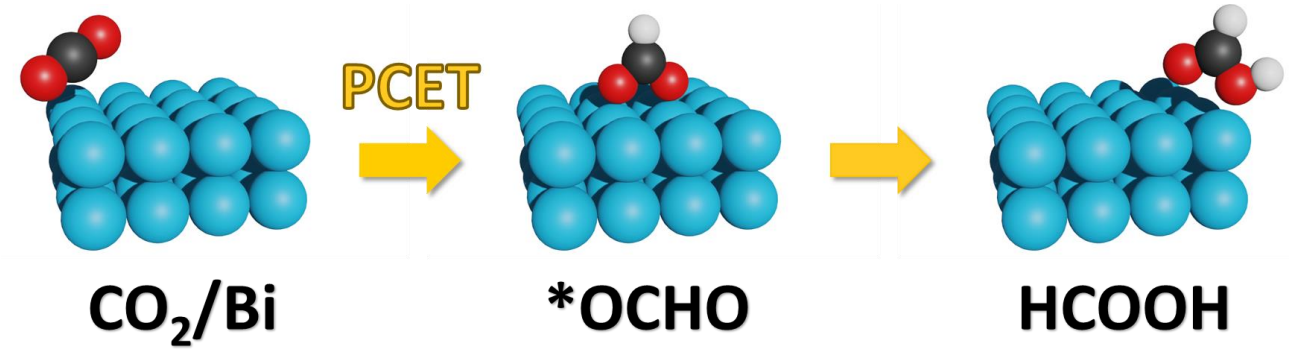

*Figure 2.2 General scheme of the proposed pathway for CO_2 electroreduction to HCOOH with corresponding *OCHO intermediates on the Bi surface. In this case, the PCET mechanisms have not been reported in detail, because they can change according to the morphology of the catalyst and the reaction environment.*

introduction of defects (such as doping atoms, oxygen vacancies, etc) can increase the catalytic activity and stabilize determined reaction intermediates, in this case *OCHO. It has been demonstrated that the addition of oxygen atoms (as a doping agent) in the bismuth structure helps to stabilize the *OCHO intermediate: the free energy for $*CO_2 \rightarrow$ *OCHO passes from 0.46 eV on the Bi surface to 0.17 eV on Bi-O surface. The O atom help to decrease the free energy barrier for *OCHO formation.[21]

2.1.4 Outlook

In the context of a more sustainable energy and with the aim of reducing CO_2 emissions, the electrochemical conversion of CO_2 into chemical products of high interest is inserted. Among different CO_2 reaction products, we can find the formic acid, a very useful chemical for the chemical and fuel cell industry. From this point of view, bismuth-based heterogeneous catalysts represent a good strategy for the formation of formic acid, because they are able to reduce the CO_2 with high selectivity and efficiency. Several studies have shown how metal Bi favours the adsorption of *OCHO reaction intermediate, which is responsible for the pathway to formic acid formation. Nevertheless, on metallic Bi, the reaction takes place at usually large overpotentials and with modest current densities, without to forget the HER remains a parasitic reaction especially at moderate potentials. To circumvent these problems and increase the intrinsic catalytic activity of the material, the research focused on the engineering study of the material, on its nanostructuring. The realization of a catalyst with a rational and innovative design offers an excellent solution. The introduction of defects in the crystal structure of bismuth, such as oxygen atoms, create new more reactive catalytic sites and modify the electronic structure of bismuth, influencing the energy barriers of reaction intermediates formation. Furthermore, the integration of a carbonaceous nanostructure (CNS) to the metal oxide (MO) catalysts leads to the formation of a nanocomposite material with innovative properties and considerable advantages for which the catalyst is more efficient, selective, and stable.

In fact, the formation of an adequate interface between the carbonaceous structure and the metal oxide, allows: 1) a better transfer of charge in the material, and in particular in the interface between the metal/metal oxide, 2) increases the stability of the catalyst, 3) enlarges the surface area exposed and therefore the number of catalytic sites for CO_2 absorption.

The formation of suitable carbon-inorganic interfaces, whereby the CNS is able to: i) improve charge transfers at the interface with the metal/metal oxide, ii) enhance the catalyst stability, iii) increase the surface area and therefore the catalytic sites for CO_2 adsorption.[22] For these reasons, we chose to explore the synergistic combination of graphene oxide (GO) and Bi_2O_3 nanoparticles towards improved CO_2RR (figure 3.3). In this case the GO was chose as the nanocarbon phase because of its large two-dimensional (2D) morphology, which allows optimum deposition of the MO nanoparticles with no size limitations, and to focus on the

electronic effects, excluding the contributions deriving from the high surface area that could arise in the case of carbon nanohorns (CNHs) or carbon nanotubes (CNTs). Furthermore, the oxygenated functional groups of GO allow for better anchoring of the MO nanoparticles on carbonaceous surface.

The GO/Bi_2O_3 nanocomposite shows a different catalytic behaviour of CO_2RR depending on the specific structural evolution during synthesis. The observed electrocatalytic behaviour in relation to the nanocomposite structure allows to discover many of the subtle nuances that strongly influence the complex dynamics of CO_2RR driven by the carbon-MO interfaces. In particular, the catalytic performances of CO_2RR were correlated as a function of the evolution of the material according to the synthesis protocol: from a core-shell configuration Bi@BiO_x, characterized by an amorphous BiO_x shell to: 1) a fully oxidized and partially crystalline β-Bi_2O_3 NPs interfaced with GO, and 2) a core-shell NPs with metal Bi core, and crystallin β-Bi_2O_3 (Bi@β-Bi_2O_3) interfaced with reduced GO (rGO), obtained via a reductive thermal treatment. The identified correlations offer significant information for the rational design of future and advanced multiphase CO_2RR electrocatalysts that integrate the CNS.

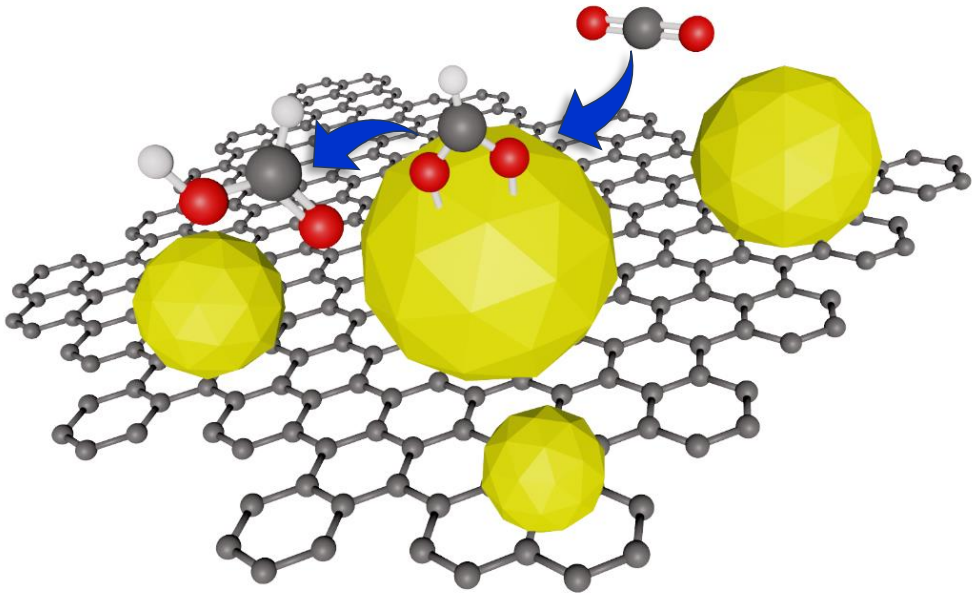

*Figure 2.3 Graphic representation of the GO/Bi_2O_3 catalyst for the reduction of CO_2 with the formation of *OCHO reaction intermediate. For simplicity, the functional groups of the GO have not been represented.*

2.2 Synthesis and characterization of GO-Bismuth oxide nanocomposites

The $Bi@BiO_x$ NP were synthesized via a facile solvothermal method with the use of glucose as the additional reducing and stabilizing agent.[23] The as obtained $Bi@BiO_x$ NP were then deposited onto GO in an ethanol dispersion, thanks to the presence of adsorbed glucose on NPs surface, the coupling with the GO surface is favoured. The formation of the nanocomposite ($GO/Bi@BiO_x$) is confirmed by transmission electron microscopy (TEM) investigation, which shows that the $Bi@BiO_x$ NP are well dispersed onto the GO (Figure A.8). After separation, the solid was divided into two fractions, which were independently subjected to two different thermal treatments that lead to BiO_x crystallization and remove the organic groups. One part of the sample $GO/Bi@BiO_x$ was calcined in static air conditions at 250 ° C (GO/Bi_2O_3), while the other part of the sample was calcined in a dynamic H_2/Ar atmosphere ($rGO/Bi@Bi_2O_3$). The figure 2.4 shows a sketch of the synthesis of the two final nanocomposites.

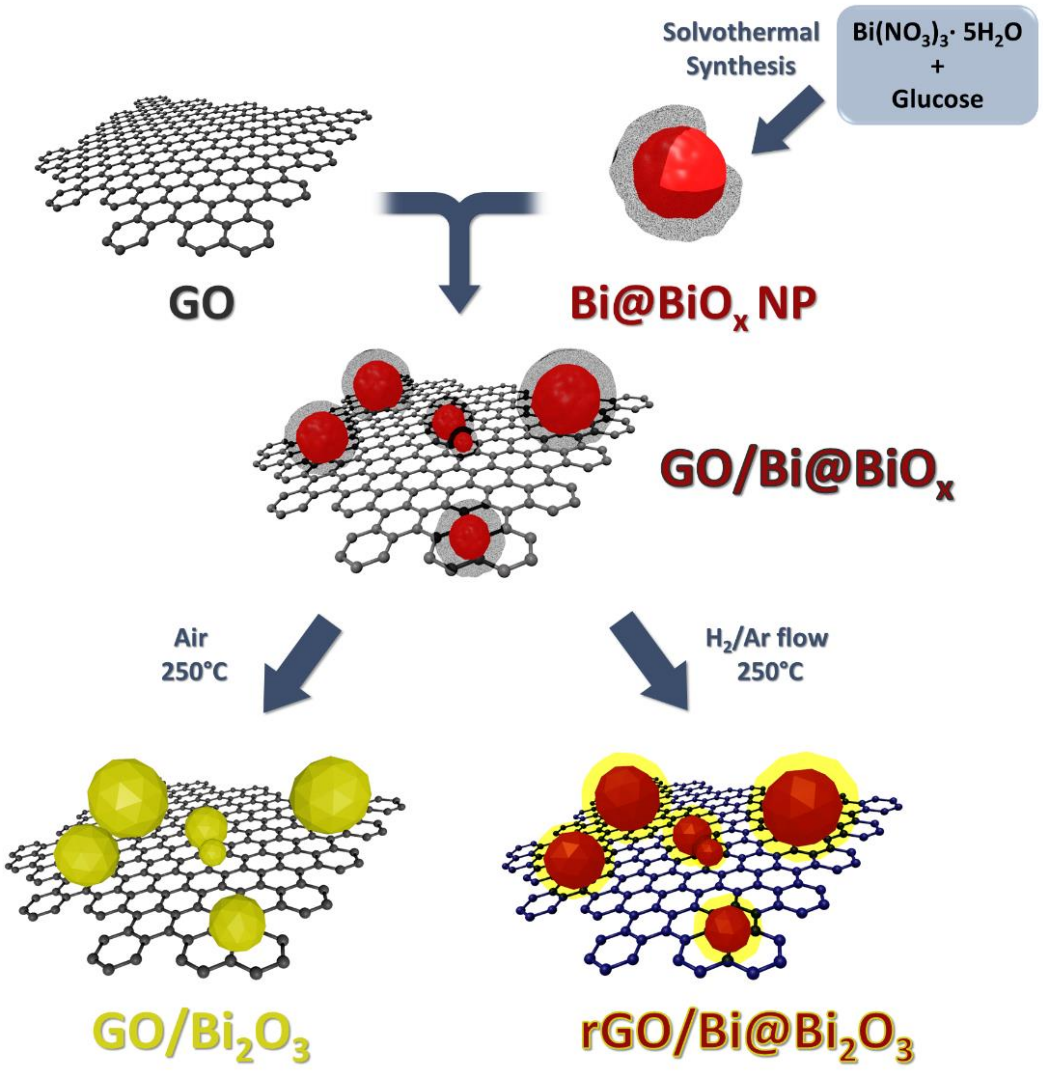

Figure 2.4 ***Synthesis of materials****: graphical sketch of the synthetic procedure to GO/Bi_2O_3 and $rGO/Bi@Bi_2O_3$.*

The evolution of the nanocomposite structures was inspected by high resolution TEM (HRTEM), and energy dispersive X-ray analysis (EDX), which maps the presence of the elements of C, O and Bi (Figure 2.5). HRTME highlights a core-shell configuration for inorganic nanoparticles both before and after combining with GO. In particular, in both **Bi@BiO$_x$** and **GO/Bi@BiO$_x$** the inorganic core consists of rhombohedral metallic Bi, identified by the interplanar d-spacing of 0.32 nm, typical of the Bi (012) plane (Figure 2.5 A),[24] while the shell is made of amorphous BiO_x (Figure 2.5A) Interestingly, both the core and shell present a hexagonal geometry. The line profile spectra of EDX confirms the core-shell nature of the nanoparticles (Figure 2.5A and 2.5B). Indeed, the calcination treatment in air causes a full oxidation of the metal Bi core to bismuth oxide, with partial formation of the metastable β-Bi_2O_3, as indicated by the Fast Fourier Transform (FFT) analysis and by

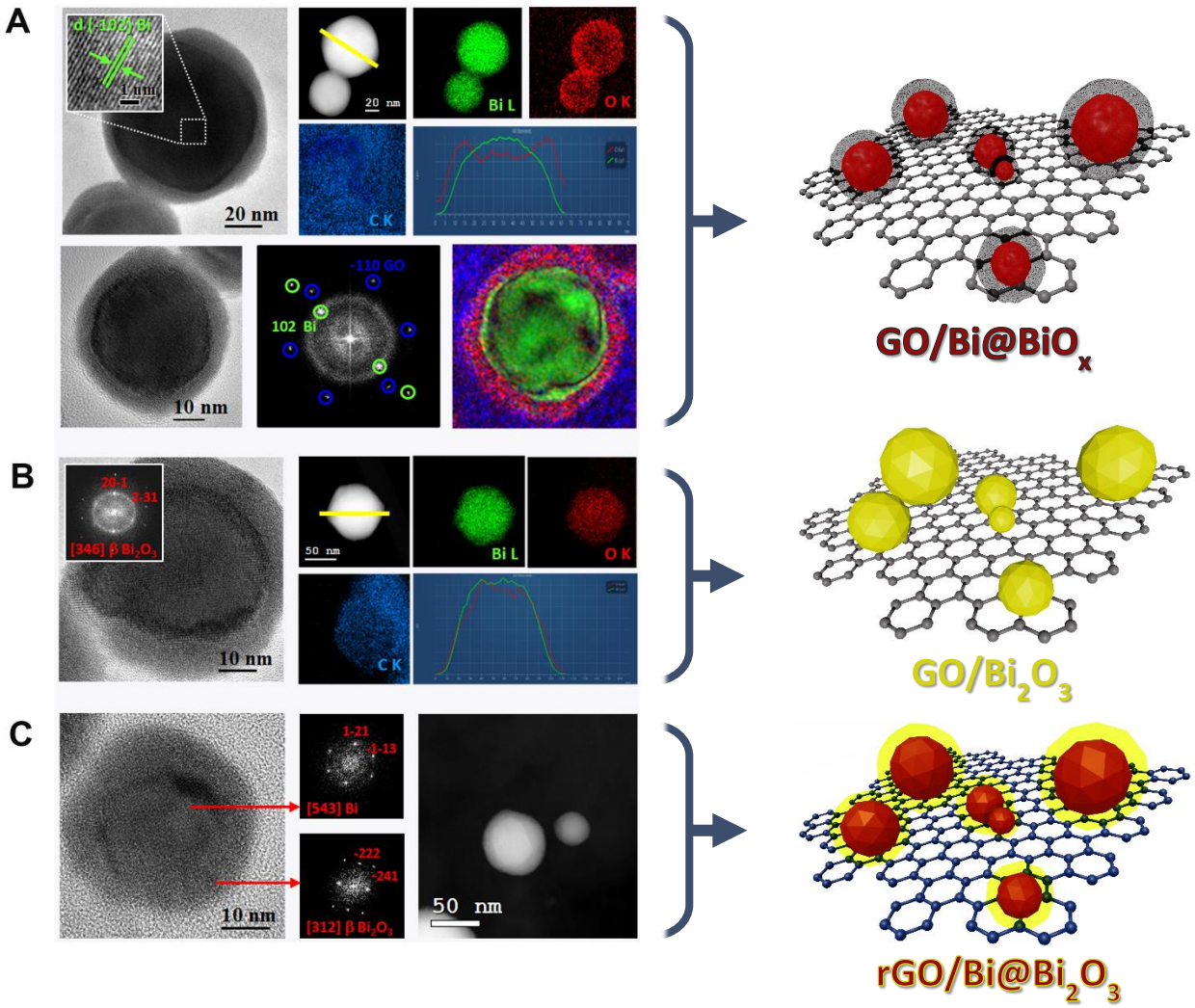

Figure 2.5 ***Electron microscopy study of the nanocomposites with graphical sketch of the three nanostructures.*** *A) top panels from left to right: representative HRTEM image of GO/Bi@BiO$_x$ with the inset showing the d-spacing (-102) of Bi, HAADF-STEM image with the corresponding C, Bi, O EDX maps. The EDX line-scan profile across the yellow line evidences the core–shell structure of Bi@Bi$_2$O$_3$; bottom panels from left to right: HRTEM of GO/Bi@BiO$_x$ with corresponding FFT showing the reflections from the (-102) planes of Bi and the [001] zone axis of GO, and the diffuse ring of the amorphous shell, color map displaying the inverse FFT generated by selecting the reflections relative to the Bi core (green), the oxide shell (red) and the GO layer (blue); B) large panel: HRTEM of GO/Bi$_2$O$_3$; In the inset the FFT of the core showing the [346] zone axis of β-Bi$_2$O$_3$; small panels clockwise, HAADF-STEM image of GO/Bi$_2$O$_3$ with the corresponding C, Bi, O EDX maps, and EDX line-scan profile across the yellow line; C) main panel: HRTEM of rGO/Bi@Bi$_2$O$_3$ showing the crystalline core/shell structure; small panels: the FFTs of the core and the shell showing the Bi and β-Bi$_2$O$_3$ phases respectively; last panel: representative HAADF-STEM image.*

EDX mapping and line profile (Figure 2.5B). The HRTEM highlights, even, that the nanoparticles maintain their core-shell structure despite being completely oxidized to the same Bi_2O_3 phase. On the contrary, calcination in a reducing atmosphere (H_2/Ar) causes the metal core to be preserved, while the BiO_x amorphous shell is crystallized to the β-Bi_2O_3 phase. Bi@β-Bi_2O_3 core-shell nanoparticles are thus created, as also confirmed by the FFT analysis (Figure 2.5C). Annular dark-field scanning transmission electron microscopy (HAADF-STEM) analysis provides neater evidence of the core-shell configuration (Figure 2.5C).

Furthermore, as a yardstick, the GO-free Bi_2O_3 nanoparticles were investigated, which were prepared by direct calcination in air of Bi@BiO_x NPs, skipping the mixing phase with GO. The analyzes conducted on this sample confirm what was previously reported: calcination in air involves the complete oxidation of the nanoparticles and their crystallization to the β-Bi_2O_3 phase. Furthermore, the direct comparison between GO-supported and GO-free samples, highlights how, in the sample without GO, the calcination treatment leads to the formation of numerous aggregates of the nanoparticles. In this case, the GO plays a fundamental role in stabilizing the NPs, preventing them from coalescing. Figure 2.6 shows the comparison between the HAADF-STEM images of the alone Bi@BiO_x NP as prepared and post-calcination (Figure 2.6A and 2.6B respectively) with the ones stabilized by supporting them on GO, namely GO/Bi@BiO_x and GO/Bi_2O_3 (Figure 2.6C and 2.6D respectively).

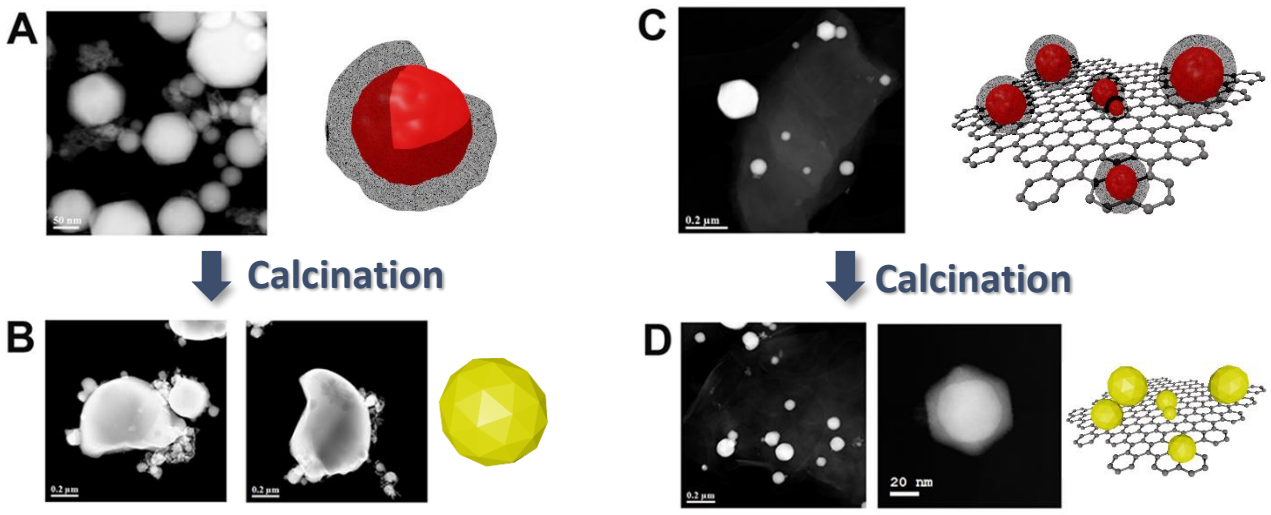

Figure 2.6 ***HAADF-STEM images****. A) free standing Bi@BiO_x NP, B) free standing Bi@BiO_x after calcination at 250 C (sample Bi_2O_3 NP), C) as prepared GO/Bi@BiO_x, D) GO/Bi_2O_3*

The nanoscale transmission electron microscopy results are in excellent agreement with large-scale X-ray diffraction (XRD) and Raman analysis.

The figure 2.7 shows the XRD spectrums of all samples. The XRD analysis highlights the presence of only the metal Bi phase for the Bi@BiO_x and GO/Bi@BiO_x samples, indexed to the Bi rhombohedral (JCPDS n. 05-0519), while it was not possible to detect any relevant Bi_2O_3, confirming the amorphous nature of the BiO_x shell.[23,25]

After the calcination treatment in air, in the sample GO/Bi_2O_3 there is the complete crystallization and oxidation of Bi(0) core with the formation of β-phase of Bi_2O_3 (tetragonal) readily indexed to the P-421c space group (ICDD crystallographic card number 01-077-5341),[26] and the complete disappearance of Bi^0 reflections. It is worth noting that calcination also causes a broadening of the reflection at ~27°, typical of graphitic carbon, suggesting that a reduction in the number of stacked layers of the multi-layer GO has occurred.[27] In contrast, the thermal treatment under reducing conditions (rGO/Bi@Bi_2O_3) produces the crystallization only of the BiO_x shell, while the core preserves its metallic nature, as observed by the co-existence of the reflections assigned to rhombohedral Bi and β-Bi_2O_3 in the XRD.

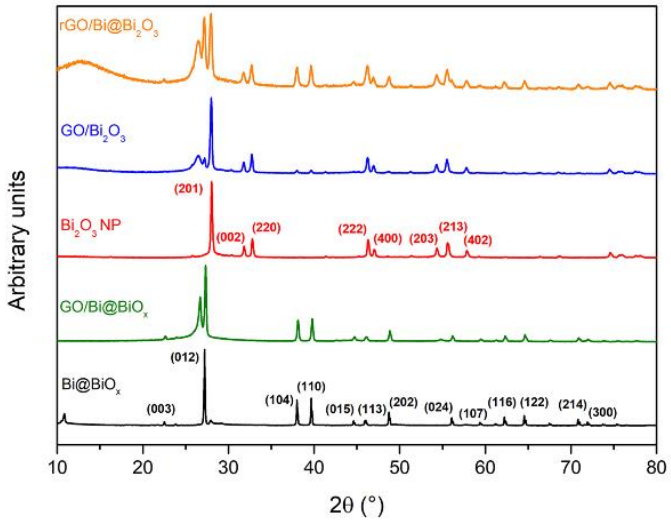

Figure 2.7 ***XRD analysis****: Powder XRD patterns of rGO/Bi@Bi_2O_3(orange), GO/Bi_2O_3 (blue), Bi_2O_3 NPs (red), GO/Bi@BiO_x (green) and Bi@BiO_x (black).*

Additionally, MicroRaman analysis confirms XRD results (figure 2.8). The spectrum of the as-prepared Bi@BiO_x nanoparticles confirms the presence of metal Bi through the two peaks (respectively at 85 and 105 cm^{-1}) which can be assigned to the E_g and A_{1g} vibrational modes of Bi-Bi in metallic bismuth. In this case, the frequencies are slightly blue-shifted with respect to bulk Bi due to the particle size in the nanoscale.[28] A less intense peak at 605 cm^{-1} is also observed, attributed to the amorphous BiO_x phase, probably carbonated following glucose binding,[29] confirming that the BiO_x shell in the non-calcined samples is not crystalline. Unfortunately, it was not possible to establish the origin of the third peak at 293 cm^{-1}, as it is not present in literature; thus, we can only hypothesize that it is due to some specific Bi-O Raman mode of the amorphous oxide shell still covered by carbonaceous species deriving from glucose. The subsequentially combination of NPs with GO introduces some change in the spectrum, such as in the case of the peak at 293 cm^{-1} is broader and significantly blue-shifted (308 cm^{-1}), and the same happens to the BiO_x peak that is blue-shifted to 627 cm^{-1}. It was not possible to assign any signal pattern associable with specific Bi_2O_3 phases, confirming the amorphous nature of the Bi oxide. We interpret this result as an effect of the electronic interaction between GO and the amorphous BiO_x shell, in agreement with the X-ray photoelectron spectroscopy (XPS) discussed

later. Raman analysis also confirms the crystallization of the bismuth oxide in GO/Bi_2O_3 with the presence of three new peaks at ca. 123, 315 and 465 cm^{-1} attributed to Bi-O stretching modes in β-Bi_2O_3.[16,29,30] Meanwhile, the signature of graphene is clearly visible in all nanocomposites sample (GO/Bi@BiO_x, GO/Bi_2O_3 and rGO/Bi@Bi_2O_3) with the characteristic D and G bands appearing at 1350 and 1570 cm^{-1} respectively, the former related to the A_{1g} breathing mode and the latter, together with another band (2D band) at 2700 cm^{-1}, associated to the first- and second-order allowed Raman mode E_{2g}.[31] The ratio of the D/G bands and the sharpness and intensity of the 2D band provide information on the level of defects present in graphene. In the case of starting GO, the intensity ratio and 2D band are low, indicating a low oxidation level and a small disorder. The calcination treatment in air induces creation of defects, presumably by insertion of additional oxygen functionalities.[32] While the reducing treatment has a beneficial effect in partially restoring a small level of defects, as evidenced by the decrease in intensity of the D band compared to the G band and as expected for reduced GO.[33] It is worth noting that for the rGO/Bi@Bi_2O_3 sample, together with a peak 103 cm^{-1} characteristic of metallic Bi, the β phase pattern is also found, in accordance with the metal-MO core-shell structure identified by HRTEM and FFT analysis.

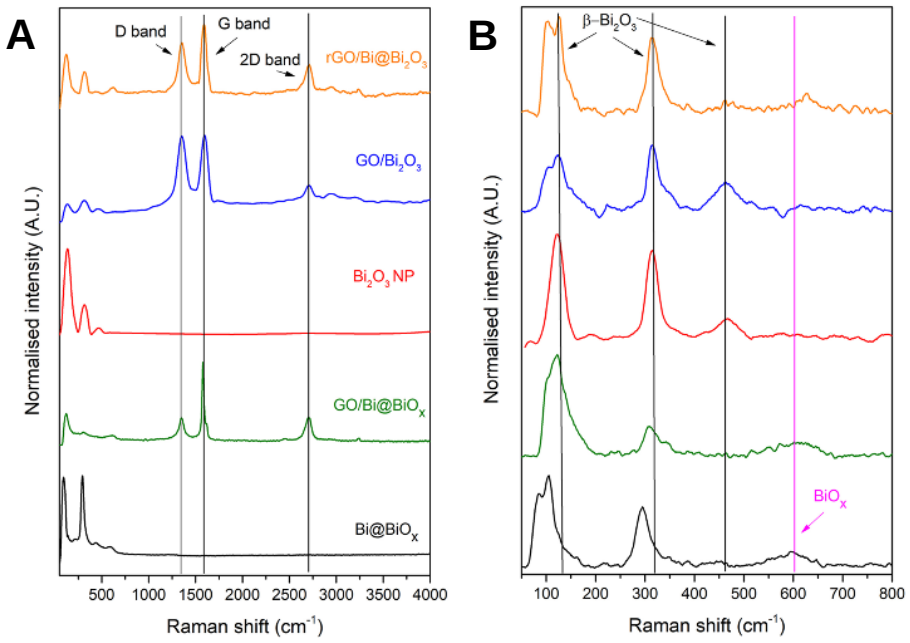

Figure 2.8 ***Raman analysis:*** *A) full range Raman spectra of GO/Bi_2O_3 NPs, Bi@BiO_x and of all three nanocomposites also showing the D, G and 2D bands relative to GO; B) Raman in the range 0-800 nm showing the bands relative to β-Bi_2O_3 and amorphous BiO_x.*

The XPS analysis confirms the presence of the C, Bi and O elements in the analysed samples, and especially provides information on the oxidation states of the surface and subsurface bismuth. For the as-prepared Bi@BiO_x NPs, the high resolution XPS of the Bi 4f core level shows the distinctive doublet of Bi with binding energies (BE) at 159.2 eV and 164.5 eV associated to the Bi^{3+} $4f_{7/2}$ and Bi^{3+} $4f_{5/2}$.[34] These peaks are present in all samples, albeit with some interesting differences. As anticipated, in the as-prepared Bi@BiO_x NPs the BE

of the two main peaks (to be precise 158.3 and 163.7 eV) coincide with those assigned in literature to oxidized Bi, with the additional presence of two small contributions at 156.5 and 162.1 eV, associated with metallic Bi (Figure 2.9, black line).[35,36] This data is consistent with the small penetration range of XPS, which makes difficult to detect the internal Bi core, while the oxidized shell is easily observed. However, once the Bi@BiO_x NPs are combined with GO (GO/Bi@BiO_x), the peaks are shifted towards higher BE (163.7 and 163.2 eV) confirming, as previously hypothesized, that there is an electronic interaction between the GO and Bi@BiO_x (Figure 2.9, green line). While the calcination of the composite (GO/Bi_2O_3) does not cause any shift in the BE, from which it can be deduced that despite the crystallization process, Bi_2O_3 continues to interact electronically with GO. As expected, the metallic Bi components disappear, while two new peaks arise at higher BE (168.7 and 163.2 eV), which have been attributed to higher Bi oxidation states (Figure 2.9, blue line). Although the presence of higher Bi oxidation states appears obvious for GO/Bi_2O_3, it does not seem so obvious for non-calcined sample (GO/Bi@BiO_x), as the XRD and Raman analysis indicated. It can therefore be assumed that GO may contribute to the depletion of electron density of outermost Bi atoms that make up the core, favouring their oxidation.[37] The XPS analysis of the sample treated in a reducing atmosphere does not show high oxidation peaks, but only two peaks associated to Bi^{3+}. While, the Bi^0 peaks are not detected, implying that the Bi_2O_3 shell is thicker than in the freshly made Bi@BiO_x NP (Figure 2.9, orange line).

The O1s region is influenced by the interaction between GO and NPs, therefore this consideration is valid for all nanocomposite materials, and not for as-prepared Bi@BiO_x. For the nanocomposites, the O1s peak can be deconvoluted into three components (Figure 2.9, O1s graph), which however present different relative intensities across the materials. From the deconvolution an interesting peak is identified at higher BE, it falls at 535.8 eV for GO/Bi_2O_3 and at 535.1 eV for GO/Bi@BiO_x and rGO/Bi@Bi_2O_3. This peak is associated with a partially covalent bonded superoxide.[37] Furthermore, from the quantitative analysis, it can be observed that the percentage of oxygen in the rGO/Bi@Bi_2O_3 sample is significantly lower than in all other nanocomposites, suggesting that the reducing treatment removes a large number of oxygen atoms from both Bi_2O_3 and from the GO (Table 2.1).

C1s peaks of GO/Bi@BiO_x were deconvoluted into four components at 284.4, 285.6, 287.5, and 288.9 eV, which are attributed to the C−C, C−O, C=O bond, and O-C=O respectively, arising from the functional groups of GO (Figure 2.9, graph C1s).[38] Consistently, the relative intensities of these peaks are modified following the thermal treatment, since the latter remove most of the GO oxygenated functional groups. It can also be noted how the calcination treatment removes most of the O-C=O component in both GO/Bi_2O_3 and rGO/Bi@Bi_2O_3, following decarboxylation. This results in the appearance of a new peak at 290.1 eV associated with π-π* bonding, as a result of restoration of sp^2 carbon network and thus the enhanced graphitization of the graphene due to high-temperature annealing (Figure 2.9, graph C1s, blue and orange lines).[39] Following

the XPS analysis, it can be deduced that GO does not act as a mere inert support for the nanoparticles but alters the electronic states of the Bi_2O_3 phase.

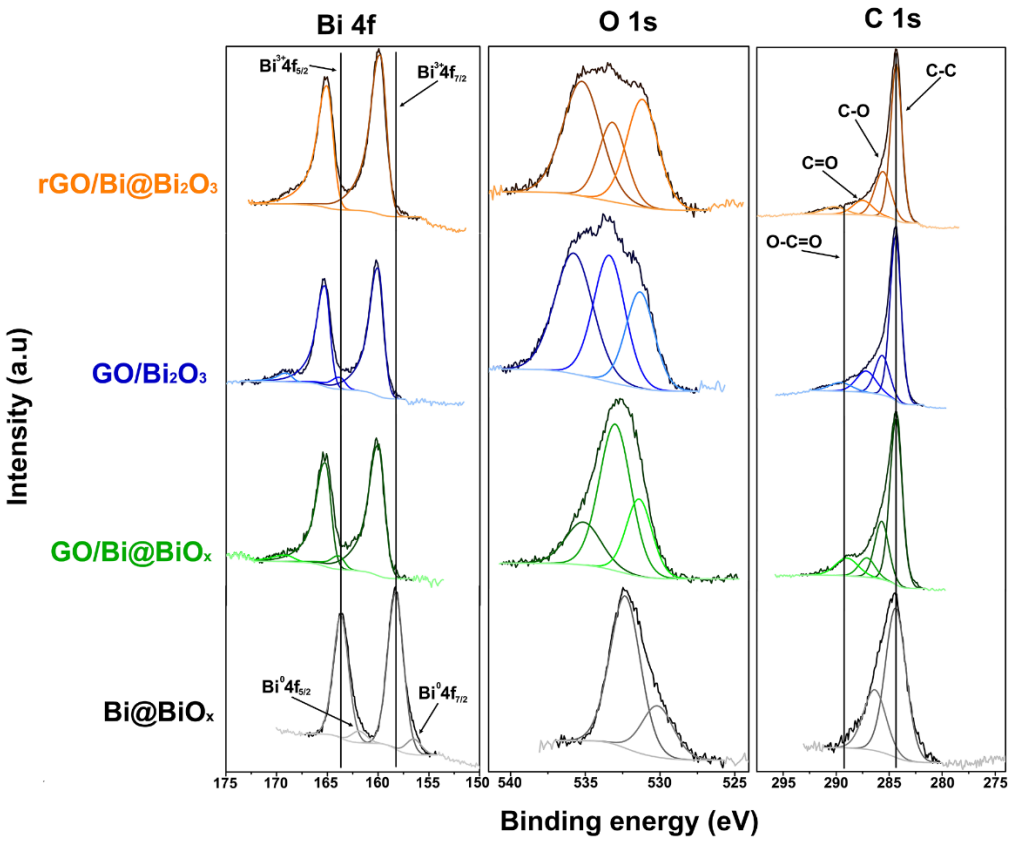

Figure 2.9 ***XPS analysis.*** *High-resolution XPS spectra in the Bi 4f B.E., O 1s B.E. range and C 1s B.E. range. Colours of the profile are associated to the materials as follows: black ($Bi@BiO_x$), green ($GO/Bi@BiO_x$), blue (GO/Bi_2O_3), orange ($rGO/Bi@Bi_2O_3$).*

Table 2.1 Quantitative XPS relative to the %at of C, O and Bi

SAMPLE	%at C	%at O	%at Bi
$Bi@BiO_x$	69.2	27.5	3.3
$GO/Bi@BiO_x$	76.6	22.7	0.7
GO/Bi_2O_3	77.0	21.7	1.2
$rGO/Bi@Bi_2O_3$	79.9	18.4	1.7

2.3 Electrochemical characterization and CO_2RR performance

The nanocomposites materials were characterized electrochemically through cyclic voltammetries (CVs) in KOH 0.1 M using a three-electrode electrochemical cell. The electrochemical characterization allows to better understand the system, its peculiarities and the relationship between inorganic NPs and the carbonaceous support, in order to correlate this information with the catalytic performance of CO_2RR. First, the electrochemical characteristics of Bi_2O_3 nanoparticles, prepared by conventional synthesis, were studied to have a reference. Figure 2.10 reports the CV of bulk Bi_2O_3 at 20 mV s^{-1} in Ar-saturated KOH 0.1 M.

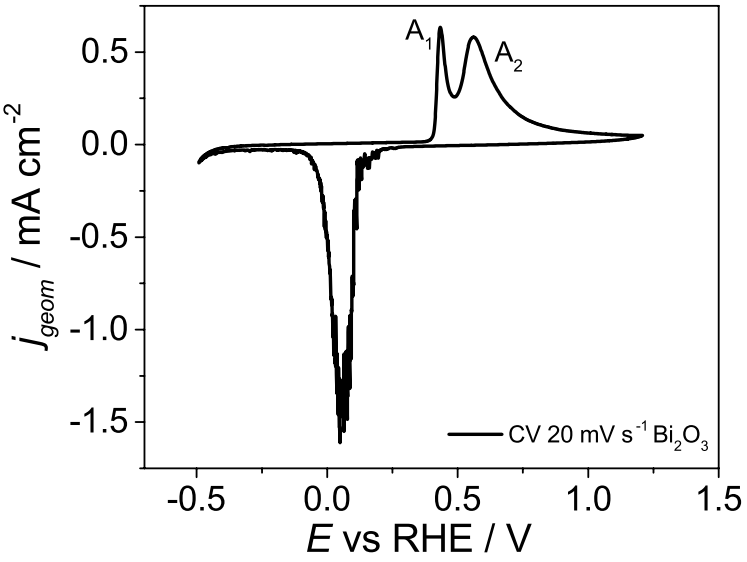

Figure 2.10 ***Cyclic voltammetry investigation.*** *CV at 20 mV s^{-1} in Ar-saturated KOH 0.1 M of Bi_2O_3 NPs. Two peaks are identified for the oxidation reaction: A_1 is the oxidation of Bi metal sites presents in the porosity of nanoparticles, while the A_2 peak is due to oxidation of Bi metal sites on surface. The potentials were corrected post measurement for the ohmic drop, considering the resistance of system (pH 13). The current was normalized for the geometric area of the electrode.*

At open circuit potential condition, the material is completely oxidized (E_{oc} = 0.89 V vs RHE). Once the bismuth oxide is put in contact with the alkaline solution, it undergoes a partial dissolution into ionic specie BiO_2^-.[40] The cathodic peak is due to main to reduction of BiO_2^-dissolved species, according to these reactions (2.1), (2.2) and (2.3):

$$BiO_2^- + e^- \rightarrow BiO_2^{2-} \quad (2.1)$$

$$2H_2O + 3BiO_2^{2-} \leftrightarrow 2BiO_2^- + 4OH^- + Bi^0 \quad (2.2)$$

$$Bi^0 \rightarrow Bi_{(metal)} \text{ metal deposition} \quad (2.3)$$

The oxidation peak A_2 and the subsequently plateau are due to the oxidation of Bi metal to Bi^{3+}. While the peak A_1 is described by *Vivier et al.* as oxidation of small fraction of Bi metal sites to Bi^{3+} in the microporous cavities, where the amount of reactant is limited, and the oxidation happen until exhaustion of OH^- species.[41] In both cases, the electrochemical reactions follow these reaction mechanisms:

$$Bi_{(metal)} \rightarrow Bi^{+} + e^{-} \quad (2.4)$$

$$3Bi^{+} \leftrightarrow Bi^{3+} + 2Bi_{(metal)} \quad (2.5)$$

$$3OH^{-} + Bi^{3+} \rightarrow Bi(OH)_3 \quad (2.6)$$

$$Bi(OH)_3 \rightarrow BiOOH + H_2O \quad (2.7)$$

When no potential is applied, the $Bi(OH)_3$ and BiOOH evolve spontaneously to form Bi_2O_3.[41] Unfortunately, due to the complexity of the processes in place, it is not possible to use the Bi redox peaks to calculate the electrochemically active surface area (ECSA), but to make only a qualitative estimate. The figure 2.11 shows the cyclic voltammetries of all samples of interest. From the direct comparison of the CVs of **GO/Bi_2O_3** and **rGO/Bi@Bi_2O_3** nanocomposite with Bi_2O_3, the first thing worth noting is the much higher current for CNS supported samples. In fact, the carbonaceous nanostructures help to improve the conductivity inside the material, activating a greater number of active sites. As already highlighted in the previous chapter, elevated electrical conductivity of the GO reduces the internal system resistance and supplies electrons to the metal oxide, activating it. Furthermore, the CNS contribute to increasing the surface area, and consequently the number of active sites. This last point was particularly highlighted by the capacitive of the double layer, which

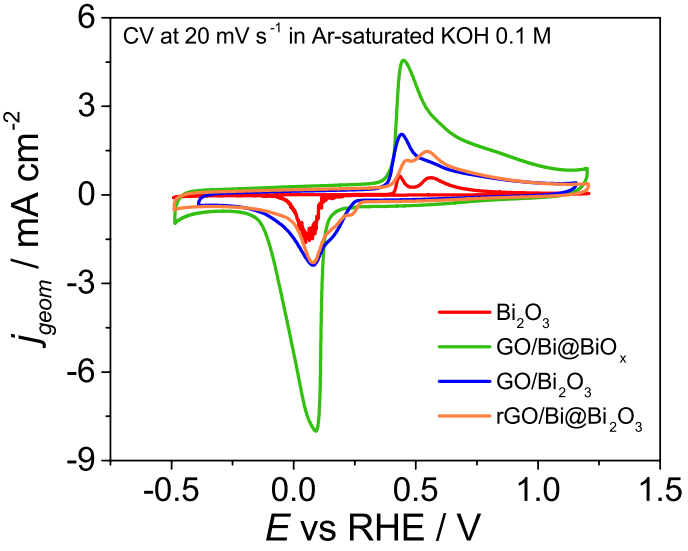

Figure 2.11 ***Cyclic voltammetry investigation.*** *Cyclic voltammetries at 20 mV s^{-1} in Ar-saturated KOH 0.1 M of Bi_2O_3 NPs (red), GO/Bi@BiO_x (green), GO/Bi_2O_3 (blue) and rGO/Bi@Bi_2O_3 (orange). The potentials were corrected post measurement for the ohmic drop, considering the resistance of system (pH 13). The current was normalized for the geometric area of the electrode.*

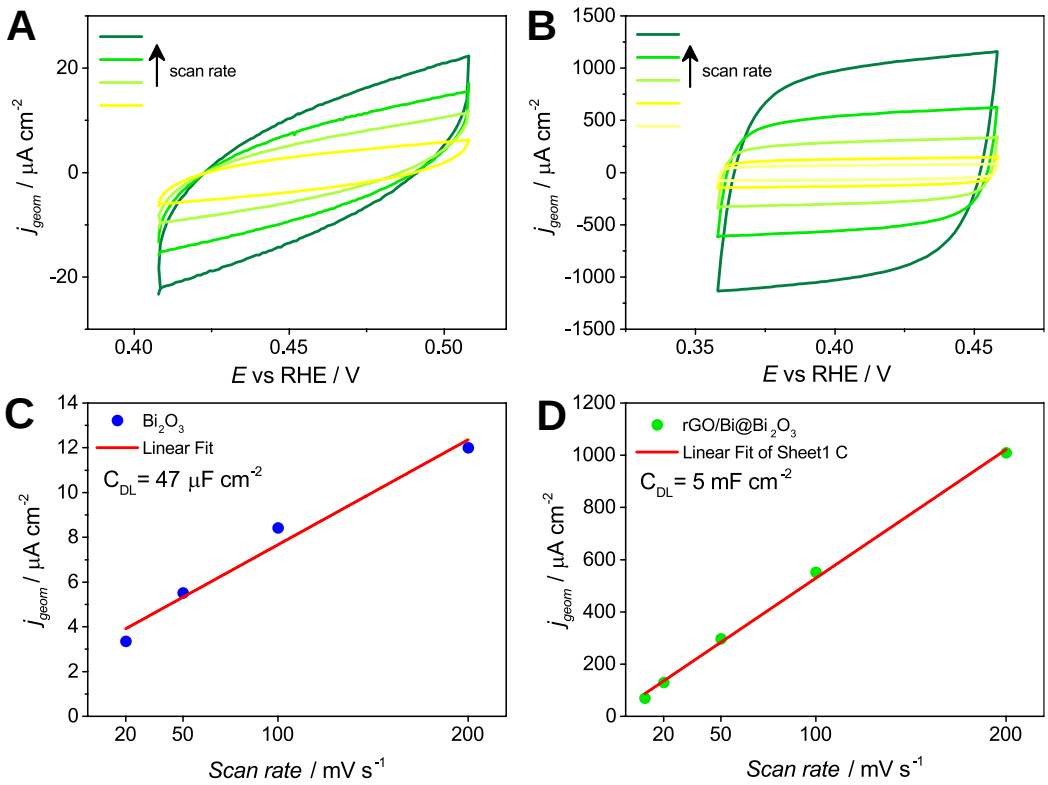

*Figure 2.12 Measured CVs for **A)** Bi_2O_3, **B)** rGO/BI@Bi_2O_3 in Ar-saturated KOH 0.1 M. The current density vs scan rate was plotted to extract the value of double layer capacitance (C_{DL}) of **C)** Bi_2O_3 and **D** rGO/Bi@Bi_2O_3. The current densities were obtained from the double layer charge/discharge curves at -0.45 V for Bi_2O_3 and -0.40 V for rGO/Bi@Bi_2O_3.*

turns out to be 100 times higher with the weight of the GO (Figure 2.12). Moreover, the resistance and aggregation of pure Bi_2O_3 NPs can decrease the electrochemical active surface area and the stability of the electrocatalyst. In fact, the CNS support increases the stability of the Bi_2O_3 nanoparticles: it was observed that in sample without CNS, the faradic current decreases with the increase in the number of cycles. Finally, it is possible to notice the different CV evolution between **GO/Bi_2O_3** and **rGO/Bi@Bi_2O_3**, where in the first case the A_1 peak is larger than A_2, while for sample with rGO the A_1 peak decreases in favour of the A_2 peak. This observation well fits with the different structures of the two nanocomposites, whereby the metallic Bi core in the **rGO/Bi@Bi_2O_3** and the particular core-shell motif plays a role in determining the electrochemical behaviour.

The CO_2RR catalytic activity was evaluated as a function of applied potential, performing chronoamperometry (CA) experiments in CO_2-saturated $KHCO_3$ 0.5 M for 1 hour and 50 minutes (ranging from -0.4 to -0.9 V vs RHE). The gas phase was quantified during the electrolysis using an online gas chromatograph (GC), while the liquid phase was analyzed in a second moment with ionic chromatography (IC). From these analyses, it was possible to determinate the product selectivity, reported as the Faraday efficiency (FE). Figure 2.13 shows, in addition to the FE values, the average values of the involved current density (*j*) during the electrolysis for all the sample mentioned above. The product analysis highlights the

presence of three products: hydrogen, carbon monoxide and formic acid. The amount of CO is so low, that its FEs never exceed 0.5 %, for this reason its contribution can be neglected. All the nanocomposites (**GO/Bi@BiO$_x$**, **GO/Bi$_2$O$_3$** and **rGO/Bi@Bi$_2$O$_3$**) exhibit good catalytic activity for CO_2RR with HCOOH as the dominant product, and with the onset potential for the HCOOH formation very near the thermodynamic potential.[42] In all cases, also hydrogen evolution reaction occurs to different extents depending on the

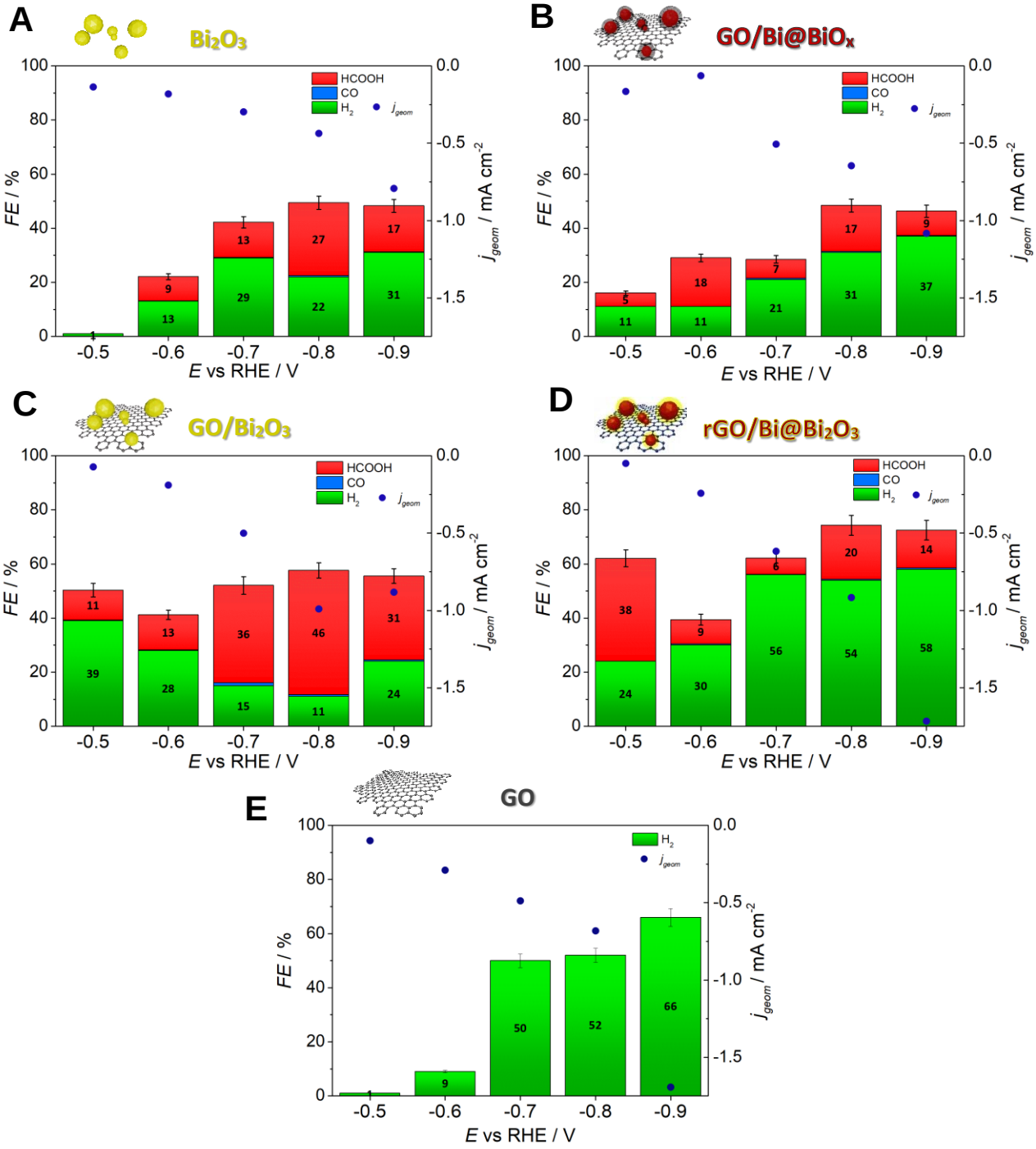

Figure 2.13 ***CO_2RR performance.*** *Faradaic Efficiency (FE) of detectable CO_2RR products in CO_2-saturated $KHCO_3$ 0.5 M (pH 7.5): H_2 (green), CO (light blue) and HCOOH (red) for A) Bi_2O_3, B) GO/Bi@BiO$_x$, C) GO/Bi_2O_3, D) rGO/Bi@Bi_2O_3 and E) GO. In the case of GO, the CO and HCOOH data have not been reported in the legend because they are not present, the only measurement value is the FE for HCOOH of 1% at -0.9 V. The blue points indicate the mean current density of sample at that potential; the values are shown on right axis.*

catalyst and the applied potential. Any kind of contribution in the production of HCOOH by the GO can be excluded, as additional experiments were performed which demonstrated the only production of hydrogen (Figure 2.13 E). The presence of GO and rGO significantly increase the current density for CO_2RR and thus the FE_{HCOOH}, but above all reduces the onset of potential of 200 mV (Figure 2.13 and Figure A.9). The performance for the **GO/Bi@BiO$_x$** sample, which has not undergone calcination processes, shows significantly lower performance than the other nanocomposite samples. The explanation for this behavior can be attributed to the amorphous structure of oxide shell and to the presence of some carbonaceous residues of glucose on the nanoparticles surface that together with the presence of a larger number of O-C=O groups in the GO, they contributions reduce the efficiency of electronic communication with the carbonaceous support and the number of active sites. These adverse contributions are removed with the calcination treatment.

In addition, the difference in the hierarchical structures is reflected in significantly different catalytic behaviour. The FE_{HCOOH} for rGO/Bi@Bi_2O_3 reaches a maximum value of 38% at -0.5 V vs RHE (corresponding to a HCOOH production rate of 3 ppm h^{-1}), with a very small overpotential (100 mV), and declines with increasing potential. Unlike HER which always remains present and with relatively high FEs throughout the explored potential range (Figure 2.13 D). On the other hand, GO/Bi_2O_3 is able to form HCOOH with a higher absolute FEs, but in a more negative range (-0.7 to -0.9V). The peak of FE_{HCOOH} is at -0.8 V with 46% and an HCOOH production rate of 73 ppm h^{-1}, while the FE for the HER process is relatively small. Nevertheless, the FE_{HCOOH} at -0.5 V is definitely lower (11%) in comparison with that of rGO/Bi@Bi_2O_3.

It has been widely demonstrated that the presence of oxygen atoms in a bismuth structure helps to reduce the energy barrier for the *OCHO formation, thus promoting the production of formic acid.[21] *Chen et al.* demonstrated that a heterojunction of Bi/BiO_2, with the metal phase deriving from Bi_2O_3, can preferentially produce HCOOH with lower overpotential than the metal Bi. In fact, they observed how in heterojunctions the number of electrons in the 6p orbital of Bi with *OCHO intermediate adsorbed was 2.77 (when the reference value is 3), while for the *COOH intermediate it was 2.89. The lower electrons value indicates a better charge transfer from the Bi site to *OCHO and consequently by its easier formation.[18] It can be hypothesized that at low overpotential the Bi_2O_3 shell of rGO/Bi@Bi_2O_3 undergoes a partial reduction, forming a great interaction between metal superficial Bi and Bi_2O_3 that lead to high FE_{HCOOH} at low overpotential. While as the potential increases, the shell of the nanoparticles is completely reduced, partly favouring the HER, and requiring a greater overpotential for the production of formic acid on metallic bismuth. We can hypothesize that in the case of rGO/Bi@Bi_2O_3, the metallic Bi core has a beneficial effect in anticipating the potential for HCOOH formation, ensuring better charge transfer, and reducing the internal resistance of the material, up to the complete reduction of the oxide. In the case of sample GO/Bi_2O_3, the oxidizing nanoparticles do not undergo a complete reduction during the electrolysis but manage to maintain an oxidized core. It is probably for this reason that a higher efficiency is observed for formic acid and with a

higher production in terms of quantity, but at more negative potentials, where the metal oxide increases the internal resistance of the material.

The formic acid production rate plot (Figure 2.14) remarks the difference in the potential range for CO_2RR selectivity: the HCOOH production is higher for $rGO/Bi@Bi_2O_3$ until -0.6 V, while GO/Bi_2O_3 becomes more active in the range -0.7 to -0.9 V. However, it is worth noting that in terms of productivity, GO/Bi_2O_3 reaches a peak at -0.8 V and then there is a decline, whereas for $rGO/Bi@Bi_2O_3$ the HCOOH productivity increases linearly with moving towards more negative potential, despite the drop in selectivity. These data are in accordance with the above hypothesis, the complete reduction of the nanoparticles shifted the formic acid formation process to higher potentials. One thing that can be noticed about the sample GO/Bi_2O_3 is the current density go to plateau, indicating a mass transport limit. Furthermore, the essential role of liming in making a more efficient material must be emphasized. The thermal treatment induces the crystallization of the nanoparticles, removes the organic residues of the stabilizing agent (glucose), and ensures a better interaction at the metal MO-CNS interface. All these contributions improve the transfer of charge between metal oxide NPs and CNS support.

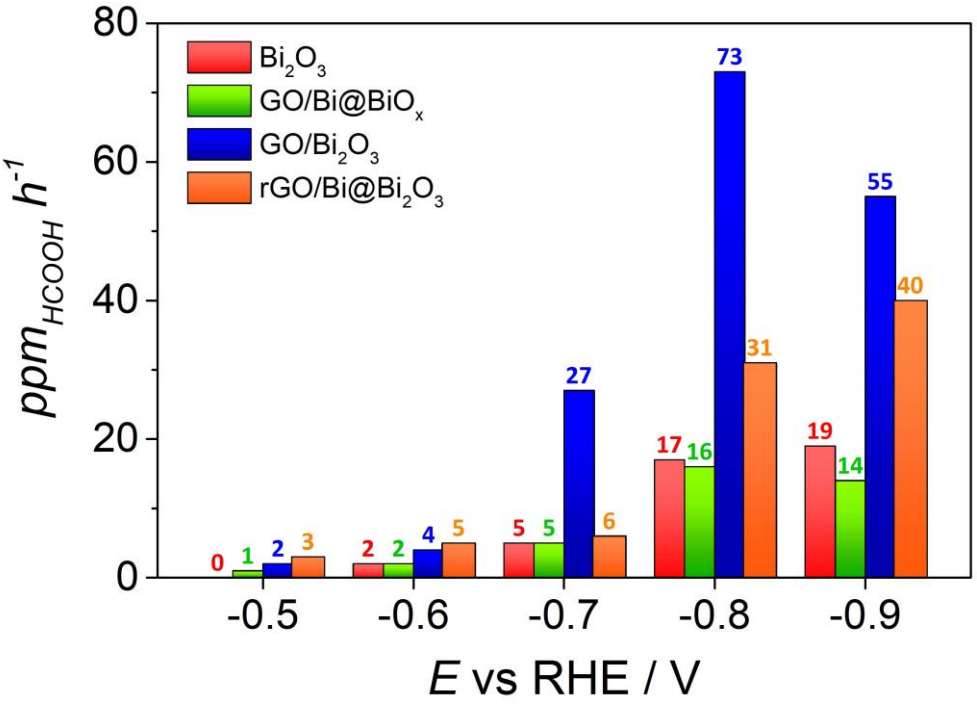

Figure 2.14 ***HCOOH productivity by the different catalysts.*** *Formic acid production rate in ppm h^{-1} at different potentials for Bi_2O_3 (red), $GO/Bi@BiO_x$ (green), $rGO/Bi@Bi_2O_3$ (orange) and GO/Bi_2O_3 (blue).*

Finally, an optimization study was carried out on the quantity of Bi_2O_3 in relation to GO, to further increase the production of HCOOH. For this purpose, two additional samples were investigated, with a higher (**GO/Bi_2O_3 3:1**) or lower Bi_2O_3 loadings (**GO/Bi_2O_3 5:1**) respectively (Figure 2.15); while the ratio of previous sample **GO/Bi_2O_3** was **4:1**. Interestingly, although the current densities do not change among the three catalysts, the FE is not directly proportional to the amount of Bi_2O_3 present in the GO. In fact, the **GO/Bi_2O_3**

4:1 catalyst shows the best performance for CO_2RR, with FE_{HCOOH} as high as 46 % at -0.8 V, where the normalised formic acid production rate for bismuth oxide mass is $484\ ppm_{HCOOH}\ h^{-1} g^{-1}_{Bi_2O_3}$. On the other hand, for **GO/Bi_2O_3 3:1**, which has a higher amount of Bi_2O_3, the FE_{HCOOH} never exceed 10 % until -0.8 V, with increment at -0.9 V (Figure 2.14 and Figure A.10). In contrast, the **GO/Bi_2O_3 5:1** shows significantly poorer activity for CO_2RR, where the top FE_{HCOOH} is only 8% (at -0.9 V), while the parasitic HER remains the predominant process. Probably this behaviour derives from the GO, active only for HER, present there in much greater relative quantities (Figure 2.13 D). It can therefore be concluded that a GO/Bi_2O_3 optimised can favour the reduction of CO_2 to formic acid upon a fine balancing between the number of active sites and the material resistance.

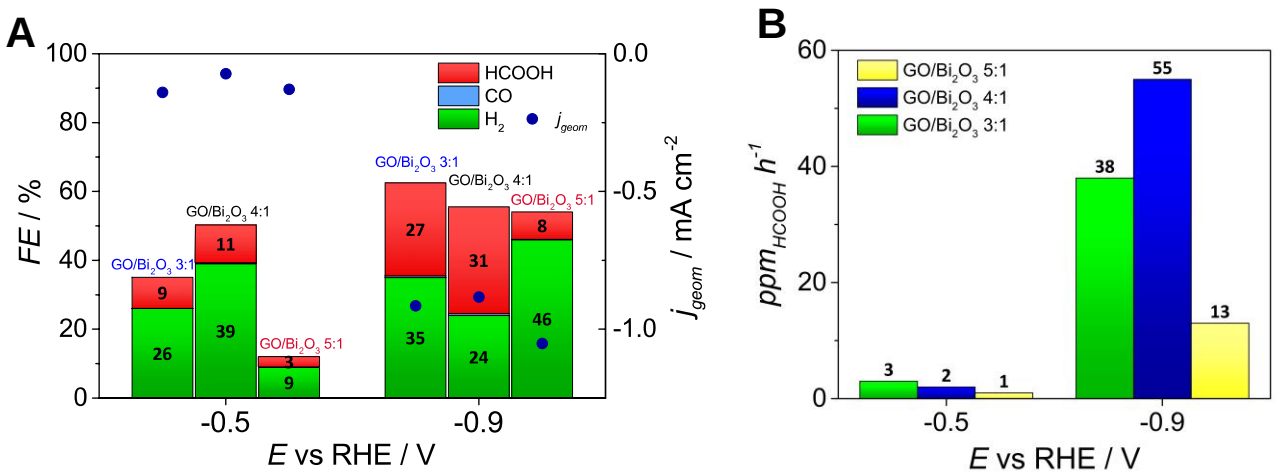

Figure 2.15 ***Loading optimization.*** *A) Faradaic Efficiency (FE) of detectable CO_2RR products in CO_2-saturated $KHCO_3$ 0.5 M (pH 7.5): H_2 (green), CO (light blue) and HCOOH (red) for GO/Bi_2O_3 3:1 (blue), GO/Bi_2O_3 4:1 (black) and GO/Bi_2O_3 5:1 (red); the blue points indicate the mean current density of sample at that potential; the values are shown on right axis. B) Formic acid production rate in ppm h^{-1} at different potentials for GO/Bi_2O_3 3:1 (green), GO/Bi_2O_3 4:1 (blue) and GO/Bi_2O_3 5:1 (yellow).*

2.4 Conclusions

In conclusion, we conducted an in-depth analysis on the role of GO when supplemented with Bi_2O_3 nanoparticles in the electrocatalytic reduction of CO_2, revealing notable differences depending on the structure. The presence of GO in close contact with the active phase (Bi_2O_3) causes a significant increase in the performance of CO_2RR with selectivity for the synthesis of formic acid. The results presented in this chapter reinforce the concept already expressed in the previous chapter, whereby an adequate interaction between MO and CNS promotes the catalytic activity and selectivity of MO catalysts; where, the creation of an optimal interface is able to increase the mobility of electrons in the MO and significantly contribute to the long-term stability of nanostructured catalysts. Differences were noted based on the degree of oxidation of the carbon scaffold, with the rGO being more effective in favouring electron mobility as compared with the GO, thus facilitating electron transfers.

Finally, the effect of the structure and nature of bismuth oxide nanoparticles was explored, and how the presence of a metal core can greatly influence the selectivity and efficiencies for CO_2 reduction; in this case anticipating the onset potential for CO_2RR with rather high efficiencies for formic acid close to the thermodynamic potential.

Reference

1. Kortlever, R., Balemans, C., Kwon, Y. & Koper, M. T. M. Electrochemical CO2 reduction to formic acid on a Pd-based formic acid oxidation catalyst. *Catal. Today* **244**, 58–62 (2015).

2. Chen, Z., Wang, N., Yao, S. & Liu, L. The flaky Cd film on Cu plate substrate: An active and efficient electrode for electrochemical reduction of CO2 to formate. *J. CO2 Util.* **22**, 191–196 (2017).

3. Hara, K., Kudo, A. & Sakata, T. Electrochemical reduction of carbon dioxide under high pressure on various electrodes in an aqueous electrolyte. *J. Electroanal. Chem.* **391**, 141–147 (1995).

4. Hoffman, Z. B., Gray, T. S., Moraveck, K. B., Gunnoe, T. B. & Zangari, G. Electrochemical Reduction of Carbon Dioxide to Syngas and Formate at Dendritic Copper-Indium Electrocatalysts. *ACS Catal.* **7**, 5381–5390 (2017).

5. Cheng, F. *et al.* Recent Progress of Sn-Based Derivative Catalysts for Electrochemical Reduction of CO2. *Energy Technol.* **9**, 1–18 (2021).

6. Han, N. *et al.* Ultrathin bismuth nanosheets from in situ topotactic transformation for selective electrocatalytic CO2 reduction to formate. *Nat. Commun.* **9**, 1–8 (2018).

7. World Health Organization. Regional Office for Europe & Joint WHO/Convention Task Force on the Health Aspects of Air Pollution. *Health risks of heavy metals from long-range transboundary air pollution*. (2007).

8. Chen, Y. & Kanan, M. W. Tin oxide dependence of the CO 2 reduction efficiency on tin electrodes and enhanced activity for tin/tin oxide thin-film catalysts. *J. Am. Chem. Soc.* **134**, 1986–1989 (2012).

9. Li, Q., Wang, Z., Zhang, M., Hou, P. & Kang, P. Nitrogen doped tin oxide nanostructured catalysts for selective electrochemical reduction of carbon dioxide to formate. *J. Energy Chem.* **26**, 825–829 (2017).

10. Guan, Y., Liu, M., Rao, X., Liu, Y. & Zhang, J. Electrochemical reduction of carbon dioxide (CO2): bismuth-based electrocatalysts. *J. Mater. Chem. A* **9**, 13770–13803 (2021).

11. Medina-Ramos, J., Dimeglio, J. L. & Rosenthal, J. Efficient reduction of CO2 to CO with high current density using in situ or ex situ prepared bi-based materials. *J. Am. Chem. Soc.* **136**, 8361–8367 (2014).

12. Atifi, A. *et al.* Insights into the Composition and Function of a Bismuth-Based Catalyst for Reduction of CO2 to CO. *J. Phys. Chem. C* **123**, 9087–9095 (2019).

13. Atifi, A., Boyce, D. W., Dimeglio, J. L. & Rosenthal, J. Directing the Outcome of CO2 Reduction at Bismuth Cathodes Using Varied Ionic Liquid Promoters. *ACS Catal.* **8**, 2857–2863 (2018).

14. Zhang, Z. *et al.* Rational Design of Bi Nanoparticles for Efficient Electrochemical CO2 Reduction: The Elucidation of Size and Surface Condition Effects. *ACS Catal.* **6**, 6255–6264 (2016).

15. Gong, Q. *et al.* Structural defects on converted bismuth oxide nanotubes enable highly active electrocatalysis of carbon dioxide reduction. *Nat. Commun.* **10**, 1–10 (2019).

16. Kim, S. *et al.* Shape-controlled bismuth nanoflakes as highly selective catalysts for electrochemical carbon dioxide reduction to formate. *Nano Energy* **39**, 44–52 (2017).

17. Gao, T. *et al.* Morphology effects of bismuth catalysts on electroreduction of carbon dioxide into formate. *Electrochim. Acta* **305**, 388–393 (2019).

18. Feng, X. *et al.* Bi2O3/BiO2Nanoheterojunction for Highly Efficient Electrocatalytic CO2Reduction to Formate. *Nano Lett.* **22**, 1656–1664 (2022).

19. Oh, W., Rhee, C. K., Han, J. W. & Shong, B. Atomic and Molecular Adsorption on the Bi(111) Surface: Insights into Catalytic CO2 Reduction. *J. Phys. Chem. C* **122**, 23084–23090 (2018).

20. Lu, P. *et al.* Facile synthesis of a bismuth nanostructure with enhanced selectivity for electrochemical conversion of CO2 to formate. *Nanoscale* **11**, 7805–7812 (2019).

21. Yang, J. *et al.* Bi-Based Metal-Organic Framework Derived Leafy Bismuth Nanosheets for Carbon Dioxide Electroreduction. *Adv. Energy Mater.* **10**, 1–7 (2020).

22. Melchionna, M., Fornasiero, P., Prato, M. & Bonchio, M. Electrocatalytic CO2reduction: Role of the cross-talk at nano-carbon interfaces. *Energy Environ. Sci.* **14**, 5816–5833 (2021).

23. Chen, M. *et al.* Controllable Synthesis of Core-Shell Bi@Amorphous Bi2O3 Nanospheres with Tunable Optical and Photocatalytic Activity for NO Removal. *Ind. Eng. Chem. Res.* **56**, 10251–10258 (2017).

24. Lamagni, P. *et al.* Restructuring Metal–Organic Frameworks to Nanoscale Bismuth Electrocatalysts for Highly Active and Selective CO2 Reduction to Formate. *Adv. Funct. Mater.* **30**, 1–11 (2020).

25. Wang, Z., Jiang, C., Huang, R., Peng, H. & Tang, X. Investigation of optical and photocatalytic properties of bismuth nanospheres prepared by a facile thermolysis method. *J. Phys. Chem. C* **118**, 1155–1160 (2014).

26. Dias, L. P., Correia, F. C., Ribeiro, J. M. & Tavares, C. J. Photocatalytic Bi2O3/TiO2:N thin films with enhanced surface area and visible light activity. *Coatings* **10**, (2020).

27. Rao, C. N. R., Biswas, K., Subrahmanyam, K. S. & Govindaraj, A. Graphene, the new nanocarbon. *J. Mater. Chem.* **19**, 2457–2469 (2009).

28. Onari, S., Miura, M. & Matsuishi, K. Raman spectroscopic studies on bismuth nanoparticles prepared by laser ablation technique. *Appl. Surf. Sci.* **197**–**198**, 615–618 (2002).

29. Dutta, A. *et al.* A tandem (Bi2O3 → BiMet) catalyst for highly efficient EC-CO2 conversion into formate: Operando Raman spectroscopic evidence for a reaction pathway change. *ACS Catal.* **11**, 4988–5003 (2021).

30. Pereira, A. L. J. *et al.* Isostructural second-order phase transition of β-Bi2O3 at high pressures: An experimental and theoretical study. *J. Phys. Chem. C* **118**, 23189–23201 (2014).

31. Claramunt, S. *et al.* The importance of interbands on the interpretation of the raman spectrum of graphene oxide. *J. Phys. Chem. C* **119**, 10123–10129 (2015).

32. Martins Ferreira, E. H. *et al.* Evolution of the Raman spectra from single-, few-, and many-layer graphene with increasing disorder. *Phys. Rev. B - Condens. Matter Mater. Phys.* **82**, (2010).

33. Criado, A., Melchionna, M., Marchesan, S. & Prato, M. The Covalent Functionalization of Graphene on Substrates. *Angew. Chemie - Int. Ed.* **54**, 10734–10750 (2015).

34. Wang, J. *et al.* Synthesis and Characterisation of Reduced Graphene Oxide/Bismuth Composite for Electrodes in Electrochemical Energy Storage Devices. *ChemSusChem* **10**, 363–371 (2017).

35. Hu, J., Li, H., Huang, C., Liu, M. & Qiu, X. Enhanced photocatalytic activity of Bi2O3 under visible light irradiation by Cu(II) clusters modification. *Appl. Catal. B Environ.* **142**–**143**, 598–603 (2013).

36. Sun, J. *et al.* Bi/Bi2O3 nanoparticles supported on N-doped reduced graphene oxide for highly efficient CO2 electroreduction to formate. *Chinese Chem. Lett.* **31**, 1415–1421 (2020).

37. Barreca, D., Morazzoni, F., Rizzi, G. A., Scotti, R. & Tondello, E. Molecular oxygen interaction witha spectroscopic and Bi2O3: Spectromagnetic investigation. *Phys. Chem. Chem. Phys.* **3**, 1743–1749 (2001).

38. Johra, F. T., Lee, J. W. & Jung, W. G. Facile and safe graphene preparation on solution based platform. *J. Ind. Eng. Chem.* **20**, 2883–2887 (2014).

39. Zhang, W., He, W. & Jing, X. Preparation of a stable graphene dispersion with high concentration by ultrasound. *J. Phys. Chem. B* **114**, 10368–10373 (2010).

40. Vivier, V. *et al.* Electrochemical Study of Bi[sub 2]O[sub 3] and Bi[sub 2]O[sub 2]CO[sub 3] by Means of a Cavity Microelectrode. I. Observed Phenomena and Direct Analysis of Results. *J. Electrochem. Soc.* **147**, 4252 (2000).

41. Vivier, V. *et al.* Cyclic voltammetry study of bismuth oxide Bi2O3 powder by means of a cavity microelectrode coupled with Raman microspectrometry. *Electrochim. Acta* **46**, 907–914 (2001).

42. Kortlever, R., Shen, J., Schouten, K. J. P., Calle-vallejo, F. & Koper, M. T. M. M. Catalysts and Reaction Pathways for the Electrochemical Reduction of Carbon Dioxide. *J. Phys. Chem. Lett.* **6**, 4073–4082 (2015).

Chapter III

Nickel Oxide nanoparticles on Covalent Triazine Framework for Syngas production

Synthesis and characterization were performed in collaboration with Prof. Giuliano Giambastiani and Dr. Giulia Tuci of ICOOM-CNR

3.1 Introduction

As already expressed previously, in recent years research has focused on the study of the CO_2 reduction reaction with the prospect of reducing CO_2 emissions and producing useful chemical reagents. In addition to the problem of global warming and therefore of climate change, there is also the problem of scarce energy resources. Indeed, the demand for fuels and energy is continuously increasing, driven by the growth in the global population, and by the increase in the production and use of electronic devices. Within this context, research into alternative energy sources finds its flourishing development, especially for the CO_2 reduction products. From this point of view, CO_2RR can lead to the formation of numerous reaction products useful for energy and industrial purposes. Unfortunately, when the reaction takes place inside aqueous solutions there is the presence of the parasitic reaction of the HER, which reduces the efficiency of the CO_2RR. About that, the research has turned the hydrogen evolution reaction at its own advantage, combining it with CO_2RR to obtain syngas, that is a mixture of H_2/CO whose use is quite wide and whose application depends on the ratio of the mixture (Figure 3.1). Syngas can be used as a raw material or as an intermediate for the production of chemicals, fertilizers, pharmaceuticals, plastics, solvents, intermediates in chemical processes (es. methanol), or intermediates for the production of synthetic natural gas (CH_4), biodiesel and fuels.[1] The applications of syngas are numerous and the possibility of combining two reactions that usually compete with each other represents a considerable advantage. Currently the market price of syngas is so low (0.06 $/kg) that its profitability is impossible, regardless of the performance of the technology adopted.[2] The real advantage of the syngas produced by electrochemical conversion of CO_2 is represented by the reduction of CO_2 emissions.

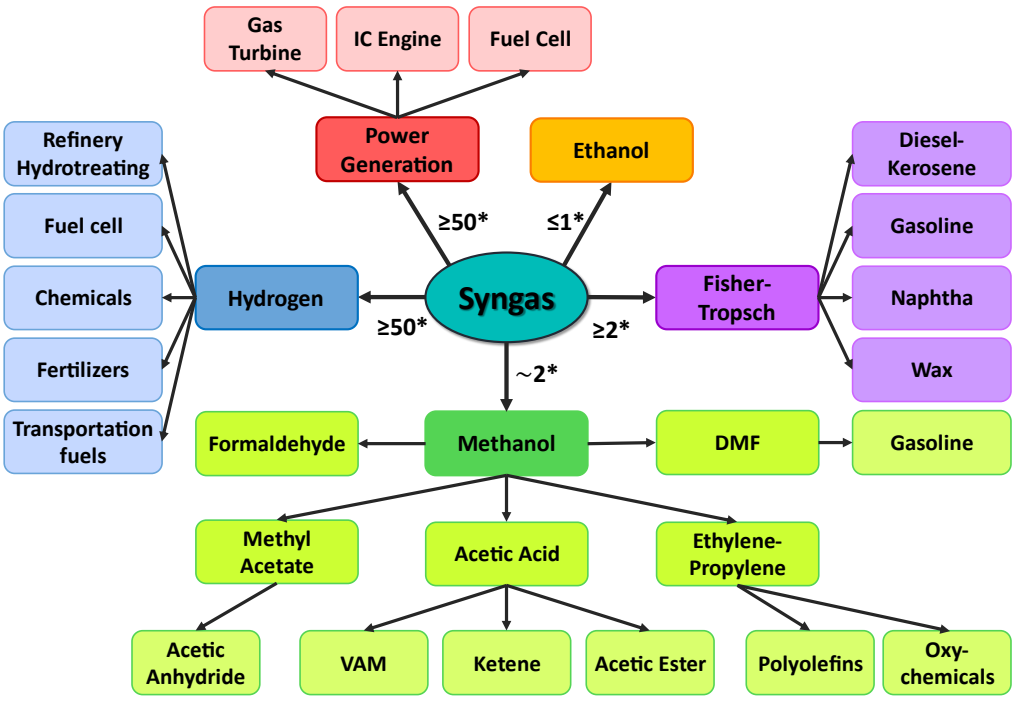

Figure 3.1 Application and derivates of Syngas with reference to their composition (H_2/CO molar ratio). Adapted from Green Chem.* ***19****, 2326–2346 (2017).*[1]

The CO_2 reduction reaction to CO can be summarized in the following equations:[3]

$$CO_2(g) + * + H^+(aq) + e^- \leftrightarrow {}^*COOH \quad (3.1)$$

$${}^*COOH + H^+(aq) + e^- \leftrightarrow {}^*CO + H_2O \quad (3.2)$$

$${}^*CO \leftrightarrow CO(g) + * \quad (3.3)$$

where the *COOH is the reaction intermediate that lead to the formation of CO, and unlike the formic acid pathway, this reaction intermediate binds to the surface via the C atom (Figure 3.2). The *COOH adsorption energy is an indicator of CO production.[3] Based on the nature of the material and its morphology, the rate determining step of this reaction falls either into the activation of CO_2 with the first electron transfer or with the first protonation.[4] Also in this case, as in the production of formic acid, it will be necessary to carefully select the materials that will make up the electrocatalyst, in order to obtain the right mixture ratio, without the formation of other side products. In recent years, research has focused above all on the study of catalysts that produce only and exclusively CO, such as Au and Ag. Their advantage is that they do not produce other reaction products, but the big disadvantage is the high price and low abundance which makes them inaccessible. There are some transition metals where HER remains favoured over CO_2RR (e.g., Ni, Fe, Ti, Pt),[5] but whose properties are modifiable to achieve better CO_2RR efficiency. Among these elements, Ni-based materials are considered to be potential electrocatalysts for CO_2RR.

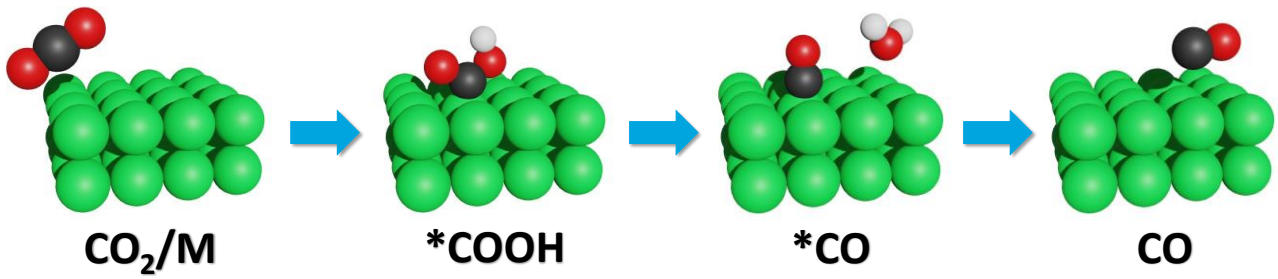

*Figure 3.2 General scheme of the proposed pathway for CO_2 electroreduction to CO with corresponding *COOH and *CO intermediates on the metal surface (M).*

3.1.1 Ni-based electrocatalysts for CO_2RR

The primary difficulty in using non-noble metals for CO_2RR is their high activity for the HER parasite reaction. Ni bulk is unable to produce CO, for two reasons: (i) on the one hand the adsorption of the H atoms on the surface is favoured with respect to CO_2, thus preventing it from accessing the catalytic sites; (ii) on the other hand, the binding energy with the intermediates *COOH and *CO is too high, such as to poison the surface and inhibit the production of CO.[6,7] From this point of view, several strategies have been adopted to implement efficiency and selectivity for CO_2RR: downsizing the material at the nanoscale and modification of

the band state by introducing a strain or a heteroatom.[8] As already mentioned above, reducing a material to nanodimensions increases the reactivity of the material and concurrently increases the number of active sites for the same amount of material. On the other hand, the addition of heteroatoms electronically modifies the material, having either a positive or negative action (based on the interaction) on the reactivity of the metal for CO_2RR. From this point of view, research in recent years has focused on positive interaction between nickel-nitrogen-carbon (Ni-N-C), which leads to the selective formation of CO.[9,10] *Froehlich and Kubiak* studied catalysts based on nickel-1,4,8,11-tetraazacyclotetradecane (Ni-cyclam) and its derivates. These homogenous catalysts are able to reduce CO_2 to CO with a FE of 90% and the almost absence of HER.[11,12] But the homogeneous complexes are very fragile, difficult to separate from the reaction product and to recycle. For this reason, it is better to focus on heterogeneous catalysts that involve the Ni-N bond in their structure. Carbon-based materials are excellent candidates for replacing organometallic compounds and providing robustness to catalyst. From this perspective, a broad branch of research has opened focused on the study of the introduction of Ni atoms into the different carbon structures, coordinated with N atoms, and the effect of these structures for CO_2RR. *Hashimoto and al.* synthesized a graphene oxide modified electrocatalyst with Ni and N atoms (Ni-N-Gr) and observed how CO production was increased with a FE of 90%, unlike a Ni foil, which produces only H_2.[13] This change in selectivity is associated with the possibility or not of adsorbing protons on the Nickel surface: in the case of CO_2RR, there is a first adsorption of CO_2 on the surface and a subsequent protonation of the intermediate which occurs from the water and not from adsorbed H. While in the case of HER, protons are more easily adsorbed on the surface, blocking any access to CO_2. This mechanism depends on the pK_a of the complex (Ni-L).

In literature one can find numerous examples of Ni, atomically dispersed or in the form of nanoparticles, bonded to carbonaceous nanostructures doped with N, where it has been effectively demonstrated that N-doping induces the electrochemical reduction of CO_2 to CO on the carbon support material, consistent with the experiments.[14,15,16]

The choice of the carbonaceous material is fundamental to obtain a good conductivity, a better stabilization and adsorption of CO_2. A new class of material has taken hold in recent years in research, it is the covalent organic frameworks (COFs), a sort of porous organic polymer networks, which are considered particularly promising in the field of catalysis due to the high density of coordination sites.[17] Special attention is paid to a nitrogen-rich subtype of COFs, the covalent triazine frameworks (CTFs), which we will see in detail now.

3.1.2 Covalent Triazine Frameworks (CTFs)

As already anticipated, COFs are materials that are receiving particular attention in recent years as metal-free materials that cover a wide range of applications and have a high thermal stability and a high porosity that can be adjusted to one's liking.[18] A subcategory of COFs are the covalent triazine framework (CTF),

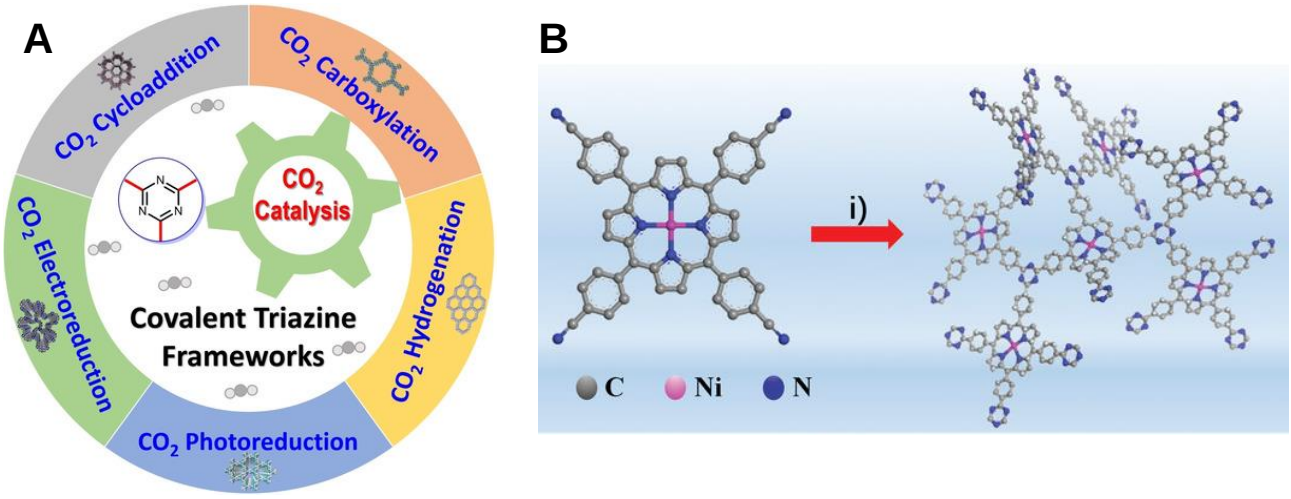

Figure 3.3 A) Schematic illustration of CTFs for CO_2 catalysis.[19] B) Example of CTF for CO_2 redcution: schematic illustration of synthesis of NiPor-CTF starting from a single unit of porphyrin nickel (NiPor) through ionothermal strategy. Balls in grey, blue, and pink represent C, N, and Ni atoms, respectively.[22]

nitrogen-rich polymers made up of triazine units linked together by extended conjugated π-bounds. CTFs are considered one of the most promising functional materials for various applications due to their high specific surface area, adjustable pore size, physicochemical stability, and the ability to delineate surface active sites.[19] The CTF represent an excellent and versatile platform for heterogeneous catalysis, especially for CO_2 adsorption and conversion (Figure 3.3 A).[20] In general, CTFs are constructed from triazine moieties that bind to each other via covalent bond. The CTFs can be divided into two main categories: amorphous and crystalline. Most of the CTFs reported in the literature are amorphous due to the synthesis conditions and the high stability of the strong covalent linkage (C=N). Crystalline CTFs can also be found, which are carefully designed with abundant highly ordered pores and periodic structures; these characteristics provide substrate specificity and select the proprieties of material.[19]

The reason why CTFs find a flourishing application in CO_2 reuse (CO_2 reduction, cycloaddition, carboxylation, etc.) is due to their great ability to adsorb CO_2 on its surface, which can be modulated according to the design of the material (pore size, surface area, etc.).[21] The advantage of CTF, unlike metal organic frameworks (MOFs), is that they can be used in conditions of great humidity. *Zhuang and al.* they tested a CTF doped with atomic Ni anchored to four N atoms for the CO_2RR. This type of material was able to reduce CO_2 to CO with high efficiency and selectivity (FE over 90%), exploiting the catalytic power of the Ni-N_4 centres and the high affinity of the CO_2 molecule with CTF.[22]

3.1.3 Outlook

The combination of Ni with the support of CTF can lead to the effective reduction of CO_2. In this case, in order to obtain a favourable syngas mixture, it was decided to modulate the Ni activity through nanostructuring and oxidation of Ni. Differently from the Ni atoms dispersed in the structure, the Ni nanoparticles can produce both H_2 and CO.

The size of the nanoparticles has a strong impact on CO_2RR, as it affects its selectivity and efficiency. *Cuenya et al.* studied the effect of nanoparticle size for CO_2RR, identifying how for nanoparticles below 5 nm, the evolution of H_2 becomes predominant over the production of CO and other hydrocarbons.[23] Indeed, at dimensions below 5 nm, the surface atoms are undercoordinated, and for this reason they are more reactive and increase the bond strength of the adsorbed species as for atomic H and *COOH, positively influencing the determination of the reductive adsorption rate. This dimensional effect increases the faradic activity of the material, reducing the selectivity window of the reaction products: the undercoordination accelerates the adsorption reactions of the species, but reduces the mobility of the reaction intermediates, inhibiting further hydrogenation processes. A high selectivity for H_2 and CO is thus obtained. For this reason, a synthesis method was chosen that would allow the formation of NiO nanoparticles with dimensions below 5 nm, which were then deposited on two different CTFs. Two different types of CTF were chosen, with a different percentage of N-pyrrole and N-pyridine, in order to correlate the influence of the N defect to the catalytic activity for the syngas production: NiO-CTF1 and NiO-CTF2.

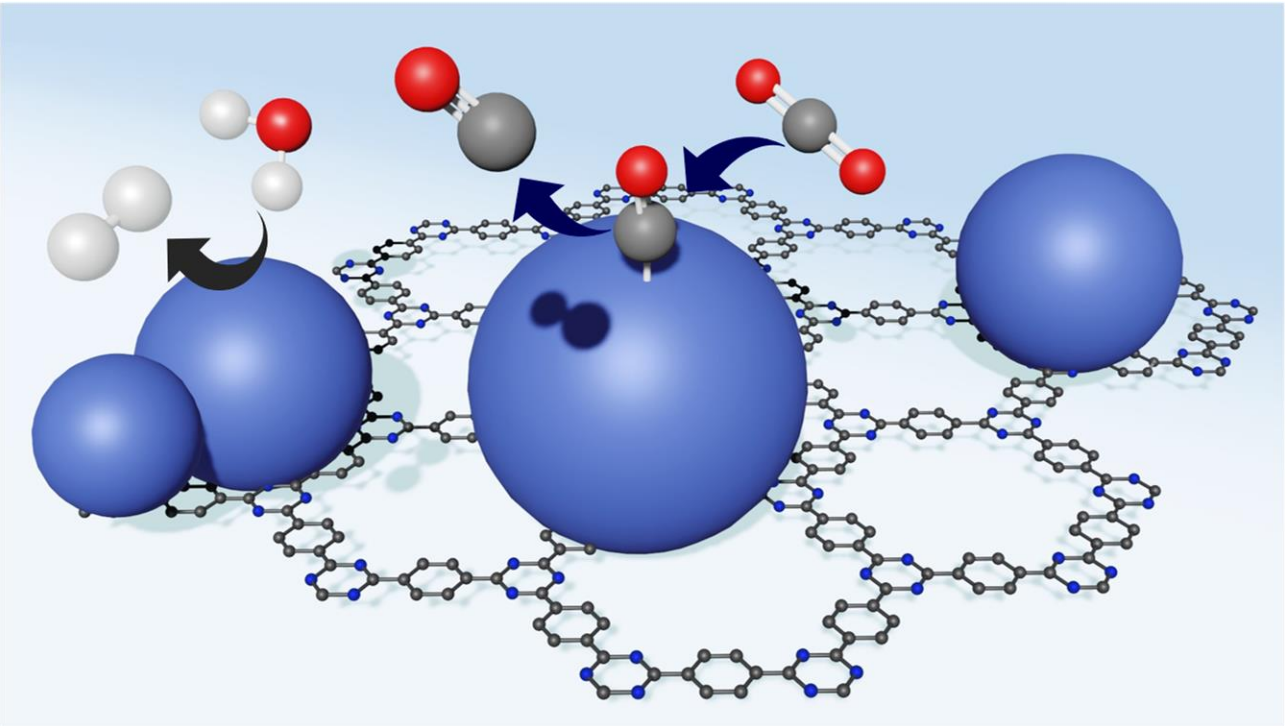

*Figure 3.4 Graphic illustration of the CO_2 reduction to CO and H_2 on NiO nanoparticles supported by CTF1, with the formation of *CO reaction intermediate.*

3.2 Synthesis and characterization of NiO-CTFs electrocatalysts

Two different CTFs were synthesized starting from two different monomers, but under the same synthesis conditions. The synthesis was carried out in ionothermal condition, using molten $ZnCl_2$ as reaction medium and Lewis acid cyanotrimerization catalyst. Since $ZnCl_2$ acts as a porogene, it has been added in excess of the monomer ($ZnCl_2$ monomer = 5:1 molar ratio). Subsequently, the two materials were heat treated at 400 and 600 °C.[24,25] The monomers are 1,4-dicyanobenzene (p-DCB) for CTF1 and 1,3-dicyanobenzene (1,3-DCB) for CTF2 (Figure 3.5).

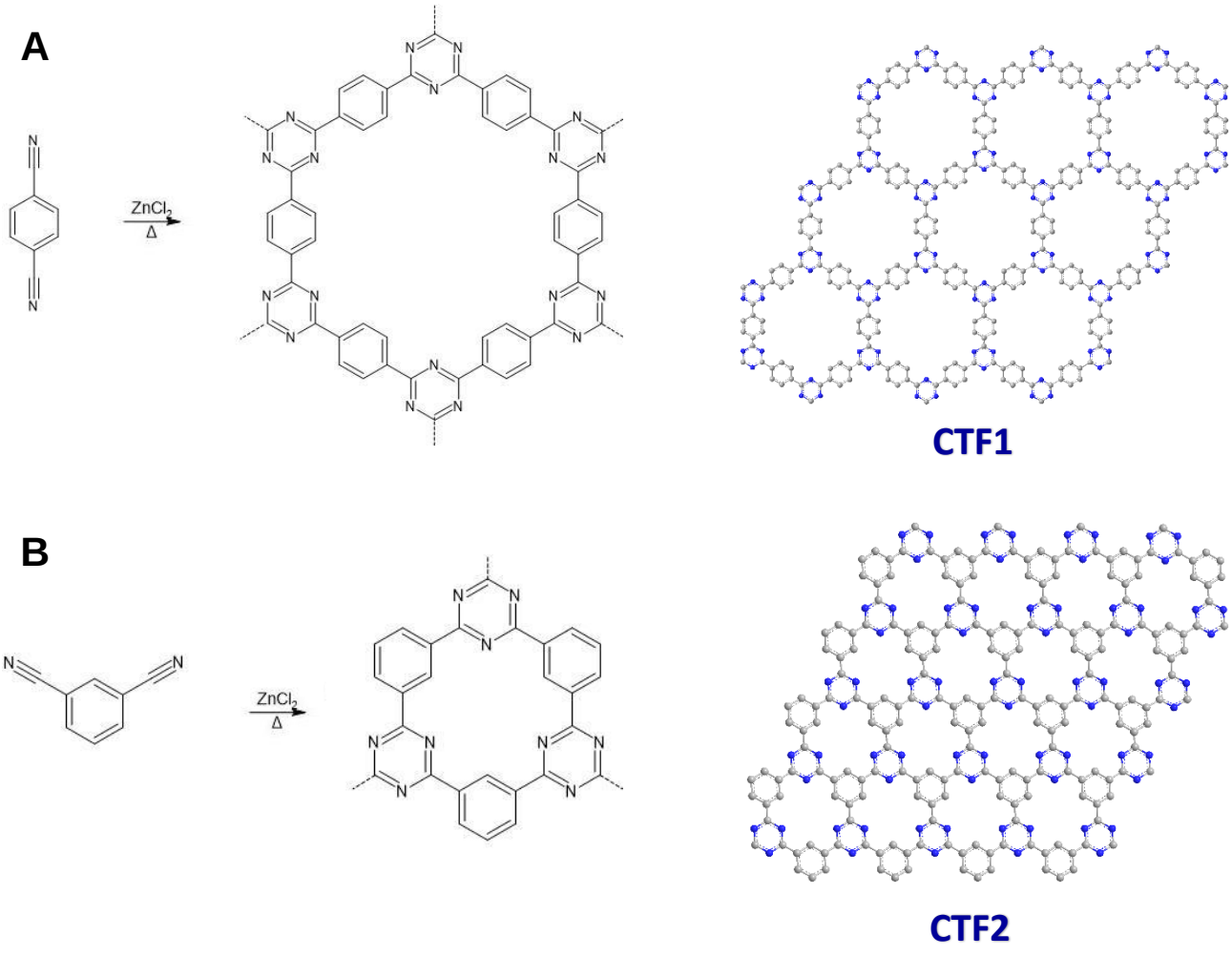

Figure 3.5 Monomer A) 1,4-dicyanobenzene (p-DCB) and B) 1,3-dicyanobenzene (1,3-DCP) conversion into covalent triazine frameworks (CTFs) CTF1 and CTF2 respectively, using molten $ZnCl_2$ as solvent. The 3D representation of the structure of the corresponding CTF is shown alongside.

The nature of the synthesized CTFs is amorphous, as confirmed by XRD analysis.[25] The properties of the two CTF samples were investigated by XPS analysis which reveals the content of the N sites and their nature (Figure 3.6).

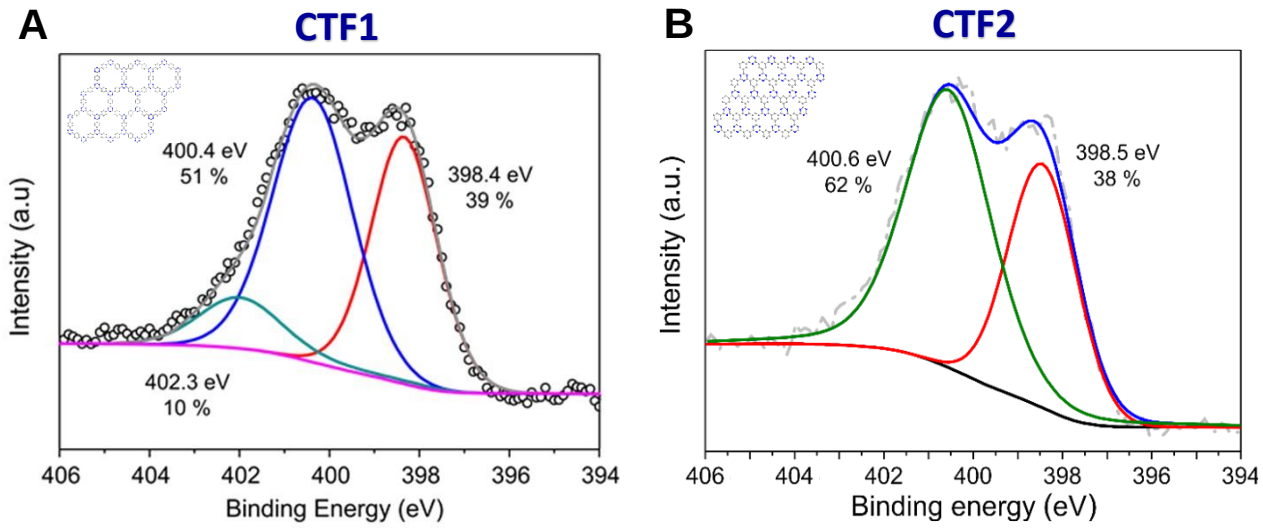

*Figure 3.6 XPS spectra in N 1s B.E. range of A) **CTF1** and B) **CTF2** along with theirrelative curve fittings. The peak at ~398.4 eV is associated to N-pyridinic, while the peak at ~400.5 eV is associated to N-pyrrolic. Finally, only for the CTF1 sample is present the N-oxide at 402.3 eV.*

The peak a lower binding energy (~398.4 eV) is associated to N-pyridinic sites, while the peak at ~400.5 eV is due to the N-pyrrolic sites species mostly deriving from a partial decomposition/rearrangement of the thermal treatment. The XPs analysis underlines that in the CTF2 sample there is a higher quantity of N-pyrrolic sites than in the CTF1 sample, with a value of 62 % against 51 %. While the amount of N-pyridinic sites are almost unchanged in the two samples (39 % and 38 % respectively). While only the CTF1 sample has a minor shoulder with higher binding energy (402.3 eV), which is attributed to the formation of the N-O species.[26] In both samples, the XPS analysis does not detect the presence of Zn which could be trapped within the carbonaceous structure during synthesis.

By N_2 physisorption isotherms, it was possible to determine the specific surface area (SSA), the volume total of pores and the volume of micropores. The values have been reported in table 3.1 together with the XPS data. Both samples have a high and comparable specific surface area, in the case of CTF2 this is slightly higher with a value of 1991 $m^2\ g^{-1}$ compared to SSA of CTF1 sample equal to 1654 $m^2\ g^{-1}$. The volume of the micropores is slightly larger for the CTF2 sample than CTF1, which helps to increase the SSA. The N content and the relative basicity of the surface play a fundamental role in the adsorption capacity of CO_2 by CTF

Table 3.1 Specific surface area, pore size distribution and N content as measured for CTF1 and CTF2.

Sample	SSA [$m^2\ g^{-1}$]	$V_{p\ (total)}$ [$cm^3\ g^{-1}$]	$V_{p\ (micro)}$ [$cm^3\ g^{-1}$]	$N_{pyridinic}$ [%]	$N_{pyrrolic}$ [%]	$N_{oxidized}$ [%]
CTF1	1654	1.06	0.42	39	51	10
CTF2	1991	1.11	0.56	38	62	0

samples. In this case the structural properties are promising, but the N content remains moderate: 7.5 wt % of N for CTF1 versus 10.1 wt % of N for CTF2.

The NiO nanoparticles were prepared and deposited on the material by Metal Vapor Synthesis (MVS). Thanks to this technique, very small and well dispersed nanoparticles can be obtained, which can be deposited on different matrices.[27] As can be seen from the TEM images, the Ni nanoparticles are monodisperse, with the absence of clusters and agglomerates (Figure 3.7 and 3.8). The nanoparticles on CTF1 have an average size slightly smaller than those of CTF2: 1.84 ±0.06 nm versus 2.11 ±0.02 nm.

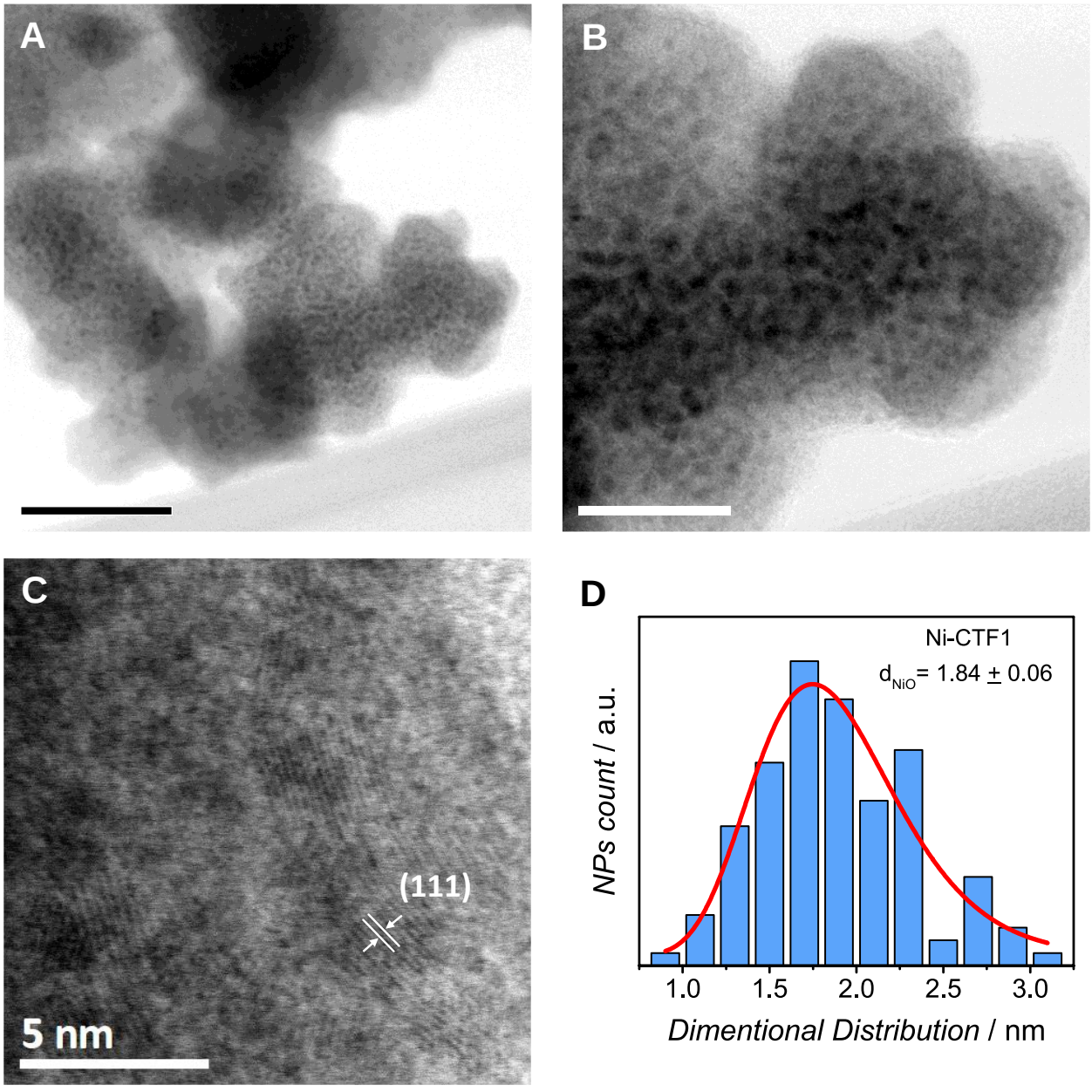

Figure 3.7 HRTEM images of NiO-CTF1 at different scale: A) 50 nm, B) 20 nm and C) 5 nm. This last image highlights the crystallographic planes of the Ni nanoparticles, corresponding to the (111) plane of the NiO. D) Size distribution of NiO NPs.

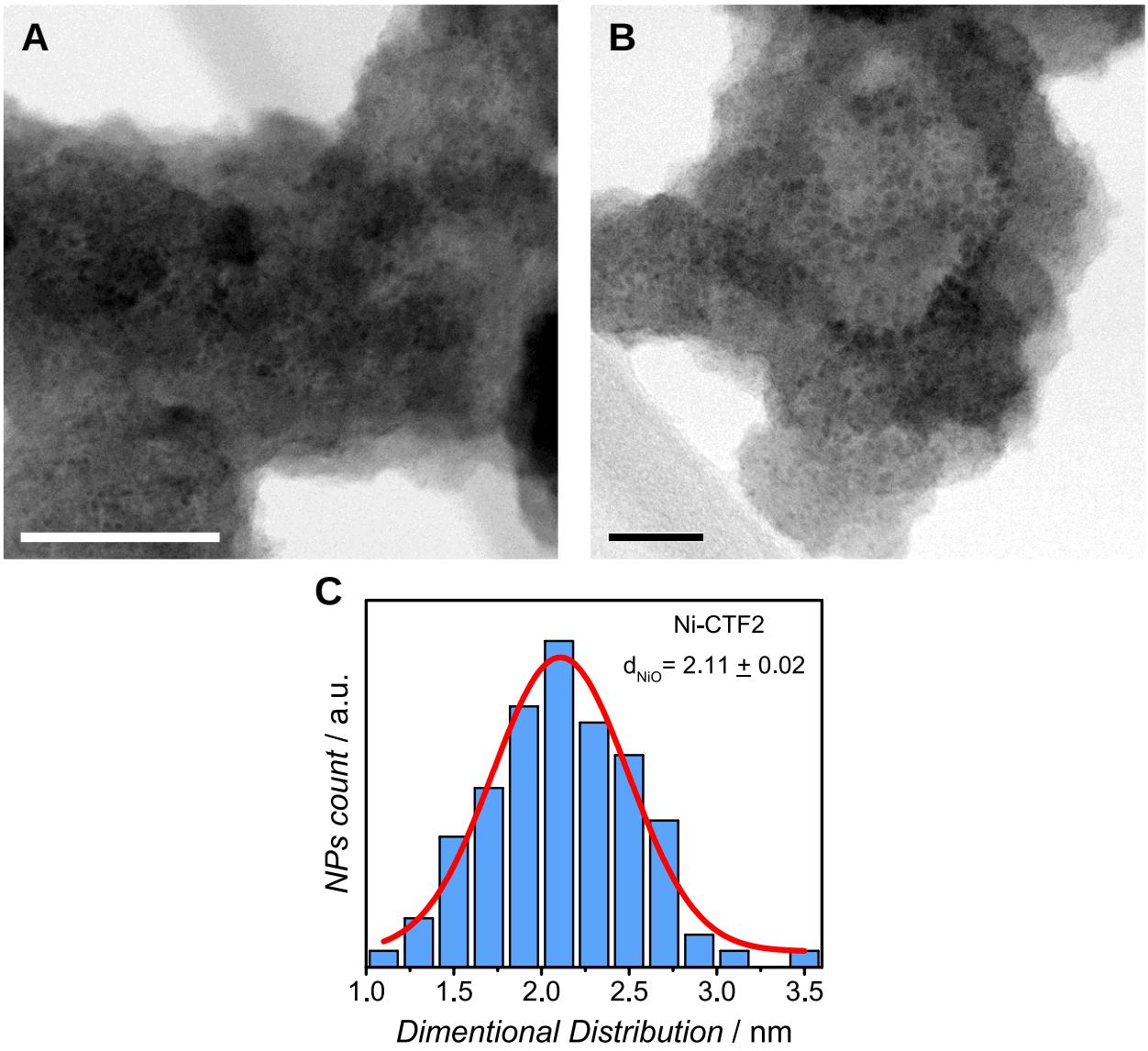

Figure 3.8 HRTEM images of NiO-CTF2 at different scale: A) 50 nm and B) 20 nm. C) Size distribution of NiO NPs.

The 5 nm HRTEM image of the Ni-CTF1 sample highlights the crystallographic planes of the Ni nanoparticles. The mean interplanar distance in the single NPs is 0.237 nm. This length corresponds to the plane (111) following a strain. In fact, the theoretical interplanar distance of the plane (111) is 0.203 nm, this value increases in the case of a deformation induced by the presence of other atoms such as oxygen.[28] Therefore, HRTEM provides us with a first information on the oxidation state of the NPs. This information is confirmed by the XPS analysis of Ni 2p spectrum (Figure 3.9). The peaks located at 856.1 eV and 874.1 eV with relative satellite peaks can be assigned to Ni^{2+} $2p_{3/2}$ and Ni^{2+} $2p_{1/2}$, respectively.[29,30] Hence, the XPS spectrum highlights the oxidized nature of the nanoparticles, with the total absence of metallic Ni.

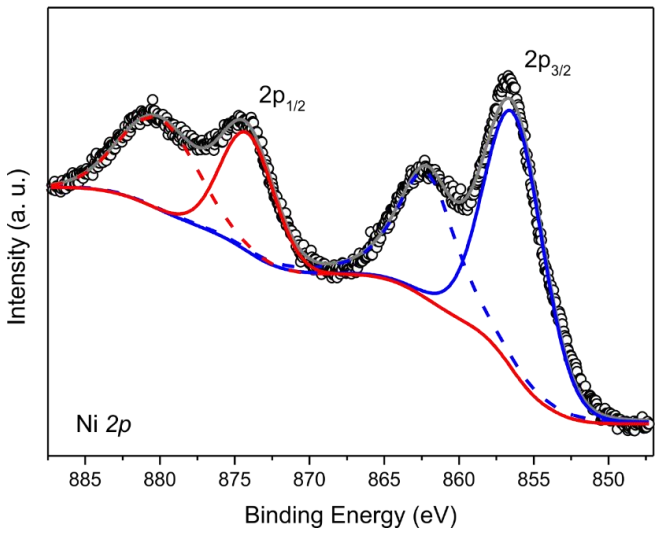

*Figure 3.9 XPS spectra in Ni 2p B.E. range of **NiO-CTF2** along with theirrelative curve fittings.*

3.3 Electrochemical characterization and CO_2RR performance of NiO-CTFs

The nanocomposites materials were characterized electrochemically through cyclic voltammetries (CVs) in KOH 0.1 M using a three-electrode electrochemical cell. The electrochemical characterization allows to better understand the system, and the electrochemical active surface area (ECSA). Initially, the NiO-CTFs materials were characterized in Ar-saturated 0.1 M KOH, using CVs at 50 mV s^{-1}. By cycling the system, two peaks are formed, one of oxidation and one of reduction, whose intensity increases as the number of cycles increases and then stabilizes at the 35th cycle. The redox peaks are due to the oxidation/reduction of Ni^{2+}/Ni^{3+}.

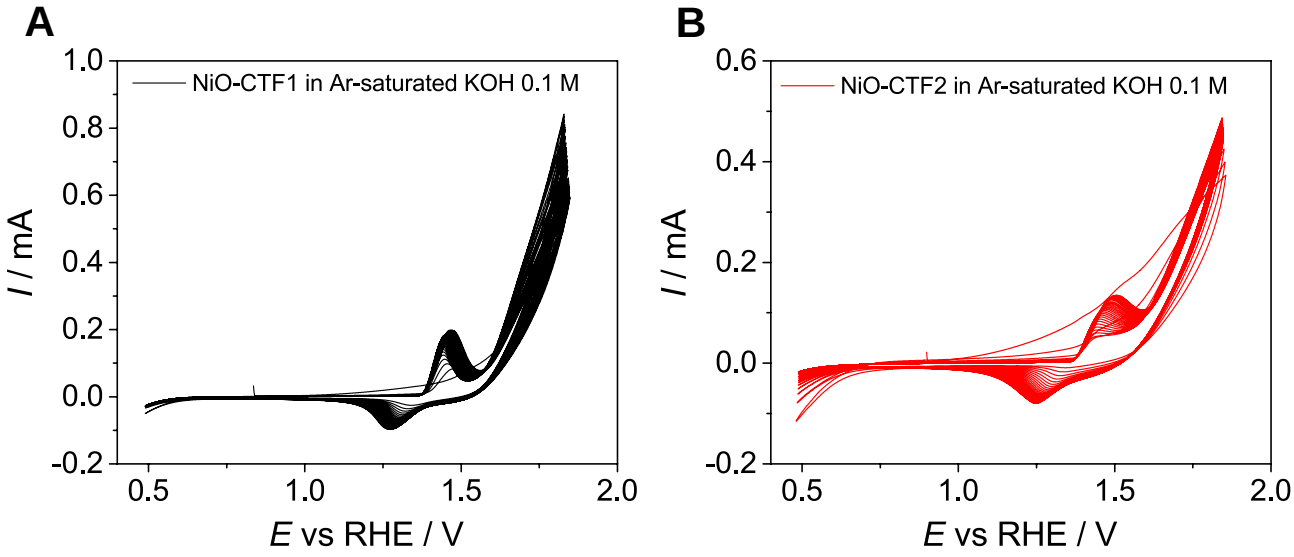

*Figure 3.10 **Cyclic voltammetry activation.** CVs at 50 mV s^{-1} in Ar-saturated KOH 0.1 M of A) NiO-CTF1 and B) NiO-CTF2.The current intensity increases as number cycles increases until 35th cycle. The potentials were corrected post measurement for the ohmic drop, considering the resistance of system (pH 13).*

Usually, when the metallic Ni enter to contact with the OH^- ions there is the transformation of superficial Ni into unstable α-$Ni(OH)_2$ phase, this process is described by the following reaction (3.4):[31]

$$Ni^0 + 2OH^- \rightarrow Ni(OH)_2 + 2e^- \quad (3.4)$$

Subsequently there is the surface reconstruction into β-$Ni(OH)_2$ phase, this reconstruction is irreversible, so the material cannot be further reduced applying cathodic potential.[32] While, applying an anodic polarization result in the oxidation of the surface hydroxide to β-NiOOH. This last transition results to reversible:[33]

$$Ni(OH)_2 + OH^- \leftrightarrow NiOOH + e^- + H_2O \quad (3.5)$$

Figure 4.11 shows the reversibility of this latter redox process as the scanning speed of the CVs varies. Therefore, in the case of NiO-CTF1 and NiO-CTF2, the redox peaks that are observed are due to the oxidation-reduction of β-$Ni(OH)_2$ and β-NiOOH, whose peaks are respectively at 1.46 V and 1.27 V vs RHE. As the number of cycles increases, the surface transformation to phase β-$Ni(OH)_2$ increases, causing a growth of the faradic current, up to the complete activation of the surface nickel hydroxide. From the voltammetries reported here it is not possible to uniquely establish the species linked to the atoms of Ni^{2+}, whether it occurs as an oxide or as a hydroxide of the beta phase. In the latter case, the reduction to a metal nanoparticle would be almost impossible, as the reversibility of the β-Ni(OH)2 phase to Ni0 occurs only under certain experimental conditions.[34]

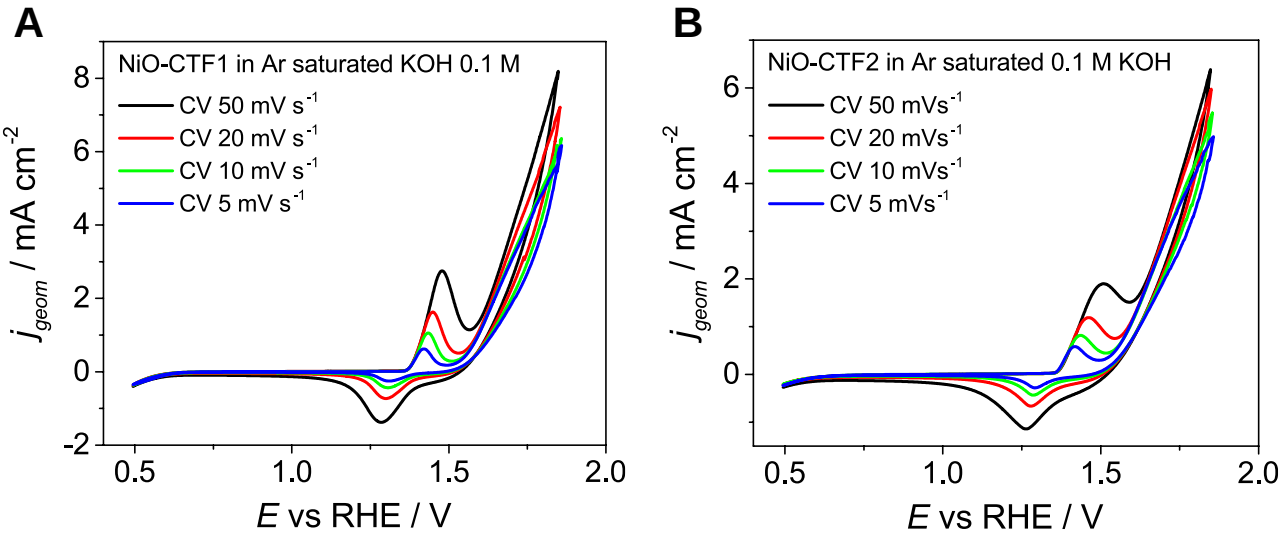

Figure 3.11 ***Cyclic voltammetry at different scan rates.*** *CVs at 50 mV s^{-1} (black), 20 mV s^{-1} (red), 10 mV s^{-1}(green) and 5 mV s^{-1} (blue) in Ar-saturated KOH 0.1 M of A) NiO-CTF1 and B) NiO-CTF2. The potentials were corrected post measurement for the ohmic drop, considering the resistance of system (pH 13), while the current intensity was normalized for the geometric area of the electrode (j_{geom}).*

For Ni-based electrocatalysts it is essential to know the ECSA to understand the intrinsic activity of the material and to compare it with other Ni electrocatalysts. For some materials it is really easy to calculate this parameter, as in the case of the Pt, in which it is sufficient to exploit the charge associated to one monolayer

of under deposited hydrogen (UPDH) desorption in the CVs.[33] In the case of Ni it is much more complex, and there is no single calculation method. Among the best known and most accredited are the "Alpha method" and the "Oxalate method". The alpha method, introduced by *Machado et al.*,[35] and subsequently developed,[36] consists in exploiting the charge associated with the oxidation peak of α-$Ni(OH)_2$ in 0.5 M KOH, assumed that the specific charge density of one monolayer of α-$Ni(OH)_2$ is 514 µC cm^{-2}. While, in the case of the oxalate method, the charge associated with the formation of one monolayer of Ni-oxalate complex $[Ni(OH_{2-x}(C_2O_4)_{x(ads)}]$ in a solution of 0.1 M KOH and 0.08 M oxalic acid is exploited, assuming that the specific charge density is 195 µC cm^{-2}.[37] Unfortunately, these two methods for calculating the ECSA cannot be used for these samples, as they are in the oxidized state.[33]

The ECSA can be calculated using the "Beta" method, namely, exploiting the OH_{ads} desorption peak in the region of Ni^{2+}/Ni^{3+}. In this case, the system is left to cycle until a steady state is reached, in which the reduction current of the β-NiOOH species remains stable, and ECSA is calculated using the theoretical surface charge associated with this peak which corresponds to 420 µC cm^{-2}.[38,39] The equation used to calculate the ECSA for Ni-based materials with this methos is (3.6):

$$ECSA = \frac{Q_{des}}{420\ \mu C\ cm^{-2}} \tag{3.6}$$

In literature this area is indicated as ECSA for the oxygen evolution reaction (OER), as the species involved are active for the production of oxygen, and if the CVs are observed, as the anode potential, the current suddenly increases due to the evolution of oxygen. The "Beta" method was used to calculate the ECSA of these materials, integrating the area of β-NiOOH reduce peak, as it highlighted in figure 3.12. The calculation was also applied to CVs at different scan rates. In table 3.2 the ECSA of samples is reported.

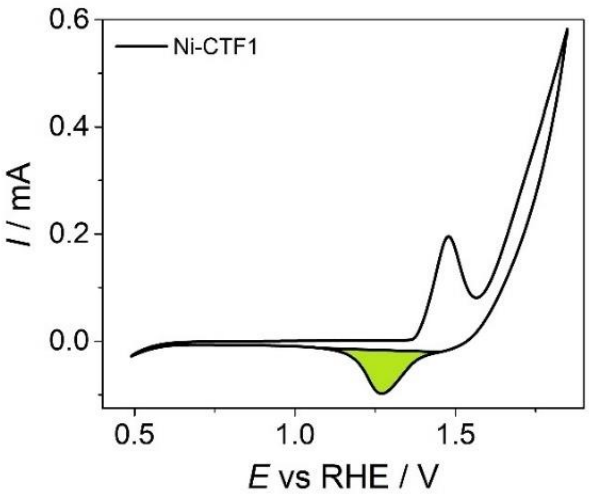

Figure 3.12 ***Beta method****. Example of the integration area (green) for NiO-CTF1 from 35th cycle of a CV at 50 mV s^{-1} in KOH 0.1 M.*

Table 3.2 ECSA values of NiO-CTFs samples

Sample	ECSA [cm^2]
NiO-CTF1	0.65 ± 0.07
NiO-CTF2	0.52 ± 0.06

The calculation of the ECSA is in line with the size distribution obtained from the TEM images: the NiO-CTF1 sample has a slightly higher electrochemically active area than the Ni-CTF2 sample, since it has nanoparticle size distribution centred at smaller values, consequently they have a greater surface.

Figure 3.13 shows a direct comparison of the CVs of the two composite NiO-CTFs at 50 mV s^{-1}. It can be noted that the capacitive current is the same for the two electrocatalysts, while the faradic current is lower for the NiO-CTF2 sample. In fact, it has a lower electrochemically active area than the NiO-CTF1 sample, and consequently a lower catalytic activity for OER. Finally, another thing that can be noted is the different position of the redox peaks: the NiO-CTF2 sample has a greater spacing than the two reversible peaks, due to a greater internal resistance of the system. This phenomenon causes the anodic peak to overlap the OER process, and seems to modify the shape of the peak, in reality this change is simply induced by the superposition of the two redox processes. The different resistance of the two systems could be induced by a different interaction and conductivity of the CTF support.

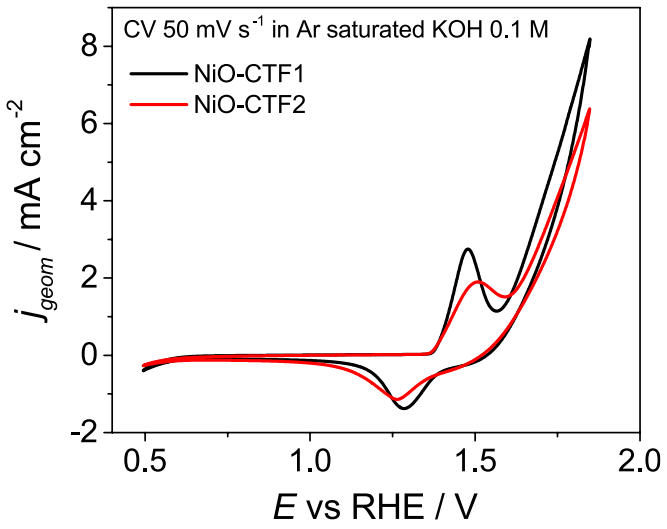

Figure 3.13 ***Cyclic voltammetry characterization.*** *CVs at 50 mV s^{-1} for NiO-CTF1 (black) and NiO-CTF2 (red) in Ar-saturated KOH 0.1 M. The potentials were corrected post measurement for the ohmic drop, considering the resistance of system (pH 13), while the current intensity was normalized for the geometric area of the electrode (j_{geom}).*

The CO_2RR catalytic activity was studied at stationary conditions at different potentials, performing chronoamperometry (CA) experiments in CO_2-saturated $KHCO_3$ 0.5 M in the range between -0.35 to -0.85 V vs RHE. As already mentioned in the previous chapters, the gas phase was quantified during the electrolysis using an online gas chromatograph (GC), while the liquid phase was analyzed in a second moment with ionic chromatography (IC). The material performances for CO_2RR were reported in terms of FE. Figure 3.14 shows, in addition to the FE values, the average values of the involved current density (j_{geom}) during the electrolysis for all the sample mentioned above. The product analysis highlights the presence of three products: hydrogen, carbon monoxide and formic acid.

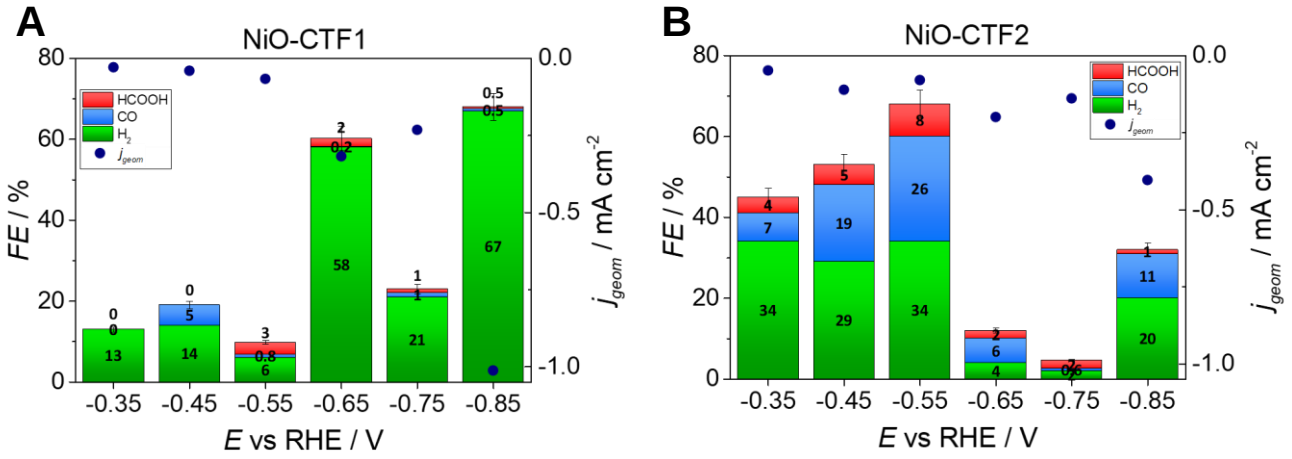

Figure 3.14 ***CO_2RR performance.*** *Faradaic Efficiency (FE) of detectable CO_2RR products in CO_2-saturated $KHCO_3$ 0.5 M (pH 7.5): H_2 (green), CO (light blue) and HCOOH (red) for A) NiO-CTF1 and B) NiO-CTF2. The blue points indicate the mean current density of sample at that potential; the values are shown on right axis.*

Observing the performance of the two materials, a clear distinction can be seen. In fact, NiO-CTF1 does not seem reactive to the reduction of CO_2, showing rather poor performance with only the evolution of hydrogen, where the maximum FE achieved for CO is 5%. While the NiO-CTF2 sample shows excellent performance for the production of syngas, with the maximum production at -0.55 V vs RHE, which corresponds to a mixture of 34 % H_2 and 26 % CO. Overpotential required for maximum CO production is 450 mV,[40] but with CO formation already at -0.35 V vs RHE, unlike the NiO-CTF1 sample, where the onset of potential is shifted of 100 mV. It is also noted the formation of formic acid, which appears to be predominant in the NiO-CTF2 sample. The currents of the two samples are similar to each other, except for the NiO-CTF1 at -0.85 V, where the HER takes over. In fact, at this potential an increase in current has been observed over time, passing from an initial value of -0.26 mA cm^{-2} to -2.6 mA cm^{-2} after 85 minutes, with a consequent increase in the ppm of H_2 (Figure 3.15). This behavior appears to indicate material activation over time for HER. For some potentials the FE do not exceed 20%, the main reasons for this phenomenon can be summarized in two points: (i) for low concentrations the quantification of gaseous products can be underestimated, as part of these products can dissolve in the electrolyte and (ii) for very high kinetics, the rate of CO_2 that is consumed exceeds the rate of dissolution of the CO_2 in the electrolyte, resulting in a limit of mass transport.[41] Finally, as in the case of

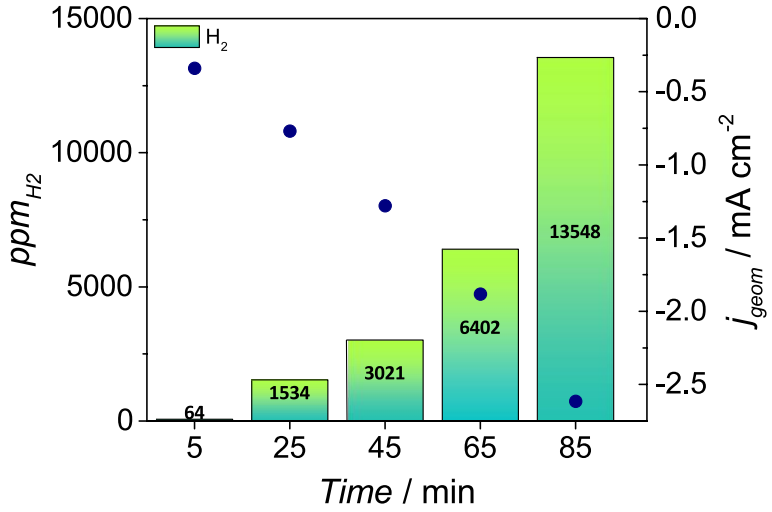

Figure 3.15 ppm of H_2 quantified during the electrochemical measurement using the GC, as a function of time. The blue points indicate the current density of sample at that time; the values are shown on right axis. These CO_2RR measurements were realized using an electrode with an area of 2.5 cm^2.

the HER at high potentials, the detected hydrogen concentration exceeded the limits of the GC calibration line, thus being incorrectly quantified (example provided by Figure 3.15).

Since a sort of "activation" of the material is observed at -0.85 V, the Ni-CTF1 sample was also tested for a more cathodic potential, equal to -1.1 V vs RHE (Figure 3.16). As for the previous potential, also in this case an increase in current is observed over time, with an average current density of 7.5 mA cm^{-2} and a quantity of hydrogen produced that reaches up to 26000 ppm, a value well beyond outside the calibration limit of the GC, in fact the FE recorded for H_2 is equal to 60 %. Interestingly, more complex CO_2RR products were observed at this potential: CO, CH_4, C_2H_4 and C_2H_6. Although the FE of these products are completely traceable for practical purposes, it is interesting to observe their presence in a similar system, as they have never been identified as reaction products on CTFs or on Ni nanoparticles. Explaining the presence of such products is

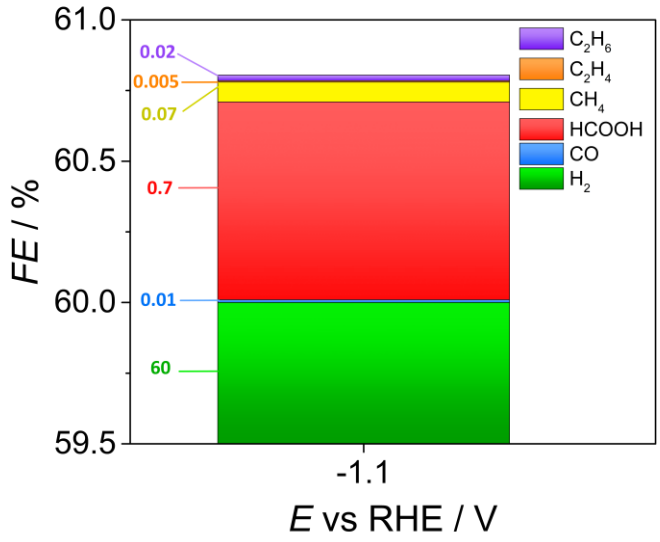

Figure 3.16 Zoom of the FE graph of NiO-CTF1 to -1.1 V. In this case the FE values are shown on the left: H_2 (green), CO (light blue), HCOOH (red), CH_4 (yellow), C_2H_4 (orange) and C_2H_6 (purple).

not easy at all, two explanations can be identified. The first involves the reduction of CO_2 at the interface between Ni NPs and CTF, where the CO_2 is adsorbed on the CTFs and the reduction occurs by the Ni NPs, at this potential the adsorption of the reaction intermediates favors further reduction steps. The second explanation, instead, partly involves the degradation of the CTF. Currently there is no univocal evidence of this phenomenon, what is certain is that nitrogen products deriving from CTFs have not been identified in the electrolyte.

To better understand the performance of electrocatalysts and the possible contributions, carbonaceous nanostructures are usually analyzed separately. Unfortunately, this was not possible for the CTF1 sample, as DMSO was the only solvent capable of dispersing it sufficiently but making it impossible to realize a reproducible deposit on the electrode by drop casting. For this reason, it is currently not possible to uniquely establish the different contributions to the catalytic activity for HER and CO_2RR in the NiO-CTF1 sample. However, based on the data in the literature, the HER can be attributed to the NiO nanoparticles, which at potentials higher than -0.55 V and in this pH range, undergo the reduction to metallic Ni with the loss of oxygen atoms.[42] As previously mentioned, metallic Ni is able to evolve hydrogen, favoring the adsorption of atomic H on its surface, and inhibiting the adsorption of CO_2. In this case, the Ni in the NiO-CTF1 sample is not affected by the interaction with N contained in the CTF1 support and given the size of the nanoparticles and the defects induced by the oxygen loss, these are particularly reactive for HER. Unlike the NiO-CTF2 sample in which there is both HER and CO_2RR.

DFT calculations have shown that Ni coordinated with N-pyrrole atoms, is able to modify its selectivity passing from HER to CO production.[15] Within this context, Ni plays a fundamental role in stabilizing the reaction intermediate *COOH on its surface without compromising the easy desorption of CO.[16] In the case of the NiO-CTF2 sample, the amount of nitrogen present in the CTF2 support is greater than in the CTF1 (10.1 % vs 7.5 %), especially the 62% of them are of N-pyrrolic sites. This explains the better performance for CO production in the NiO-CTF2 sample. Furthermore, the presence of oxygen atoms in the nanoparticles of Ni, which is in the oxidized state, must be considered. In fact, as pointed out in the Pourbaix diagram (Figure 3.17), at a pH of 7.5 and at potentials below -0.5 V vs SHE, Ni is in an oxidized state, with a mixed phase of NiO and $Ni(OH)_2$.[42] As the potential increases, the Ni^{2+} is reduced to metallic Ni^0. From -0.35 V to -0.55 V vs RHE an increase in the FE for CO is observed, with a drastic fall starting from -0.65 V. The presence of oxygen, which electronically modifies the Ni and induces a strain in the material, helps to favor the reduction of CO_2 starts, where the maximum catalytic activity is reached when the nanoparticles are in a mixed state of oxide and metal. As already reported in the previous chapters, the defects induced by the removal of oxygen help to activate and bind the CO_2 more easily on the surface and the oxygen atoms present in the material influence the stability of the reaction intermediates. The drastic drop in performance starting from -0.65 V vs RHE could be induced by the reduction of the nanoparticles to metallic Ni, and by their detachment from

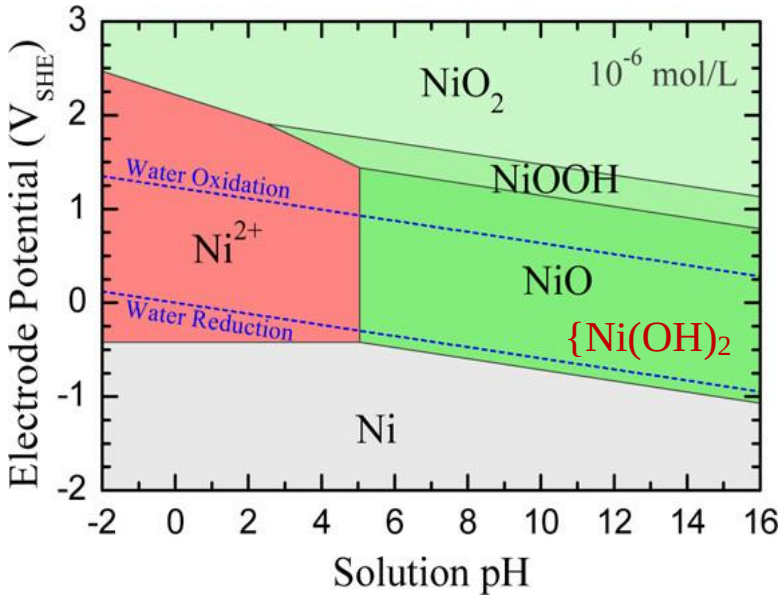

Figure 3.17 ***Pourbaix diagram.*** *The diagram represents the possible stable states of Ni under electrochemical conditions: in aqueous solution, at constant temperature and pressure (at T = 25 ° C and p= 1 atm). Adapted with permission from J. Phys. Chem. C, 2017, 121, 18, 9782–9789. Copyright© 2017 American Chemical Society.*[42]

the carbonaceous nanostructure. In fact, it can be noted that the currents remain rather low compared to the NiO-CTF1 sample, where at the same potential the HER is predominant, and the currents reach values of -2.6 mA cm^{-2}.

Finally, these two electrocatalysts also lead to the formation of formic acid, particularly in the NiO-CTF2 sample. In the literature, usually, this type of material consisting of CTF decorated with atomic Ni, show an exclusive selectivity towards carbon monoxide in the CO_2RR. The production of formic acid can be explained by the presence of N-pyrrole groups in the CTFs. In fact, DFT calculations have shown how the N-pyrrole sites have a better catalytic activity for CO2RR than other N-sites, whose selectivity is towards formic acid.[43] For this reason, the CTF2 support was tested, which, unlike CTF1, is soluble in DMF and therefore it is possible to deposit the material on the electrode. Two significant potentials for the performance of the CTF2 carbonaceous structure have been reported in the figure 3.18. It is observed that at low potentials, the Ni-free CTF2 structure can produce HCOOH with an FE of 53%. This efficiency is reached at an overpotential of 150 mV. While increasing the potential there is a drastic reduction of formic acid and the predominant production of H_2, in accordance with what was shown in the previous samples. Therefore, the N-pyrrolic sites that interact with the Ni lead to the catalyzation of the reduction of CO_2 by the Ni with the production of CO and H_2, while the undecorated N-pyrrolic sites produce formic acid. From this point of view, CTF2 produces a greater quantity of formic acid than CTF1, based on the FE identified in the NiO-CTF1 and Ni-CTF2 samples and on the quantity of N-pyrrolic sites identified by the XPS analysis.

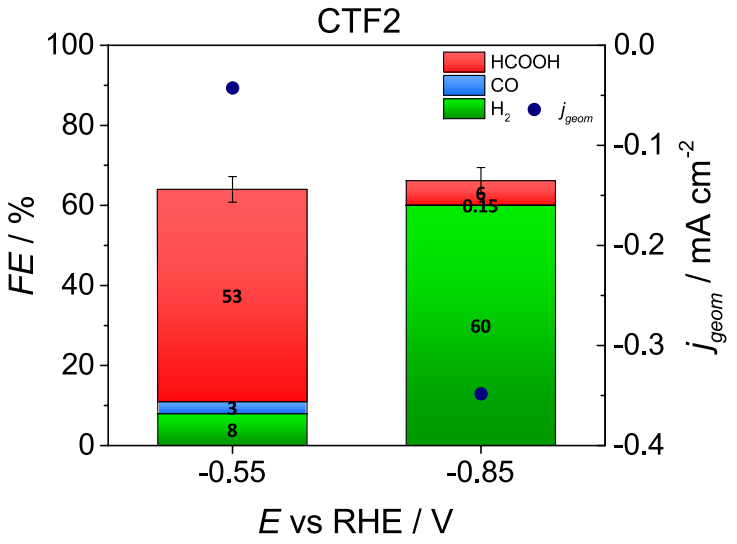

Figure 3.18 ***CTF2 performance.*** *Faradaic Efficiency (FE) of CO_2RR products in CO_2-saturated $KHCO_3$ 0.5 M (pH 7.5) at two significative potentials: H_2 (green), CO (light blue) and HCOOH (red) for CTF2. The blue points indicate the mean current density of sample at that potential; the values are shown on right axis.*

3.4 Conclusions

In conclusion, the interaction between NiO nanoparticles and CTFs for the production of syngas was investigated. The presence of the N-pyrrolic sites of the CTFs plays a fundamental role in the activation of the catalysis on the NiO nanoparticles: if the Ni is affected by this interaction, it is able to reduce the CO_2 to CO, while if this interaction is lost, HER takes over. A close contact of the active phase of NiO with the support of CTF is therefore essential, which adsorbs the CO_2 and favors its reduction. Furthermore, the oxygen atoms integrated into the Ni structure increase the performance of the system by creating defects on the surface of the NPs during reduction. Finally, the catalytic effect of N-pyrrole sites was experimentally observed in a metal free electrocatalyst for CO_2RR, which can produce formic acid with an FE of 53% at an overpotential of 150 mV. The CTF2 metal-free electrocatalyst is able to produce formic acid with higher FE than the bismuth samples seen above, and with FE similar to MWCNTs@CeO_2, but unlike these two samples, the reducing currents of the CTF2 sample are quite low for which the amount of formic acid produced is not comparable. The interesting thing about this system is how the combination and interaction of the different building-blocks can modify the selectivity for CO_2RR and HER. These materials offer an excellent starting point for the realization of future electrocatalysts with transformable properties, whose catalytic activity derives from the interaction between MO and CNS.

Reference

1. Hernández, S. *et al.* Syngas production from electrochemical reduction of CO2: Current status and prospective implementation. *Green Chem.* **19**, 2326–2346 (2017).

2. Jouny, M., Luc, W. & Jiao, F. General Techno-Economic Analysis of CO2 Electrolysis Systems. *Ind. Eng. Chem. Res.* **57**, 2165–2177 (2018).

3. Su, P., Iwase, K., Harada, T., Kamiya, K. & Nakanishi, S. Covalent triazine framework modified with coordinatively-unsaturated Co or Ni atoms for CO2 electrochemical reduction. *Chem. Sci.* **9**, 3941–3947 (2018).

4. Lee, C. W. *et al.* New challenges of electrokinetic studies in investigating the reaction mechanism of electrochemical CO2 reduction. *J. Mater. Chem. A* **6**, 14043–14057 (2018).

5. Franco, F., Rettenmaier, C., Jeon, H. S. & Roldan Cuenya, B. Transition metal-based catalysts for the electrochemical CO2reduction: From atoms and molecules to nanostructured materials. *Chem. Soc. Rev.* **49**, 6884–6946 (2020).

6. Kuhl, K. P. *et al.* Electrocatalytic conversion of carbon dioxide to methane and methanol on transition metal surfaces. *J. Am. Chem. Soc.* **136**, 14107–14113 (2014).

7. Feaster, J. T. *et al.* Understanding Selectivity for the Electrochemical Reduction of Carbon Dioxide to Formic Acid and Carbon Monoxide on Metal Electrodes. *ACS Catal.* **7**, 4822–4827 (2017).

8. Li, M. *et al.* Toward Excellence of Transition Metal-Based Catalysts for CO2 Electrochemical Reduction: An Overview of Strategies and Rationales. *Small Methods* **4**, 2000033 (2020).

9. Zhu, Z. *et al.* Achieving efficient electroreduction of CO2 to CO in a wide potential window by encapsulating Ni nanoparticles in N-doped carbon nanotubes. *Carbon N. Y.* **185**, 9–16 (2021).

10. Mao, F., Liu, P. F., Yang, P., Gu, J. & Yang, H. G. One-step coating of commercial Ni nanoparticles with a Ni, N-co-doped carbon shell towards efficient electrocatalysts for CO2reduction. *Chem. Commun.* **56**, 7495–7498 (2020).

11. Froehlich, J. D. & Kubiak, C. P. Homogeneous CO2 Reduction by Ni(cyclam) at a Glassy Carbon Electrode. *Inorg. Chem.* **51**, 3932–3934 (2012).

12. Froehlich, J. D. & Kubiak, C. P. The Homogeneous Reduction of CO2 by [Ni(cyclam)]+: Increased Catalytic Rates with the Addition of a CO Scavenger. *J. Am. Chem. Soc.* **137**, 3565–3573 (2015).

13. Su, P., Iwase, K., Nakanishi, S., Hashimoto, K. & Kamiya, K. Nickel-Nitrogen-Modified Graphene: An

Efficient Electrocatalyst for the Reduction of Carbon Dioxide to Carbon Monoxide. *Small* **12**, 6083–6089 (2016).

14. Yang, H. Bin *et al.* Atomically dispersed Ni(i) as the active site for electrochemical CO2 reduction. *Nat. Energy* **3**, 140–147 (2018).

15. Fan, Q. *et al.* Activation of Ni Particles into Single Ni–N Atoms for Efficient Electrochemical Reduction of CO2. *Adv. Energy Mater.* **10**, (2020).

16. Jia, M. *et al.* Carbon-supported Ni nanoparticles for efficient CO2 electroreduction. *Chem. Sci.* **9**, 8775–8780 (2018).

17. Wu, Y. *et al.* Electrochemical CO2reduction using gas diffusion electrode loading ni-doped covalent triazine frameworks in acidic electrolytes. *Electrochemistry* **88**, 359–364 (2020).

18. Zhao, T. *et al.* Rational construction of Ni(OH)2 nanoparticles on covalent triazine-based framework for artificial CO2 reduction. *J. Colloid Interface Sci.* **602**, 23–31 (2021).

19. Luo, R. *et al.* Covalent Triazine Frameworks Obtained from Nitrile Monomers for Sustainable CO2 Catalysis. *ChemSusChem* **13**, 6509–6522 (2020).

20. Puthiaraj, P., Lee, Y. R., Zhang, S. & Ahn, W. S. Triazine-based covalent organic polymers: Design, synthesis and applications in heterogeneous catalysis. *J. Mater. Chem. A* **4**, 16288–16311 (2016).

21. Wang, H. *et al.* Covalent triazine frameworks for carbon dioxide capture. *J. Mater. Chem. A* **7**, 22848–22870 (2019).

22. Lu, C. *et al.* Atomic Ni Anchored Covalent Triazine Framework as High Efficient Electrocatalyst for Carbon Dioxide Conversion. *Adv. Funct. Mater.* **29**, 1806884 (2019).

23. Reske, R., Mistry, H., Behafarid, F., Roldan Cuenya, B. & Strasser, P. Particle size effects in the catalytic electroreduction of CO2 on Cu nanoparticles. *J. Am. Chem. Soc.* **136**, 6978–6986 (2014).

24. Tuci, G. *et al.* Unraveling Surface Basicity and Bulk Morphology Relationship on Covalent Triazine Frameworks with Unique Catalytic and Gas Adsorption Properties. *Adv. Funct. Mater.* **27**, 1605672 (2017).

25. Tuci, G. *et al.* Playing with covalent triazine framework tiles for improved CO 2 adsorption properties and catalytic performance. *Beilstein J. Nanotechnol* **10**, 1217–1227 (2019).

26. Osadchii, D. Y., Olivos-Suarez, A. I., Bavykina, A. V. & Gascon, J. Revisiting Nitrogen Species in Covalent Triazine Frameworks. *Langmuir* **33**, 14278–14285 (2017).

27. Aronica, L. A. *et al.* Palladium nanoparticles supported on Smopex® metal scavengers as catalyst for carbonylative Sonogashira reactions: Synthesis of α,β-alkynyl ketones. *Appl. Catal. A Gen.* **480**, 1–9 (2014).

28. Liu, B., Liu, L. R., Liu, X. J., Liu, M. J. & Xiao, Y. S. Variation of crystal structure in nickel nanoparticles filled in carbon nanotubes. *Mater. Sci. Technol.* **28**, 1345–1348 (2012).

29. Gong, Y. *et al.* 3D self-supported Ni nanoparticle@N-doped carbon nanotubes anchored on NiMoN pillars for the hydrogen evolution reaction with high activity and anti-oxidation ability. *J. Mater. Chem. A* **7**, 13671–13678 (2019).

30. Mansour, A. N. Characterization of NiO by XPS. *Surf. Sci. Spectra* **3**, 231–238 (1994).

31. Urso, M. *et al.* Ni(OH)2@Ni core-shell nanochains as low-cost high-rate performance electrode for energy storage applications. *Sci. Rep.* **9**, 1–11 (2019).

32. Medway, S. L., Lucas, C. A., Kowal, A., Nichols, R. J. & Johnson, D. In situ studies of the oxidation of nickel electrodes in alkaline solution. *J. Electroanal. Chem.* **587**, 172–181 (2006).

33. Cossar, E., Houache, M. S. E., Zhang, Z. & Baranova, E. A. Comparison of electrochemical active surface area methods for various nickel nanostructures. *J. Electroanal. Chem.* **870**, 114246 (2020).

34. Ferreira, E. B. & Jerkiewicz, G. On the Electrochemical Reduction of β-Ni(OH)2 to Metallic Nickel. *Electrocatalysis* **12**, 199–209 (2021).

35. Machado, S. A. S. & Avaca, L. A. The hydrogen evolution reaction on nickel surfaces stabilized by H-absorption. *Electrochim. Acta* **39**, 1385–1391 (1994).

36. Alsabet, M., Grden, M. & Jerkiewicz, G. Electrochemical Growth of Surface Oxides on Nickel. Part 1: Formation of α-Ni(OH) 2 in Relation to the Polarization Potential, Polarization Time, and Temperature. *Electrocatalysis* **2**, 317–330 (2011).

37. Hall, D. S., Bock, C. & MacDougall, B. R. An Oxalate Method for Measuring the Surface Area of Nickel Electrodes. *J. Electrochem. Soc.* **161**, H787–H795 (2014).

38. Ho, J. C. K. & Piron, D. L. Active surface area in oxide electrodes by overpotential deposited oxygen species for the oxygen evolution reaction. *J. Appl. Electrochem.* **26**, 515–521 (1996).

39. Lyons, M. E. G. & Brandon, M. P. A comparative study of the oxygen evolution reaction on oxidised nickel, cobalt and iron electrodes in base. *J. Electroanal. Chem.* **641**, 119–130 (2010).

40. Kortlever, R., Shen, J., Schouten, K. J. P., Calle-vallejo, F. & Koper, M. T. M. M. Catalysts and Reaction Pathways for the Electrochemical Reduction of Carbon Dioxide. *J. Phys. Chem. Lett.* **6**, 4073–4082

(2015).

41. Lv, W., Zhang, R., Gao, P. & Lei, L. Studies on the faradaic efficiency for electrochemical reduction of carbon dioxide to formate on tin electrode. *J. Power Sources* **253**, 276–281 (2014).

42. Huang, L. F., Hutchison, M. J., Santucci, R. J., Scully, J. R. & Rondinelli, J. M. Improved Electrochemical Phase Diagrams from Theory and Experiment: The Ni-Water System and Its Complex Compounds. *J. Phys. Chem. C* **121**, 9782–9789 (2017).

43. Liu, Y., Zhao, J. & Cai, Q. Pyrrolic-nitrogen doped graphene: A metal-free electrocatalyst with high efficiency and selectivity for the reduction of carbon dioxide to formic acid: A computational study. *Phys. Chem. Chem. Phys.* **18**, 5491–5498 (2016).

Chapter IV

The crucial role of the electrochemical cell design for the optimization of CO_2RR

4.1 Introduction

In the previous chapters, several electrocatalysts for the CO_2 reduction reaction have been explored. The approach used in the design of the electrocatalyst was always of the modular type, namely, by combining different building-blocks in a single nanostructure, an innovative material with added functionality can be obtained. Various aspects have been studied from the morphology to the oxidation state of the active phase of the catalyst. In tackling this study several problems were found mainly due to the limit of mass transport of CO_2 on the surface of the catalyst. As already mentioned in the general introduction, CO_2 has a poor solubility in aqueous solvents, which in environmental conditions is equal to 0.034 M.[1] A low concentration of CO_2 favours the concurrent reaction that occurs in the same window of potential: hydrogen evolution reaction (HER). The low solubility of CO_2 in the electrolyte negatively affects the catalytic performance of the materials, and an incorrect design of the electrochemical cell can lead to an error in the evaluation of the performance of the materials under study. In fact, the CO_2RR does not depend only on the catalyst, but numerous parameters come into play by influencing it: electrolyte, applied potential, temperature, pressure, pH, and the type of reactor.[2] By modifying these parameters, the efficiency and selectivity of the reaction can be increased, as well as the stability of the catalyst. Some of these parameters have been chosen a priori on the basis of the data in the literature and operational needs, while the design of the reactor is an interesting aspect to explore in the optimization of the CO_2RR study, as it affects the reduction processes, current density, Faraday efficiencies and stability.

4.1.1 Parameters of mass transport limitation on CO_2RR

Mass transport of CO_2 for CO_2RR means transporting CO_2 from the gas phase to the region adjacent to the electrode surface, which mainly depends on the type of **CO_2 supply method**, and significantly affects the activity of the catalyst. Pre-bubbling is essential to achieve system saturation. It has been widely accepted that the real reactant in CO_2RR is dissolved CO_2 referred to as CO_2(aq) or H_2CO_3*, and not HCO_3^- and CO_3^{2-}.[3] Mass transport takes place in two main steps: the first involves the dissolution of the gaseous CO_2 in solution, while the second step involves the diffusion of CO_2 from the bulk phase to the active sites. The first step involves a physical transfer process from the gas phase to the liquid phase:

$$CO_2(g) + H_2O\ (l) \overset{K_0}{\leftrightarrow} CO_2(aq) + H_2O\ (l) = H_2CO_3^* \tag{4.1}$$

This process is recognized as a positive process, as it increases the concentration of CO_2 in the electrolyte. At the same time, in this step, two chemical reactions can take place that depend on the pH of the solution (8 < pH < 10), and which are classified as negative processes, as they consume CO_2:

$$CO_2(aq) + H_2O\ (l) \overset{k_{\pm 0}}{\leftrightarrow} H_2CO_3 \leftrightarrow H^+ + HCO_3^- \quad (4.2)$$

$$CO_2(aq) + OH^- \leftrightarrow HCO_3^- \quad (4.3)$$

The rate of reaction (4.1) depends on several factors and is described by equation (4.4):

$$R_{MT} = k_{G/L} \cdot a \cdot p_{CO_2} \cdot K_0 \quad (4.4)$$

where $\boldsymbol{k_{G/L}}$ is the gas/liquid mass transfer coefficient, $\boldsymbol{a}$ is the specific gas/liquid surface area, $\boldsymbol{p_{CO_2}}$ is the CO_2 partial pressure, and $\boldsymbol{K_0}$ is the equilibrium constant. All these parameters can be optimized to improve the bulk transfer process.[4] An example is provided by the work of *Hori et al.*, who demonstrated that on the gold electrode the faradic current associated with the production of CO is linearly dependent on the CO_2 partial pressure and therefore directly proportional to the CO_2 concentration [CO_2]. As the pressure increased, the CO current increased.[5] While, it is possible to act on the specific gas/liquid surface area parameter by introducing a bubbler with a porous frit to create CO_2 micro-bubbles. *Ager et al.* demonstrated how the replacement of a capillary with a porous frit reduces the size of CO_2 bubbles and guarantees a constant concentration of CO_2 over time, reducing its depletion and increasing the hydrocarbons/hydrogen ratio produced.[6] Bubbling large CO_2 bubbles, in addition to increasing the depletion of CO_2 in the electrolyte, can cause them to block on the electrode surface, partially removing contact with the electrolyte and in actual fact blocking a portion of it for CO_2RR. At pH below 8 the reaction (4.2) is a rather slow reaction ($\boldsymbol{k_{+0} = 3.0 \cdot 10^{-2} s^{-1}}$), especially compared to the reverse reaction rate ($\boldsymbol{k_{-0} = 23.7\ s^{-1}}$). For this reason, acid electrolytes are preferred in many studies. The concentration of the electrolyte influences the concentration of dissolved CO_2: the higher the concentration, the greater the amount of CO_2 in the solution. This has a negative impact in the second step of mass transport, namely diffusion. The second step is regulated by Fick's Second Law. In this case a too high concentration hinders the diffusion of the species in the electrolyte.

All these parameters come into play in the event that the CO_2 is bubbled directly into the electrolyte where the CO_2RR is studied. The reactions and parameters change as the CO_2 supply method changes. The low solubility of CO_2 causes the main mass transport problems in the reaction and represents a general rate determining step of the system. It is possible to circumvent this problem, and to improve the mass transport, by directly feeding the CO_2 onto the electrode and creating a three-phase solid-liquid-gaseous boundary (electrode-elctrolyte-CO_2). It is possible to realize a system of this type using the gas diffusion electrode (GDE), a porous electrode consisting, mostly, of carbon fibres on which the catalyst is deposited.[7] Then, by directly injecting the CO_2 on the electrode, it is directly adsorbed and activated (4.5), without the need to go through the slow and inefficient steps mediated by the electrolyte:[4]

$$CO_2(g) + e^- \rightarrow CO_2^{-\bullet}(ads) \quad (4.5)$$

In this system it is possible to reach current densities of hundreds of mA cm^{-2}, values that would make the system commercially applicable.[8]

4.1.2 The design of electrochemical cell for CO_2RR

On the basis of the above, the electrochemical cells for CO_2RR can be divided into two categories: the H-cell and the flow cell. The most used cell design in the laboratory is the H cell, so called because it resembles the shape of an H (Figure 5.1).[9] It consists of an anode compartment and a cathode compartment, connected to each other by a circular channel, but separated by an ion exchange membrane. In the cathode compartment there is the working electrode together with the reference electrode. The membrane has the purpose of preventing the cathodic reaction products from reaching the anode and undergoing further electrochemical reactions, avoiding falsifying the quantification of the reaction products. During electrolysis, gaseous CO_2 is continuously flowed into the cathode compartment, in order to keep the CO_2 concentration in the electrolyte constant, and to allow the gas to escape along with reaction products, which are directly injected into the GC to on-line analysis of gaseous products. The flow of CO_2 gas is controlled by a mass flow control.

The problems of this type of cells are different, from the need to dissolve the CO_2 in the electrolyte, which limits the reaction efficiencies, to the quantification of the products in the liquid phase. For the quantification of the liquid phase, it is essential to find a right compromise between the duration of the electrolysis and the volume of the electrolyte. In fact, an electrolysis that is too short and a volume that is too large could lead to an incorrect quantification of the products, as they are too diluted and below the quantification limit of the instruments. Another problem encountered with H cells is the high ohmic drop due to the resistance of the solution and the large distance between WE and CE. Consequently, the cell voltage, which includes the potentials for both the anode and cathode processes, can increase up to the limit of the potentiostat,[2] preventing the success of the measurement.

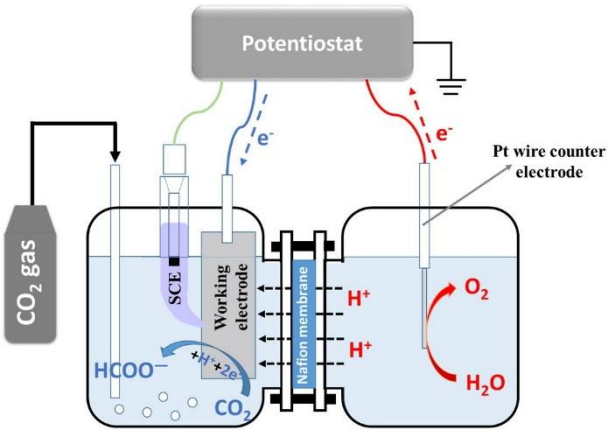

Figure 4.1 A schematic diagram of the conventional H-type electrochemical cell with 3 electrode. Reprinted from Chem. Eng. J. 293 (2016) 161–170.[9]

The other type of cell that is gaining ground in CO_2RR research is the flow cell, as it allows to overcome mass transport problems and reach currents of the order of a hundred of mA cm^{-2}. Its origin derives from fuel cells and water electrolyzers. There are different designs for flow cells, a first distinction is made between two- and three-electrode cells. The first ones do not have a reference electrode (RE), consequently in these cells it is possible to control only the current and not the potential, while in the second type, a RE is inserted near the WE to be able to control its potential.[10] Controlling the potential is essential for those electrocatalysts that modify their selectivity as a function of the potential, or for the study of completely new electrocatalysts. Figure 4.2 shows the universal architecture of a flow cell. It consists of two flow channels, the catholyte and the anolyte, which are separated by an ion exchange membrane. The electrocatalyst under study is immobilized on the gas diffusion layer, which, on the one hand, is in direct contact with the flowing electrolyte, while on the other the gaseous CO_2 is directly injected. From this general architecture there are several with some changes in the set up. An example is given by zero-gap cells or also called polymer electrolyte membrane (PEM) flow cell. In this case the cathode and anode are pressed together with the ion exchange membrane that separates them, forming membrane electrode assemblies (MEA). The advantage of these cells is given by the practically zero distance between WE and CE which significantly reduces the ohmic drop of the system. Furthermore, the high concentration of CO_2 allows to obtain high currents. Despite the advantages, this type of cell presents some problems. One is due to the liquid products that are formed as a result of CO_2RR, which can stay in the GDL and block the pores,[11] the second is due to the membrane,

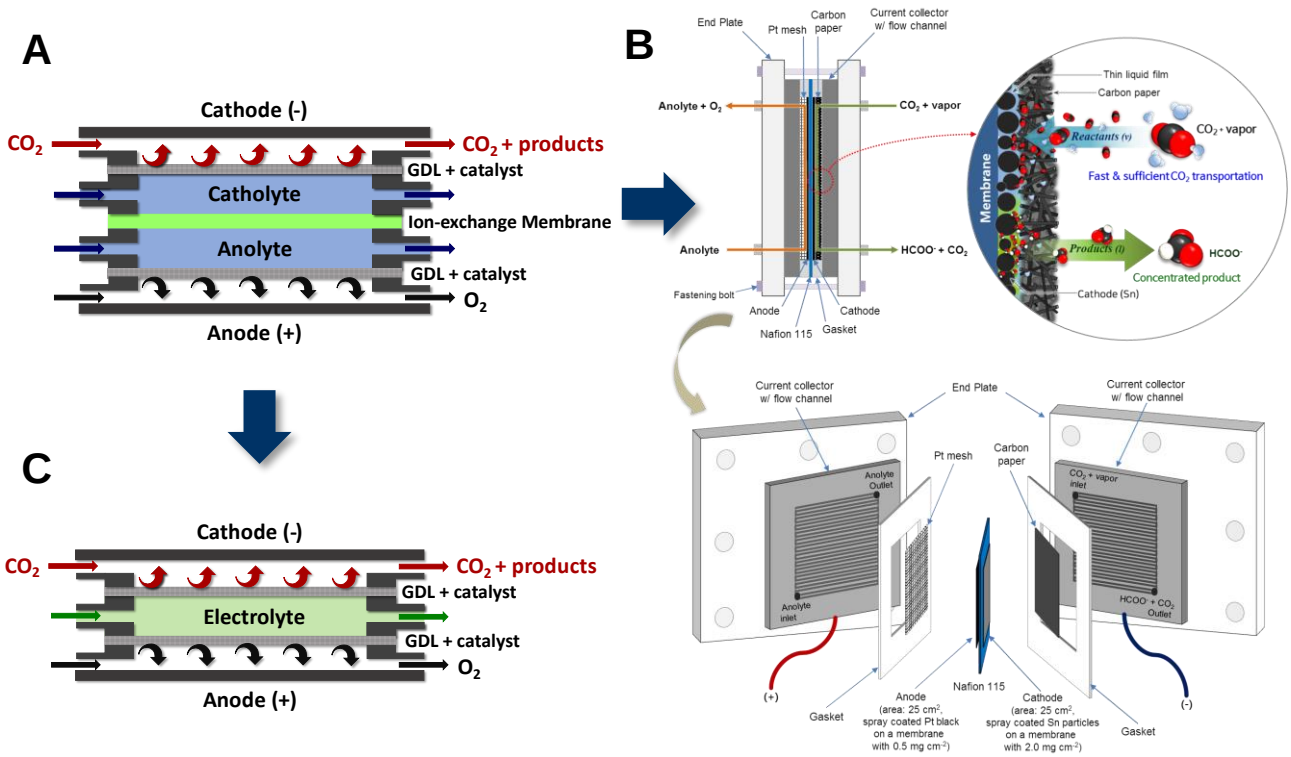

Figure 4.3 ***Electrochemical Flow Cell.*** *Schematic diagram of A) universal architecture of a flow cell, B) polymer electrode membrane flow cell (in close e open configuration) [Reprinted from Angew. Chem., Int. Ed., 2018, 57, 6883–6887][12] and C) microfluidic cell (MFC) without membrane.*

which facilitates the acidification of the catholyte leading to an increase in HER. Adding a buffer layer between the electrodes can bypass this effect, but at the same time leads to increased cell resistance.[13]

Finally, another type of cell is provided with microflow cells (MFC). In this setup a thin layer of flowing electrolyte is placed between the cathode and anode. The flow causes the reaction products and excess protons to be carried away.[14] Alternatively, a membrane can be inserted which separates the anode and cathode electrolyte, always in flow.

The use of these flow cells is possible only thanks to porous electrodes that allow the CO_2 to flow directly into the electrode and form the three-phase contact, where the CO_2RR occurs. There are different types of porous electrodes, but the most used are the gas diffusion layers (GDLs).

4.1.3 Gas Diffusion Electrode (GDE)

The gas diffusion electrode consists of the gas diffusion layer above which the catalyst is immobilized (catalyst layer, CL). The GDL is a porous and conductive structure consisting of two layers: a macroporous substrate (MPS) and a microporous layer (MPL) (Figure 4.3 B).[7] The macroporous substrate usually consists of densely packed carbon fibres of carbon paper or carbon cloth, while the microporous carbon layers can be carbon nanofibers or compressed carbon powder.[11] The MPS provides mechanical stability and good electrical conductivity to the GDE. In addition to good porosity, GDL must find a good compromise between hydrophobicity and hydrophilicity. In fact, a completely hydrophilic electrode would cause flooding of the porosities of the GDL, blocking them and favouring the HER,[2] while a completely hydrophobic material could result in lower electronic conduction due to the excessive presence of a non-conductive polymer. To achieve a good hydrophilicity/hydrophobicity ratio, GDLs are treated with a fluorinated polymer, such as polytetrafluoroethylene (PTFE). Usually, the loading of PTFE on MPS is in the range of 5–20 wt%. In this case, an excess of PTFE loading would lead to a blockage of the porosities of the GDL. While the MPL is located between the MPS and the CL, which is added to the GDE to improve the interfacial electrical connection with the catalyst and prevent flooding in the GDE. As for MPS, MPL consists of a mixture of carbon black nanoparticles with a hydrophobic polymer, such as PTFE, to increase the hydrophobic nature of the GDL, which thanks to this latter property and together with the nanometric dimensions of the pores, a good transport of gas molecules in the GDE is achieved and flooding is prevented. MPL is not simply resting on top of MPS, but they are pressed together. During this compression process, a part of the MPL penetrates inside the MPS, thus ensuring good stability, cohesion, and compactness of the GDL. The morphology, porosity, thickness, and hydrophobicity of MPL are very important parameters that determine the transport of the gas and the creation of an optimal three-phase interface, which in turn affect the CO_2RR. These properties can be adjusted according to the composition, for example the ratio of carbon nanoparticles to PTFE.[7] The GDEs allow an optimal CO_2 mass transport, in which the diffusion path of CO_2 is significantly reduced, in addition

the properties of the GDE can be easily modified by adjusting the constitutive and structural parameters. The main problem with GDEs is their tendency to lose their hydrophobic property during long-term electrolysis, resulting in flooding of the GDL and a loss of CO_2RR performance.[15]

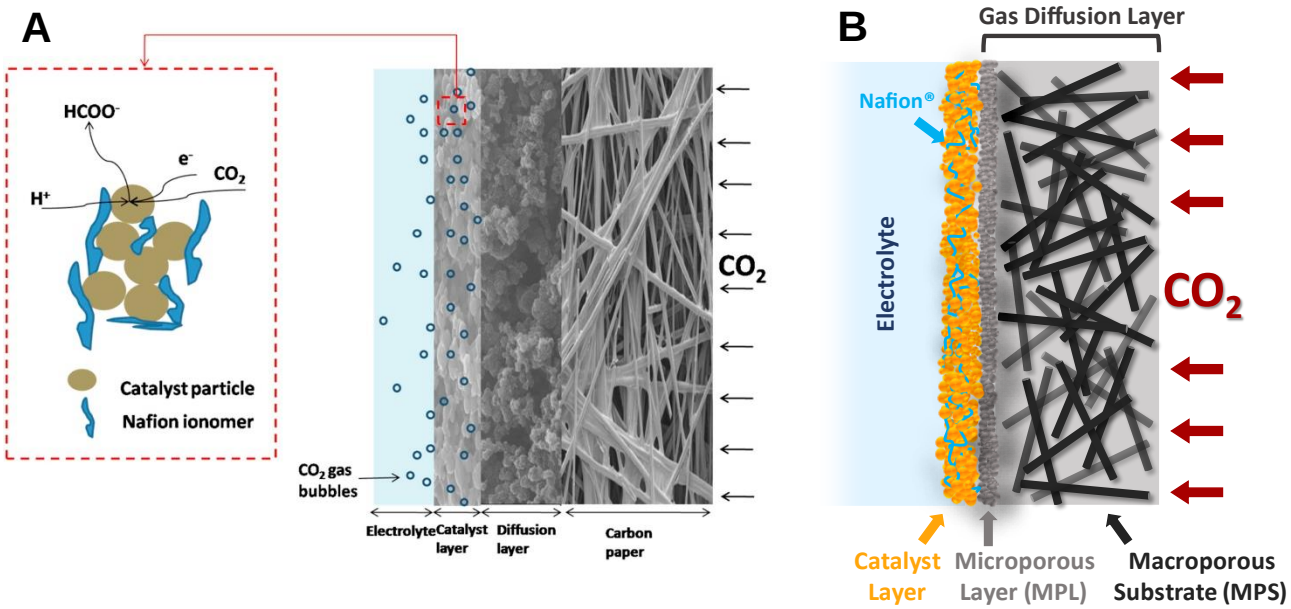

Figure 4.5 ***Gas Diffusion Electrode (GDE).*** *A) A schematic diagram of composition of a gas diffusion electrode (GDE) and the three-phase interface,[16] and B) the corresponding graphic representation*

4.1.4 Outlook

The use of an electrochemical cell with a different design, and a different approach to the CO_2 supply at the cathode can result in drastic changes in CO_2RR performance. The possibility of improving the efficiencies and selectivity of the reaction make the flow cell and the application of GDL particularly promising. In some cases, this set up demonstrated a change in the selectivity of the catalyst, leading to an increase in the production of products with more carbon atoms (C_{2+}).[17] For this reason, as the last part of this project it was decided to study the effect of changes in the experimental setup for CO_2RR on CNH@CeO_2. Although the CHN@CeO_2 were not the catalysts with the best performances in the production of HCOOH, we wanted to carry out a first test to verify if a new setup could influence the selectivity of the catalyst and its efficiencies. A tailor-made cell was used for this, together with a commercial GDL. The peculiarity of this cell is the supply of CO_2 by direct flow on the GDL, while the electrolyte is kept static. In particular, two GDLs with two different thickness were tested.

4.2 CO_2RR performance of CHN@CeO_2 electrocatalysts on CO_2-flow Cell

The electrocatalysts used to test the new electrochemical cell are the same as in chapter 1.3, i.e., the CNHs decorated with CeO_2 nanoparticles at two different loading. The cell used is a custom-made cell, specially designed, modifying the cell already used for the electrochemical measurements of this project (Figure 4.4). The peculiarity of this cell is that only the method by which CO_2 is supplied to the system is changed. Instead of bubbling the CO_2 into the electrolyte, it is supplied with a direct flow on a GDL. Inside this cell the electrolyte is kept static, as we wanted to observe only the effect of the different CO_2 supply. We can say that the design of this cell comes from the combination of an H-cell and a flow cell.

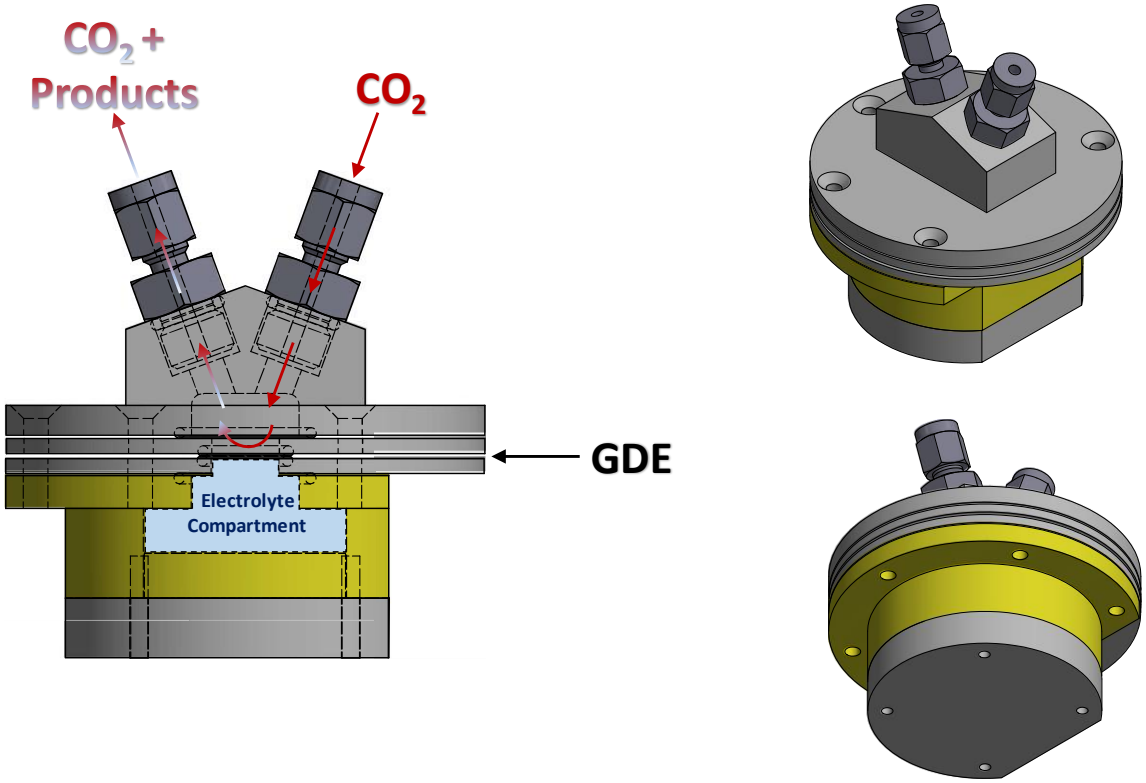

Figure 4.6 Design of the new custom-made cell, where on the left you have an idea of the internal space with the flow of CO_2 and the electrolyte compartment, while on the right there is the external 3D image. The yellow-coloured piece is the original piece of the cell used for the other CO_2RR measurements. In this drawing the space of the RE and the CE have not been shown. The photographs have been shown in the appendix.

To study the effect of the CO_2 supply method, in the CO_2RR, all parameters were kept constant, i.e., same CO_2 flow (5 sccm), same geometric size of the electrode (1 cm^2), same loading of catalyst on electrode (505 µg cm^{-2}) and same electrolyte ($KHCO_3$ 0.5 M). For this method, it was necessary to change the electrode passing from a glassy carbon electrode (GCE) to a GDL. Two different commercial GDLs from SIGRACET® were used, 28BC and 38BC (Figure 4.5). In both, a treatment with PTFE was carry out to ensure the hydrophobicity

of the system and both have a high density of fibres, the difference between the two GDLs depends on the thickness. The main properties have been summarized in the table 4.1.

Table 4.1 Material data of SIGRACET® GDL

GDL	Areal weight [g/m²]	Thickness (@5 psi load) [µm]	Electrical Resistance (@1 MPa) [mΩ· cm²]
28BC	105 ± 10	235 ± 20	< 11
38BC	125 ± 10	325 ± 25	< 11

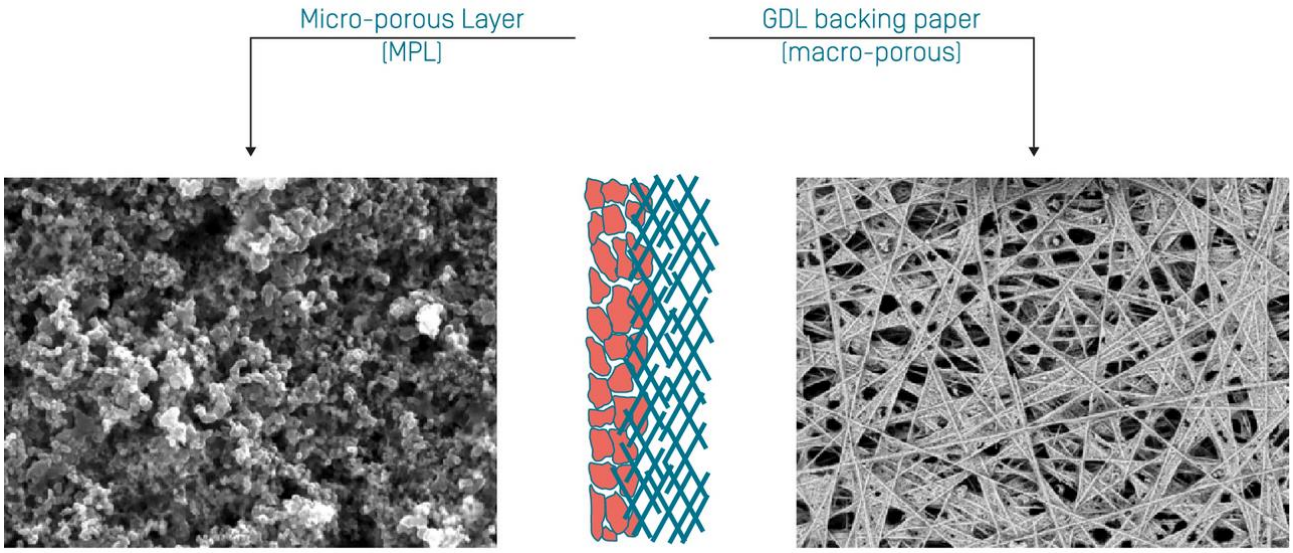

Figure 4.7 SEM image of the MPL (left) and MPS (right) of the used GDLs. The image was taken from the SIGRACET® website.

To deposit the electrocatalysts and ensure a good homogenous catalyst layer, it was necessary to modify the ink formula, adopting a mixture of ⅔ of isopropanol and ⅓ water due to the hydrophobicity of GDL.

The measurements below were performed on the samples 20CNH@CeO_2 and 30CNH@CeO_2, and are preliminary measurements aimed at testing the new electrochemical cell, for which a measurement protocol has not yet been established.

Two CA of 20CNH@CeO_2 were performed on GDLs 28BC and 38BC at -0.5 V and -0.9 V vs RHE, adopting the same measurement protocol of the static cell for the reasons described above. Figure 4.6 reports the CO2RR performance of this system. As in the case of the chapter II, the analysis of the products revealed only the presence of H_2, CO and HCOOH, where the CO production is neglected, as the FE never exceed 0.5%.

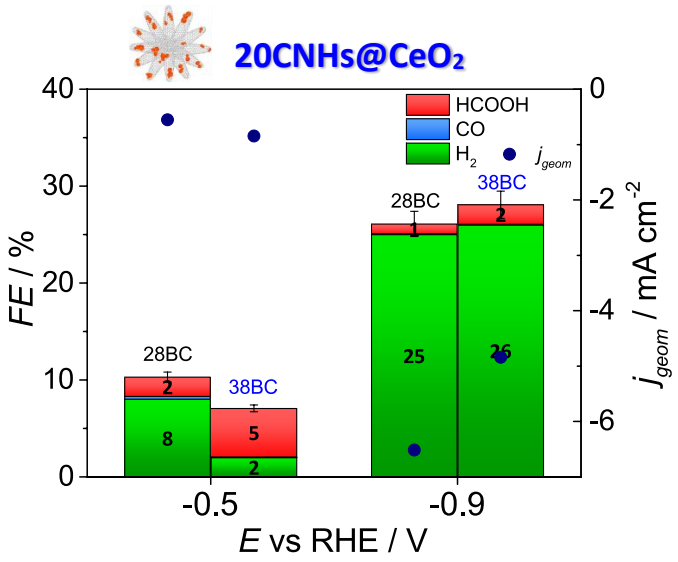

Figure 4.8 ***CO_2RR performance.*** *Faradaic Efficiency (FE) of detectable CO_2RR products in CO_2-saturated $KHCO_3$ 0.5 M (pH 7.5): H_2 (green), CO (light blue) and HCOOH (red) for 20CNHs@CeO_2 on 28BC and 38BC GDL. The blue points indicate the mean current density of sample at that potential; the values are shown on right axis.*

From this first analysis it can be seen that the thickness of the GDL does not significantly affect the CO_2RR. The FE values are very similar to each other, and also in terms of current density there are no significant variations. Based on the data in the literature, the greater the thickness of the GDL, the greater the resistance to mass transport of CO_2.[18] In this case the difference in thickness between the two GDLs is not so high as to induce a significant change in performance. While, comparing the observed data for 20CNH@CeO_2 on GDL (38BC) and on GCE there is a noticeable difference (Figure 4.7).

The big difference between the two electrodes is recorded in the current, which is up to 8 times greater with the use of GDL, and so far, it has never been possible to reach such high values of current density (-5 mA cm-

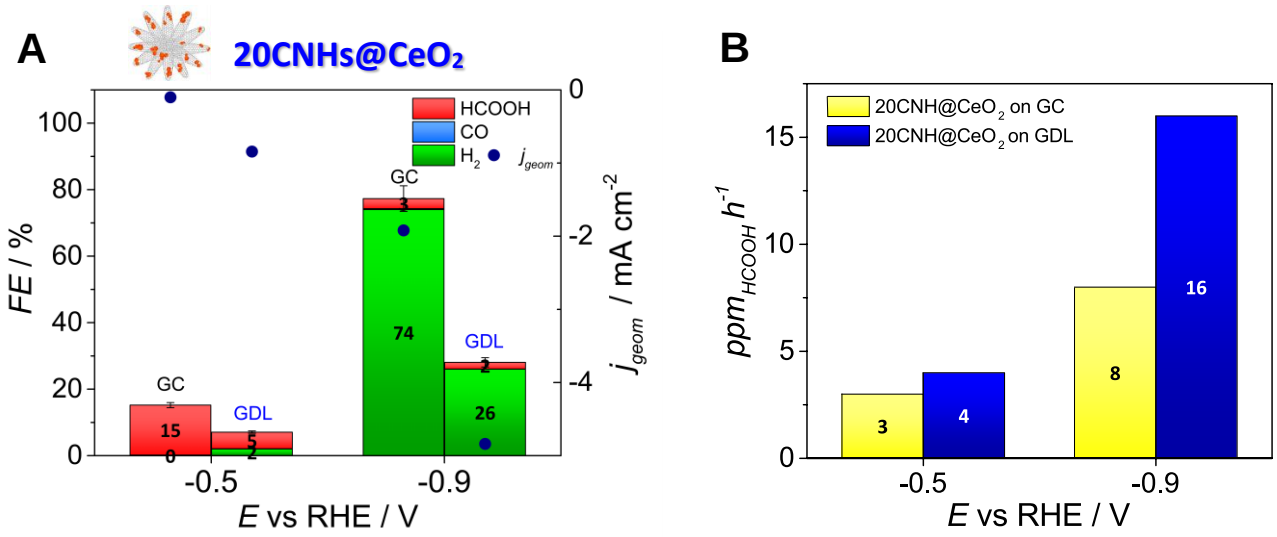

Figure 4.9 ***CO_2RR performance and Formic acid production.*** *A) Faradaic Efficiency (FE) of detectable CO_2RR products in CO_2-saturated $KHCO_3$ 0.5 M (pH 7.5): H_2 (green), CO (light blue) and HCOOH (red) for 20CNHs@CeO_2 on GCE and 38BC GDL. The blue points indicate the mean current density of sample at that potential; the values are shown on right axis. B) Formic acid production rate in ppm h^{-1} at -0.5 V and -0.9 V vs RHE for 20CNHs@CeO_2 on GCE (yellow) and 38BC GDL (blue).*

^{2}). The other difference is recorded at the level of the FE, which turn out to be lower decisively with the use of GDL. In the system with GDL, H_2 production is revealed also at -0.5 V, a phenomenon not observed in the case of GCE. The explanation of this behaviour is certainly to be attributed to the different CO_2 supply method, which, in the case of GDL, allows to reach very high currents, which in turn consume a greater quantity of CO_2, but the flow adopted for these measurements on GDL is not adequate, both for the supply of CO_2 and for the adequate transport of more concentrated gaseous products. An increase in CO_2 flow would lead to better performance. In fact, in flow systems of this type, the flows adopted are around 50 and 100 sccm, depending on the catalyst and the currents reached.[19,20] Furthermore, it must be remembered that the increase in current also derives from the 3D porous structure of the GDLs, which allow greater dispersion of the material on the electrode, increasing its electrochemically active area, and reducing the catalyst packing that usually occurs on the GCE.

The same behaviour revealed for sample 20CNH@CeO_2 is found in sample 30CNH@CeO_2 (Figure 4.8). The FE of the GDL sample does not exceed 30%, with a 50% reduction of the formic acid FE and 63% of the H_2. As in the previous case, the current increases by 7 times, reaching -10 mA cm^{-2}. Once again, this phenomenon derives from the failure to set up the setup, necessary to achieve maximum performance. An improvement in CO_2RR can be noted, observing in addition to the increase in current, the doubling of the production of formic acid, passing from 24 to 48 ppm in one hour. In addition to fine-tuning the gas flow, it is necessary to determine the proper amount of catalyst to be deposited on the GDL. In fact, for these preliminary analyses, the same loading of the static cell was used. Instead, it is necessary to consider the three-dimensional porous structure of the GDL which significantly increases the exposed area of the electrode, which no longer corresponds to the geometric area. Usually, the loading of the catalyst for this type of cell is between 0.2 mg cm^{-2} and 10 mg cm^{-2}, among which it is found that 1 mg cm^{-2} is the most used loading of all.[10]

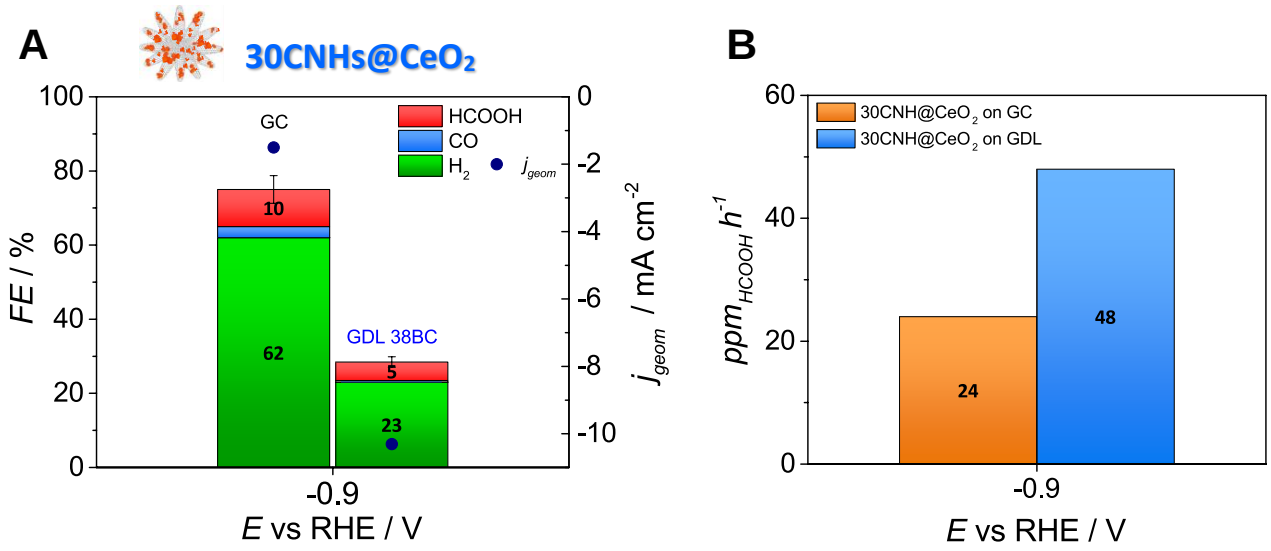

Figure 4.10 ***CO_2RR performance and Formic acid production.*** *A) Faradaic Efficiency (FE) of detectable CO_2RR products in CO_2-saturated $KHCO_3$ 0.5 M (pH 7.5): H_2 (green), CO (light blue) and HCOOH (red) for 30CNHs@CeO_2 on GCE and 38BC GDL. The blue points indicate the mean current density of sample at that potential; the values are shown on right axis. B) Formic acid production rate in ppm h^{-1} at -0.9 V vs RHE for 30CNHs@CeO_2 on GCE (orange) and 38BC GDL (light blue).*

4.3 Conclusions and prospects

Influencing the efficiencies and selectivity of CO_2RR is not just a matter of electrocatalyst and materials, but various parameters come into play, including the CO_2 supply method. In fact, this last parameter can clearly determine the limit of mass transport in the system and consequently the possibility of reaching current values and commercial efficiencies. In this last chapter these aspects have been highlighted, with a direct comparison between the supply of CO_2 directly on gas diffusion layer or through bubbling on glassy carbon. For this purpose, a custom designed hybrid electrochemical cell was used which features a flow compartment for the CO_2 gas and a static compartment for the electrolyte. From these preliminary measurements it has been observed how the direct supply of CO_2 to the electrode can increase the faradic current and the quantity of derived CO_2 products, without however observing an increase in the FE. This is due to the fact that the measurements presented here are preliminary measurements, for which a measurement protocol has not yet been defined, ranging from the choice of the CO_2 flow rate to the quantity of catalyst to be deposited on the GDL. These parameters will be defined in the future with the use of materials with known properties, such as Ag.[21] Furthermore, as a future prospect, there is the intention to adopt a commercial flow cell (Figure 4.9)[22] and to compare how the electrolyte flow can affect the CO_2RR.

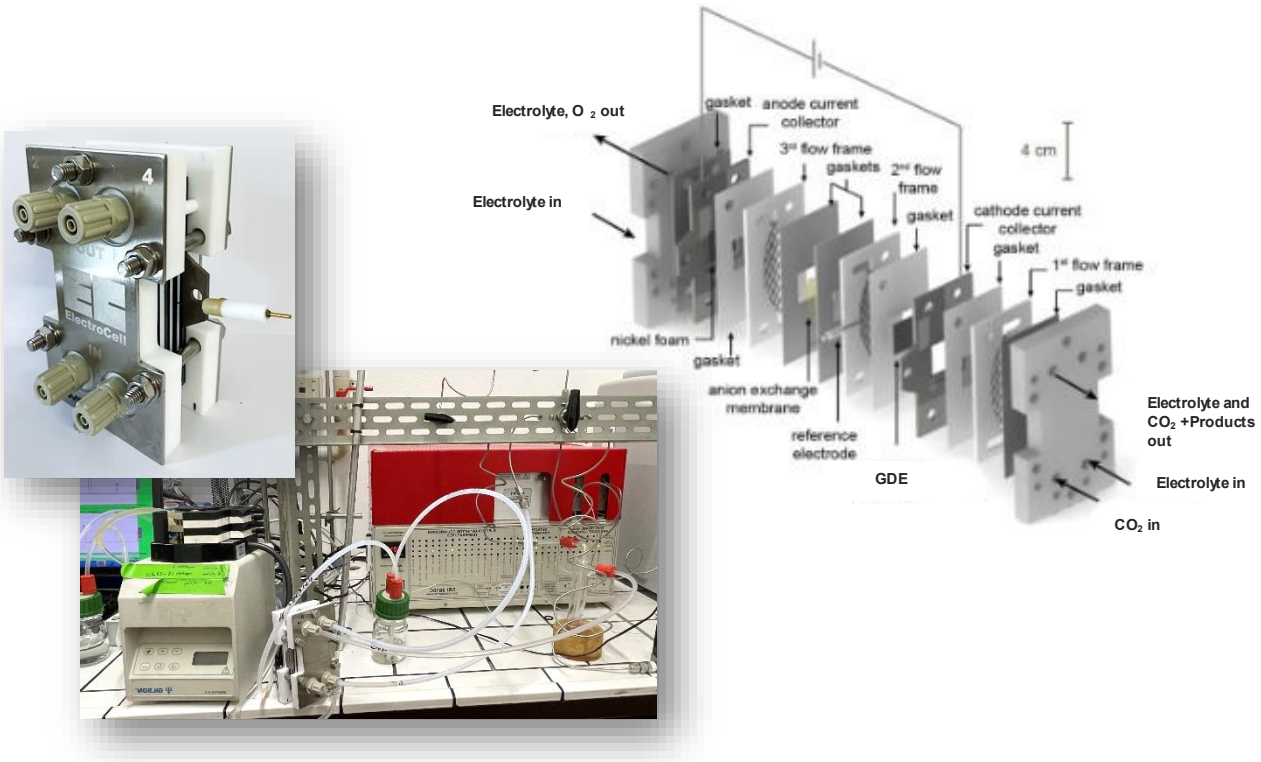

Figure 4. 11 (left) photo of the purchased commercial cell (ElectroCell); (down) photo of the experimental setup of the commercial cell coupled with the GC; (right) expanded visualization of architecture of commercial microfluidic flow cell that will be used for the future CO_2RR measurements. Reprinted from Chem. Eur. J. 2022, 28 e202200340.[22]

Reference

1. Sun, Z., Ma, T., Tao, H., Fan, Q. & Han, B. Fundamentals and Challenges of Electrochemical CO2 Reduction Using Two-Dimensional Materials. *Chem* **3**, 560–587 (2017).

2. Liang, S., Altaf, N., Huang, L., Gao, Y. & Wang, Q. Electrolytic cell design for electrochemical CO2 reduction. *J. CO2 Util.* **35**, 90–105 (2020).

3. Zhong, H., Fujii, K., Nakano, Y. & Jin, F. Effect of CO2 bubbling into aqueous solutions used for electrochemical reduction of CO2 for energy conversion and storage. *J. Phys. Chem. C* **119**, 55–61 (2015).

4. Lu, S. *et al.* Mass transfer effect to electrochemical reduction of CO2: Electrode, electrocatalyst and electrolyte. *J. Energy Storage* **52**, 104764 (2022).

5. Hori, Y., Murata, A., Kikuchi, K. & Suzuki, S. Electrochemical reduction of carbon dioxides to carbon monoxide at a gold electrode in aqueous potassium hydrogen carbonate. *J. Chem. Soc. Chem. Commun.* 728–729 (1987). doi:10.1039/C39870000728

6. Lobaccaro, P. *et al.* Effects of temperature and gas-liquid mass transfer on the operation of small electrochemical cells for the quantitative evaluation of CO2 reduction electrocatalysts. *Phys. Chem. Chem. Phys.* **18**, 26777–26785 (2016).

7. Nguyen, T. N. & Dinh, C. T. Gas diffusion electrode design for electrochemical carbon dioxide reduction. *Chem. Soc. Rev.* **49**, 7488–7504 (2020).

8. Song, J. T., Song, H., Kim, B. & Oh, J. Towards higher rate electrochemical CO2 conversion: From liquid-phase to gas-phase systems. *Catalysts* **9**, 224 (2019).

9. Zhao, C. & Wang, J. Electrochemical reduction of CO2 to formate in aqueous solution using electro-deposited Sn catalysts. *Chem. Eng. J.* **293**, 161–170 (2016).

10. Endrődi, B. *et al.* Continuous-flow electroreduction of carbon dioxide. *Prog. Energy Combust. Sci.* **62**, 133–154 (2017).

11. Ma, D., Jin, T., Xie, K. & Huang, H. An overview of flow cell architecture design and optimization for electrochemical CO2reduction. *J. Mater. Chem. A* **9**, 20897–20918 (2021).

12. Lee, W., Kim, Y. E., Youn, M. H., Jeong, S. K. & Park, K. T. Catholyte-Free Electrocatalytic CO2 Reduction to Formate. *Angew. Chemie - Int. Ed.* **57**, 6883–6887 (2018).

13. Wu, J. *et al.* Electrochemical Reduction of Carbon Dioxide: II. Design, Assembly, and Performance of Low Temperature Full Electrochemical Cells. *J. Electrochem. Soc.* **160**, F953–F957 (2013).

14. Whipple, D. T., Finke, E. C. & Kenis, P. J. A. Microfluidic reactor for the electrochemical reduction of carbon dioxide: The effect of pH. *Electrochem. Solid-State Lett.* **13**, B109–B111 (2010).

15. Yang, K., Kas, R., Smith, W. A. & Burdyny, T. Role of the Carbon-Based Gas Diffusion Layer on Flooding in a Gas Diffusion Electrode Cell for Electrochemical CO2Reduction. *ACS Energy Lett.* **6**, 33–40 (2021).

16. Wu, J., Sharma, P. P., Harris, B. H. & Zhou, X. D. Electrochemical reduction of carbon dioxide: IV dependence of the Faradaic efficiency and current density on the microstructure and thickness of tin electrode. *J. Power Sources* **258**, 189–194 (2014).

17. Fan, L. *et al.* Strategies in catalysts and electrolyzer design for electrochemical CO2 reduction toward C2+ products. *Sci. Adv.* **6**, 1–18 (2020).

18. Schwartz, N., Harrington, J., Ziegler, K. J. & Cox, P. Effects of Electrode Support Structure on Electrode Microstructure, Transport Properties, and Gas Diffusion within the Gas Diffusion Layer. *ACS Omega* **7**, 29832–29839 (2022).

19. Dinh, C. T. *et al.* CO2 electroreduction to ethylene via hydroxide-mediated copper catalysis at an abrupt interface. *Science (80-.).* **360**, 783–787 (2018).

20. Ren, S. *et al.* Molecular electrocatalysts can mediate fast, selective CO2 reduction in a flow cell. *Science (80-.).* **365**, 367–369 (2019).

21. Clark, E. L. *et al.* Standards and Protocols for Data Acquisition and Reporting for Studies of the Electrochemical Reduction of Carbon Dioxide. *ACS Catal.* **8**, 6560–6570 (2018).

22. Ren, S. *et al.* Electrocatalysts Derived from Copper Complexes Transform CO into C2+ Products Effectively in a Flow Cell. *Chemi. Eur. J.* **28**, e202200340 (2022).

Conclusions and Prospects

The CO_2RR represents an excellent strategy for the production of fuels and reagents useful in the perspective of a carbon neutral circular economy. Unfortunately, as has been observed, CO_2RR poses numerous challenges, ranging from poor selectivity to low reaction efficiencies. In fact, the reduction of CO_2 leads to the formation of numerous reaction products, resulting in a reduction in the efficiency and effectiveness of the reaction. For this reason, it is necessary to use catalysts capable of selecting the reaction pathway, through the stabilization of certain reaction intermediates.

In this thesis project three different families of heterogeneous electrocatalysts were presented, designed through a common approach, namely, an approach of modular type, where the combination of different building-blocks with unique chemical physical properties, allows to obtain a completely new material with certain functionalities. The common thread of these three catalysts is the type of materials chosen and combined with each other: carbon nanostructures decorated with nanocrystalline metal oxide (MO). The materials studied can be divided into three categories: (i) multi-wall carbon nanotubes and carbon nanohorns decorated with ceria oxide nanoparticles (MWCNT@CeO_2 and CNH@CeO_2 chapter I); (ii) graphene oxides and reduced decorated with Bi_2O_3 nanoparticles (GO/Bi_2O_3 and rGO/Bi@Bi_2O_3 chapter II); and finally (iii) covalent triazine frameworks decorated with nickel oxide nanoparticles (NiO-CTFs chapter II).

Heterogeneous catalysts based on transition metal, such as oxide-derived catalysts, are among the most promising candidates for CO_2 reduction. In fact, it has been observed that the presence of oxygen in the active phase of the catalyst is a crucial factor for CO_2RR. Under the conditions of electrolysis, the metal oxides are reduced, forming surface defects that allow to activate and bind the CO_2 on the catalyst more easily, compared to the pristine metal. This is the case of cerium oxide, which has a reversible redox pair $Ce^{4+/3+}$, which in reduction conditions releases oxygen atoms, forming superficial oxygen vacancies. These vacancies represent the active site of the catalyst, where CO_2 can bind and be activated by the Ce^{3+} site. But as it has been observed, the metal oxides alone are not sufficient to catalyse the reaction, they need a support, which not only stabilizes the MO nanoparticles, but also supplies electrons to the system, counteracting the insulating effect of the MO and promoting the formation of oxygen vacancies on the surface. Here, therefore, that the combination of **CeO_2 with MWCNTs** allows to reduce CO2 to formic acid with high selectivity to a potential close to the equilibrium potential of formic acid: an **FE_{HCOOH} of 65% is obtained at an overpotential of 0.02V**, by means of a CO_2 electrohydrogenation mechanism. To benefit from the combination of CNS with MO it is necessary to form an adequate interface between the two components. In fact, in the case of CNH@CeO_2, the lack of an adequate connection between the two phases has significantly reduced the efficiencies of the formic acid production, while maintaining a low overpotential. In that sense, the study

conducted on **Bi_2O_3 and GO**, reinforced the concept that adequate interaction between MO and CNS promotes the catalytic activity and selectivity of MO catalysts, increasing electron mobility in MO and **significantly contributing to long-term stability of nanostructured catalysts**. As already mentioned for ceria-based materials, the effect of the valence of the metal oxide nanoparticles strongly influences the CO_2RR. In a core-shell system (rGO/Bi@Bi_2O_3), with a bismuth oxide shell, the presence of a metal core may anticipate the onset potential of formic acid production (**FE_{HCOOH} of 38 % at -0.5 V vs RHE, 3 ppm_{HCOOH} h^{-1}**), but at higher potentials, the complete reduction of NPs favours the competitor HER, while in a completely oxidized system (GO/Bi_2O_3), the oxygen atom favours the stabilization of the reaction intermediate *OCHO, which is responsible for the reduction to formic acid (FE_{HCOOH} of 46 % at -0.8 V vs RHE, 73 ppm_{HCOOH} h^{-1}).

Finally, the interaction between **NiO nanoparticles and CTF was investigated for the production of syngas**, where CNS not only plays a role in the reduction and stabilization of MO nanoparticles but activates the NiO nanoparticles for CO_2RR. In fact, it has been observed that the interaction between the N-pyrrole and Ni sites is fundamental to reduce CO_2 to CO, while where this interaction fails, HER takes over. Furthermore, the CTFs adsorb the CO_2 on its surface and favour its reduction by the Ni. But the CTFs possess in themselves a high catalytic power, due to the N-pyrrole sites, in favour of the reduction of CO_2 to formic acid. This metal-free electrocatalyst is capable of producing formic acid with an FE of 53% with an overpotential of 150 mV. We can conclude that the combination and interaction of the different constituent elements play a fundamental role in the modulation of the selectivity for CO_2RR. These materials offer an excellent starting point for the realization of future electrocatalysts with transformable properties, whose catalytic activity derives from the interaction between MO and CNS.

However, the efficiency and selectivity of CO_2RR depend not only on the electrocatalyst used, but also on various experimental parameters, including the CO_2 supply method which determines the mass transport limit of the reaction. In **the last part of this project, two methods of CO_2 supply were compared**, the direct flow one on the GDE and the one through bubbling in the electrolyte, to do this a custom-made hybrid cell was used. From these preliminary measurements it was observed how the direct supply of CO_2 to the electrode can increase the faradic current and the amount of CO_2 derived products. These measurements are only preliminary, as this setup requires the optimization of various parameters with the stabilization of a measurement protocol. Furthermore, as a future perspective, it is also intended to adopt a commercial flow cell to compare how the electrolyte flow can affect the CO_2RR

Appendix

A.1 Materials physical characterizations and instrumentation

Transmission electron microscopy (TEM)

HRTEM and STEM were performed on a JEOL 2200FS microscope, working at 200 kV, and equipped with an energy dispersive X-ray spectrometer (EDX), a high-angle annular dark-field (HAADF) detector, and an in-column energy Omega filter. EDX maps were obtained in scanning TEM (STEM) mode.

Thermogravimetric analysis (TGA)

TGA of approximately 1 mg of each compound is recorded on a TGA Q500 (TA Instruments) under air, by equilibrating at 100 °C, and following a ramp of 10 °C min^{-1} up to 800 °C.

RAMAN spectroscopy

Raman spectra were recorded with an Invia Renishaw microspectrometer equipped with He−Ne laser at 532 nm. To avoid sample damage or laser-induced heating/crystallization of the materials, the incident power was kept at 1 % (full power of the laser is 100 mV). Powders were dispersed in EtOH, drop-cast onto a quartz slide and the solvent evaporated; at least 10 spectra per sample in different spots were collected to check their homogeneity.

X-Ray diffraction (XRD)

X-ray diffraction (XRD) was performed on a Philips X'Pert diffractometer using a monochromatized Cu Kα (λ= 0.154 nm) X-ray source in the range 10° < 2θ < 100°.

X-Ray photoelectron spectroscopy (XPS)

XPS measurements were performed in a SPECS Sage HR 100 spectrometer, where the UHV chamber had a base pressure lower than $10^{-9}/10^{-10}$mbar. The chamber was equipped with nonmonochromatized Al radiation ($h\upsilon$ = 1486.6 eV) and a hemispherical electron/ion energy analyzer (VSW mounting a 16-channel detector). The operating power of the X-ray source was 1440 W (12 kV and 12 mA) and photoelectrons were collected normal to the sample surface, maintaining the analyzer angle between analyzer axis and X-ray source fixed at 54.5°. All the samples were adsorbed on aluminium foil, and XPS spectra were acquired in a fixed analyzer transmission mode with a pass energy of 44.0 eV. The spectra were analyzed by using the

CasaXPS software. Shirley functions have been used to subtract the background. The deconvolution of the The XPS spectra of *Chapter I* were defined as 40% Lorentzian and 60% Gaussian, while the XPS spectra of *Chapter II* has been carried out employing a Lorentzian asymmetric. The binding energies (B.E.) were calibrated upon fixing the Al 2p component of Al(0) at 71.8 eV.

Inductively coupled plasma-optical emission spectrometry (ICP-OES)

ICP-OES (Optical emission spectrometry) analysis was recorded on an Optima 8000 Perkinelmer instrument.

Gas adsorption measurements

The nitrogen physisorption experiments were conducted on a Micromeritics ASAP 2010 instrument. The CTF1 were degassed for at least 15 h at 150 °C using a FloVacDegasser, while the CTF2 were degassed/activated at T = 200 °C for 12 h before the measurement. The N_2 physisorption isotherms were recorded at 77 K. The specific surface area (SSA) for each sample was determined by the Brunauer–Emmet–Teller method (BET) using data points at a relative pressure p/p_0 between 0.05 and 0.3. The total pore volume was determined at a relative pressure of 0.98. The pore size distribution was calculated using the density functional theory (DFT) N_2 model for CTF1, while non-local density function theory (NLDFT) method (assuming a slit-like pore shape) were used for CTF2.

A.2 Electrochemical characterization

The experiments in linear scanning voltammetry (LSV), cyclic voltammetry (CV), and electrochemical impedance spectroscopy were conducted in a three-electrode electrochemical cell using glassy carbon electrodes (CH Instruments, diameter 3 mm) as working electrodes. An SP-300 potentiostat (*Biologic Instruments*) was used as a workstation for all electrochemical characterizations. The reference electrode used is a saturated SCE, while the CE is a spiral of Pt. All applied potentials were measured against a reference electrode and converted to the RHE reference scale:

$$E_{RHE} = E_{App(SCE)} + 0.241V + 0.0591 \times pH \quad \text{(A.1)}$$

The electrolytes used vary according to the system studied. In the case of MWCNT@CeO_2 (Chapter I), HNO3 0.1 M and PB 0.2 M was used, while for CNH@CeO_2, KHCO3 0.5 M was used. The electrochemical characterization for bismuth oxide sample (Chapter II) and nickel oxide samples (Chapter III) the KOH 0.1 M was used.

For the electrochemical characterization the different catalysts were deposited on the glassy carbon electrode by drop-casting, reaching a loading of 505 µg cm^{-2} for the materials in chapter I (except for MWCNT@CeO_2 at 170 µg cm^{-2}) and II, while for nickel composites in chapter III, the loading used is 207 µg

cm^{-2}. The inks used have a concentration of 1.6 mg mL^{-1} and they are generally composed of ⅔ of MilliQ water, ⅓ of isopropanol and 0.5% of Nafion®, to ensure good film stability, without compromising the reactions involved. In the case of NiO and CTF based samples it was necessary to readjust the ink solutions due to their high hydrophobicity: the Ni-CTFs were dispersed in ethanol and 0.5% Nafion with concentration of 1.6 mg mL^{-1}; while the CTF-2 support was dispersed in DMF and 0.5% Nafion at the same concentration. The only solvent capable of dispersing the CTF-1 compound is DMSO with 0.5% Nafion. Unfortunately, this solvent requires too long evaporation times, which make it impossible to obtain a good deposit for an electrochemical characterization.

A.3 Electrochemical measurement protocol for CO_2RR

A SP-150 potentiostat (*Biologic Instruments*) workstation and a custom-made electrochemical cell with three-electrode configuration were used for the CO_2RR electrochemical measurements. This electrochemical cell was made to couple with the Gas Chromatograph for online product analysis. The peculiarity of this electrochemical cell is the position of the working electrode, which is in the lower part of the cell, with the electrode face facing upwards, positioned near the gas outlet hole. In this configuration, the gas bubbles that form on the electrode detach from it and enter directly into the line for the analysis of gas products (Figure A.1) Also in this case the CE is custom-made, with a Pt spiral/mesh contained in a glass pipe and separated from the main electrolyte through porous frit, in this way the CO_2 reaction products cannot reach the CE and oxidize. The effectiveness of the porous frit in separating the products was tested by analyzing the CE electrolyte, in which no CO_2 reduction products were detected. The RE is a Ag/AgCl (LowProfile 3.5mm OD of *PINE research*). The peculiarity of this electrode is the use of a gel instead of a KCl solution. The gel and the ceramic porous frit guarantee a low mobility of the chloride ions, preventing them from escaping from the electrode and consequent poisoning of the catalyst. To ensure the stability of the RE and its lack of ion depletion, before each CO_2RR measurement, the potential of the RE was measured. The WEs used are glassy carbon plate, which are cleaned using diamond pastes (*Struers*) with decreasing granulometry (3 µm, 1 µm and 0.25 µm). It has been shown that the use of diamond pastes is the best method for cleaning electrodes with application for CO_2RR, as Al_2O_3 suspension tends to remain on the electrode surface and helps to increase HER in the reduced condition.[1,2] The electrochemical cell used allows the use of small volumes of electrolyte, ranging from 4 to 6 ml depending on the material and the currents involved. The CO_2 flow is always regulated by a mass flow control and kept at 5 sccm during the electrochemical measurements. The GC is calibrated once a week, using a gas mixture of known concentrations of 5, 20 and 100 ppm of H_2, CO, CH_4, CO_2, C_2H_4 and C_2H_6 (*Air Liquide*). Due to the amount of hydrogen developed by some electrocatalysts it was necessary to add a standard at concentrations higher than 1000 ppm.

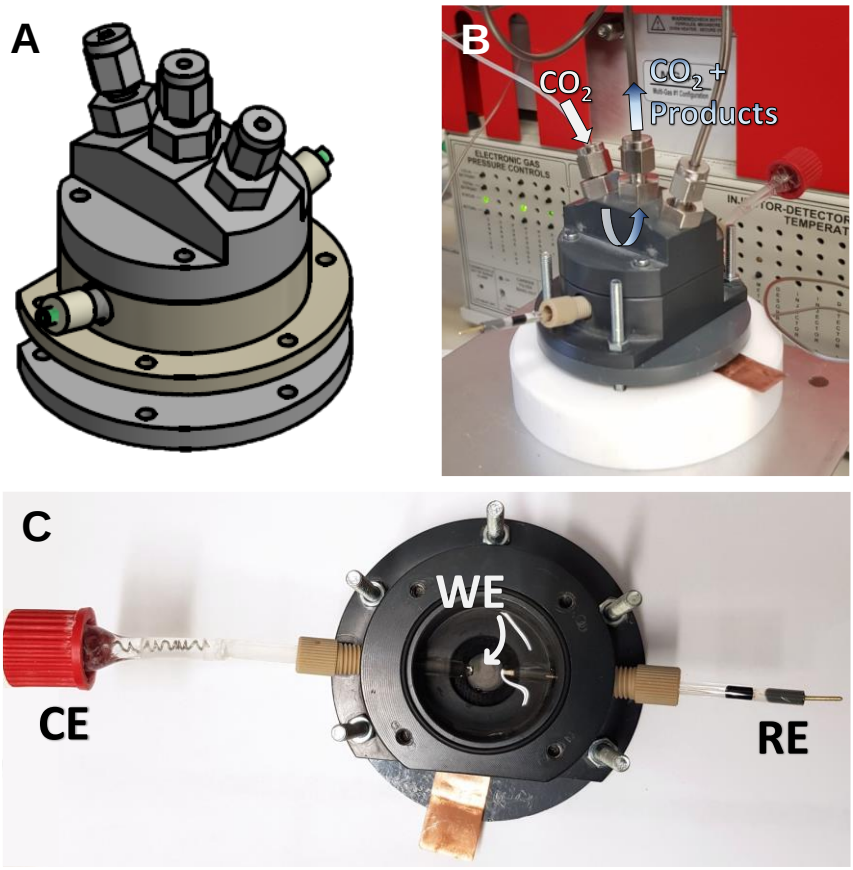

Figure A.1 ***Costume-made Electrochemical Cell.*** *A) Graphic design of the electrochemical cell project. B) The electrochemical cell connected to the gas chromatograph, with the indication of the CO_2 gas flow. C) Open electrochemical cell, where the various electrodes (WE, RE and CE) are indicated.*

The electrolyses were performed in a near-neutral bicarbonate buffer, $KHCO_3$ 0.5 M. This electrolyte was pre-electrolysed before use to guarantee high purity, as it is known that even small amounts of metal impurities can lead to surface interference with electrochemical reactions. Pre-electrolysis was carried out in a cell with two-electrodes configuration, with Pt wire as a counter electrode and a Pt mesh as a working electrode; electrolysis of electrolyte was performed for at least 24 h at a current of -0.1 mA while stirring the solution and Ar-saturated.[3]

As for electrochemical characterization, the same inks and loading of materials were used for CO_2RR study, but in this case a bigger electrode area was used (GCE, geometric surface area 1 cm^2). The electrode area is important because the larger the electrode area, the higher the concentration of the reaction products, in this way the detection limit of the instrument (GC) is exceeded, guaranteeing the reliability and reproducibility of the measurements. While the characterizations of NiO-CTFs (Chapter III were carried out on electrodes with an area of 2.5 cm^2, for a matter of cell configuration.

The CO_2RR activity was evaluated by chronoamperometry (CA) of 1 hour and 51 minutes in CO_2-saturated electrolytes. The gaseous products were analyzed during measurements by on-line Gas Chromatography (GC) directly connecting the headspace of the electrochemical cell to the sample loop of a GC, while formic acid

was detected by analysis of the liquid phase by Ionic Chromatography (IC) at the end of electrolysis. In the case of MWCNT@CeO_2 the liquid products were also analyzed with ^{1}H- NMR to confirm the analyses carried out with IC. The gas phase quantification was carried out during the electrolysis with sampling every 15 minutes. The Faradaic Efficiency (FE) for the gas products of CO_2RR was quantified following the procedure previously described by Baltrusaitis *et al.*[4]:

$$FE\ (\%)\ =\ \frac{nF\varphi F_m}{I} \tag{A.2}$$

where n is the number of electrons needed for CO_2RR; F is the Faraday constant; φ is the volume fraction of the gas; I is the current and F_m is the molar CO_2 gas flow rate.

While the analyses of the liquid products were performed by means of a Metrohm model 850 Professional IC Ion Chromatograph equipped with a Metrosep a Supp 4-250/4.0 anion column and a conductivity detector. The eluent used was 0.5 mM H_2SO_4, with 15% acetone. The Faradaic Efficiency (FE) for the formic acid products was quantified following way:

$$FE = \frac{Q(COO^-)}{Q_{TOT}} * 100 \tag{A.3}$$

Development of the measurement protocol

To establish a measurement protocol, an electrodeposited copper film was initially used to test the coupling of the electrochemical cell with the gas chromatograph. Copper was chosen as this material can produce a large number of gaseous reaction products (CO, CH_4 and C_2H_6). The copper was electrodeposited on a glassy carbon electrode (3 mm of diameter), using the procedure previously described by *Verlato et al*.[5] Two copper films were deposited: one under stirring and one under static conditions. The film deposited under stirring shows a more homogeneous surface and a more compact film (Figure A.2 A), compared to the film deposited under static conditions. The latter shows a three-dimensional dendritic surface (Figure A.2 B), which following the CO_2RR leads to its partial dissolution in solution and an easier oxidation to the air (Figure A.2 C). The FE

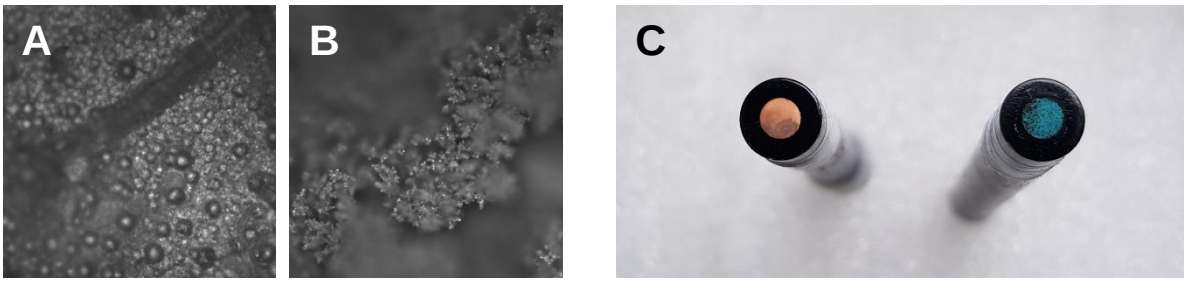

Figure A.2 Optical microscope image of two different electrodeposited Cu films A) under stirring and B) under static conditions. C) Photo of the copper electrodes: on the left the deposit of (A) before the CO_2RR, while the one on the right is the copper film (B) after the CO_2RR.

values recorded for this Cu film were compared with those reported by Jaramillo (Figure A.3), who used a modified H-cell.[6] The trend of the gaseous products is similar to those identified by Jaramillo's experiments, but in our case, the FE of the hydrocarbons are decidedly underestimated compared to those identified in the paper, moreover the HER minimum is anticipated. From these preliminary analyzes we have seen some parameters to be adjusted: (i) keep the bubbling of CO_2 in the electrolyte active even during electrolysis, so as to reduce the depletion of CO_2 from the electrolyte (previously the flow was kept swinging); (ii) use a more concentrated electrolyte to increase the concentration of CO_2 in the electrolyte and reduce the ohmic drop; (iii) to study how the electrode area can influence the determination of the reaction products.

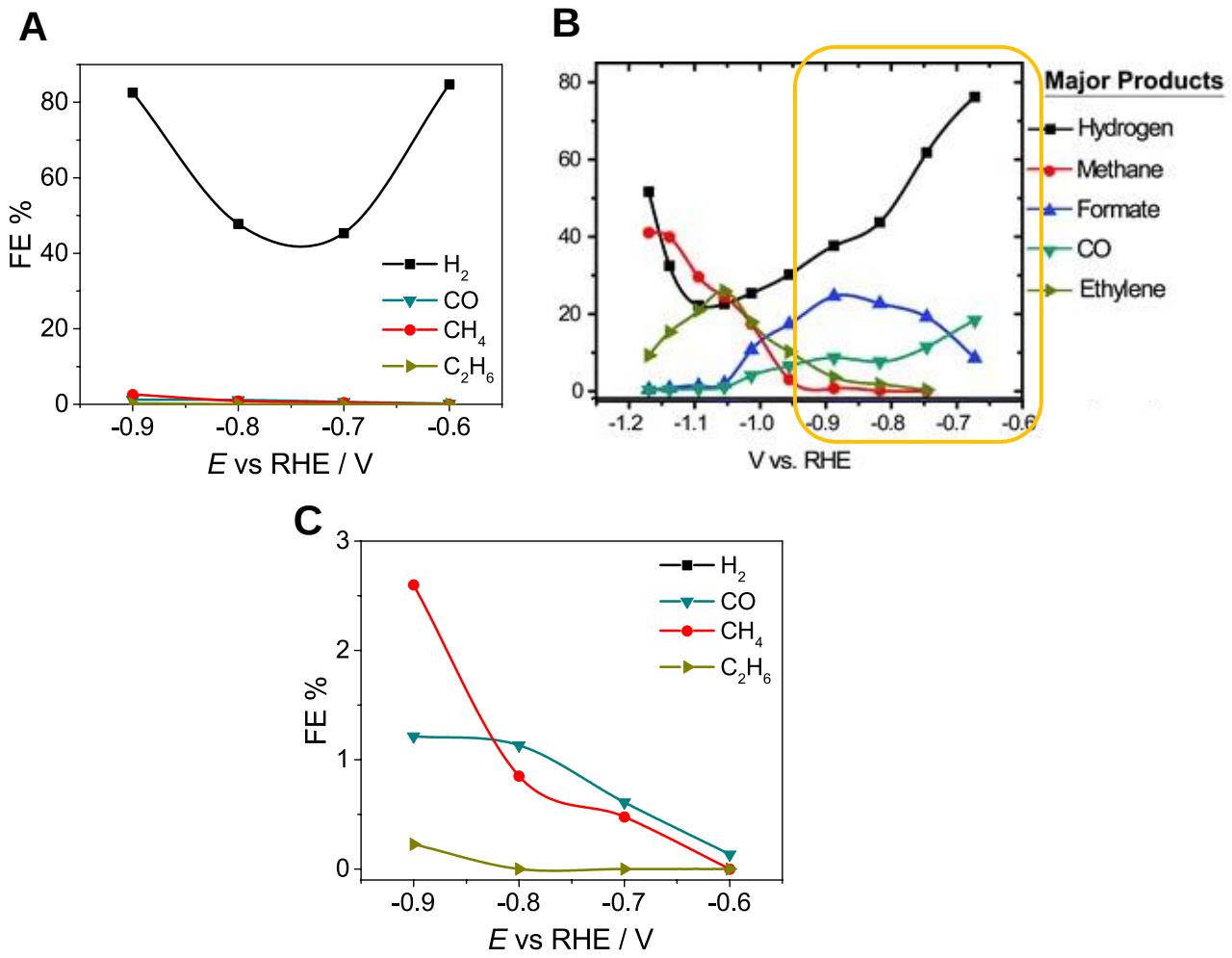

Figure A.3 Faradaic Efficiency (FE) values of detectable gas CO_2RR products: H_2 (black), CO (cyan), CH_4 (red) and C_2H_6 (green) for A) Cu film in CO_2-saturated $KHCO_3$ 0.1 M. The C) is a zoom of A graph, while B) is the graph of Jaramillo's paper [Adapted from Energy Environ. Sci., 2012, 5, 7050].[6] The area selected in yellow highlights the potentials studied by us.

To study the effect of the geometric area of the electrode on the determination of the concentration of gaseous products, electrodeposited silver on a glassy carbon plate was used, the area of which was modified using masks and O-rings to ensure the watertight seal of the cell. Ag has been chosen in this because it has a single reaction product of the CO_2 reduction, and that is CO, and above all the selectivity of the Ag does not depend on its crystallographic faces as for Cu.[1,7] The procedure adopted for the electrodeposition of Ag is

previously described by *Papanastasiou et al*.[8] Three diameters were selected: 3 mm, 6 mm and 11.2 mm. From these diameters the following areas are obtained: 0.071 cm^2, 0.28 cm^2, 1 cm^2. The FE of the CO were reported in Figure A.4. For the area at 1 cm^2, the calculated FE are twice as high, if not more, than those identified for the area of 0.28 cm^2. Furthermore, these values are in line with those identified in the literature.[9] Without forgetting that at -0.5 V vs RHE with an area of 1 cm^2 it is possible to identify the production of CO, albeit in very small values. From these data it can be seen that the electrode area has an enormous influence in the detection of the products and therefore in the determination of the FE. In fact, in a system in which the electrode area is too small there is a risk that the concentration of the reaction products is below the detection limit of the instrument, and this leads to an inevitable underestimation of the electrocatalytic performances. For this reason, it was decided to adopt the area of 1 cm^2 for the study of experimental electrocatalysts.

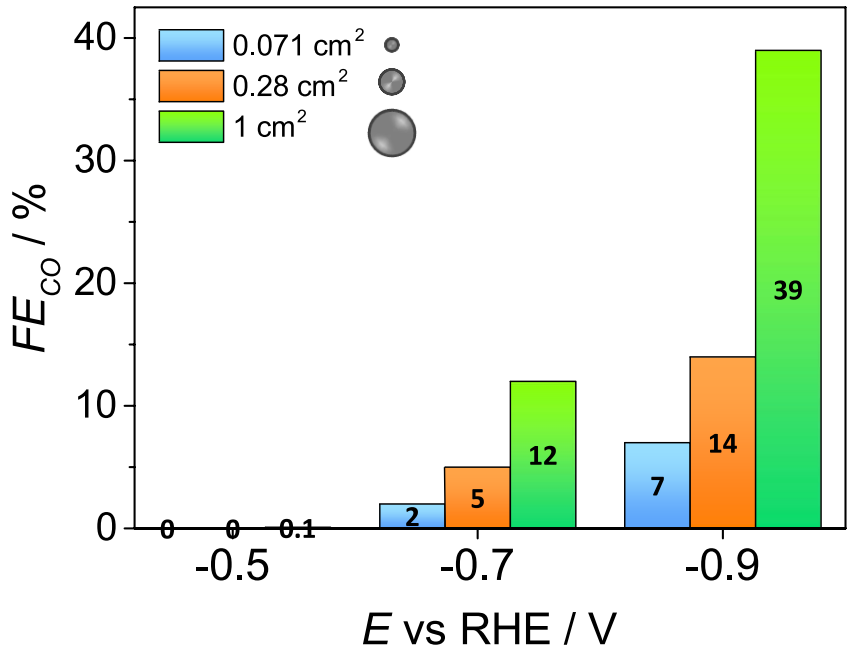

Figure A.4 Faradaic Efficiency (FE) of CO for electrodeposited Ag film on GCE with area of 0.071 cm^2 (light blue), 0.28 cm^2 (orange) and 1 cm^2 (green) in CO_2-saturated $KHCO_3$ 0.1 M.

A.4 Differential electrochemical mass spectrometry (DEMS) measurements

The electrochemical measurements in chapter 1.4 were performed with a home-built DEMS configuration (described in detail elsewhere).[10] A thin bilayer cell with a flow cell geometry was used to achieve well-defined mass transport conditions (already described in detail elsewhere).[11] The CO_2RR measurements were made under CO_2-saturated conditions. Then for all CO_2RR measurements, a CO_2 saturated electrolyte (0.1 M

$LiHCO_3$ + 0.4 M $LiClO_4$, 0.1M $NaHCO_3$ + 0.4 M $NaClO_4$, 0.5 M $KHCO_3$ and 0.5 M $CsHCO_3$) was introduced into the top of the cell where the electrode was placed of work. For all CO_2RR studies, CVs were recorded indicatively between -0.2 V and -0.8 V vs RHE, at a scan rate of 5 mV s^{-1}. The electrolyte flow (5 µL s^{-1}) through the cell was achieved with a syringe pump which swept the electrolyte (along with the reaction products and unreacted analyte) from the upper compartment to the lower compartment of the cell which it was interfaced with the vacuum of the mass spectrometer with the aid of a porous Teflon membrane and a porous steel frit. The products of HER and CO_2RR were detected at the ionic signal at m/z 2 (H_2) and m/z 28 (CO), respectively. The ionic current obtained with the DEMS is related to the molar flux of the species from (A.3):

$$I_{ionic(i)} = \frac{dn_{(i)}}{dt} \times K * \tag{A.4}$$

where, $I_{ionic(i)}$ is the ionic current due to a species i, $dn_{(i)}/dt$ is the molar flux of i into the mass spectrometer and K^* is a proportionality constant that reflects the sensitivity of the DEMS setup for i, which is dependent on the ionization probability of i. The molar flux is connected to the faradaic current $I_{Faradaic(i)}$ by (A.5) equation:

$$\frac{dn_{(i)}}{dt} = \frac{I_{faradaic(i)} \times N}{zF} \tag{A.5}$$

where N is the transfer efficiency of species i in a given cell geometry/assembly, z is the number of electrons involved in the electrochemical reaction and F is Faraday constant. By substitution of (A.5) into (A.4) equation, we obtain:

$$I_{ionic(i)} = I_{ionic(i)} \frac{I_{faradaic(i)} \times K°}{zF} \tag{A.6}$$

where $K° = K * \times N°$ is the cell calibration constant. This last parameter changes every time the cell is opened, so the system must be calibrated every time the cell is assembled and calculated for the individual species H_2 and CO. For the $K°$ of H_2, the system is calibrated in conditions of Ar-saturated electrolyte, where the system produces 100% of the H_2:

$$K°_{H_2} = \frac{I_{ionic(H_2)} \times zF}{I_{faradaic(HER)}} \tag{A.7}$$

While for the $K°$ of CO one works in conditions of CO_2-saturated electrolyte by exploiting the CO oxidation current:

$$K^{\circ}_{CO} = \frac{I_{ionic(CO)} \times zF}{I_{faradaic(CO\ ox.)}} \quad \text{(A.8)}$$

The ionic signals obtained at mass 2 and mass 28 during CO_2RR measurements can be used to calculate the partial current densities for H_2 and CO formation using the equation (A.6). Finally, from these parameters the FE for CO_2RR and HER can be calculated:

$$FE_{CO_2RR} = \frac{I_{faradaic(CO)}}{I_{faradaic(CO)} + I_{faradaic(H_2)}} \times 100 = \frac{I_{faradaic(CO)}}{I_{measured}} \times 100 \quad \text{(A.9)}$$

$$FE_{HER} = \frac{I_{faradaic(H_2)}}{I_{faradaic(CO)} + I_{faradaic(H_2)}} \times 100 = \frac{I_{faradaic(H_2)}}{I_{measured}} \times 100 = 100 - FE_{CO_2RR} \quad \text{(A.10)}$$

Basically, from the determination of the calibration constants it is possible to use the online DEMS technique for the quantitative study of CO_2RR.

A.5 Carbon Nanostructures decorated with Cerium Oxide in multi-functional electrocatalysts for CO_2 reduction

- ## Synthesis of MWCNT@CeO_2 and CNH@CeO_2

As a first step uncontaminated MWCNTs were oxidized with a mixture of H_2SO_4 and HNO_3. In detail, 150 mg of uncontaminated MWCNT (NanoAmor) was dispersed in a concentrated mixture of concentrated H_2SO_4/HNO_3 (3: 1 v/v, 100 mL) by sonication (6 h at 30-50 °C) and magnetic stirring (12 h at 50 °C). The suspension was washed six times by filtration [twice with water (250 mL), twice with NaOH (0.1 M, 250 mL), once with dimethylformamide (DMF) (250 mL) and once with tetrahydrofuran (THF) (250 mL)] from which Ox-MWCNT was obtained.

MWCNTs@CeO_2 structures were prepared with a sol-gel method. The appropriate amount of Ce^{4+} tetrakis (decyloxide) was dissolved in 25 mL of tetrahydrofuran (THF). Subsequently, the solution was added to the Ox-MWCNT EtOH dispersion and maintained under sonication for 30 minutes. Subsequently a mixture of H_2O (1 mL) and THF (10 mL) was added to ensure complete hydrolysis of the alkoxide precursor, and the mixture was sonicated for another 15 minutes. The solid was then recovered by filtration and washed with THF three times and then dried at 120 °C overnight. Finally, the solid obtained was calcined at 250 ° C in static air. The

procedure adopted for the synthesis of CNH@CeO_2 is the same as described above, the only change introduced is the different amount of CeO_2 precursor added. Three different amounts of precursor were evaluated in order to obtain a different loading of CeO_2 on the CNHs. Finally, the CeO_2 reference material was prepared in a similar way, but in the absence of Ox-MWCNT.

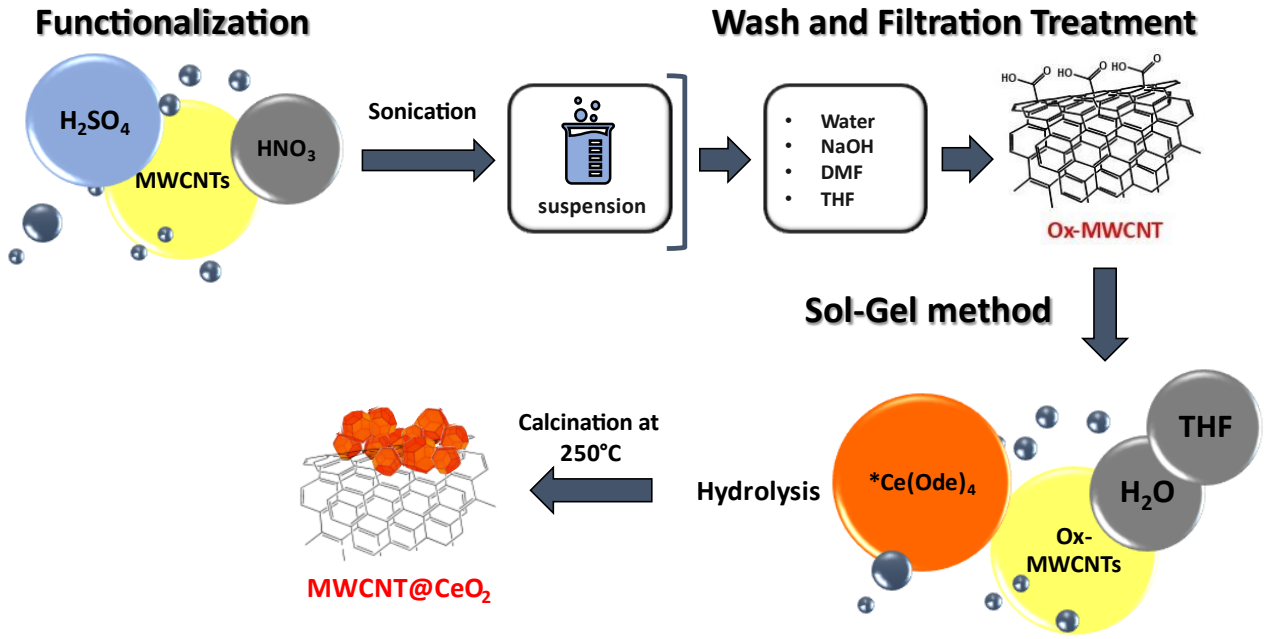

*Figure A.5 Complete synthesis scheme of MWCNT@CeO_2. * Ce^{4+} tetrakis (decyloxide)*

- Thermogravimetric Analysis (TGA) of MWCNT@CeO_2

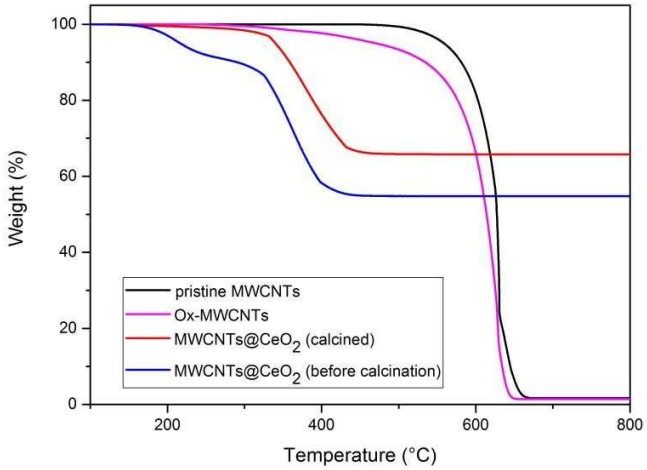

Figure A.6 TGA profiles recorded under air flow of pristine MWCNTs (black), ox-MWCNTs (pink), calcinated nanocomposite MWCNTs@CeO_2 (red) and the fresh nanocomposites MWCNTs@CeO_2 (blue).

A.6 The electrocatalytic performance for CO2 reduction through interface tuning in graphene oxide-bismuth oxide nanocomposites

- Synthesis of bismuth oxide and GO nanocomposites

Graphene Oxide

The GO was prepared by adopting the same procedure previously reported.[12] First, 200 mg of pristine graphene was added into a 100 mL round-bottomed flask with $K_2S_2O_8$ (200 mg, 0.37 mmol), P_2O_5 (100 mg, 0.35 mmol), and H_2SO_4 (10 mL). The solution was sonicated for 30 min and stirred at 80 °C for 4 h. The crude was cooled down, diluted with deionized water (50 mL), filtered through a Millipore membrane (JHWP, 0.45 µm), and washed with deionized water until neutralization of the washings. The black powder collected from the Millipore membrane was transferred into a round-bottom flask and dispersed in 20 mL of H_2SO_4 at 0 °C. Then, 100 mg of $KMnO_4$ (0.63 mmol) were added into the dispersion under stirring. The final was stirred at 35 °C for 2 h. After that, deionized water (20 mL) and H_2O_2 30% (2.4 mL) were added, and the reaction was stirred for 15 min. The crude was filtered through a Millipore membrane (JHWP, 0.45 µm) and washed with HCl 1 M (100 mL) and deionized water until neutralization of the washings occurred. Finally, the black powder was washed one time with MeOH and dried with Et_2O, affording 210 mg of GO.

Bi@BiOx Nanoparticle

The pristine Bi@BiOx core-shell nanoparticles were prepared by a solvothermal method by adapting a previously reported procedure.[13] The precursor of bismuth, $Bi(NO_3)_3{\cdot}5H_2O$ was dissolved together with glucose in a molar ratio (1:1.5) in ethylene glycol, so as to have a concentration of 0.067 and 0.1 M, respectively. The solution was stirred for 30 minutes and then transferred to a Teflon-lined stainless autoclave, which was heated to 120 °C for 12 hours. Once concluded, the black solid was recovered by centrifugation and subsequently washed with H_2O and ethanol.

Bi@Bi_2O_3 Nanoparticles

The as prepared Bi@BiO_x nanoparticles were subjected to calcination at 250 °C under static air atmosphere, with a ramp of 3 °C min^{-1}.

GO/Bi@BiO_x Nanocomposite

GO and Bi@BiO_x NPs were prepared in different weight ratios (3:1, 4:1, 5:1). The two compounds were dispersed ethanol with a GO dispersion of approximately 2:1 mg mL^{-1}, and subsequently sonicated. After

sonication, the mixture was stirred at room temperature for 24 hours. Finally, the solid was recovered by centrifugation.

GO/Bi_2O_3 Nanocomposite

The as prepared GO/Bi@BiO_x samples were subjected to calcination at 250 °C under static air atmosphere, with a ramp of 3 °C min^{-1}.

rGO/Bi@Bi_2O_3 Nanocomposite

The as prepared GO/Bi@BiO_x samples were subjected to thermal treatment at 250 °C in a tubular furnace under a flowing stream of a mixture of H_2/Ar (the flow was 230 mL min^{-1}, with 30 mL of H_2 and 200 mL of Ar).

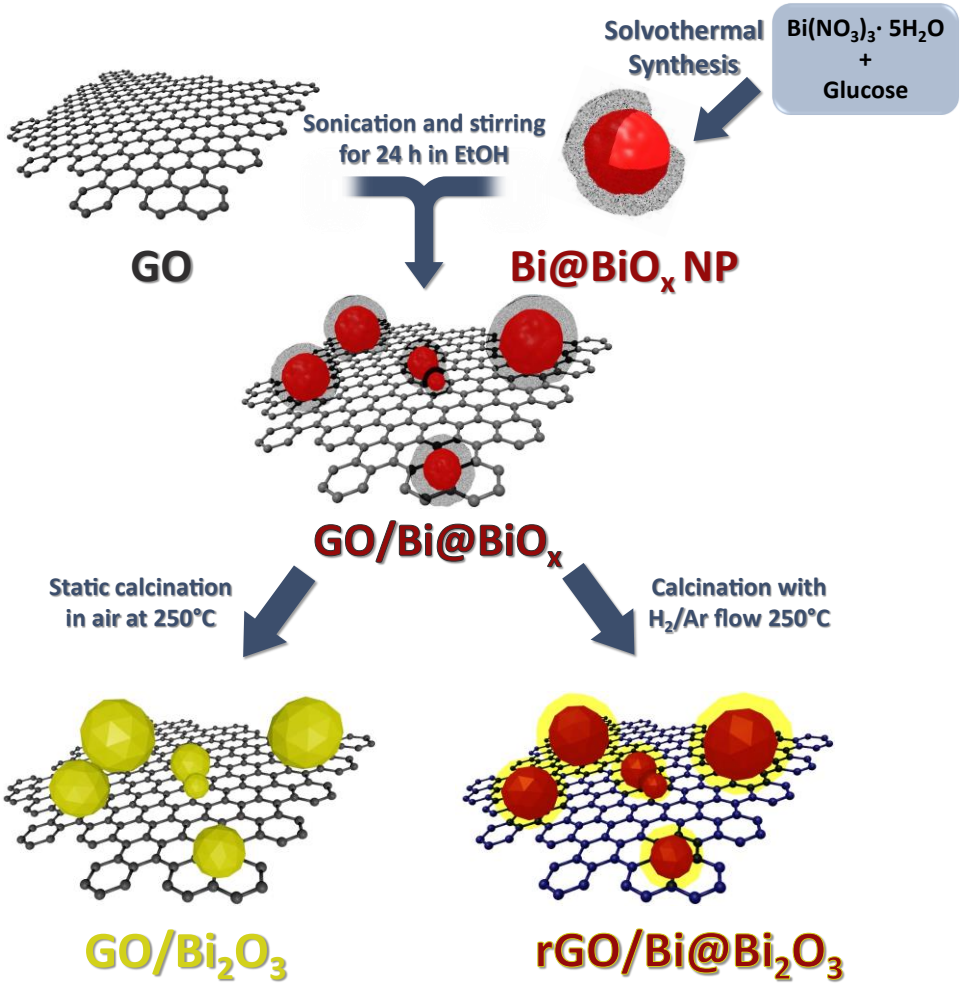

Figure A.7 Synthesis scheme of bismuth oxide and GO nanocomposites.

- TEM Analysis

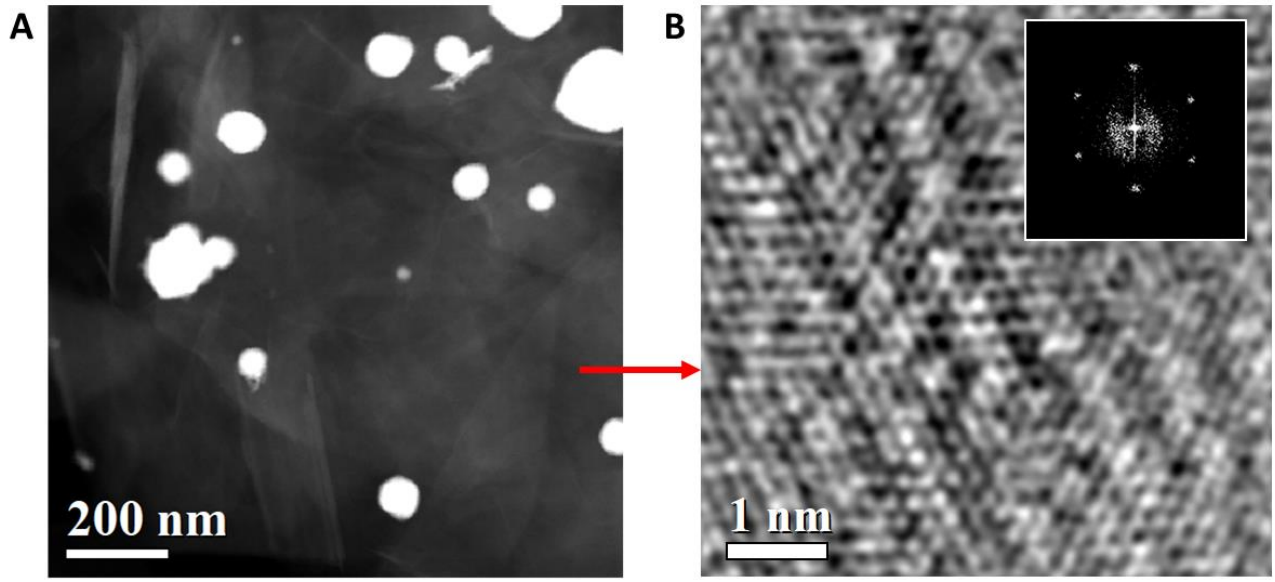

Figure A.8 A) HAADF-STEM image of the Bi@BiO$_x$ NP dispersed on the GO, B) Filtered HRTEM image of a selected area in (red arrow) with the corresponding FFT in the inset, showing the typical 6-fold symmetry of a monolayer GO.

- CO_2RR catalytic performance

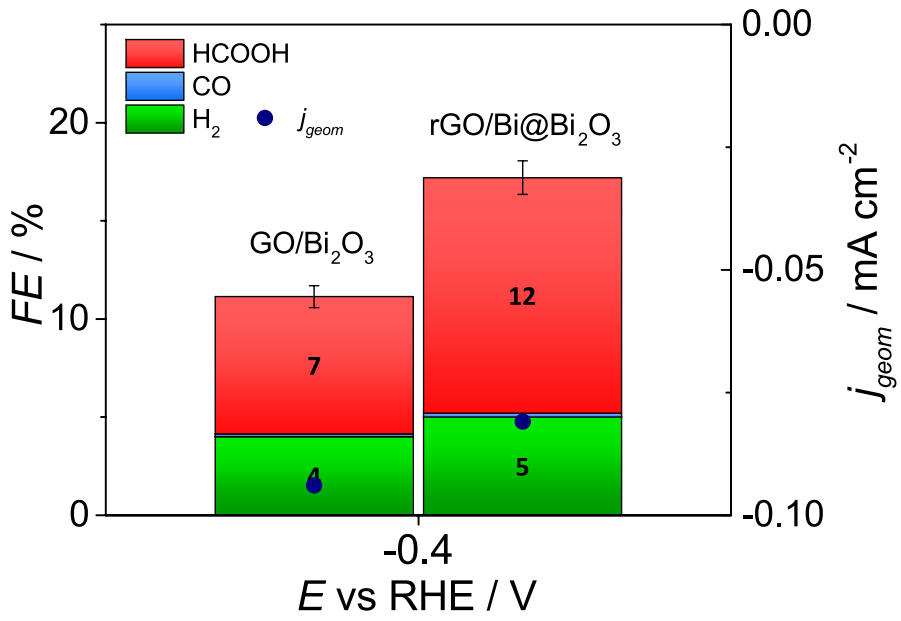

Figure A.9 . Faradaic Efficiency (FE) values are shown on left axis of detectable CO_2RR products: H_2 (green), CO (light blue) and HCOOH (red) for GO/Bi_2O_3 and rGO/Bi@Bi_2O_3 at -0.4 V vs RHE in CO_2-saturated $KHCO_3$ 0.5 M. The blue points indicate the mean current density; the values are shown on right axis.

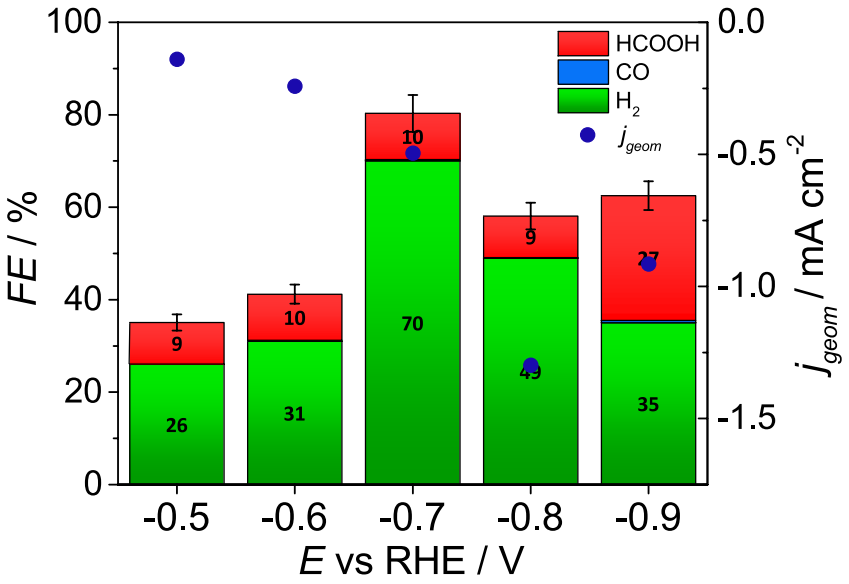

Figure A.11 Faradaic Efficiency (FE) values are shown on left axis of detectable CO_2RR products: H_2 (green), CO (light blue) and HCOOH (red) for GO/Bi_2O_3 3:1 in CO_2-saturated $KHCO_3$ 0.5 M. The blue points indicate the mean current density; the values are shown on right axis.

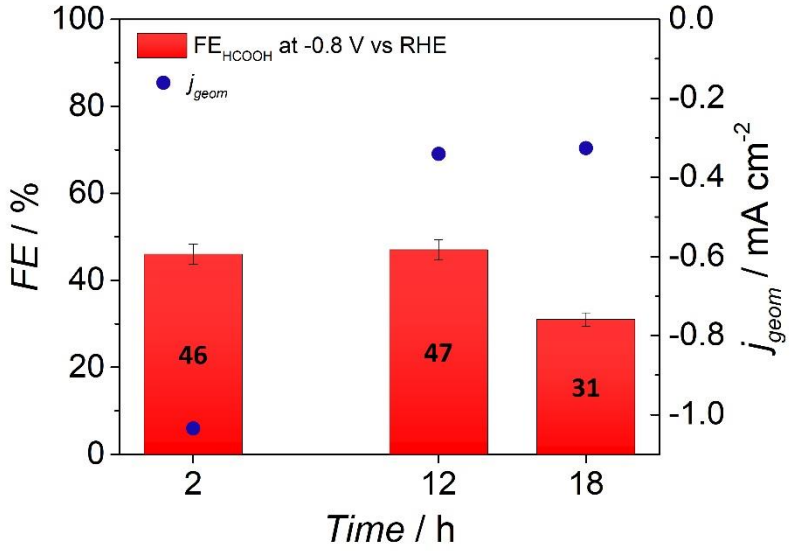

Figure A.10 ***Stability.*** *HCOOH Faradaic Efficiency and mean current density of GO/Bi_2O_3 at -0.8 V vs RHE in CO_2-saturated $KHCO_3$ 0.5 M at different time (2,6, 12 and 18 h). The blue points indicate the mean current density of sample at that potential; the values are shown on right axis.*

A.7 Nickel Oxide nanoparticles on Covalent Triazine Framework for Syngas production

- Synthesis of NiO-CTF1 and NiO-CTF2 nanocomposites

Covalent Triazine Frameworks

CTF materials were synthesized by ionothermic synthesis in quartz glass ampoules according to the procedures reported in the literature.[14,15,16,17] The monomers used are 1,4-dicyanobenzene (p-DCB) for CTF1 and 1,3-dicyanobenzene (1,3-DCB) for CTF2. In general, the CTF1–2 were prepared as follows: 3 g of the selected monomer were finely mixed and subsequently ground with 5 equivalents of $ZnCl_2$ inside a glove box and transferred to a quartz vial (12 cm high and 3 cm in diameter). Subsequently, the material was dried under vacuum for at least 3 h, after which the ampoule was sealed with a flame, placed inside an oven and heated up to 400 °C with a heating ramp of 10 °C · min^{-1}. Once the temperature of 400 °C was reached, it was maintained for 10 h before further increasing the temperature to 600 °C (second heating phase) and maintaining it for another 10 h. After heat treatment, the vials were allowed to cool to room temperature and opened, from which the monolithic solids were recovered. Subsequently, the solids were first ground and washed thoroughly with water and diluted HCl (0.1 M), and then finely ground using a laboratory ball mill (Fritsch Pulverisette 23, 5 min, 30 Hz) to obtain black powders, which were washed again in sequence with water, diluted HCl, diluted NaOH, water and THF. At the end of the synthesis, the materials were dried under vacuum at constant weight (at least 12 hours at 60 ° C). CTFs were obtained with an almost quantitative yield (≥90% after work-up). Two clarifications: it is necessary to pay particular attention to the opening of the ampoules after the heat treatment, as they are under pressure and can release it during this passage; moreover, to avoid the bursting of the ampoules inside the oven, they have been loaded up to a maximum of half their volume.

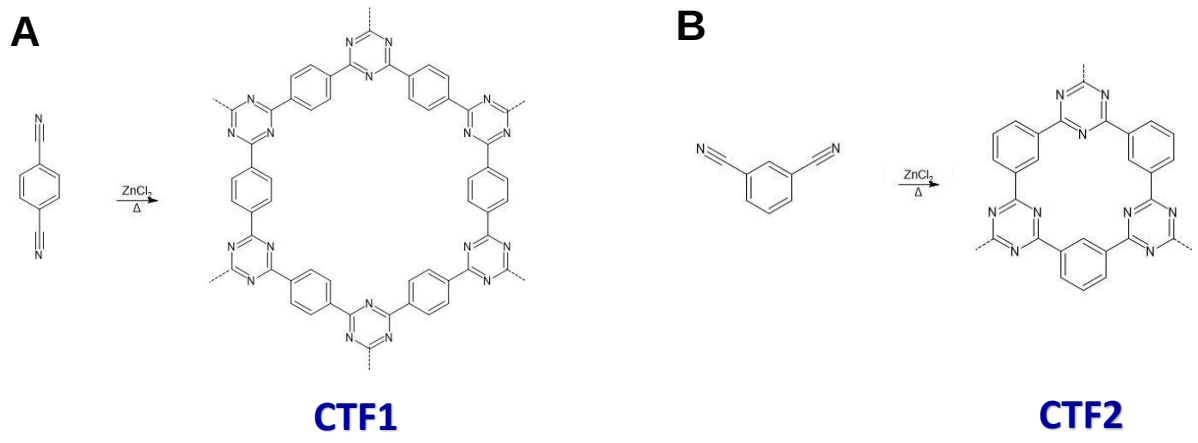

Figure A.12 Monomer A) 1,4-dicyanobenzene (p-DCB) and B) 1,3-dicyanobenzene (1,3-DCP) conversion into covalent triazine frameworks (CTFs) CTF1 and CTF2 respectively, using molten $ZnCl_2$ as solvent.

NiO-CTFs Nanocomposites

The NiO nanoparticles were synthesized directly on the CTFs using the Metal Vapor Synthesis method. All the synthesis operations were performed in a dry argon atmosphere. The condensation of nickel and mesitylene/1-hexene were carried out in a static reactor, previously described in literature.[18] Ni/mesitylene-1-hexene solution (1 mL, 5 mg Ni) was added to a suspension of CTF (0.500 g) in mesitylene (10 mL). The mixture was stirred for 24 hours at room temperature. The colourless solution was removed and the dark grey solid, containing in Ni, was washed with n-pentane, and dried under reduced pressure.

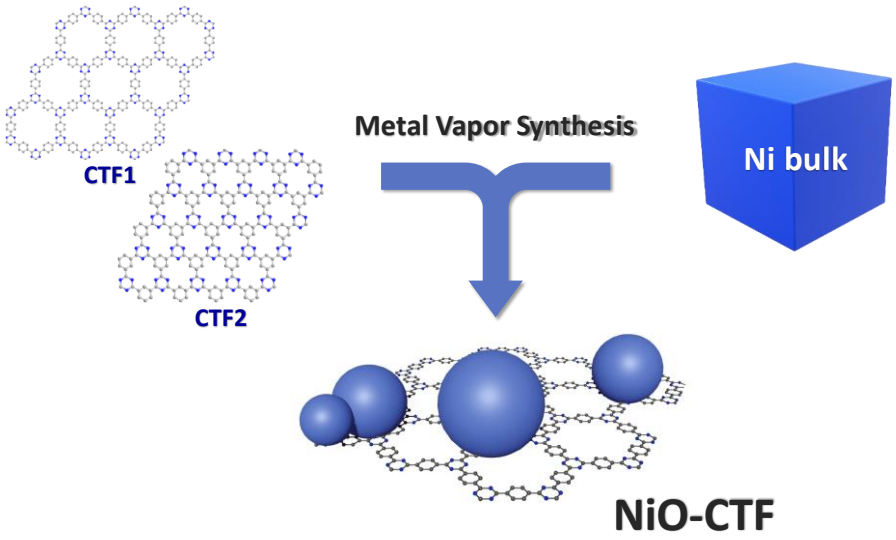

Figure A.13 Synthesis scheme of NiO-CTFs nanocomposites.

Reference

1. Clark, E. L. *et al.* Standards and Protocols for Data Acquisition and Reporting for Studies of the Electrochemical Reduction of Carbon Dioxide. *ACS Catal.* **8**, 6560–6570 (2018).

2. Monteiro, M. C. O. & Koper, M. T. M. Alumina contamination through polishing and its effect on hydrogen evolution on gold electrodes. *Electrochim. Acta* **325**, 134915 (2019).

3. Hori, Y. *et al.* 'Deactivation of copper electrode' in electrochemical reduction of CO2. *Electrochim. Acta* **50**, 5354–5369 (2005).

4. Kas, R. *et al.* Electrochemical CO2 reduction on Cu2O-derived copper nanoparticles: Controlling the catalytic selectivity of hydrocarbons. *Phys. Chem. Chem. Phys.* **16**, 12194–12201 (2014).

5. Verlato, E. *et al.* Electrodeposition of Cu+PdO and (Cu–Pd)+PdO Composites. *J. Electrochem. Soc.* **157**, D248 (2010).

6. Kuhl, K. P., Cave, E. R., Abram, D. N. & Jaramillo, T. F. New insights into the electrochemical reduction of carbon dioxide on metallic copper surfaces. *Energy Environ. Sci.* **5**, 7050–7059 (2012).

7. Kortlever, R., Shen, J., Schouten, K. J. P., Calle-vallejo, F. & Koper, M. T. M. M. Catalysts and Reaction Pathways for the Electrochemical Reduction of Carbon Dioxide. *J. Phys. Chem. Lett.* **6**, 4073–4082 (2015).

8. Zarkadas, G. M., Stergiou, A. & Papanastasiou, G. Influence of citric acid on the silver electrodeposition from aqueous AgNO3 solutions. *Electrochim. Acta* **50**, 5022–5031 (2005).

9. Guo, W. *et al.* Highly active coral-like porous silver for electrochemical reduction of CO2to CO. *J. CO2 Util.* **41**, 101242 (2020).

10. Bondue, C. J. & Koper, M. T. M. A DEMS approach for the direct detection of CO formed during electrochemical CO2 reduction. *J. Electroanal. Chem.* **875**, 113842 (2020).

11. Abd-El-Latif, A. A. *et al.* Insights into electrochemical reactions by differential electrochemical mass spectrometry. *TrAC - Trends Anal. Chem.* **70**, 4–13 (2015).

12. Iglesias, D. *et al.* Oxidized Nanocarbons-Tripeptide Supramolecular Hydrogels: Shape Matters! *ACS Nano* **12**, 5530–5538 (2018).

13. Chen, M. *et al.* Controllable Synthesis of Core-Shell Bi@Amorphous Bi2O3 Nanospheres with Tunable Optical and Photocatalytic Activity for NO Removal. *Ind. Eng. Chem. Res.* **56**, 10251–10258 (2017).

14. Artz, J. *et al.* Sulfonated covalent triazine-based frameworks as catalysts for the hydrolysis of cellobiose to glucose. *RSC Adv.* **8**, 22392–22401 (2018).

15. Artz, J., Mallmann, S. & Palkovits, R. Selective aerobic oxidation of hmf to 2,5-diformylfuran on covalent triazine frameworks-supported ru catalysts. *ChemSusChem* **8**, 772–789 (2015).

16. Tuci, G. *et al.* Playing with covalent triazine framework tiles for improved CO 2 adsorption properties and catalytic performance. *Beilstein J. Nanotechnol* **10**, 1217–1227 (2019).

17. Tuci, G. *et al.* Unraveling Surface Basicity and Bulk Morphology Relationship on Covalent Triazine Frameworks with Unique Catalytic and Gas Adsorption Properties. *Adv. Funct. Mater.* **27**, 1605672 (2017).

18. Evangelisti, C. *et al.* Palladium nanoparticles supported on polyvinylpyridine: Catalytic activity in Heck-type reactions and XPS structural studies. *J. Catal.* **262**, 287–293 (2009).